THE UNIVERSITY OF CHICAGO

QUANTUM INFORMATION PROCESSING WITH ELECTRONIC AND NUCLEAR SPINS IN SEMICONDUCTORS

A DISSERTATION SUBMITTED TO
THE FACULTY OF THE INSTITUTE FOR MOLECULAR ENGINEERING
IN CANDIDACY FOR THE DEGREE OF
DOCTOR OF PHILOSOPHY

BY
PAUL VICTOR KLIMOV

CHICAGO, ILLINOIS
MARCH 2016

to my family, friends, and mentors...

CONTENTS

LIST OF FIGURES vii

LIST OF TABLES ix

ACKNOWLEDGMENTS x

ABSTRACT xiii

1 INTRODUCTION 1
1.1 Perspective 1
1.2 Thesis Organization 4

2 CLASSICAL AND QUANTUM INFORMATION 5
2.1 The Bit 5
2.2 The Qubit 5
2.3 Qubit Relaxation 9
2.4 DiVincenzo Criteria 11

3 SEMICONDUCTOR DEFECT SPINS AS QUBITS 13
3.1 Atom-Like Point Defects in Semiconductors 13
3.2 The Divacancy Family of Defects in Silicon Carbide 16
3.3 Optical Properties of Defects in the Divacancy Family 16
3.4 The Spin Hamiltonian 19
3.5 Encoding Qubits 21
3.6 SiC Defect Qubits and the DiVincenzo Criteria 26
3.7 Conclusions 31

4 IMPLEMENTING QUANTUM ALGORITHMS 32
4.1 Overview of the Apparatus 32
4.2 Confocal Photoluminescence Microscope 32
4.3 Microwave and Radiofrequency Electronics Setup 36
4.4 Cryogenics Setup 38
4.5 Magnet Setup 39

5 TUNING SPINS WITH ELECTRIC FIELDS AND STRAIN 42
5.1 Introduction 42
5.2 Spin Coupling to Electric and Strain Fields 42
5.3 Conclusions 51

6 ELECTRICALLY DRIVEN SPIN RESONANCE 53
6.1 Introduction 53
6.2 Theory of Electrically Driven Spin Resonance 53
6.3 Experimental Setup 57
6.4 Electrically Driven Optically Detected Magnetic Resonance 58

6.5 Control Measurements . . . 60
6.6 Spatially Resolved EODMR . . . 62
6.7 Conclusions . . . 62

7 DYNAMIC POLARIZATION OF NUCLEAR SPINS . . . 64
7.1 Introduction . . . 64
7.2 Theory of Dynamic Nuclear Polarization . . . 65
7.3 Experimental Observation of Dynamic Nuclear Polarization . . . 66
7.4 Conclusions . . . 74

8 ENTANGLEMENT AT AMBIENT CONDITIONS IN A SPIN ENSEMBLE . . . 75
8.1 Introduction . . . 75
8.2 Hybrid 2-Qubit Registers . . . 77
8.3 Register Initialization . . . 77
8.4 Register Readout . . . 79
8.5 Identifying Registers' Electron Spin Transitions . . . 79
8.6 Identifying Registers' Nuclear Spin Transitions . . . 80
8.7 Quantum Gates . . . 80
8.8 Quantum State Tomography . . . 83
8.9 Entanglement . . . 86
8.10 Conclusions . . . 88

9 OUTLOOK . . . 90
9.1 Summary . . . 90
9.2 Outlook . . . 91

A TUNING SPINS WITH ELECTRIC FIELDS AND STRAIN - DETAILS . . . 95
A.1 Strain Calibration . . . 95
A.2 Strain Sensitivity Estimation . . . 96
A.3 ODMR Pulse Sequences . . . 99
A.4 Discussion of PL Intensity Contrasts in ODMR Measurements . . . 101
A.5 Time-Resolved PL for Determining Optical Lifetimes . . . 104
A.6 Theoretical Simulations . . . 105

B ELECTRICALLY DRIVEN SPIN RESONANCE - DETAILS . . . 111
B.1 ODMR and EODMR with $S = 1$ and $S = 3/2$ systems . . . 111
B.2 QL1 Defect Production . . . 113
B.3 EODMR Device and Apparatus Details . . . 114
B.4 Additional Frequency- and Time-Domain Data . . . 115
B.5 Calibrating the Magnetic Field Strength . . . 115
B.6 Interdigitated Capacitor Capacitance . . . 116
B.7 Further Discussion of Coherent Spin Coupling to an AC Electric Field . . . 118
B.8 Calculation of the AC Electric Field Spatial Profile . . . 119
B.9 ODMR Response to a DC Electric Field . . . 121

C DYNAMIC POLARIZATION OF NUCLEAR SPINS - DETAILS 123
C.1 Sample Preparation and Experimental Techniques 123
C.2 Concentration of Optically Polarized Nuclei 124
C.3 ESEEM Measurement of the Hyperfine Spectrum 125
C.4 Sign of Nuclear Spin Polarization 126
C.5 Determining the Nuclear Polarization from ODMR 128
C.6 Fitted Nuclear Polarization at Multiple Nuclear Sites 131
C.7 Further Characterization of the PL6 Excited State 132

D ENTANGLEMENT AT AMBIENT CONDITIONS IN A SPIN ENSEMBLE - DETAILS 134
D.1 Register Hamiltonian 134
D.2 Experimental Apparatus 134
D.3 Multi-Nuclei Registers 136
D.4 Electron Spin Polarization 138
D.5 Register Density Calculation 144
D.6 Identification of Nuclei in R1 and R2 145
D.7 Optical Initialization Calibration 145
D.8 Optical Detection of Nuclear Spins 146
D.9 Coherent Nuclear Spin Control 147
D.10 Calibrating Quantum Gates 150
D.11 Quantum State Tomography 153
D.12 Example Tomography Data 157
D.13 Consolidated Initialization and Entanglement Data 160

E BLUEPRINTS FOR MACHINED PARTS 162

BIBLIOGRAPHY 177

LIST OF FIGURES

2.1 A classical and a quantum bit 6

3.1 A deep level defect in a tetrahedrally coordinated semiconductor 14
3.2 A 4H-SiC unit cell with a basal and c-axis oriented divacancy 17
3.3 Nearest neighbor sites indicated on a basal and a c-axis divacancy 21
3.4 A SiC divacancy defect with a nearby ^{29}Si isotopic defect 24
3.5 Isolating qubits in SiC 27
3.6 Optical and microwave spectroscopy of defects in the divacancy family 28

4.1 A schematic of the apparatus built for performing quantum algorithms 33
4.2 A photograph of the optical setup 35
4.3 A photograph of the electronics setup 36
4.4 A photograph of the cryostat 37
4.5 The cryostat sample space 38
4.6 Some custom coldfingers 40

5.1 The effect of strain on SiC-defect photoluminescence 45
5.2 DC and AC strain sensing using SiC defect spins 46
5.3 AC electric field sensing using SiC defect spins 48
5.4 Photoluminescence contrast and decay of SiC defect spins 50

6.1 Electric- and magnetic-field coupling to SiC defects 55
6.2 Optically detected magnetic resonance in 6H-SiC 56
6.3 Electrically driven optically detected magnetic resonance 59
6.4 Ruling out magnetic-field driving 61
6.5 Spatially confined spin control and GHz-frequency electric field imaging 63

7.1 Dynamic nuclear polarization using SiC defect spins 67
7.2 Dynamic nuclear polarization as a function of magnetic field 70
7.3 Identification of the excited-state spin transitions of SiC defect spins 71
7.4 Temperature dependence of dynamic nuclear polarization 74

8.1 A hybrid two-qubit register in SiC 78
8.2 Characterizing the electron-spin transitions of hybrid registers 81
8.3 Characterizing the nuclear-spin transitions of hybrid registers 82
8.4 Quantum gates and their implementation using hybrid registers 84
8.5 Quantum state tomography of hybrid registers 85
8.6 Entanglement of hybrid register ensembles 87
8.7 Entanglement metrics 88

A.1 Strain-calibration device 96
A.2 Longitudinal relaxation of SiC defect spins 98
A.3 Pulse sequences used for AC strain and electric field sensing 100
A.4 Photoluminescence contrast of SiC defect spins 102
A.5 Photoluminescence contrast versus microwave and optical attenuation 103

A.6 Photoluminescence decay of SiC defect spins . . . 105
A.7 Spin density and energy level structures . . . 106
A.8 Schematic of strain-induced distortions of a SiC defect . . . 108
A.9 Simulation of the effect of strain on the crystal field splittings . . . 109
A.10 The effect of an electric field on the divacancy electron orbitals . . . 110

B.1 Electrically driven optically detected magnetic resonance . . . 116
B.2 Calibration measurement . . . 117
B.3 Simulation of the electric field produced by the electrode device . . . 120
B.4 Optically detected magnetic resonance as a function of DC electric field . . . 122

C.1 Electron spin echo envelope modulation of SiC defect spins . . . 127
C.2 Dynamic nuclear polarization of specific ^{29}Si and ^{13}C sites . . . 131
C.3 Excited state spin transitions of PL6 . . . 133

D.1 Electron spin polarization measurement . . . 142
D.2 Initialization rate of hybrid registers . . . 146
D.3 Optical Readout of Nuclear Spins . . . 147
D.4 Coherent nuclear spin control in SiC . . . 149
D.5 Nuclear Rabi Oscillations of R2 . . . 150
D.6 Quantum Gate Calibration . . . 152
D.7 Tomography Measurements . . . 158
D.8 Quantum state reconstructions after various gates . . . 159
D.9 Entanglement of the R1 ensemble . . . 161

E.1 A coldfinger with 4 RF lines . . . 163
E.2 A two-sided coldfinger with 3 total RF lines (1 of 2) . . . 164
E.3 A two-sided coldfinger with 3 total RF lines (2 of 2) . . . 165
E.4 A Helmholtz coil assembly (1 of 4) . . . 166
E.5 A Helmholtz coil assembly (2 of 4) . . . 167
E.6 A Helmholtz coil assembly (3 of 4) . . . 168
E.7 A Helmholtz coil assembly (4 of 4) . . . 169
E.8 Vaccum shroud with optical access for a Janis flow cryostat . . . 170
E.9 Radiation shield for a Janis flow cryostat . . . 170
E.10 A mount for SiC wafers for NMR studies . . . 171
E.11 Goniometer assembly for a Montana instruments system (1 of 5) . . . 172
E.12 Goniometer assembly for a Montana instruments system (2 of 5) . . . 173
E.13 Goniometer assembly for a Montana instruments system (3 of 5) . . . 174
E.14 Goniometer assembly for a Montana instruments system (4 of 5) . . . 175
E.15 Goniometer assembly for a Montana instruments system (5 of 5) . . . 176

LIST OF TABLES

3.1 Optical and microwave resonances of SiC defect spins 22
3.2 Electric field and strain parameters of SiC defect spins 23
3.3 Hyperfine constants of SiC defect spins 25

5.1 Electric field coupling parameters of SiC defects 51

7.1 Hyperfine parameters of SiC defect spins 72

A.1 Crystal field splittings of SiC defect spins 107

D.1 The relative signal of multi-nuclear hybrid registers 138
D.2 Quantum gate sequences used to measure the density-matrix coherences 155
D.3 Quantum gate sequences used to measure the density-matrix populations 156
D.4 Measurements Made 158
D.5 Consolidated initialization and entanglement data 160

ACKNOWLEDGMENTS

First, I thank my advisor David Awchalom. Over the course of my graduate-school career, David has consistently given me great direction and has helped me pick up interesting and challenging projects. Along the way, he has opened opportunities for me that are available to few graduate students, and is continuing to do so even now as I prepare to take the next step in my career. In addition to being a great advisor, I also praise David for his ability to seek out motivated individuals with unique talents. The group that he has assembled is remarkably driven and the collective skillset within it would be hard to find anywhere else. I am fortunate to have worked with these individuals and am thankful beyond words for all they have taught me.

Among my labmates, I will start off by acknowledging those who I worked most closely with: Abram Falk, who I collaborated with my last year in Santa Barbara and who I shared a lab with in Chicago. Working with Abram has been not only enjoyable and educational, but also incredibly productive. We managed to knock out several projects while Abram was in the group, and we have continued to collaborate even after his departure to IBM. I have no doubts that we will stay lifelong friends and I hope we continue to collaborate throughout our careers. Charles de las Casas, who was my housemate during my first two years in Chicago and who became one of my best friends. I had a blast exploring the city with him and am thankful to him for the many history and politics lessons. My lab neighbor, David Christle, who has been and an excellent resource for all-things statistics. I also thank him for taking my coffee game to the next level by upgrading my coffee maker. The legendary Bob Buckley, whose intuition for theory and experiment kept many of us afloat in Santa Barbara. I am indebted to him for the many talks and the great times in Boston. Will Koehl, who has something interesting to say about almost any topic, ranging from quantum mechanics to California quail. Through the random facts that he has taught me, I feel like I have fulfilled some graduate enrichment requirement. Greg Fuchs, who introduced me to many of the experimental and theoretical techniques used in the group, and imparted upon me

some important philosophies. Andrew Yeats, who introduced me to many optics tricks and who was a great travel pal in the Netherlands. Chris Anderson, who has an incredibly deep understanding of the theory and literature, and has been a go-to for bouncing random ideas off of. And of course, I thank him for introducing me to turtle racing. Kevin Miao, Seung Hwan Lee, and Erzsebet Vincent, who I helped mentor during my last years as a graduate student. They have quickly become independent researchers, producing top-notch work. I look forward to the great things that they will surely accomplish in their careers. Peter Mintun, whose incessant punnery has left a permanent mark on me. I will be thoroughly upset if he ever makes a presentation that does not incorporate the IME hexagons. The older students who I didnt work as closely with, but who have nonetheless taught me many things: David Toyli, Greg Calusine, Paolo Andrich, Chris Yale, Joe Heremans, Brian Zhou, Ken Ohno, Viva Horowitz, Brian Maertz, and Shawn Mack. And finally, the groups newest members, who I have had the least overlap with: Berk Diler, Alex Bourassa, Sam Whiteley, Alex Crook, Agnetta Cleland, Masaya Fukami, and Paul Jerger. I look forward to seeing where this bright bunch takes the group.

I also acknowledge our theory collaborators: Slava Dobrovitski, who never hesitated to perform complex derivations in real-time during our video chats, and who has a remarkable understanding of experimental techniques. Adam Gali and Viktor Ivady, who have helped model many of our experimental results through their density functional theory calculations. All of their hard work has significantly advanced our understanding of semiconductor spins.

Beyond my coworkers, I thank my parents and my brother. They have given me constant support and encouragement throughout my whole life. Moreover, they have been excellent at putting things into perspective for me, particularly during the long and arduous grinds. And finally, I thank all of the people who I am lucky to call friends. Those from Santa Barbara: Sam, Josh, Konstantin, Lauren, George, Heather, Julian, Eugeniu, Nadia, Sonja, Bryana, and Marla. The northern Californians: Bobby, Jerry, Tui, Pardip and Estes. My New York friends: Sean and Mason. My Chicago buds: Samwise and many of the labmates

mentioned above. The Los guys: Bobby, Ricks, Dval, Marr, and Yarbro. And the many others. The importance of these people in my life and the positive impact that they have had cannot be understated. I can confidently say that I would not be where I am today without them.

With the support of these great people in my life, I have reached and surpassed all of my graduate school goals. I cannot thank them all enough.

ABSTRACT

Traditional electronic and communication devices operate by processing binary information encoded as bits. Such digital devices have led to the most advanced technologies that we encounter in our everyday lives and they influence virtually every aspect of our society. Nonetheless, there exists a much richer way to encode and process information. By encoding information in quantum mechanical states as qubits, phenomena such as coherence and entanglement can be harnessed to execute tasks that are intractable to digital devices. Under this paradigm, it should be possible to realize quantum computers, quantum communication networks and quantum sensors that outperform their classical counterparts.

The electronic spin states of color-center defects in the semiconductor silicon carbide have recently emerged as promising qubit candidates. They have long-lived quantum coherence up to room temperature, they can be controlled with mature magnetic resonance techniques, and they have a built-in optical interface operating near the telecommunication bands. In this thesis I will present two of our contributions to this field. The first is the electric-field control of electron spin qubits. This development lays foundation for quantum electronics that operate via electrical gating, much like traditional electronics. The second is the universal control and entanglement of electron and nuclear spin qubits in an ensemble under ambient conditions. This development lays foundation for quantum devices that have a built-in redundancy and can operate in real-world conditions. Both developments represent important steps towards practical quantum devices in an electronic grade material.

CHAPTER 1

INTRODUCTION

1.1 Perspective

The theory of the modern digital computer was set forth in 1936 by Alan Turing, when he described a machine that would algorithmically manipulate binary information on a tape according to a set of internal states and some instructional program [1]. The first realizations of such computers encoded the binary information, or "bits," in electromechanical switches [2], then vacuum tubes [3], and finally transistors in the mid 1950s [4–11]. Alongside the rapid advances in their underlying fabric, computers evolved from monstrosities consumed by the military, data centers, and major corporations, to tiny integrated circuits [12, 13] available to the average consumer. Today computers are ubiquitous and they influence virtually every aspect of our everyday lives.

Historically, performance advances in integrated circuits have been driven by shrinking circuit components [14]. Over five decades, this trend has increased transistor density from several thousand [15] to several billion transistors per square-inch. The individual transistors have correspondingly shrunk from the scale of microns to nanometers, with individual features spanning hundreds of atoms. Thus far, human ingenuity has managed to overcome the formidable engineering challenges associated with producing higher- and higher-density integrated circuits [16]. In recent years, however, fundamental physical barriers have become ever apparent [17]. At nanometer scales, quantum mechanical phenomena such as Heisenberg uncertainty and tunneling present themselves and degrade device performance. Anticipating the saturation of circuit miniaturization due to such effects, many have pondered the fundamental limits of traditional computing and have been inspired to rethink the computing paradigm [16, 18–21].

One idea that could lead to a fundamentally new class of computers has been around since the first integrated circuit. In his famous 1959 talk, Richard Feynman suggested

miniaturizing circuitry to the few-atom level, at which scale "we can use not just circuits, but some system involving the quantized energy levels, or the interactions of quantized spins, etc" [22]. Indeed, research into this field, now known as quantum information science [23], suggests that by abandoning traditional binary logic in favor of much richer quantum logic, it should be possible to realize quantum computers [24] that outperform even the most powerful modern computers for certain problems. These devices operate by manipulating information encoded in quantum bits, or "qubits," which can harness quantum coherence and entanglement to perform functions intractable to traditional electronic devices.

The development of quantum computers has primarily been motivated by the existence of ultra-efficient quantum algorithms for factoring prime numbers [25], searching databases [26], and simulating biological, chemical, and physical systems [27]. More recently, quantum algorithms have been devised for solving systems of linear equations [28], which could be used as subroutines for machine learning, pattern recognition and many other practical applications [16, 29–31]. To date, prototypes of general-purpose quantum computers have contained tens [32] of qubits, while the execution of many useful algorithms could require millions [33]. Identifying a system that can be scaled to include this many qubits and developing a framework for managing the classical resources necessary to precisely address these qubits remain important outstanding challenges.

In addition to quantum computers, coherence and entanglement can be harnessed to realize quantum communication networks [23, 34] and quantum sensors, which have greater functionality than their classical counterparts. These technologies generally require far fewer qubits than a quantum computer, on the order of one to one hundred, and so they hold high potential for real-world applications.

Quantum communication protocols employ qubits distributed between distant parties for sending quantum information, distributing keys in manner that is secured against eavesdroppers through fundamental physical laws [23,35–37], or even for synchronizing global positioning satellites [38]. To date, several quantum networks have been established [39] and com-

mercial quantum-key-distribution systems [40] are available. Nonetheless, these networks are currently limited to hundred-kilometer distances. In the future, quantum networks could be realized across arbitrary distances by establishing intermediate quantum-repeater nodes [41]. This goal will require the rapid long-distance distribution [42] and preservation [23, 43, 44] of entanglement between nodes, which remain important outstanding challenges.

In quantum sensing, qubits are used for detecting light, magnetization, mechanical vibrations, and other degrees of freedom [45, 46]. This broad class of technologies can be applied to study fundamental physics down to the single-quantum level and also shows promise for many practical applications. To date, qubits have been used to sense intracellular magnetic fields [47] and thermal gradients [48], and to realize the world's most precise clock [49]. In the future they could be used to resolve the atomic structure of complex biomolecules, such as proteins, which could aid in the development of novel drug-delivery systems or even medication [50]. This latter goal will require the isolation of long-lived qubits that are capable of sensing external matter [51] and novel tomographic techniques for inferring angstrom-scale structural information from algorithms applied to these qubits.

With expectations high as we march into the new millennium, quantum computers, quantum communication networks, and quantum sensors have been deemed sufficiently promising to launch a world-wide effort to identify and engineer qubits in a broad range of physical systems. With theoretical, experimental, and engineering efforts underway, the field of quantum information science is progressing at an unprecedented rate. In this thesis, I will present the research conducted by my colleagues and myself on electronic and nuclear spin qubits in the semiconductor silicon carbide (SiC), highlighting two developments.

The first development is the control of electron spin qubits with electric fields. This is an unusual control pathway because spin states are typically only susceptible to magnetic fields. Since electric fields are easy to confine on nanometer scales, unlike magnetic fields, this development lays foundation for the localized control of individual qubits in nanoscale arrays. Moreover, it could enable future quantum electronics that execute quantum algorithms via

electrical gating techniques, similar to those employed in traditional electronics.

The second development is the universal control and entanglement of electron and nuclear spin qubits in an ensemble, at ambient conditions. This is a surprising result because spin ensembles have previously only been entangled by employing cryogenics, high magnetic fields, or photochemical reactions. The ability to realize quantum effects at ambient conditions in a macroscopic system could facilitate the development of practical quantum devices, in particular those that harness collective excitations and the redundancy afforded by ensembles.

1.2 Thesis Organization

In **Chapter 2**, I give a brief introduction to bits and qubits and conclude with a discussion of the criteria that a qubit in any physical system should meet to be viable for quantum technologies - the DiVincenzo criteria. In **Chapter 3**, I introduce atom-like points defects in semiconductors and narrow the focus to the divacancy family of defects in SiC. I then discuss how the electron spin of such defects and the nuclear spin of isotopic defects can be used to encode qubits. In **Chapter 4**, I describe the apparatus that we have built to execute quantum algorithms on electron and nuclear spin qubits. In **Chapter 5**, I describe an experiment in which we showed that static electric fields and mechanical strain can be used to tune the energy-level structures of electron spin qubits. In **Chapter 6**, I describe an experiment in which we showed that time-varying electric fields can be used to coherently control electron spin qubits. In **Chapter 7**, I describe an experiment in which we showed that optical pumping of electron-spin qubits can be be used to polarize nearby nuclear spin qubits. In **Chapter 8**, I describe an experiment in which we showed that an ensemble of electron-spin qubits and nuclear-spin qubits can be genuinely entangled at ambient conditions. In **Chapter 9**, I conclude this thesis and give an outlook. In the **Appendices**, I present non-essential experimental and theoretical details for **Chapters 5 - 8**, and give blueprints for useful machined parts.

CHAPTER 2

CLASSICAL AND QUANTUM INFORMATION

2.1 The Bit

A bit is a binary unit of information that can take on one of the two states $|0\rangle$ or $|1\rangle$. A single bit can be represented by the state of any classical two-state system, such the on/off state of an electromechanical switch, vacuum tube, or transistor. A network of n bits can be represented as the bit string $|\mathbf{x}\rangle = |x_1, x_2, ..., x_{n-1}, x_n\rangle$, where each $x_i \in \{0, 1\}$.

Computational algorithms can be carried out by executing logic operations called "gates". Each gate computes the Boolean (true/false) function $f : \{0, 1\}^n \rightarrow \{0, 1\}$, which maps from the states of n input bits to the state of a single output bit. An example of a gate is the NAND, which maps from two input bits to a single output bit, according to the following truth table:

NAND→

Input		Output
bit 1	bit 2	bit 3
0	0	1
0	1	1
1	0	1
1	1	0

Though simple, the NAND is a "universal gate", which means that any computation can be reduced to some sequence of NAND gates [52]. Virtually all electronic and communication technologies that we encounter in our everyday lives encode information as bits and operate by performing strings of simple logic gates on those bits.

2.2 The Qubit

A qubit is the fundamental unit of quantum information [23]. A single qubit can be represented by any two-state manifold of a quantum mechanical system. In analogy to a classical bit, a qubit can exist in the states $|0\rangle$ and $|1\rangle$. In stark contrast to a classical bit, however,

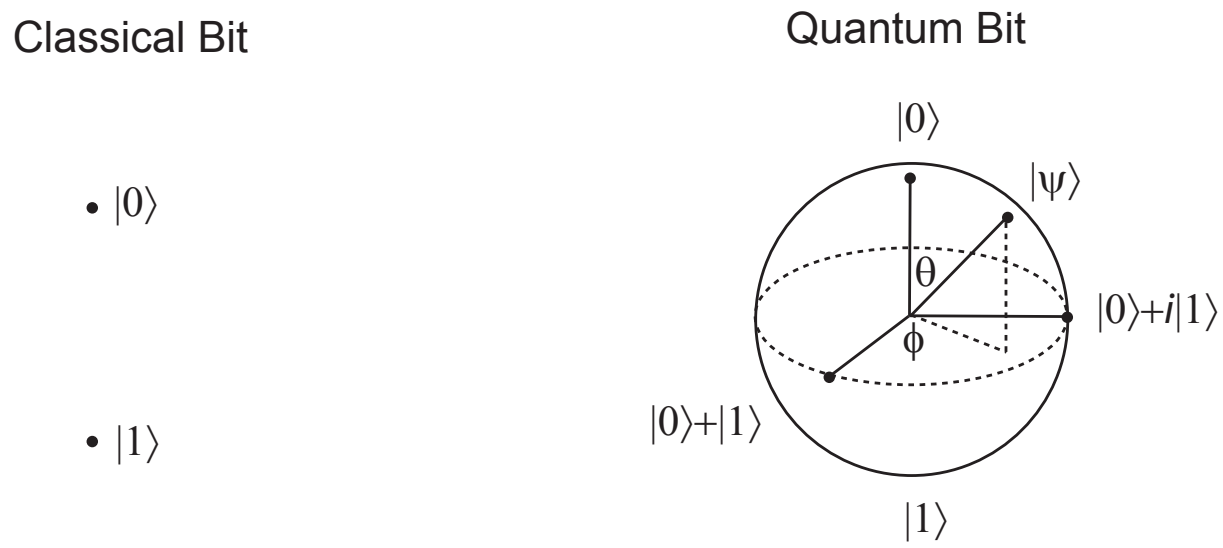

Figure 2.1: Comparison between a classical and a quantum bit. A classical bit can take on two values, $|0\rangle$ or $|1\rangle$. A quantum bit can take on any value on the Bloch sphere, parameterized by $\theta, \phi \in \mathbb{R}$.

a qubit can also exhibit "quantum coherence," a phenomenon in which it exists as a superposition of its two states. In general, the state of a qubit $|\psi\rangle$ can be represented as a vector in a 2-dimensional Hilbert space $\mathcal{H}_2$, which is spanned by the orthonormal basis vectors $|0\rangle$ and $|1\rangle$ ($\langle i|j\rangle = \delta_{ij}$, where δ is the Kronecker delta) and parametrized by the amplitudes $\alpha_0, \alpha_1 \in \mathbb{C}$:

$$|\psi\rangle = \alpha_0|0\rangle + \alpha_1|1\rangle \tag{2.1}$$

Since quantum mechanics constrains the state $|\psi\rangle$ to be normalized (i.e. $\langle\psi|\psi\rangle = 1$), the amplitudes satisfy $|\alpha_0|^2 + |\alpha_1|^2 = 1$.

The qubit state $|\psi\rangle$ has a nice geometric representation if we make the substitutions $\alpha_0 \to \cos(\theta/2)$ and $\alpha_1 \to \sin(\theta/2)e^{i\phi}$, where $\theta, \phi \in \mathbb{R}$. With these substitutions, the qubit can be mapped to a unit-vector on the 3-dimensionsal unit-sphere where θ plays the role of the azimuthal angle and ϕ the polar angle. This sphere, which is called the "Bloch sphere," is presented in see Fig. 1.1.

Since a qubit can be parametrized by two real numbers, it can in principle encode in-

finitely more information than a classical bit. Nonetheless, the rules of quantum mechanics prevent the extraction of these parameters in a single shot due to "wavefunction collapse," a phenomenon which starkly distinguishes qubits from bits. In particular, measurement of a qubit in a given basis, take here the $\{|0\rangle, |1\rangle\}$ basis, returns the state $|0\rangle$ with probability $|\langle 0|\psi\rangle|^2$ and the state $|1\rangle$ with probability $|\langle 1|\psi\rangle|^2$. Moreover, after the initial measurement, all following measurements return the initially measured state with unit probability (i.e. the superposition has collapsed into a single state of the measurement basis). This collapse prevents the extraction of any additional information about the initial state $|\psi\rangle$. Therefore, to measure the parameters θ and ϕ with high precision and thus reconstruct the state $|\psi\rangle$, one must repetitively re-prepare the state and readout on different bases.

As more qubits are added to a system, its accessible state-space grows exponentially. A general n-qubit state, which lives in $\mathcal{H}_{2^n}$ and is spanned by the 2^n basis vectors $\{|\mathbf{x}\rangle | \mathbf{x} \in \{0,1\}^n\}$, can be written as a linear combination of these basis states:

$$|\psi\rangle = \sum_{\mathbf{x}\in\{0,1\}^n} \alpha_{\mathbf{x}} |\mathbf{x}\rangle \tag{2.2}$$

with each $\alpha_{\mathbf{x}} \in \mathbb{C}$, subject to the normalization condition:

$$\sum_{\mathbf{x}\in\{0,1\}^n} |\alpha_{\mathbf{x}}|^2 = 1 \tag{2.3}$$

Since an n-qubit system is parametrized by 2^n complex coefficients, its capacity to store information is incomprehensibly large even for small n. At the level of 200 qubits, there are more complex coefficients than there are atoms in our solar system ($\sim 10^{57}$), and at 300 qubits, there are more coefficients than there are atoms in the visible universe ($\sim 10^{82}$). As with the single qubit, however, measurement of the n-qubit system returns the state $|\mathbf{x}\rangle$ with probability $|\alpha_{\mathbf{x}}|^2$ and collapses the system into that state. Therefore, even though a general n-qubit system can store an enormous amount of information, extracting this information

is a non-trivial task. Overcoming this challenge represents an important problem in the development of useful quantum algorithms.

Quantum algorithms can be performed by executing "quantum logic gates". In analogy to how a classical logic gate can be represented as a truth table, a quantum logic gate on n-qubits can be represented as an operator with the matrix representation $\hat{U} \in \mathbb{C}^{2^n \times 2^n}$. The action of the logic gate is to perform the operation $\hat{U}|\psi_i\rangle \rightarrow |\psi_f\rangle$. Since a quantum state need remain normalized at all times, $\langle\psi_f|\psi_f\rangle = \langle\psi_i|\psi_i\rangle = 1$, quantum logic gates are constrained to be unitary operations: $\hat{U}^\dagger\hat{U} = I_{2^n \times 2^n} \implies \hat{U}^\dagger = \hat{U}^{-1}$

Earlier we saw that the NAND gate was universal for classical computing. It turns out that we can also identify a set of quantum logic gates that are universal for quantum computing. One possible universal set consists of the one-qubit Hadamard gate (H), the one-qubit $\pi/8$-phase gate (T), and the two-qubit controlled-NOT gate ($\mathrm{C}_k\mathrm{NOT}_m$, which flips qubit m if the state of qubit k is $|1\rangle$) [23]. The matrix representations of these gates are:

$$
\begin{aligned}
H &\xrightarrow{\{|0\rangle,|1\rangle\}} \frac{1}{\sqrt{2}}\begin{pmatrix} 1 & 1 \\ 1 & -1 \end{pmatrix} \\
T &\xrightarrow{\{|0\rangle,|1\rangle\}} \begin{pmatrix} 1 & 0 \\ 0 & e^{i\pi/4} \end{pmatrix} \\
\mathrm{C}_1\mathrm{NOT}_2 &\xrightarrow{\{|00\rangle,|01\rangle,|10\rangle,|11\rangle\}} \begin{pmatrix} 1 & 0 & 0 & 0 \\ 0 & 1 & 0 & 0 \\ 0 & 0 & 0 & 1 \\ 0 & 0 & 1 & 0 \end{pmatrix}
\end{aligned}
\tag{2.4}
$$

Having defined a universal set of quantum gates, we now show how they can be used to

prepare a special type of superposition state of multiple qubits, called an "entangled state". For this discussion, without loss of generality, I focus on a 2-qubit system. In particular, operating on the initialized $|00\rangle$ state, we can prepare:

$$|00\rangle \xrightarrow{H\otimes I_2} \frac{1}{\sqrt{2}}(|00\rangle + |10\rangle) \xrightarrow{\mathrm{C_1NOT_2}} \frac{1}{\sqrt{2}}(|00\rangle + |11\rangle) \equiv |\Psi\rangle \tag{2.5}$$

The reason why state is special is because it cannot be decomposed into a product state of the individual qubits for any choice of $|\psi_1\rangle$ and $|\psi_2\rangle$ (i.e. $|\Psi\rangle \neq |\psi_1\rangle \otimes |\psi_2\rangle$). This inseparability can lead to correlations between qubits that are significantly larger than possible for bits. In particular, a measurement performed on one qubit in an entangled pair instantaneously collapses the other qubit too - even if the initially entangled qubits were at opposite end of the universe. Entanglement is one of the most counterintuitive phenomena predicted by quantum mechanics [53]. Nonetheless, entanglement has been produced and verified in a broad range of systems [43, 54–58], and is accepted as a fact of nature [42]. Today it is being explored as a resource for quantum computers, communication networks, and quantum sensors.

2.3 Qubit Relaxation

One primary reason why quantum devices are so difficult to realize is that qubits are remarkably fragile. Here I describe the mechanisms that can lead to the loss of quantum information through qubit relaxation [59]. For this discussion, I depart from the pure-state formalism, where a quantum system is represented by a single quantum state $|\psi\rangle$, and adopt the density-matrix formalism [23]. The density matrix contains all of the information that is extractable from a statistical mixture of quantum states. It is an indispensable tool for studying relaxation, for tracking the evolution of single qubits over many repeated experimental trials, or the evolution of an ensemble of qubits. The definition of the density matrix $\hat{\rho}$ for the statistical occupation of M n-qubit quantum states $|\psi_i\rangle$ is the convex sum:

$$\hat{\rho} = \sum_{i}^{M} p_i |\psi_i\rangle\langle\psi_i|, \tag{2.6}$$

where $\hat{\rho} \in \mathbb{C}^{2^n \times 2^n}$ and p_i is the occupation probability of $|\psi_i\rangle$, subject to the normalization condition $\sum_i p_i = 1$. The summation index i can represent independent experimental trials (i.e. when dealing with single qubits), different qubits in an ensemble, or both. By using the properties of qubits introduced in the previous section, it can be shown that the density matrix is Hermitian ($\hat{\rho} = \hat{\rho}^\dagger$), normalized ($\mathrm{Tr}(\hat{\rho}) = 1$), and positive semidefinite ($\mathrm{eig}(\hat{\rho}) \geq 0$).

To make transparent the meaning of the density matrix elements, we explicitly present $\hat{\rho}$ of an ensemble of M 1-qubit systems, in the $\{|0\rangle, |1\rangle\}$ basis:

$$\hat{\rho} \xrightarrow{\{|0\rangle,|1\rangle\}} \begin{pmatrix} \sum_i^M p_i |\langle 0|\psi_i\rangle|^2 & \sum_i^M p_i \langle 0|\psi_i\rangle\langle\psi_i|1\rangle \\ \sum_i^M p_i \langle 1|\psi_i\rangle\langle\psi_i|0\rangle & \sum_i^M p_i |\langle 1|\psi_i\rangle|^2 \end{pmatrix} \tag{2.7}$$

From this, we can see that the on-diagonal elements, $\langle 0|\hat{\rho}|0\rangle$ and $\langle 1|\hat{\rho}|1\rangle$, are the probabilities that the system will be measured to be in the states $|0\rangle$ or $|1\rangle$, respectively. Accordingly, they are called the "populations". Likewise, the off-diagonal elements $\langle 1|\hat{\rho}|0\rangle$ and $\langle 0|\hat{\rho}|1\rangle$ tell us about the presence of superpositions in the $\{|0\rangle, |1\rangle\}$ basis. They are thus called the "coherences".

When the statistical mixture is considered in the context of its larger environment, we must deal with the total density matrix $\hat{\rho}_{\mathrm{total}}$. For an initially prepared ensemble, the density matrix can be simply written as $\hat{\rho}_{\mathrm{total}} = \hat{\rho} \otimes \hat{\rho}_{\mathrm{env}}$, where $\hat{\rho}_{env}$ is the density matrix of the environment. As time progresses, however, elements of the two density matrices can become interconnected and entangled in complicated ways. In general, it is these interactions, which link $\hat{\rho}_{env}$ to $\hat{\rho}$, that lead to qubit relaxation [60]. Below we introduce the two categories of relaxation.

Longitudinal Relaxation (also known as spin-lattice relaxation or re-thermalization)

is the decay of the density matrix populations to their thermal Boltzman populations. Relaxation happens with decay constant T_1, and it results from the exchange of energy between qubits and the environment, which take $|0\rangle \rightarrow |1\rangle$, or vice versa. Although the dominant T_1 mechanism depends on the physical system that encodes the qubit, for electron spin qubits in semiconductors, T_1 relaxation is typically driven by spin-phonon interactions [59].

Transverse Relaxation (also known as decoherence or dephasing) is the decay of the density matrix coherences to zero. Decoherence happens with decay constant T_2, and it results from noise that shifts the energy levels of qubits and causes the states $|\psi_i\rangle$ in $\hat{\rho}$ to lose phase coherence with one another. In practice, the true coherence time T_2 is often obscured by quasi-static inhomogeneities between the different states in $\hat{\rho}$, which lead to an apparent and much shorter (by orders of magnitude, in some cases) decoherence with time T_2^*. Such effects can typically be reversed by "echoing" the qubits [61], to reveal a longer coherence time, in some cases as long as the fundamental limit $T_2 = 2T_1$. The coherence measured in this way strongly depends on the type of echo sequence that is used [62, 63]. As with T_1, the dominant mechanisms that lead to T_2 and T_2^* decoherence depend on the physical system that encodes the qubit. For electron-spin qubits in semiconductors, however, flip-flops between nuclear spins in the surrounding spin bath drive T_2 decoherence [64, 65]. Inhomogeneities in external magnetic, electric, and strain fields drive T_2^* decoherence [64,66].

Mitigating relaxation is a key step towards realizing quantum devices. Tools for protecting quantum information from relaxation range from the "echos" mentioned above [61–63], which rely on carefully chosen quantum control sequences to reverse decoherence, to quantum error-correcting codes. The purpose of such codes is to encode single, relaxation-resilient, logical qubits in many relaxation-susceptible physical qubits [23, 67].

2.4 DiVincenzo Criteria

Qubits realized in any physical system should meet the so-called "DiVincenzo" criteria [68] to be viable for quantum computing, communication, and sensing. For each technology,

certain criteria are more important than others. The criteria are:

1. Qubits should be well-defined and scalable
2. Qubits should be initializable into a well-defined fiducial state
3. Qubits should be controllable with a universal set of quantum gates
4. Qubits should be measurable in a projective way
5. Qubit coherence should greatly exceed the gate time

For quantum communication in particular, the following criteria are appended:

6. Qubits should be convertible into photonic qubits
7. Photonic qubits should be transmittable across long distances with low loss

Over the past several decades there has been a world-wide effort to engineer qubits in a broad range of physical platforms. Among these are liquid- [69, 70] and solid-state [71] spin ensembles, trapped ions [72], neutral atoms, quantum electrodynamic systems [73, 74], photons [75], quantum dots [76], superconducting circuits [77], and color-center defects in semiconductors. To date, qubits in all of these platforms have fulfilled some of the DiVincenzo criteria, but no qubit-type has fulfilled all of them simultaneously. In this thesis I will describe our research into defect qubits in SiC. All of our experiments address the DiVincenzo criteria in some way.

CHAPTER 3

SEMICONDUCTOR DEFECT SPINS AS QUBITS

3.1 Atom-Like Point Defects in Semiconductors

The wavefunctions of electrons in a pristine crystal can be represented as delocalized Bloch functions that extend across the full crystal. In a semiconductor, the energies associated with these wavefunctions can be grouped into two bands – the higher energy "conduction band" and the lower energy "valence band" – which are separated by the "band gap". When the periodicity of the crystal is perturbed by a point defect - such as a vacancy site, an interstitial atom, a substitutional atom, or a complex comprising several such defects - new electronic states are introduced into the band structure of the material, sometimes within the band gap. When electrons occupy these intra-band-gap states, they feel a repulsive potential when trying to escape into the delocalized Bloch states of the crystal, and thus they tend to "pool up" in the vicinity of the defect. The extent to which these wavefunctions are localized give way to two categories of defects: "shallow level defects" and "deep level defects" [78].

Shallow level defects introduce states with energy levels that are near their host semiconductor's conduction- or valence-band edges, within the thermal excitation energy kT. Electrons occupying these states are weakly bound to the defect center and their wavefunctions are delocalized over many primitive cells of the semiconductor. Deep level defects, on the other hand, introduce states with energy levels that are far from the conduction- or valence-band edges, greatly exceeding kT. Electrons occupying these states are tightly bound to the defect center, and their wavefunctions are localized within several primitive cells of the semiconductor (see Fig. 1).

Some deep level defects form atom-like states with an optical-, fine- and hyperfine-structure [79]. Those with optical transitions ranging from the near ultraviolet (NUV, 400nm = 3.1 eV) to the near infrared (NIR, 1100nm = 1.1 eV) are the so-called "color centers". These are familiar even to the non-physicist because they can give gemstones brilliant colors.

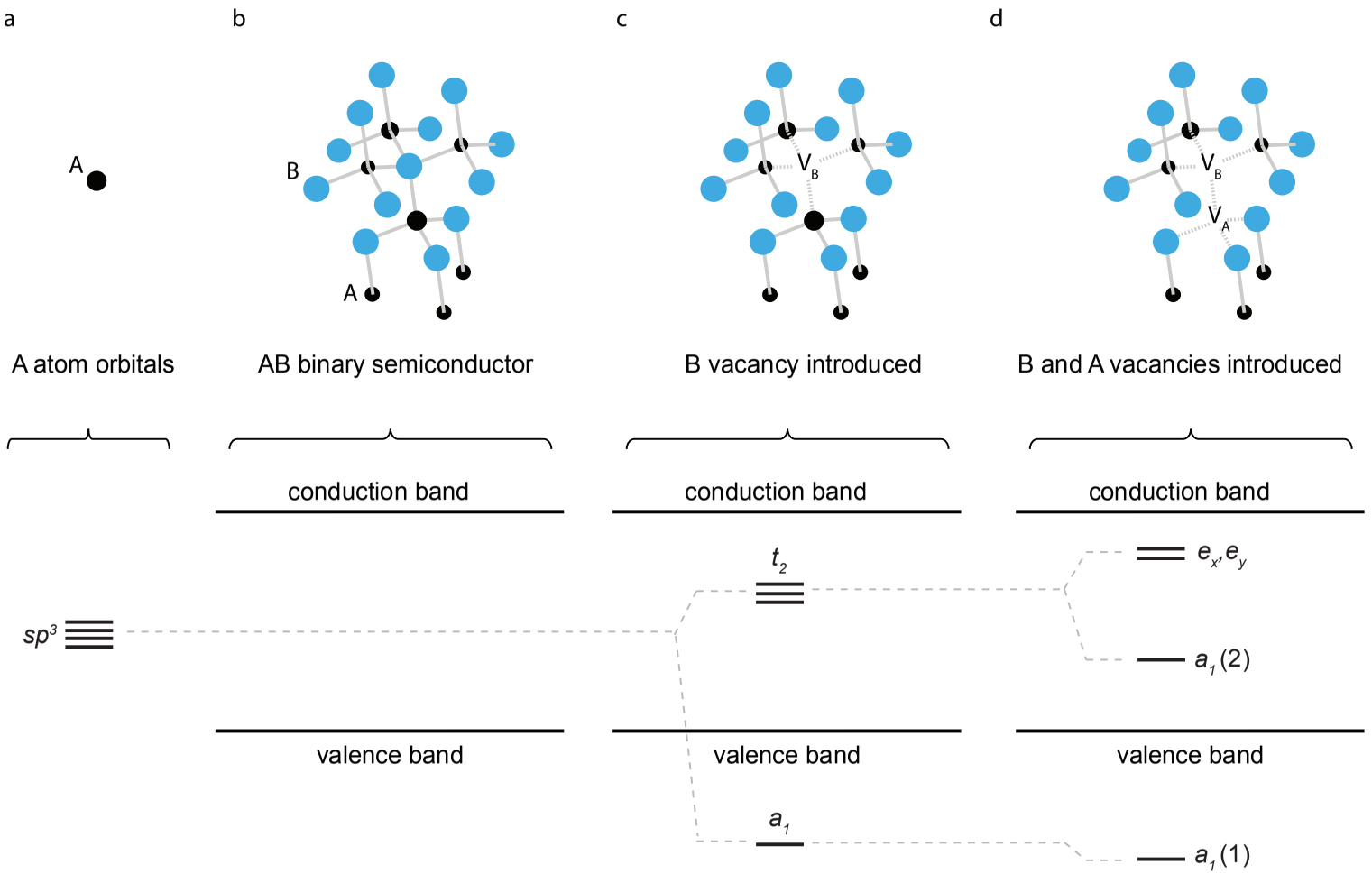

Figure 3.1: A deep level defect in a tetrahedrally coordinated semiconductor, such as diamond or SiC [79]. (a) an isolated A-atom and its corresponding sp^3 bonding orbitals. (b) A binary semiconductor comprising A and B atoms. The semiconductor's energy levels form the conduction and valence bands. (c) When a point defect, such as a vacancy, is introduced into the semiconductor, electronic states are incorporated into the band structure, sometimes within the bandgap (here the "t_2" levels), and sometimes outside of it (here the "a_1" level). (d) If the symmetry of the defect is reduced further, for example through the removal of another nearby atom, the degeneracy of the defect is reduced and the states split further. If these states are far from the band edges the electronic wave functions associated with them are tightly localized around the defect.

As it turns out, they can also be used to encode qubits with excellent properties.

Over the past two decades, the nitrogen-vacancy (NV) color center in diamond (which can give diamonds a pink glow) has attracted much attention from the quantum information community [80, 81]. It has been shown that its fine structure (i.e. its electron spin) can be used to encode single qubits that are robust against noise from cryogenic to ambient conditions. In addition to being attractive for quantum computing and sensing applications, its built-in optical interface (operating at 637 nm) can serve as a natural transducer from spin qubits to flying photonic qubits for quantum communication. To date, these properties have led to many impressive demonstrations including room-temperature entanglement and quantum-error correction [43], nanoscale sensing of small numbers of protons [82, 83], nanoscale thermometry within a living cell [48], long-distance entanglement [55], and teleportation [84].

More recently, the divacancy family of color centers in SiC have emerged as promising qubit candidates [85–92]. In addition to sharing many attractive qubit properties with NV centers, they have two unique selling points. First, their optical interface operates at infrared wavelengths (from 1 - 1.2 μm), near the established telecommunication bands. This could facilitate their integration into existing photonic networks for practical quantum communication. Second, SiC plays an important role in the high-power electronics and optoelectronics industries, and is being explored for a wide range of micromechanical sensors [93–95]. The growth, doping, and microfabrication techniques developed for these applications could be leveraged to prototype sophisticated quantum devices.

These factors have motivated our studies of SiC color centers. In the remaining sections, I introduce the divacancy family of defects, discuss their energy-level structures, and conclude with a discussion of their properties within the context of the DiVincenzo criteria. Throughout the thesis I will make many references to the extensive NV center literature, which has served as a guide in many respects.

3.2 The Divacancy Family of Defects in Silicon Carbide

The divacancy family of color centers includes the inequivalent forms of the neutral divacancy – which comprise a single C vacancy (V_{C}) adjacent to a single Si vacancy (V_{Si}) – and unidentified defects with magnetooptical properties similar to the divacancies. These unidentified defects might be different charge states of the divacancies, divacancies within polytype-inclusion growth defects, or something completely different. Determining their exact nature remains an important outstanding problem.

The divacancy family includes the PL1-PL6 defects in 4H-SiC, the QL1-QL9 defects in 6H-SiC, and the RL1 defect in 3C-SiC (I have adopted the naming convention introduced in [88]). In the 4H and 6H polytypes, the defects can be categorized based on their orientation within the SiC crystal. Those aligned with the high-symmetry SiC c-axis are the "c-axis defects" and they have C_{3v} point-group symmetry. Those aligned with the lower-symmetry SiC basal planes are the "basal defects" and they have the reduced C_{1h} point-group symmetry. Due to the existence of inequivalent lattice sites within the SiC crystal, the 4H and 6H polytypes host several inequivalent forms of both c-axis and basal divacancies. When differentiating between them, I will reference their lattice sites explicitly – for example, the kk c-axis divacancy or the hk basal divacancy, where k represents a cubic site and h a hexagonal site. In 3C-SiC, due to its high crystalline symmetry, there is a single divacancy form with C_{3v} symmetry.

3.3 Optical Properties of Defects in the Divacancy Family

Even though the divacancy family comprises many defects, they all share some general magnetooptical properties. These properties, which I discuss below, have been inferred from our experimental measurements, the theoretical calculations of our collaborators, and the extensive SiC-defect and NV-center literature.

Defects in the divacancy family have atom-like electronic states with an optical, fine, and

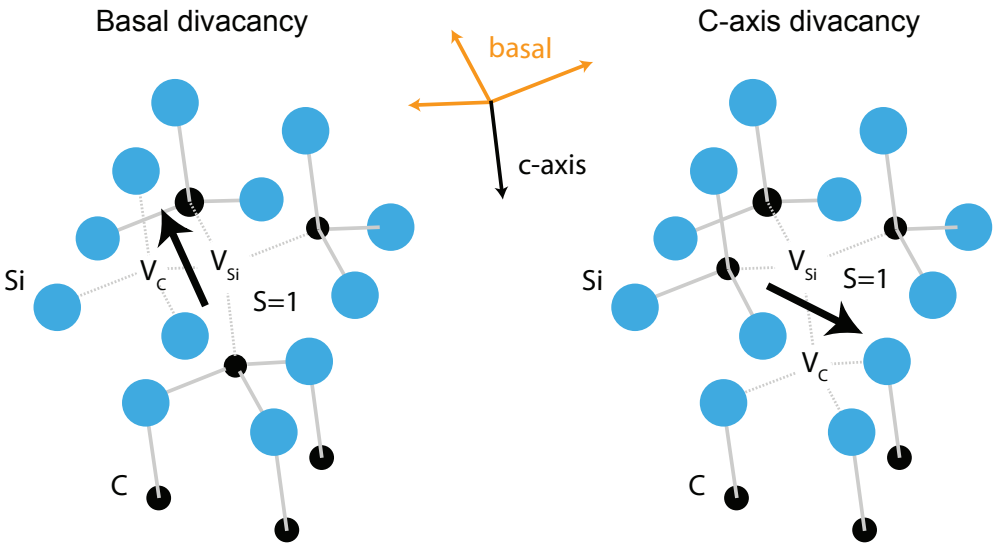

Figure 3.2: A 4H-SiC unit cell with a (left) basal and (right) c-axis oriented divacancy. Both the basal and c-axis divacancies comprise a silicon vacancy (V_{Si}) adjacent to a carbon vacancy (V_C). A

hyperfine structure. Their optical ground state is an orbital-singlet (labelled $|GS\rangle$), spin-triplet ($S = 1$, with the spin sublevels represented by $|m_S\rangle$ with $m_S \in \{0, \pm 1\}$), and their excited state is an orbital-doublet (labelled $|ES\rangle$), spin-triplet [87, 88]. Non-resonant laser light exceeding the optical transition energy can be used to drive spin-conserving transitions from the ground to excited state through a phonon sideband:

$$|GS\rangle \otimes |m_S\rangle \xrightarrow{+hf-\text{phonons}} |ES\rangle \otimes |m_S\rangle \tag{3.1}$$

Following excitation, defects can relax from their excited state to their ground state via two pathways: First, they can emit a photon (i.e. photoluminesce) and phonons, to decay in a spin-conserving way:

$$|ES\rangle \otimes |m_S\rangle \xrightarrow{-hf-\text{phonons}} |GS\rangle \otimes |m_S\rangle \tag{3.2}$$

Second, they can decay non-radiatively via a series of intersystem crossings (ISCs), through some intermediate states $|IS\rangle$. Although the finer details of this latter pathway

have not yet been determined, it is known that this process is spin-dependent and spin non-conserving:

$$|ES\rangle \otimes |m_S\rangle \xrightarrow{\text{ISCs}} |GS\rangle \otimes |m'_S\rangle, \tag{3.3}$$

where $m_S \neq m'_S$ in general, and the probability of entering ISC depends on m_S. The existence of the intersystem crossing pathway has two important consequences.

First, the existence of the ISC pathway means that repeated optical cycling of defects in thermal equilibrium will generate a non-equilibrium spin polarization in the ground state:

$$\begin{aligned} |GS\rangle \otimes \{\sqrt{p_0^B}|0\rangle, \sqrt{p_{+1}^B}|+1\rangle, \sqrt{p_{-1}^B}|-1\rangle\} \quad &\xrightarrow{\text{optical pumping}} \\ |GS\rangle \otimes \{\sqrt{p'_0}|m_S\rangle, \sqrt{p'_{\pm 1}}|m_S\rangle, \sqrt{p'_{\pm 1}}|m_S\rangle\} \end{aligned} \tag{3.4}$$

where $p_{m_S}^B$ is the Boltzmann factor $e^{-\frac{E_{m_S}}{kT}} / \sum_{m'_S} e^{-\frac{E_{m'_S}}{kT}}$, and $p'_0 \neq p'_{\pm 1}$ in general. Optical pumping thus serves as a pathway to "initialize" a defect's ground-state spin. We have characterized that $p'_0 > p'_{\pm 1}$ for some of the defects in the divacancy family, meaning that they initialize into their $|0\rangle$ states. Nonetheless, this need not be true in general, and a defect can also preferentially initialize into its $|\pm 1\rangle$ states. A straightforward way to determine the state of initialization is through optically detected nuclear magnetic resonance experiments or the quantum state tomography procedure described in Chapter 8 [54].

Second, the existence of the ISC pathway means that a spin prepared into $|0\rangle$ will emit, on average, a different number of photons than a spin prepared into $|\pm 1\rangle$. Therefore, by measuring the photoluminescence, we can "read out" a defect's ground-state spin. Unfortunately this readout pathway is non-projective since the physical process that drives it is also responsible for initialization. However, it serves as the primary readout technique in most studies of NV centers and SiC defects, and most of the research presented in this thesis.

These properties of the ISC and their facilitation of optical initialization and readout have made the ground-state spin of defects in the divacancy family and the NV center [80]

attractive qubit candidates. In the following section, I introduce the ground state spin Hamiltonian of defects in the divacancy family.

3.4 The Spin Hamiltonian

The ground-state-spin Hamiltonian of a divacancy-family defect in an electron and nuclear spin bath and an externally applied magnetic field is given by: a crystal-field term to include the spin-spin and spin-orbit interactions between the electrons that make up the defect, an electron-Zeeman term to include the interactions of the defect spin and other electron spins with the externally applied magnetic field, an electron-electron dipole term to include the interactions of the electrons spins (other divacancies, dark spins, etc.), a hyperfine term to include the interactions of the defect spin with nearby nuclear spins (predominantly ^{13}C and ^{29}Si in SiC), a nuclear Zeeman term to include the interactions of those nuclei with the externally applied magnetic field, and a nuclear-nuclear dipole term to include the interactions of the nuclear spins:

$$\begin{aligned}\hat{H}_{|GS\rangle} = & \underbrace{\hat{\mathbf{S}}\cdot\mathbf{D}\cdot\hat{\mathbf{S}}}_{\text{crystal field}} + \underbrace{\sum_i \gamma_i^e \hat{\mathbf{S}}_i\cdot\mathbf{B}_i}_{\text{electron Zeeman}} + \underbrace{\sum_i\sum_{j>i}\hat{\mathbf{S}}_i\cdot\mathbf{P}^e_{i,j}\cdot\hat{\mathbf{S}}_j}_{\text{electron-electron dipole}} \\ & + \underbrace{\sum_i \hat{\mathbf{S}}\cdot\mathbf{A}_i\cdot\hat{\mathbf{I}}_i}_{\text{electron-nuclear hyperfine}} - \underbrace{\sum_i \gamma_i^n\hat{\mathbf{I}}_i\cdot\mathbf{B}_i}_{\text{nuclear Zeeman}} + \underbrace{\sum_i\sum_{j>i}\hat{\mathbf{I}}_i\cdot\mathbf{P}^n_{i,j}\cdot\hat{\mathbf{I}}_j}_{\text{nuclear-nuclear dipole}} \end{aligned} \quad (3.5)$$

$\mathbf{S}$ is the vector of electron spin matrices, $\mathbf{I}$ is the vector of nuclear spin matrices, γ^e and γ^n are the electron and nuclear gyromagnetic ratios, respectively, $\mathbf{B}$ is the externally-applied magnetic field vector, $\mathbf{A}$ is the hyperfine tensor, and $\mathbf{P}^e$ and $\mathbf{P}^n$ are the tensors that encompass the electron-electron and nuclear-nuclear dipole couplings, respectively. The sum in the electron Zeeman term is over all of the electrons, the sums in the hyperfine and nuclear Zeeman terms are over all of the nuclear spins, and the sums in the dipole terms are over all electron

and nuclear spins. Including the dipole-dipole terms, which seems superfluous, is actually quite important since they are typically responsible for defect-spin decoherence [64, 65].

The crystal field term is typically expanded as:

$$\hat{\mathbf{S}} \cdot \mathbf{D} \cdot \hat{\mathbf{S}} = D\hat{S_z}^2 - E_x^0(\hat{S_x}^2 - \hat{S_y}^2) + E_y^0(\hat{S_x}\hat{S_y} + \hat{S_y}\hat{S_x}) \tag{3.6}$$

where D and $\mathbf{E}^0$ are the longitudinal and transverse crystal-field parameters, respectively. The C_{3v} symmetric c-axis defects have $\mathbf{E}^0 = 0$, and the C_{1h} symmetric basal defects generally have $\mathbf{E}^0 \neq 0$. The effects of strain and/or electric fields can be accommodated by making the following substitutions:

$$D \to D + d_{\parallel}E_z + \epsilon_{\parallel}\Sigma_z \qquad \text{and} \qquad E_{x,y}^0 \to E_{x,y}^0 + d_{\perp}E_{x,y} + \epsilon_{\perp}\Sigma_{x,y} \tag{3.7}$$

where Σ is the strain field vector, $\mathbf{E}$ is the electric field vector, and ϵ and d are the spin-strain and -electric field coupling constants, respectively [96, 97]. Spin coupling to these fields is driven by the spin-orbit interaction and perturbations to spin-spin interactions [80]. Although it is very likely that the hyperfine interaction is modified by strain and electric fields, this has not yet been investigated in either the SiC-defect or NV-center literature, to the best of my knowledge. This could be the topic of an interesting study in the future.

The excited-state spin Hamiltonian in the high-temperature limit, where motional narrowing averages out the two orbital branches into an effective orbital-singlet, (the transition between low and high temperature is believed to happen below 100 K) has the same form as the ground state Hamiltonian [98, 99], but with different parameters. The low-temperature Hamiltonian in the non-motionally narrowed regime is the focus of ongoing studies.

Knowledge of the ground- and excited-state Hamiltonian parameters is crucial for the precise quantum control of defect spins and for eventually implementing them in quantum technologies. To experimentally determine the many Hamiltonian parameters, we and other research groups have employed spectroscopic and time-domain photoluminescence

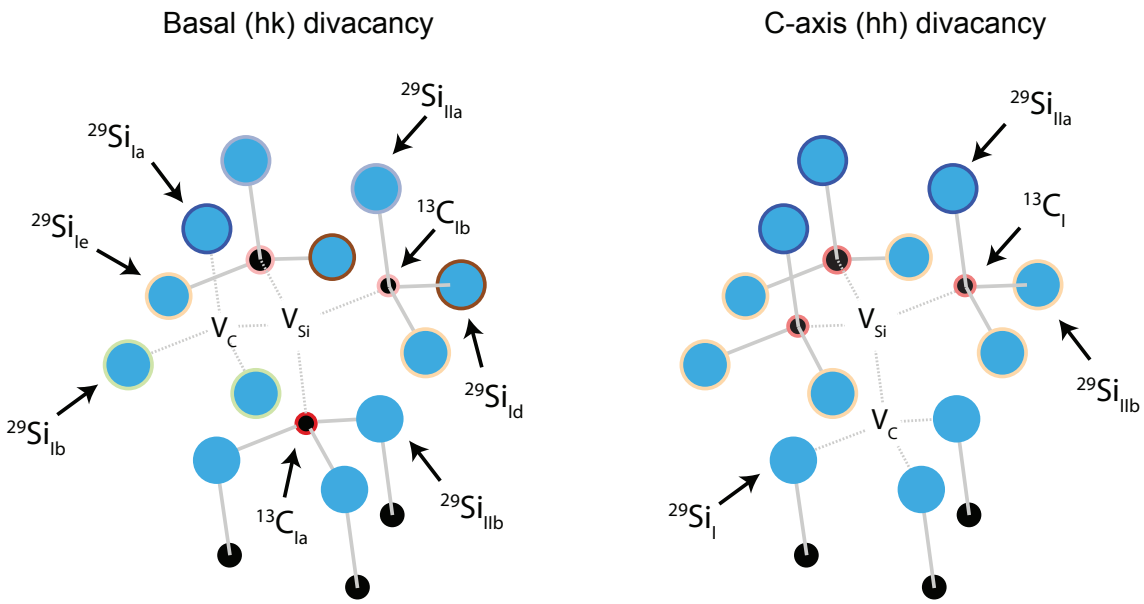

Figure 3.3: First- and second-nearest-neighbor sites indicated on a basal and c-axis divacancy. Crystallographically equivalent sites are color coded. These sites are referenced in Table 3.3.

(PL), electron paramagnetic resonance, nuclear magnetic resonance, optically detected magnetic resonance (ODMR) [86–88, 96, 97, 100], optically detected nuclear magnetic resonance (ODNMR) [54], and other techniques. Our collaborators and other groups have also approximated many of these parameters through theoretic tools such as density functional theory. All of the parameters that are presently known, to the best of my knowledge, are compiled in Tables 3.1 - 3.3.

3.5 Encoding Qubits

In this section I discuss how a single qubit can be encoded in the ground-state electron spin of a c-axis defect and how a second qubit can be encoded in the nuclear spin of a strongly coupled isotopic defect. For these discussions, I focus on the energy level structure presented in Fig. 3.4.

A single electron spin qubit can be encoded in any of the two $|m_S\rangle$ ground-state spin states, with popular choices being $\{|0\rangle, |+1\rangle\}$ or $\{|0\rangle, |-1\rangle\}$. These are attractive choices

Table 3.1: Optical and microwave resonances of defects in the divacancy family. *At B = 0 and at 20 K, unless not visible at low temperature, in which case the room-temperature values are given. ** Room temperature frequency.

Name	Structure	Orientation	Optical (eV)	ODMR 1 (GHz)	ODMR 2 (GHz)	D (GHz)	D_{ES} (GHz)	E^0 (MHz)	Room Temp?	20 K?
4H-SiC										
PL1	(hh) divacancy	c-axis	1.095	1.336	-	1.336	0.84	0	implanted	yes
PL2	(kk) divacancy	c-axis	1.096	1.305	-	1.305	0.78	0	no	yes
PL3	(hk) divacancy	basal	1.119	1.140	1.304	1.222	-	82.0	yes	yes
PL4	(kh) divacancy	basal	1.150	1.316	1.353	1.334	-	18.7	no	yes
PL5	unknown	basal	1.189	1.356	1.389	1.373	-	16.5	yes	yes
PL6	unknown	c-axis	1.194	1.365	-	1.365	0.94	0	yes	yes
PL7	unknown	basal	-	1.333	-	-	-	-	yes	yes
6H-SiC										
QL1	(k_1k_1) divacancy	c-axis	1.088	1.300	-	1.300	0.75	0	no	yes
QL2	(hh) divacancy	c-axis	1.092	1.334	-	1.334	0.85	0	yes	yes
QL3	unknown	basal	1.103	1.228	1.243	1.236	-	7.5	yes	yes
QL4	unknown	basal	1.119	1.208	1.425	1.317	-	109	no	yes
QL5	unknown	basal	1.134	1.340	-	-	-	-	yes	yes
QL6	(k_2k_2) divacancy	c-axis	1.134	1.347	-	1.347	0.95	0	no	yes
QL7	unknown	c-axis	-	1.345 (**)	-	1.345 (**)	-	0	yes	no
QL8	unknown	c-axis	-	1.371 (**)	-	1.371 (**)	-	0	yes	no
QL9	unknown	basal	-	1.332 (**)	1.365 (**)	1.349 (**)	-	17 (**)	yes	no
3C-SiC										
RL1	divacancy	[111]	1.120	1.328	1.328	1.328		< 2	wafer dep.	yes

SOURCE: [54, 86–88, 96, 97, 100, 101]

Table 3.2: Electric and strain-field coupling parameters of defects in the divacancy family. *Theoretical value, and the **Theoretical value as calculated with only piezoelectric distortions (i.e. no direct field contribution).

Name	Structure	Orientation	$d_{\parallel}$ (Hz cm/V)	$d_{\perp}$ (Hz cm/V)	$\epsilon_{\parallel}$ (GHz/strain)	$\epsilon_{\perp}$ (GHz/strain)
4H-SiC						
PL1	(hh) divacancy	c-axis	2.65 (5.2*, 0.38**)	-	-	2-4
PL2	(kk) divacancy	c-axis	1.61 (4.2*, 0.23**)	-	-	2-4
PL3	basal divacancy	basal	< 3 (0.41*)	32.3	-	2-4
PL4	basal divacancy	basal	0.44 (0.79*)	28.5	-	2-4
PL5	unknown	basal	< 3	32.5	-	-
PL6	unknown	c-axis	0.96	-	-	-
PL7	unknown	basal	-	-	-	-
6H-SiC						
QL1	(k_1k_1) divacancy	c-axis	-	26	-	-
QL2	(hh) divacancy	c-axis	-	-	-	-
QL3	unknown	basal	-	-	-	-
QL4	unknown	basal	-	-	-	-
QL5	unknown	basal	-	-	-	-
QL6	(k_2k_2) divacancy	c-axis	-	-	-	-
QL7	unknown	c-axis	-	-	-	-
QL8	unknown	c-axis	-	-	-	-
QL9	unknown	basal	-	-	-	-
3C-SiC						
RL1	divacancy	[111]	-	-	-	-

SOURCE: [54, 86–88, 96, 97, 100, 101]

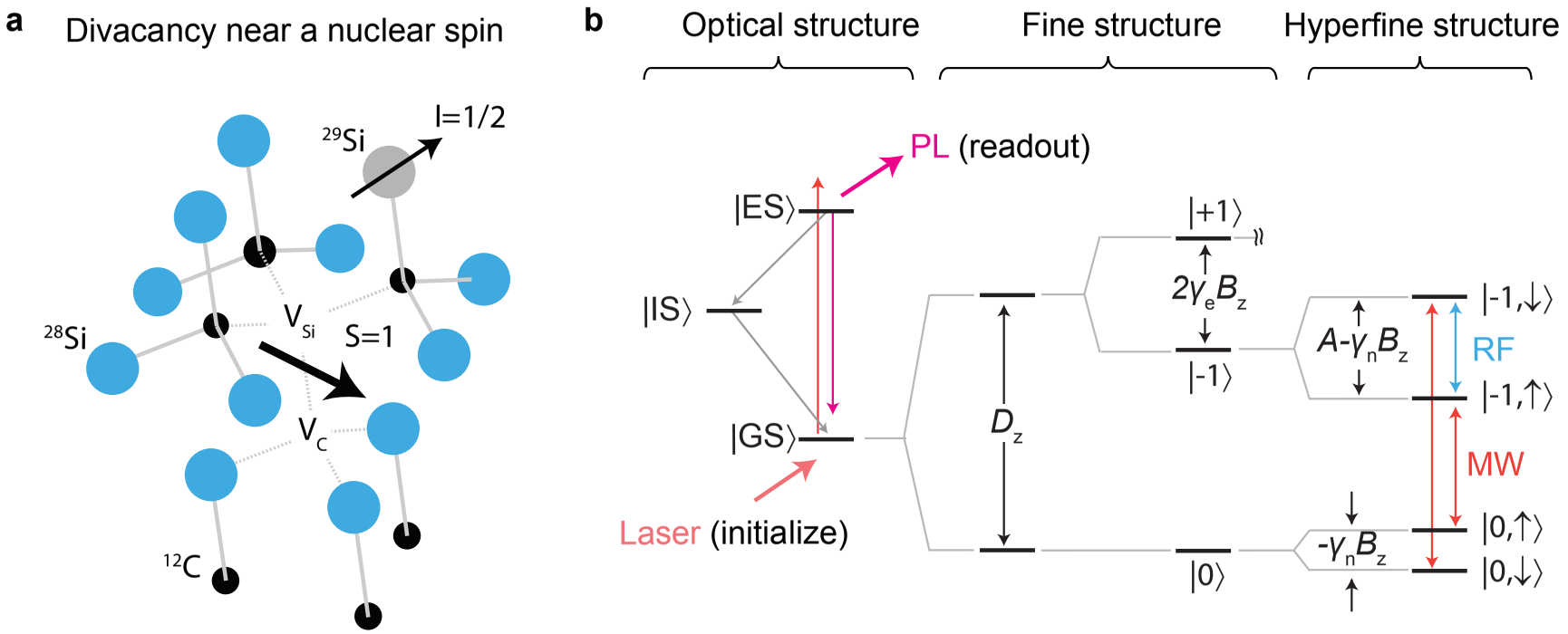

Figure 3.4: (a) A SiC divacancy defect with a nearby ^{29}Si isotopic defect, which has a nuclear spin (I=1/2). (b) The divacancy defect forms an atom-like state with an optical structure, a fine structure, and a hyperfine structure. To simplify the diagram, we have taken $E_{x,y} = 0$, which is true for c-axis oriented defects, and have assumed an isotropic hyperfine interaction $\mathbf{A} = A\mathbf{I}$, which is approximately true for coupling to ^{29}Si isotopic defects. A single qubit can be encoded in the $|0\rangle$ and $|-1\rangle$ fine-structure states. A two-qubit register can be encoded in the $|0,\uparrow\rangle, |0,\downarrow\rangle, |-1,\uparrow\rangle, |-1\downarrow\rangle$ hyperfine-structure states (see Chapter 6).

Table 3.3: Hyperfine coupling parameters of defects in the divacancy family. The "Nucleus" labels map to the labels in Figure 3.3. θ is the principal axis of the hyperfine tensor. *Theoretical value.

Name	Structure	Orient.	Nucl.	A_{xx} (MHz)	A_{yy} (MHz)	A_{zz} (MHz)	θ (degrees)
4H-SiC							
PL1	(hh) divacancy	c-axis	Si_{IIb}	9(9)	9 (9)	9 (8)	-
			C_I	53 (55*)	50 (56*)	110 (116)	73 (73*)
			Si_I	3 (3*)	3 (4*)	3(5*)	-
			Si_{IIa}	12 (9*)	12 (9*)	12 (0*)	-
PL2	(kk)	c-axis	Si_{IIb}	10 (10*)	10 (10*)	10 (9*)	-
			C_I	47 (49*)	45 (49*)	104 (110*)	73 (73*)
			Si_I	3 (1*)	3 (1)	3 (2*)	-
			Si_{IIa}	13 (10*)	13 (10*)	13 (9*)	-
PL3	(hk) divacancy	basal	C_{Ia}	51*	52*	118*	2*
			C_{Ib}	50*	50*	109*	(70*)
PL4	(kh) divacancy	basal	C_{Ia}	52 (52*)	52 (52*)	110 (116*)	0 (2*)
			C_{Ib}	48 (43*)	45 (47*)	109 (103*)	70 (70)
PL5	unknown	c-axis		-	-	-	-
PL6	unknown	c-axis	Si_{IIa}		-	12.5	-
			Si_{IIb}	-	-	9.6	-
PL7	unknown	basal		-	-	-	-
6H-SiC							
QL1	(k_1k_1) divacancy	c-axis	Si_{IIa}	-	-	12.7 (12.7*)	-
			Si_{IIb}	-	-	10 (10.5*)	70.8*
QL2	(hh) divacancy	c-axis	Si_{IIa}:	-	-	12.5 (11.8*)	-
			Si_{IIb}	-	-	9.2 (9.6*)	69.5*
QL3	unknown	basal		-	-	-	-
QL4	unknown	basal		-	-	-	-
QL5	unknown	basal		-	-	-	-
QL6	(k_2k_2) divacancy	c-axis	Si_{IIa}	-	-	13.3 (11.8*)	-
			Si_{IIb}	-	-	9.2 (9.7*)	69.4*
QL7	unknown	c-axis		-	-	-	-
QL8	unknown	c-axis		-	-	-	-
QL9	unknown	basal		-	-	-	-
3C-SiC							
RL1	divacancy	[111]		-	-	-	-

SOURCE: [54, 86–88, 96, 97, 100–102]

since quantum gates in these manifolds can be applied with a microwave magnetic field that is transverse to the c-axis ($\mathbf{B}_\perp$), via the transition element $\gamma_e\langle 0|\hat{\mathbf{S}}\cdot\mathbf{B}_\perp|\pm 1\rangle$. A qubit can also be encoded in the unconventional $\{|+1\rangle, |-1\rangle\}$ manifold, where quantum gates can be driven with a microwave electric field (or strain) via the transition element $d_\perp\langle +1|E_x(\hat{S_x}^2 - \hat{S_y}^2) + E_y(\hat{S_x}\hat{S_y} + \hat{S_y}\hat{S_x})|-1\rangle$ (this is discussed in detail in Chapter 6 and [97]). This would

be a natural basis choice in hybrid devices that interface defect qubits with, for example, mechanical resonators or superconducting qubits.

A two-qubit register can be encoded in the $\{|0,\uparrow\rangle, |0,\downarrow\rangle, |-1,\uparrow\rangle, |-,\downarrow\rangle\}$ manifold of a strongly-coupled electron-nuclear spin system (this is described in detail in Chapter 8 and [54]). Gates on the electron spin qubit can be applied as described above with a microwave magnetic field. Gates on the nuclear spin qubit can be applied with a radiofrequency magnetic field via the transition element $\gamma'_{n,i}(\gamma_{n,i}, \mathbf{A}_i)\langle \pm 1, \uparrow | \hat{\mathbf{I}} \cdot \mathbf{B}_{\perp,i} | \pm 1, \downarrow \rangle$. The oscillator strength has been modified from that of a free nucleus from $\gamma_{n,i} \rightarrow \gamma'_{n,i}(\gamma_{n,i}, \mathbf{A}_i)$. This modification accounts for the fact that the nuclear gyromagnetic ratio becomes augmented through the hyperfine interaction with the electron spin [103]. As an aside, this enhancement of the oscillator strength could enable ultra-fast nuclear-spin quantum memory in registers with a large hyperfine interaction. For example, in registers comprising either PL1, PL2, PL3 or PL4 and a nearest neighbor C atom (see Fig. 2.3 and PL1 - PL4 in Table 2.3), nuclear qubit gates within the rotating-wave should be applicable on tens-of-nanosecond timescales.

Encoding qubits in basal defects can be done in an analogous fashion. It is important to note, however, that they have a more complicated energy level structure. At zero magnetic field, their $|+1\rangle$ and $|-1\rangle$ spin states are hybridized and non-degenerate, and they have a non-linear energy dispersion with respect to an applied magnetic field.

3.6 SiC Defect Qubits and the DiVincenzo Criteria

As discussed in Section 2.4, useful qubits must fulfill the DiVincenzo criteria. In this section I will discuss electron spin qubits and nuclear spin qubits in SiC within the context of this criteria. I will make many references to the extensive NV center literature.

1. **Qubits should be well-defined and scalable** A single qubit can be encoded by single defect or by an ensemble of nominally identical defects (the general procedure was described in Section 3.5). In high purity SiC samples, single qubits can be spatially isolated and individually measured through confocal fluorescence microscopy [104]. In samples with

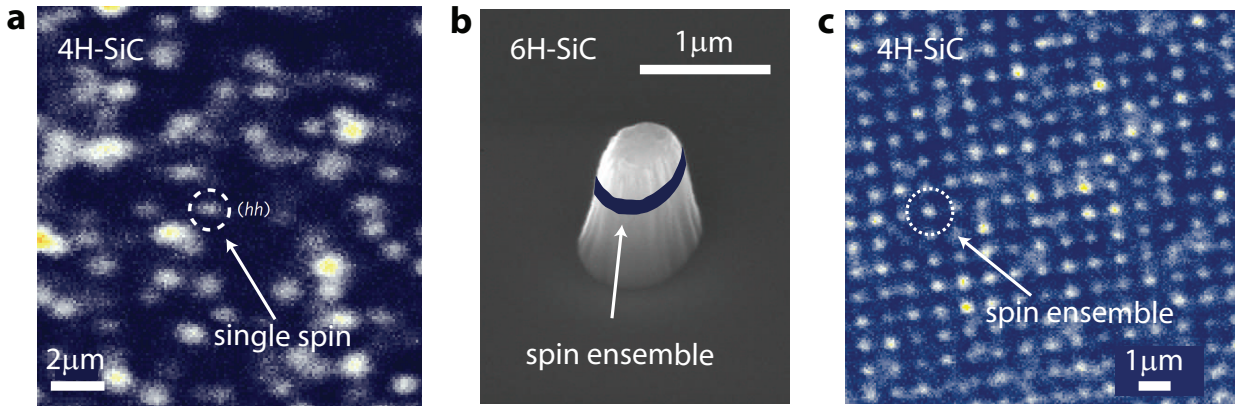

Figure 3.5: Isolating qubits in SiC. (a) Single spin qubits isolated through confocal photoluminescence microscopy. Ensemble qubits can be isolated through (b) the fabrication of nano-pillars or (c) by implanting ions through a lithographically-defined apertures. SOURCE: [88, 104]

high defect density - such as the electronic grade material that we purchase from CREE - ensemble qubits can be isolated spectrally, through their unique optical and spin transition energies [54, 87, 88]. If necessary, further isolation can be achieved spatially, by producing defect-ensemble arrays by implanting ions through apertures [88], or by fabricating micro- or nano-pillars (see Fig. 3.5).

Scaling registers to contain many qubits remains a significant challenge. In diamond, registers containing multiple NV electron spin qubits [105] and hybrid registers containing multiple NV electron and nuclear spin qubits [43, 44, 106, 107] have been realized, up to the 7-qubit level. Although multi-qubit registers at the single-defect level have not yet been realized in SiC, the same strategies should apply. Moreover, SiC shows potential for scalability beyond what is traditionally possible in diamond since (1) it hosts many distinct spin species, each with unique optical and spin transition energies (see Fig. 3.6), and (2) SiC heterostructures, which contain epilayers of distinct polytypes, can be grown [108]. Such "heteropolytype" structures could be used to increase the already-large number of individually addressable spin species and could potentially enable spin-coupling and quantum gates to be performed via interfacial 2-dimensional electron gases, which have been shown to exist at SiC heteropolytype interfaces [109–112]. I discuss this latter pathway in more

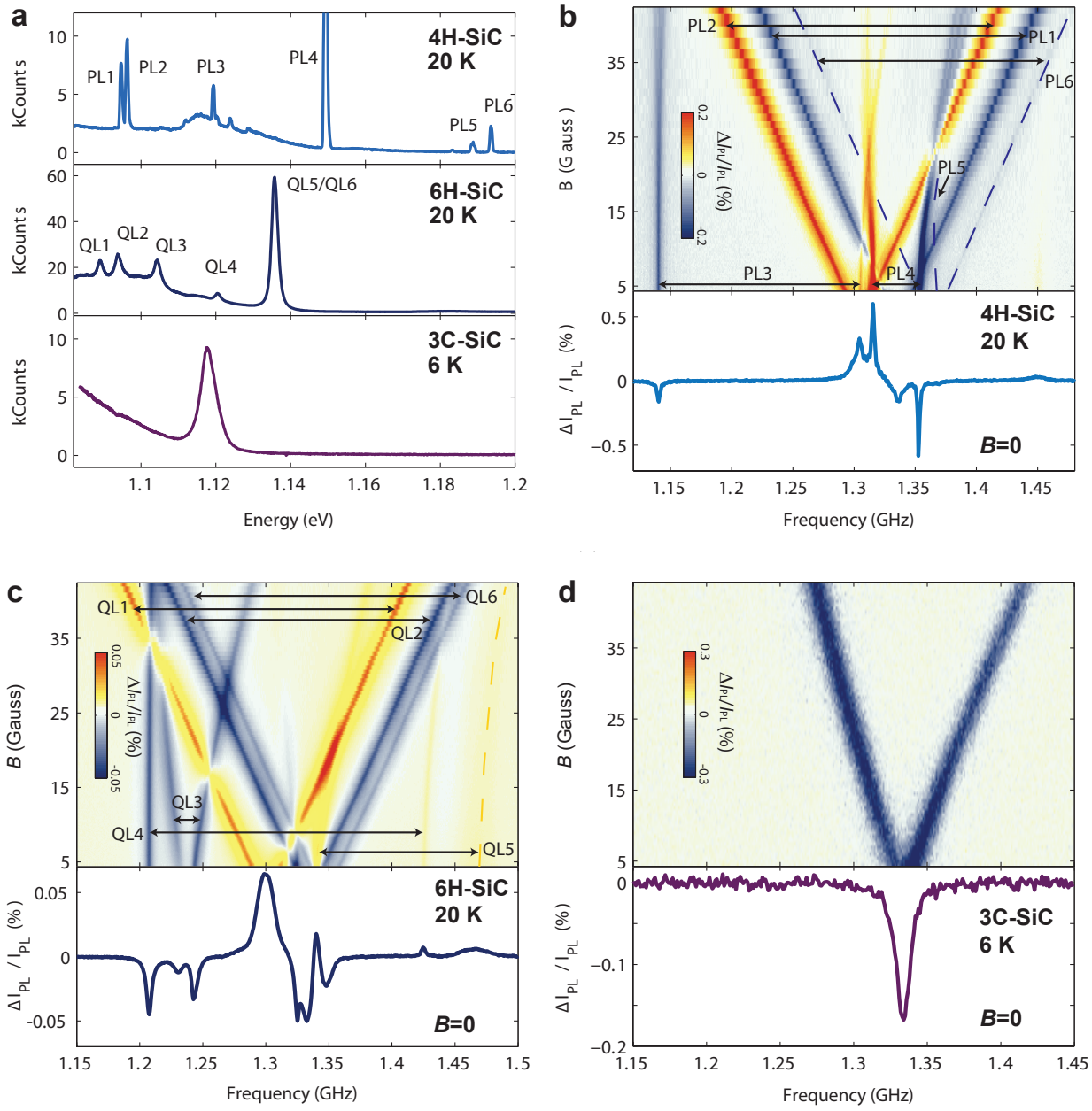

Figure 3.6: (a) Photoluminescence spectra of the divacancy family of defects in 4H-, 6H-, and 3C-SiC. (b)-(d) Optically detected magnetic resonance spectra of the defects seen in (a). The different defects are individually addressable through their spectrally isolated optical and microwave transition energies. SOURCE: [88].

detail in Chapter 9.

Scaling registers comprising ensemble qubits presents an entirely different set of opportunities. Due to collective excitations, spin ensembles can couple to external degrees of freedom orders of magnitude more strongly than can single spins. Such enormous coupling

strengths have been proposed for coupling to remote ensembles [113], to superconducting resonators [114], to mechanical resonators [115], and to optical fields [116]. Exploiting these strong interactions is a promising route to producing larger registers comprising many ensemble qubits. Of course, using ensemble qubits also comes with its own set of challenges. When compared to single-spin qubits, ensembles have faster dephasing rates, broader spin- and optical-transition lines, and they are generally more difficult to probe, especially when they are embedded within a complicated global ensemble.

2. **Qubits should be initializable into a well-defined fiducial state** Electron spin qubits can be initialized with remarkably high efficiency via non-resonant optical pumping from cryogenic to ambient conditions (the general mechanism was described in Section 3.3). It has been shown that the QL1, QL2, and QL6 defects in 6H-SiC initialize with $\geq 36\%$ $\geq 58\%$ and $\geq 60\%$ efficiencies, respectively (note that these have been quoted as rough lower bounds [88]). In Chapter 8 we show that the PL6 defect in 4H-SiC initializes remarkably strongly, with $95^{+5}_{-7}\%$ efficiency. In Chapter 7 and 8 we show that this electron polarization can be transferred to surrounding nuclei with up to 99% efficiency, via dynamic nuclear polarization. This serves as an efficient method to initialize nuclear spin qubits. Higher fidelity initialization via resonant optical pumping techniques, which were initially developed in atomic systems and then extended to NV centers in diamond [117], might be possible in SiC, though this remains an outstanding challenge.

3. **Qubits should be controllable with a universal set of quantum gates** Electron and nuclear spin qubits can be controlled with a universal set of logic gates based on microwave and radiofrequency pulses. In Chapter 8, we develop a universal set of quantum gates for a 2-qubit hybrid register with an average error rate in the 10^{-2} range. Improving the error rates to below 10^{-3} should be straightforward, by employing sophisticated magnetic resonance techniques that have been developed over decades of electron paramagnetic resonance (EPR) and nuclear magnetic resonance (NMR) research [118].

4. **Qubits should be measurable in a projective way** Electron and nuclear spin

qubits can be measured through their spin-dependent photoluminescence during repeated non-resonant optical pumping (as described in Section 3.3). We employ this as the primary measurement technique in the experiments presented in this thesis. Nonetheless, this measurement pathway is non-ideal since it is inherently non-projective. Projective measurements have been realized in multi-qubit registers based on NV centers in diamond [117], but their development in SiC remains an outstanding challenge.

5. **Qubit coherence should greatly exceed the gate time** Electron spin qubits in non-isotopically purified SiC have remarkably long Hahn-echo coherence times that range from 1 ms at 20 K [104] to 100 μs at room temperature [87]. With typical gate times in the 1-10 ns range, it should be possible to execute between 10^6 to 10^4 quantum logic operations within the coherence time. This figure of merit can be increased by extending the qubit coherence through some combination of isotopic purification of the SiC host crystal, the application of dynamical decoupling sequences [61–63], and/or quantum-error correction [23, 43, 44, 67].

Nuclear spin qubits have been shown to have reasonably long coherence times at room temperature ($\sim$300 μs), limited by the electronic $T_{1,e}$. With typical nuclear gate times on the order of 1 μs, it should be possible to execute 10^2 quantum logic operations within the coherence time. It is expected that this figure of merit will go up significantly at cryogenic conditions. For reference, $T_{1,e} \sim 5$ ms at 100 K for many of the divacancies [88] and $T_{1,n} \sim$ hours for weakly coupled nuclei at 300 K [119]. It is expected that hyperfine-induced dephasing will not be an issue, since the coupling can be "turned off" by rotating the electron spin qubit into $|0\rangle$, where the hyperfine interaction is nonexistent.

6. **Qubits should be convertible into photonic qubits** Electron spin qubits based on color centers are attractive for quantum communication since they have a built in optical interface. With NV centers in diamond, this interface has enabled demonstrations of spin-photon entanglement [120], the entanglement of distant NV centers [42, 55], and the teleportation of a quantum state between these NV centers [84]. It is expected that these

demonstrations will also be possible in SiC, though this remains an important outstanding challenge.

7. **Photonic qubits should be transmittable across long distances with low loss** Electron spin qubits in the divacancy family are particularly attractive since their useful optical emission ranges from 1140 nm to 1000 nm [87, 88], which is near the fiber-optic telecommunications "O band", which extends from 1260 nm to 1360 nm. The optical absorption of a standard silica fiber from 1000 nm to 1140 nm ranges from approximately ∼0.9 dB/ km to ∼0.5 dB/ km, which is only 1.1× higher than the least lossy telecom band (the "U band"), which is ∼0.2 dB/ km. For comparison, the NV center emission at 637 nm experiences 6.8× higher attenuation of ∼8.5 dB/ km.

3.7 Conclusions

In this chapter I have hopefully motivated that electron and nuclear spins in SiC are attractive qubit candidates. In the following chapter I describe the experimental apparatus that we have built for controlling and studying these qubits, with the primary goal of implementing quantum algorithms.

CHAPTER 4

IMPLEMENTING QUANTUM ALGORITHMS

4.1 Overview of the Apparatus

In this chapter I describe the apparatus that we have built to perform quantum algorithms on electron and nuclear spin qubits in SiC. Quantum gates in these algorithms are implemented via optical, microwave, and radiofrequency fields on ns to μs-timescales. The apparatus is schematically illustrated in Figure 3.1 and described in detail in the sections that follow. It integrates a home-built confocal photoluminescence microscope, microwave and radiofrequency electronics, a liquid-helium flow cryostat, and a movable magnet.

4.2 Confocal Photoluminescence Microscope

For continuous wave and slow-pulsed excitation, we use a 975 nm diode laser. This light is collimated with a lens and is then focused through an acousto-optic-modulator (AOM). The AOM is used to gate the laser on and off on microsecond timescales, with a typical rise time of $\sim$100 ns. There is typically a tradeoff between the rise time and the extinction ratio of the gated light (optimally near 30 dB), which can be tuned by using different focal-length lenses to focus the light through the AOM. A higher extinction ratio can be achieved by using a double-pass geometry, though we did not employ this technique. The AOM is controlled via a transistor-transistor-logic (TTL) digital signal that is sourced by an arbitrary waveform generator (AWG).

For ultrafast-pulsed excitation, we use a Ti:Sapphire laser, which is pumped by several watts of 532 nm light from a frequency-doubled Nd:YAG laser. When mode-locked, the Ti:Sapphire laser can emit pulses on femto- to picosecond timescales, depending on the internal arrangement of the cavity. The intrinsic 76 MHz repetition frequency of the laser can be reduced by using an electro-optic modulator (EOM) and the associated pulse-picking

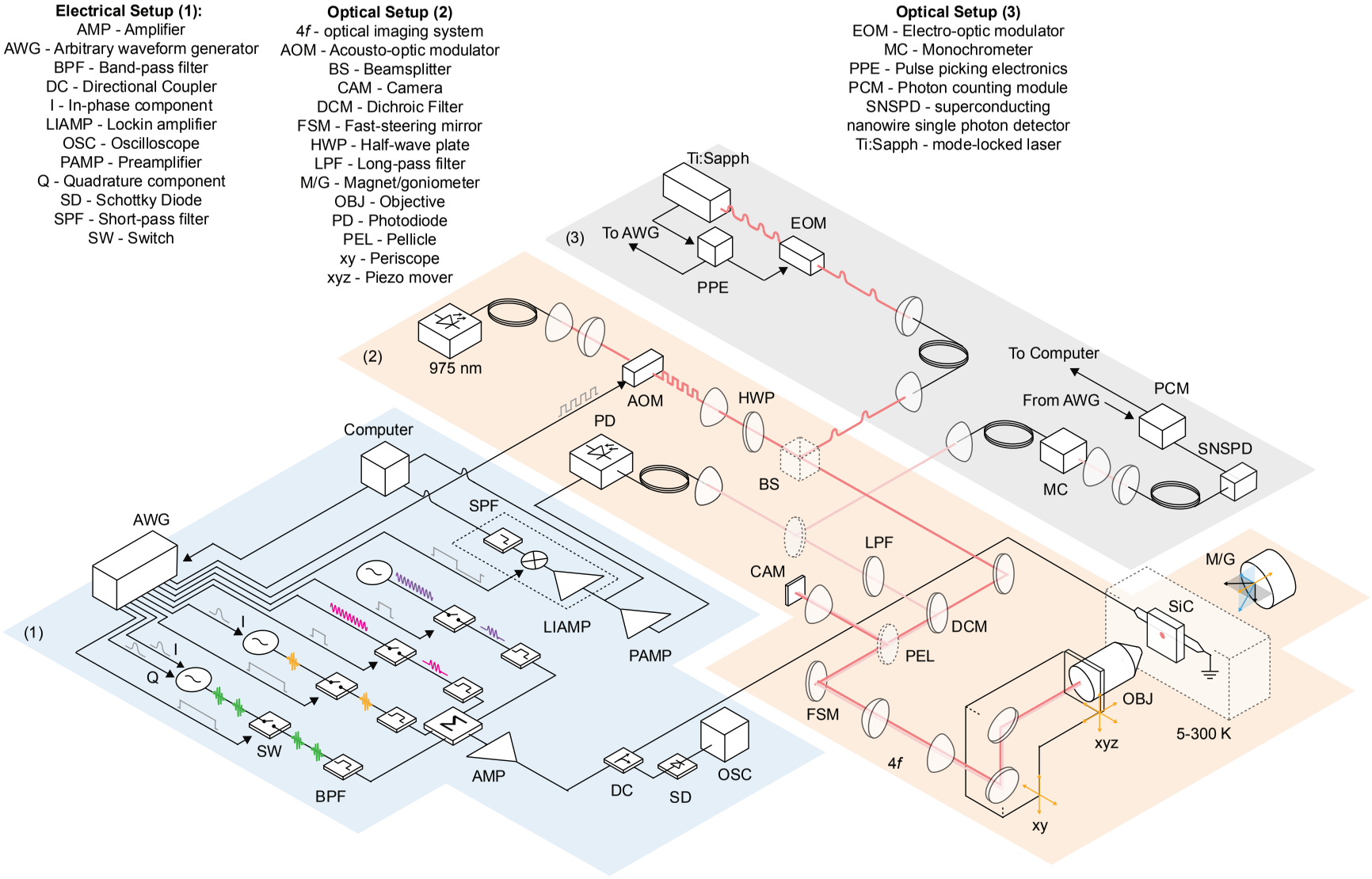

Figure 4.1: Our apparatus for executing quantum algorithms on spin qubits in SiC.

electronics (PPE).

In the excitation path, laser light passes through a half-wave-plate (HWP), which is used as a polarization rotator, a neutral density filter (NDF), which is used for intensity control, and then a short-pass dichroic filter (DCF), whose purpose we describe later. The light then passes through a pellicle beamsplitter (PEL), reflects from a fast-steering-mirror (FSM), passes through a $4f$ imaging setup, and is focused with a $50\times$ objective onto a SiC sample, which is mounted within our cryostat. When the FSM is tilted from its neutral position, the $4f$ setup guides the light so as to not displace its position on the back aperture of the objective, but rather to angle it. This angle specifies where on the sample the excitation light hits. The excitation beam can also be moved around the sample with a motorized periscope (xy; coarse) or a three-axis piezo stage (xyz; fine).

Following excitation, color centers emit photoluminescence (PL), which we detect to infer the states of the associated qubits. In the collection path, the PL, the excitation light reflected from the sample (RL), and the scattered light (SL, perhaps from a white-light source that is being used to illuminate the sample) are all collimated by the objective and they start to trace out the excitation path, away from the sample. After the $4f$ optical setup and the FSM, the light is incident on the PEL, which picks off some of the beam. This light is focused onto a CCD camera, which we use to image the sample (primarily the RL and SL).

Without the PEL, the PL, RL, and SL are incident on the DCF, at which point the PL is reflected, while the RL is predominantly transmitted. Since the SL can be made weak during experiments, I'll ignore it from here. The beam is then filtered with a long-pass filter (LPF), to remove any weakly-reflected RL, to isolate the PL. Note that the RL, when the LPF is not in place, is useful for aligning the detectors, which I describe next.

We use one of two detectors, which we toggle between using a flip mirror (shown as a dashed beamsplitter (BS) in Fig. 3.1). With the flip mirror "down," the PL is focused into an optical fiber, which acts as a pinhole and is used to achieve confocality. The fiber leads

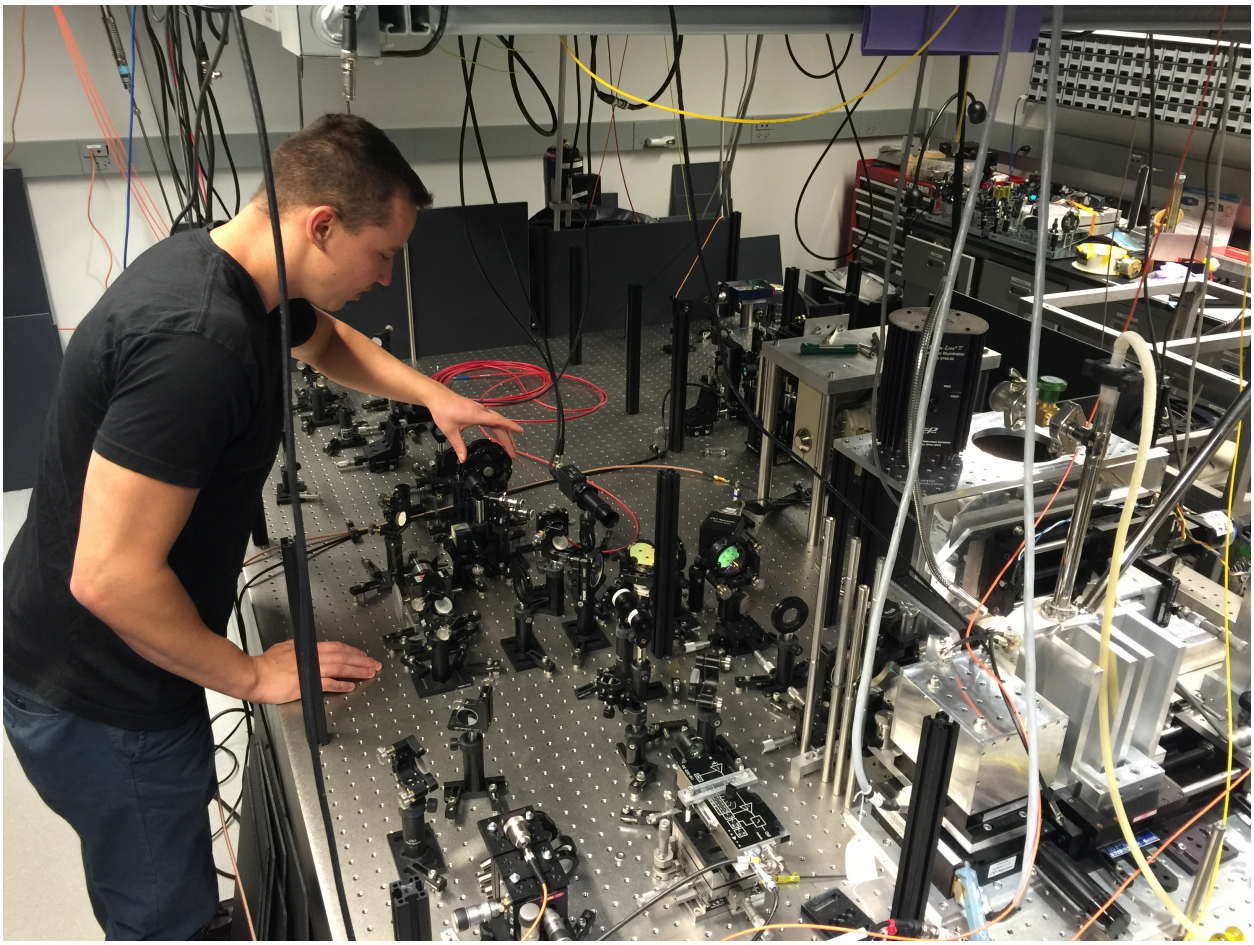

Figure 4.2: The author working on the optical setup

to a monochrometer (MC), which is used as a broadband filter, and is then focused into a single-mode optical fiber, which guides the PL to a superconducting nanowire single photon detector (SNSPD). The single photons can be time-tagged on picosecond timescales using a pulse counting module (PCM).

With the flip mirror "up," the PL is focused into an optical fiber, which, again, acts as a pinhole and is used to achieve confocality. The PL is then guided to a single-pixel InGaAs photodetector (PD). The PD signal is amplified with a preamplifier (PAMP), and then split into two. One signal is sent to a digital acquisition board (DAQ) to measure the total PL and the other to a lockin amplifier (LI). The LI is an indispensable tool, which enables us to extract a weak modulated signal from a strong constant background (this is the case in all of our ensemble measurements).

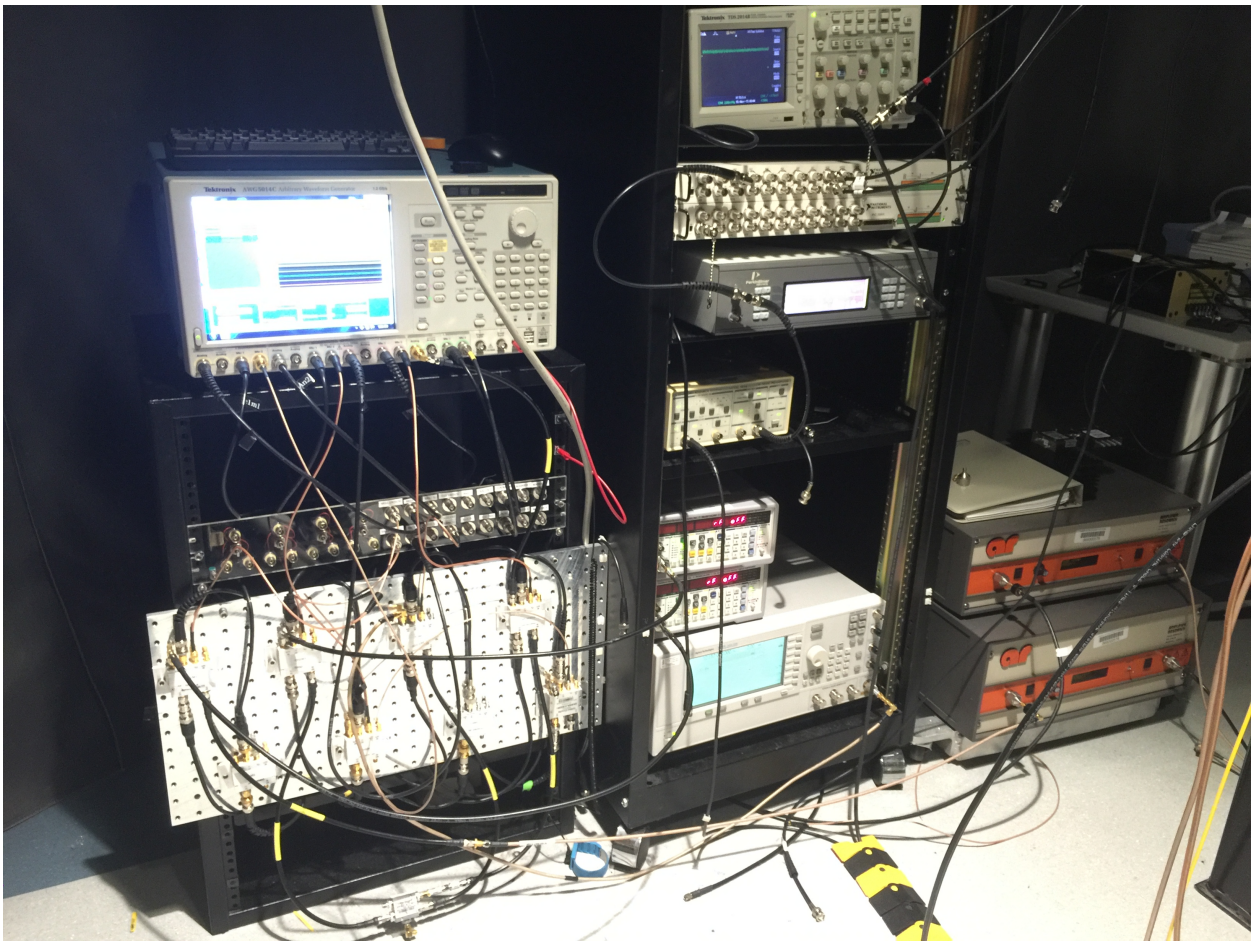

Figure 4.3: The electronics setup.

4.3 Microwave and Radiofrequency Electronics Setup

At the heart of the electronics setup is the AWG, which we use primarily for timing our experiments by triggering and gating electrical and optical pulses. In our two-qubit experiments, we use three microwave (MW) colors for electron spin qubit control and one radiofrequency (RF) color for nuclear spin qubit control. RF control pulses are synthesized directly by the AWG, while the MW control pulses are generated by two vector signal generators and a third analog signal generator. When pulse shaping and/or phase control over MW control pulses are necessary, we drive the in-phase (I) and quadrature (Q) ports of the vector signal generators via the AWG's analog outputs, with the desired envelope functions. DC blocks are used to protect the signal generators from potentially harmful DC voltages.

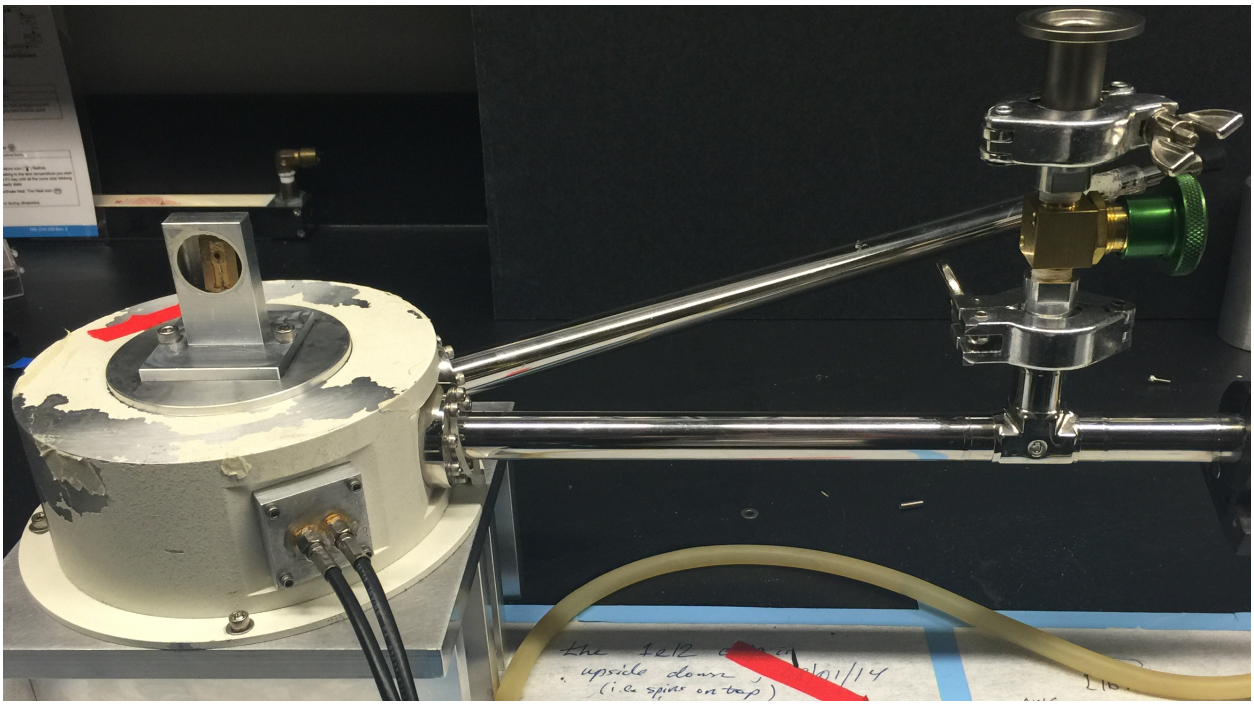

Figure 4.4: The Janis ST-500 flow cryostat.

MW and RF signals are gated on/off with switches, triggered by the AWG's markers. They are independently band-pass-filtered (BPF), multiplexed onto a single coaxial line with a power-combiner (Σ), and amplified with a broadband RF/MW amplifier (AMP). After amplification, they are directed into the cryostat, where they are delivered to the SiC chip for qubit manipulation. Between the AMP and the cryostat, we pick off part of the control signals at a -20 dB port of a directional coupler (DC), pass them through a Schottky diode (SD), and then into an oscilloscope (OSC). This enables us to monitor both the shape and the strength of our MW control pulses, which is useful for debugging the system. The output of SD is non-linear in both frequency and input power and thus it needs to be calibrated accordingly. Another way to debug the system is to monitor the MW and RF signals directly on a fast oscilloscope.

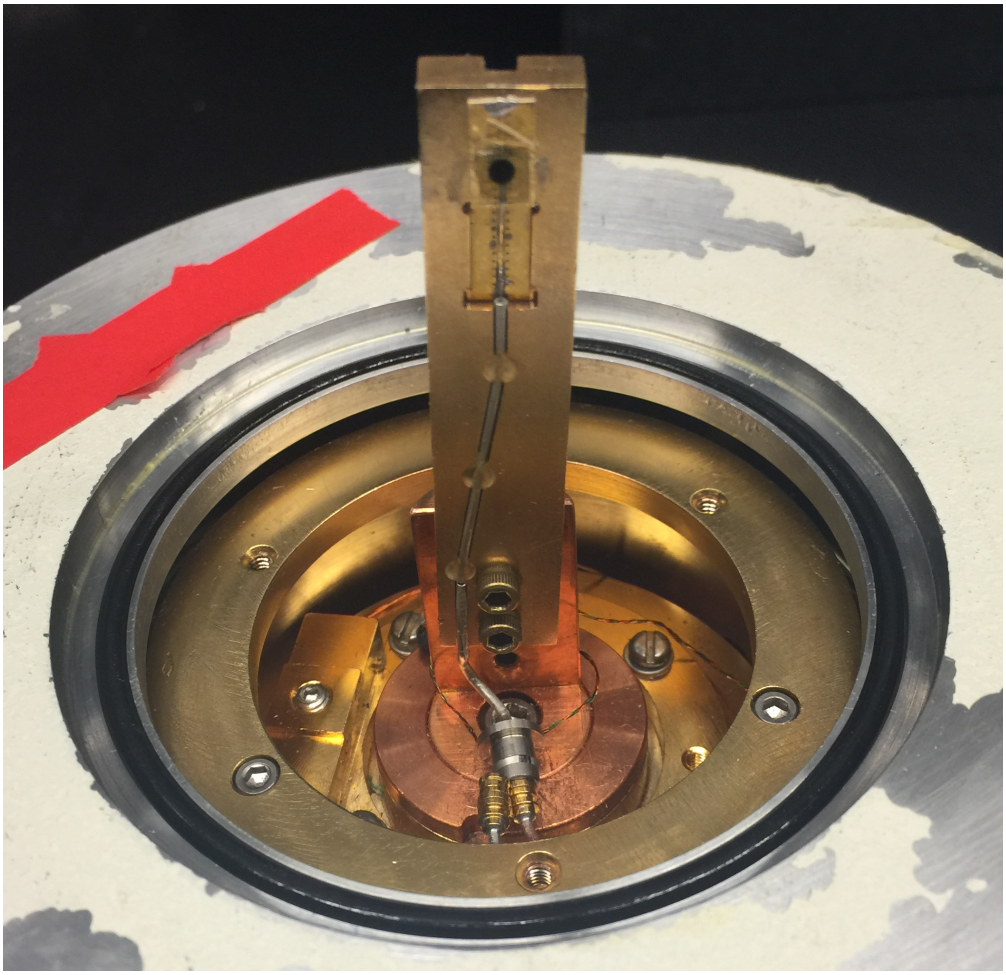

Figure 4.5: A closeup of the cryostat sample-space.

4.4 Cryogenics Setup

At the heart of the cryogenics setup is a Janis flow cryostat (see Fig. 3.4), which has optical access and a built in temperature sensor and heater. Using liquid helium, the cryostat's sample stage can reach approximately 4 K, and it can stay cold at 20 K for approximately 7 to 10 days when using a 100L dewar. If the cryostat warms up prematurely and continues to do so on several consecutive cool-downs, there might be a leak. Leaks can be detected by using a residual gas analyzer (RGA - commonly integrated with vacuum pumps), and then sealed with epoxy or vacuum grease (Down Corning or Apiezon work well).

Custom coaxial ports have been designed to inject the MW and RF control pulses into the cryostat. As a word of warning, adjusting the connectors on these ports can result in an air

leak and so this is not recommended during a cool-down or pump-out. Within the cryostat, we use semi-rigid coaxial lines (Fairview HC13000-3), which terminate in low-retention SMP connectors (Radiall R222.221.702W) that have been designed to connect to custom-built sample mounts (see Fig. 3.5).

Sample mounts, or more commonly "coldfingers," are machined from oxygen-free copper, which has a high thermal conductivity and is well-suited for cryogenic applications (Fig. 3.6). Our cold fingers have built-in semi-rigid coaxial lines that break out onto 50 Ω coplanar waveguides, which serve as antennas for the MW and RF signals (striplines are thermally grounded to the coldfinger with solder). For fast spin control, we short-terminate the coplanar waveguide, which produces a current-antinode at the short and thus a strong magnetic field. Even stronger magnetic fields can be achieved by using on-chip waveguides that have been lithographically patterned in the cleanroom (the first few chapters of Pozar's Microwave Engineering book [121] introduce important transmission-line concepts, which can aid in the design of these waveguides and other devices). In addition to RF and MW signals, DC voltages are sometimes necessary for applying a static electric field or driving a piezoelectric, for example. These can be applied either directly through the RF lines or through separate DC lines, which can be routed into the cryostat.

Our samples are thermally sunk directly to the stripline, typically with Elmer's rubber cement, which has excellent thermal cycling properties (i.e. the cement retains its high thermal conductivity even after many cool-down/warm-up cycles). GE varnish can also be used, but it tends to have worse thermal cycling characteristics. Silver paint is not recommended since it is difficult to remove without damaging the sample.

4.5 Magnet Setup

Since our qubits are spins, it is crucial that we can apply a static magnetic field at a wide range of angles. We achieve this by mounting a permanent magnet to a custom goniometer stage, which sits behind the cryostat (the focal point of the goniometer should be centered

Figure 4.6: Custom coldfingers with built-in coaxial lines.

at the interrogation volume of the sample). To give a sense of the field-strength that is achievable, a cylindrical N52 magnet that is 2 inches in diameter and length can achieve a 1600 G field one inch from the magnet face (calculated using KJ magnetics' magnetic-field calculator). A good goniometer design can save countless hours, since a precise magnet alignment is necessary for virtually every experiment (even a slight misalignment of 0.5° can substantially alter the physics of the system [102, 122]). In the future, it could pay to use Hall-bar sensors within the cryostat, or at judiciously chosen spots on the vacuum shroud of the cryostat. These could be used to get an estimate of the on-axis magnetic field, or what is usually more important, the off-axis field. Multi-axis Helmholtz coils could be employed for slight field corrections.

CHAPTER 5

TUNING SPINS WITH ELECTRIC FIELDS AND STRAIN

5.1 Introduction

In this chapter, we demonstrate that the electron spins associated with divacancy-family defects in 4H-SiC are remarkably sensitive to electrical and mechanical perturbations. Their electric field response is 2-7 times stronger than that of NV spins in diamond [123, 124], and their photoluminescence (PL) is highly spin-dependent, which is an important quality for efficient readout. Applying these facts, we demonstrate an AC strain-sensing protocol with a projected sensitivity in the $10^{-7}/\sqrt{HzN}$ range, where N is the number of interrogated spins. Although electric- and strain-field effects on SiC spins are intertwined due to SiC's piezoelectricity, our *ab-initio* simulations disentangle these two effects and attribute the strong spin response to electric fields due to the high electron polarizability in SiC. Because our techniques are based on intrinsic quantities, their applicability extends down to the single defect level and nanometer scales. In the future, they could be applied for sensing intracellular electric fields [125], coupling spin qubits to nanomechanical resonators [126], or potentially for coupling spin qubits to superconducting qubits through surface acoustic waves. This chapter and the associated Appendix A were adopted from reference [96].

5.2 Spin Coupling to Electric and Strain Fields

Neutral divacancies consist of a C vacancy adjacent to a Si vacancy and they exist in 4 inequivalent forms in 4H-SiC. These forms are distinguished by whether the vacancies occupy the hexagonal (h) or quasi-cubic (k) SiC lattice sites [87]. These forms have been alternatively labelled as PL1-PL4 [87, 88], P6/P7 centers (in electron paramagnetic resonance studies) [85, 86, 127], and the UD2 lines (in PL studies) [90]. Their electronic ground states are spin

triplets and described by the Hamiltonian [123, 128]:

$$H = hD\sigma_z^2 + g\mu_B \sigma \cdot \mathbf{B} - E_x(\sigma_x^2 - \sigma_y^2) + E_y(\sigma_x\sigma_y + \sigma_y\sigma_x) \tag{5.1}$$

where the defect axis is aligned along $\mathbf{z}$, h is Plancks constant, $g = 2.0$ is the electron g-factor, μ_B is the Bohr Magneton, σ is the vector of spin-1 Pauli matrices, $\mathbf{B}$ is the magnetic field, and D, E_x, and E_y are the zero-magnetic-field splitting parameters. These terms can be expanded as $D = D^0 + d_{||}F_z + e_{||}\epsilon_z$ and $E_{x,y} = E^0_{x,y} + d_\perp F_{x,y} + e_\perp \epsilon_{x,y}$, where the D^0 and $E^0_{x,y}$ terms are the crystal-field splittings in the absence of applied strain and electric fields, $d_{||}$ and $d_\perp$ are the Stark-coupling parameters of the ground-state spin to an electric field ($\mathbf{F}$) that is respectively parallel and perpendicular to the defect axis, $e_\parallel$ and $e_\perp$ are the strain-coupling parameters, and $\vec{\epsilon}$ is the effective strain field defined in Ref. [128].

PL1 and PL2 (the hh and kk divacancies, respectively) are oriented along the SiC c-axis and have C_{3v} symmetry (i.e. $E^0_{x,y} = 0$). PL3 and PL4 (the hk and kh divacancies, respectively) are oriented along basal planes, each 109.5 degrees from the c-axis, and have C_{1h} symmetry. Due to the lower symmetry, $E^0_{x,y} \neq 0$, and thus all three spin sub levels are non-degenerate at zero magnetic field.

Our experiments use high-purity semi-insulating 4H-SiC wafers, purchased from CREE Inc., in which neutral divacancies are incorporated unintentionally during crystal growth. We thinned 500 μm-thick chips of SiC down to 50μm-thick membranes and used epoxy to mount them to piezo actuators, which are in turn thermally grounded to copper cold fingers with rubber cement for cryogenic operation. The neutral divacancies zero-phonon line (ZPL) optical transitions can be seen as sharp peaks in their PL spectra [90] when illuminated with 1.27 eV light, at a temperature $T = 20$ K. Each inequivalent divacancy has a distinct ZPL energy ranging from 1.0-1.2 eV. In addition, two other observed species (labeled PL5 and PL6) have similar optical and spin transition energies to the neutral divacancies [87], but the defects with which they are associated have not yet been identified.

Microwave (MW) radiation for electron spin manipulation is supplied by an on-chip waveguide or a stripline antenna below the sample [87, 88]. Actuation of the piezo applies tensile strain to the SiC membrane, transverse to the c axis (Fig. 5.1a). We estimate the strain to be $5 \times 10^{-7}\text{strain}/V_{\text{piezo}} \pm 40\%$ (Appendix A.1), where V_{piezo} is the voltage applied to the piezo. Due to the macroscopic size of the piezo, the electric field produced through the application of V_{piezo} is too weak to interfere with any measurements.

As strain is applied, the energy of each defect species' ZPL splits and shifts as much as 2.3 meV, or 550 GHz (Fig. 5.1b). The ZPLs corresponding to the c-axis-oriented defects bifurcate, with the two branches having orthogonally polarized PL (Fig. 5.1c). This splitting, which is approximately 12 eV/strain, reflects the reduction of the C_{3v} symmetry of the c-axis-oriented defects. The doubly-degenerate excited state orbitals at zero strain are predicted [86] to closely match the structure of NV centers in diamond [129, 130]. In contrast, the basal-oriented defects have split ZPLs even at zero strain due to the crystal field. Each ZPL branch of the basal defects trifurcates as strain is applied, with the polarization from each branch offset by 120 degrees. This splitting indicates that, as expected, strain breaks the symmetry between the orientations of basal defects that are rotationally equivalent at zero strain.

Applying transverse strain to the SiC membrane also shifts the defects' electronic spin transition energies. We measure these shifts with optically detected magnetic resonance (ODMR). We read out the ground-state spin by exploiting the defects' spin-dependent ($m_s = 0$ vs. $m_s = \pm 1$) PL intensity (I) and monitoring the changes to I (ΔI) as an applied MW field rotates spins via electron spin resonance [87, 88]. The ΔI resonances, as the frequency of the applied MW field is swept, correspond to the spin transition energies (Fig. 3.2a).

As we apply uniaxial strain transverse to the c axis, the average frequency of the two $\Delta m_s = \pm 1$ spin transitions shift (Fig. 5.2a), corresponding to a D-term shift of the spin Hamiltonian (Eq. 5.1). Although we observe DC spin resonance shifts of up to 0.8 MHz, the resolution of DC-strain detection [128] is constrained by relatively broad $1/T_2^*$ spin-resonance linewidths, where T_2^* is the inhomogeneous spin-dephasing time (1.5 μs for the basal defects

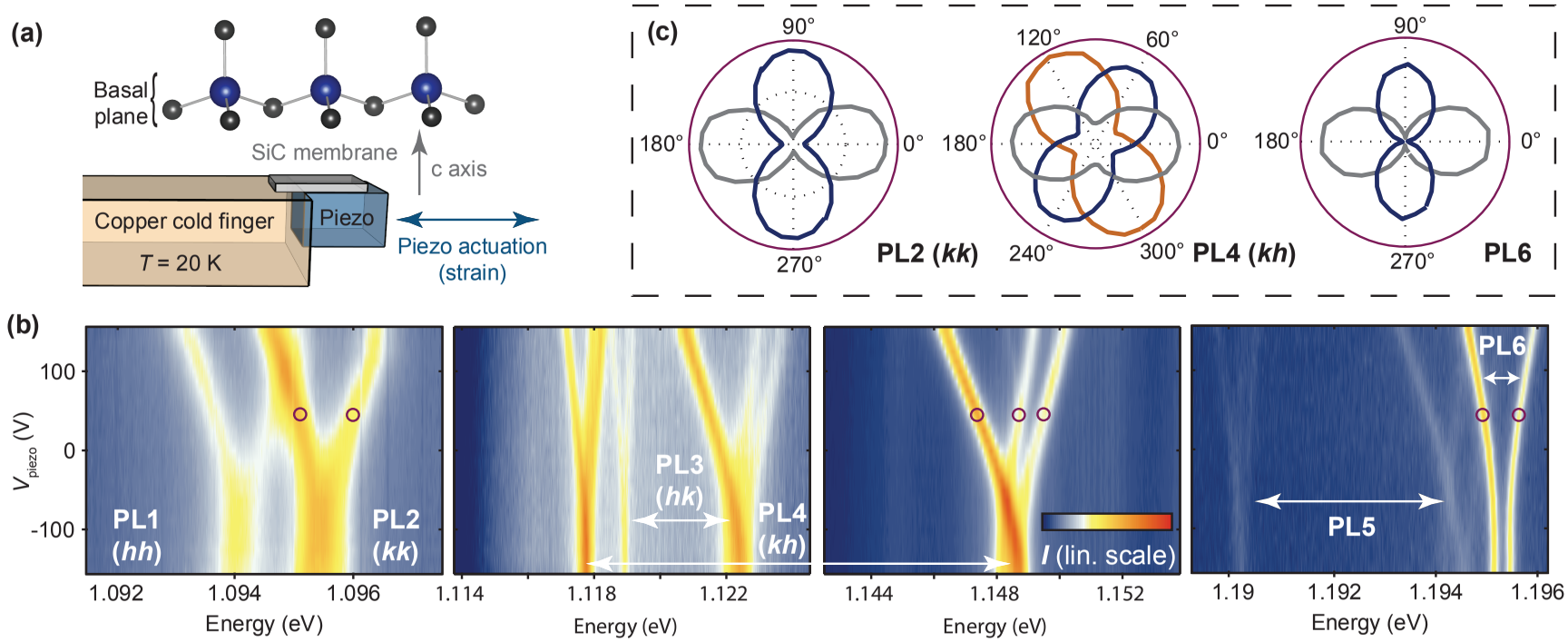

Figure 5.1: (a) A 4H-SiC membrane is mounted to the top of a piezo actuator, which applies strain to the membrane as it stretches. (b) PL spectra as a function of V_{piezo} (strain) at $T = 20K$, showing that the optical transitions of SiC defects can be tuned with strain. The strain splits the ZPL optical transitions, with the c axis-oriented defects (PL1, PL2, and PL6) bifurcating and the basal-oriented defects (PL3, PL4, and PL5) trifurcating. (c) Polarization dependence of the PL from the strain-split ZPL branches, measured at the points indicated by purple circles in (b). The analyzed polarization is in the plane perpendicular to the c axis. SOURCE: [88]

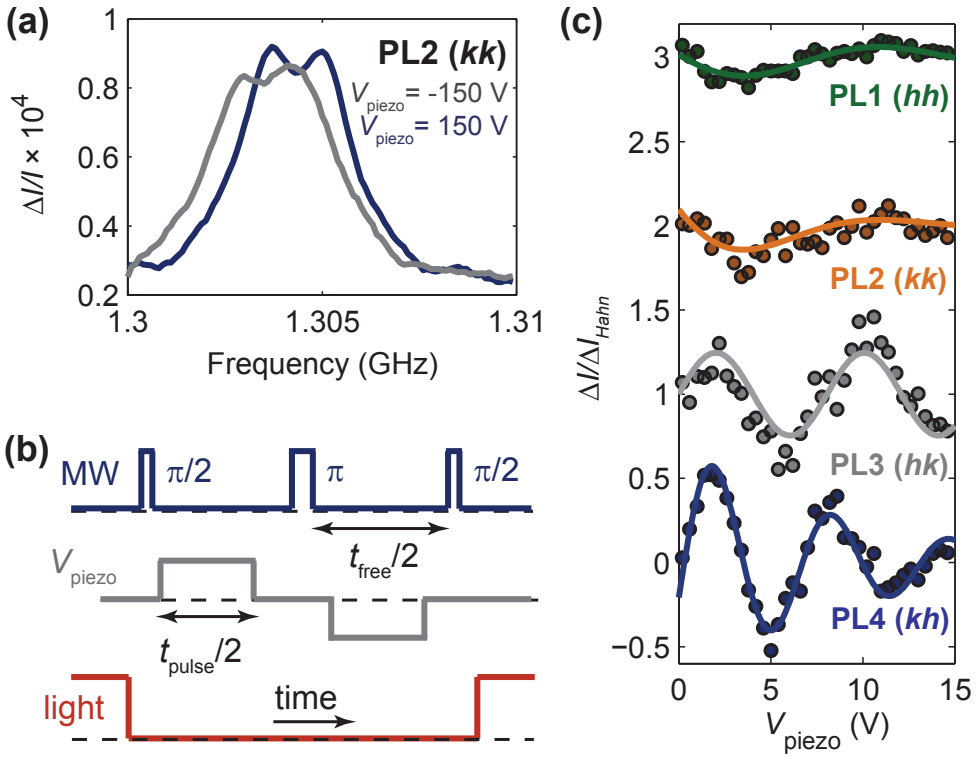

Figure 5.2: (a) Strain sensing using ODMR of divacancy spins in SiC at T=20 K. A 0.8 MHz strain-induced D-shift is observed. The peaks are split in each curve due to a stray B field of 0.35 G. (b) The Hahn-echo pulse scheme used for T_2-limited AC strain sensing. During the t_{free} evolution periods, strain induced through $\pm V_{\text{piezo}}$ pulses add a relative phase shift the spin superposition. The final pulse of the Hahn-echo sequence projects this phase onto a measurable spin population difference. (c) AC strain sensing data for the neutral divacancies, with $t_{\text{free}} = 100\mu$s, $t_{\text{pulse}} = 80\mu$s, T=20 K, and B = 0 G. The fits are to single exponentially decaying sine curves and have frequencies of 0.07 V^{-1}, 0.07 V^{-1}, 0.12 V^{-1}, and 0.16 V^{-1} for PL1-PL4, respectively. The three curves are offset for clarity. SOURCE: [88]

and approximately 300 ns for the c-axis defects [87]).

We developed an ensemble AC sensing technique that leverages the much longer homogeneous coherence time (T_2) of SiC divacancies (up to 360 μs [88]) to enable more sensitive strain measurements. Here, a Hahn-echo pulse sequence is applied between $m_s = 0$ and one of the $m_s = \pm 1$ spin states [88,123,131]. During the free precession segment (of total length t_{free}) of this sequence, a synchronized strain perturbation (generated by $\pm V_{\text{piezo}}$ applied to the piezo) causes a strain-induced phase to accumulate between the $m_s = 0$ and $m_s = \pm 1$ spin superposition (Fig. 5.2b). The final pulse of the Hahn-echo sequence projects this

strain-induced phase shift into a spin population difference and thus a measurable ΔI. We normalize ΔI by ΔI_{Hahn}, the Hahn-echo signal strength with no strain applied. As strain is increased, Δ_I oscillates (Fig. 5.2c) according to this phase shift, demonstrating coherent spin-based strain sensing.

Despite the large uncertainty in our strain calibration, we infer that the spin transitions of PL1-PL4 exhibit strain shifts that range roughly from 2-4 GHz/strain, and that our ensemble measurements demonstrate sub-10^{-6} strain sensitivity after averaging for two minutes per point. In an ideal measurement, with high optical collection and small background PL, AC strain sensing with neutral divacancies has a projected sensitivity in the $10^{-7}/\sqrt{\text{Hz}N}$ range (see Appendix A.2). Optical interferometry is a more precise technique for sensing strain in bulk samples, but it relies on measuring mechanical displacement (with sensitivities down to 10 pm [132]). Spin-based strain sensing should thus be a competitive technique for measuring strain in micro- and nanostructures, where absolute displacements are extremely small, as well as in applications involving full tensor-strain measurements [130].

To measure the response of SiC spins to electric fields, we use the same pulse sequence that we used for strain measurements (Fig. 5.2b and ref. [123]), now applying a voltage across a SiC membrane (V_{mem}, which produces a c-axis oriented electric field) instead of V_{piezo} (Fig. 5.3a). As seen in Fig. 5.2, ΔI exhibits oscillations with with increasing V_{mem}, which corresponds to an electric field-induced phase shift of the spin superposition (Fig. 5.3b-c). The basal-oriented defect spins primarily couple to the c-axis electric field via $d_\perp$ (i.e. E term shifts in Eq. 5.1). This results in mirror-image ΔI oscillations when the sequence is applied between the two $\Delta m_s = \pm 1$ transitions (Fig. 5.3b, left), which are split and evolve in opposite directions. The c-axis-oriented defects have slower ΔI oscillations (Fig. 5.3c), indicating that their $d_\parallel$ parameter (Table 5.1) is significantly smaller than $d_\perp$ for the basal-oriented defects. Using PL5, which exhibits strong room-temperature ODMR, we also demonstrate electric field sensing at room temperature (Fig. 5.3b, right). This could enable future applications such as biosensing.

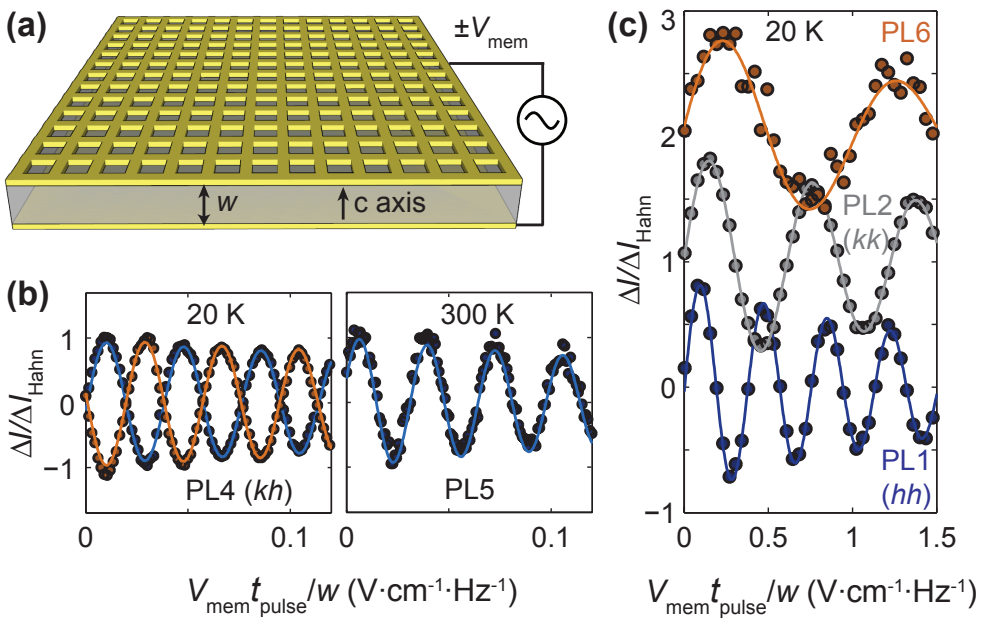

Figure 5.3: (a) Electric-field sensing with divacancies and related spins in SiC. We use the same pulse sequence as in Fig. 5.2b, but now substituting V_{mem} for V_{piezo}. $\pm V_{mem}$ is applied across a w = 53 μm thick SiC membrane, using patterned electrodes that transmit light. $B = 0$ G and t_{pulse} is held constant at 80 μs for the data at 20 K and at 20 μs for the room-temperature data. (b) AC electric field-sensing measurements for basal-oriented defects show mirror image ΔI oscillations when the higher (blue) and lower (orange) frequency spin-resonance transitions are used (left panel). The PL5 data (right panel) are taken at room temperature. (c) Electric field sensing for the c axis oriented defects at 20 K, with the three curves offset for clarity. The fits are to exponentially decaying sine curves, whose fitted frequencies give the spin-electric field coupling parameters (Table 5.1). SOURCE: [88]

An important parameter for high-precision sensing is the ODMR contrast (C_{defect}) between spin states, which is defined as the fractional change in PL due to an optically polarized spin population being flipped by $\Delta m_s = \pm 1$. We use spectrally resolved ODMR measurements to estimate C_{defect} (Fig. 5.4a). By focusing on the ZPLs, we avoid interference from background PL. Instead of applying π pulses to flip spin states, we instead mix the spin populations with strong continuously applied MW radiation and weak laser illumination. Calculating C_{defect} from the measured fractional change in PL intensity ($\Delta I_{\text{mixed}}/I$) requires detailed knowledge of spin mixing dynamics, which are not fully understood. However, by using $3/2 \times \Delta I_{\text{mixed}}/I$, we can put a lower bound on C_{defect} (see Appendix A.4 for justification). This lower bound is found to range from 0.15-0.21 for the neutral divacancies

(PL1-PL4), and from 0.33-0.36 for PL5 and PL6 at 20 K. These high C_{defect} values are comparable to the NV center in diamond, which has an ODMR contrast of ∼0.3 [117, 133]. The optical lifetimes of the SiC divacancies are another important quantity for spin readout. They are found to range from 12-15 ns (Fig. 4.4b and Appendix A.5), which is also comparable to NV center lifetime [117]. These favorable ODMR characteristics make SiC defects compelling systems for high-precision sensing.

In order to understand the interplay between strain- and electric field-induced spin shifts in SiC, we carry out ab-initio density-functional calculations of the zero-field splitting parameters in the ground-state Hamiltonian, along with electric- and strain-field perturbations to them. Since our simulations calculate spin-spin interactions between electrons localized to the defects but neglect spin-orbit coupling, we focus on the c-axis-oriented divacancies, whose C_{3v} symmetry implies low spin-orbit coupling. Our simulations (see Appendix A.6 for an overview of these simulation) are in excellent agreement with the ground state D^0 values for the c-axis divacancies in 4H-SiC as well as for the NV center in diamond (within 1.5%). As a corroboration for our simulation methods, we also verify the change in zero-field splitting due to external pressure acting on NV center in diamond (10.3 MHz/GPa (cryogenic) calculated versus 14.6 MHz/GPa (room-temperature) experiment [128].)

The experimental observation that tensile and compressive strain perpendicular to the c axis primarily shift the D term of the Hamiltonian for the c-axis oriented defects (see Fig. 5.2a) is supported by simulations. These show that this strain causes only a small deviation from C_{3v} symmetry for the defects' electronic orbitals, with their spin exhibiting a correspondingly small $E_{x,y}$ term but a larger D shift of 7 GHz / strain, neglecting Poisson effects. These magnitudes are comparable to the experimentally determined values (2-4 GHz/strain), but both are only order-of-magnitude estimates. For c-axis-oriented-strain, a D shift of 5 GHz / strain is calculated.

The measured electric field-spin coupling coefficients are consistently found to be higher than those [123, 124] for the diamond NV center, up to 1.9x higher for $d_{\perp}$ and 7.6x higher

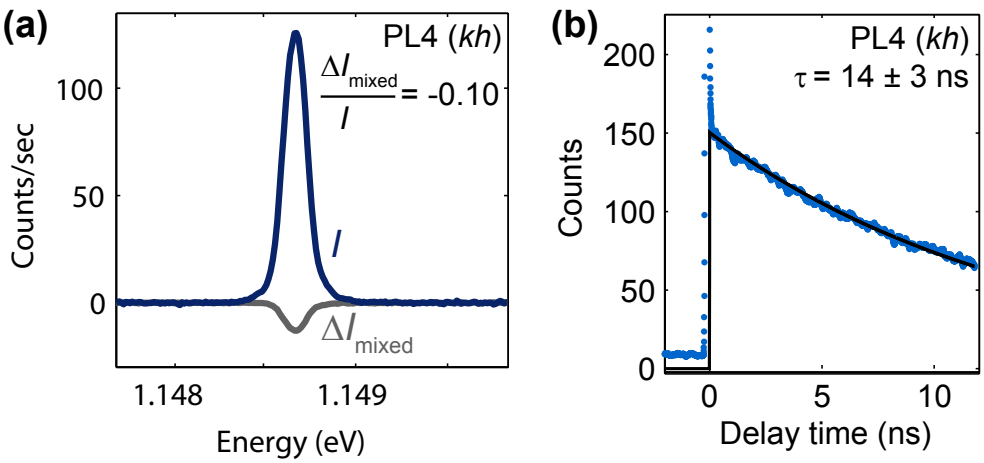

Figure 5.4: (a) A plot of the ZPL intensity of PL4 without microwave radiation (blue curve) and the change in PL when strong microwave irradiation is applied (grey curve). $\Delta I_{\text{mixed}}/I$ is measured to be -0.10, +0.11, -0.14, -0.10, -0.24, and -0.22 for PL1-PL6, respectively. (b) Time-resolved PL from PL4 as a function of delay after a picosecond excitation laser pulse (blue dots). The decay constant of the exponential fit (black) is the optical lifetime (τ). T = 20 K, $B = 0$ G. See Appendix A.4 for the calculation of C_{defect} from $\Delta I_{\text{mixed}}/I$ and for the other defect species lifetimes and ODMR contrasts. SOURCE: [88]

for $d_{\parallel}$ (Table 5.1). While our simulations overestimate $d_{\parallel}$ in both SiC and diamond, they accurately corroborate (within 30%) the experimentally observed relative enhancement of $d_{\parallel}$ for neutral divacancies in SiC over that for diamond NV centers.

Two physical effects contribute to $d_{\parallel}$. First, electric fields distort the positions of atoms in the SiC lattice neighboring the divacancy via the piezoelectric effect. Second, electric fields shift the electron distribution surrounding the defect. Although these effects occur simultaneously and cannot be distinguished by experiments alone, simulations can disentangle them. By calculating $d_{\parallel}$ with a distorted lattice but no extra field-induced shifts to electron wavefunctions, we find $d_{\parallel}$ to be an order of magnitude smaller than its value when electric fields are fully turned on (Table 5.1). Thus, direct field-induced shifts of the electron wavefunctions are primarily responsible for the Stark-shift parameters, and not the piezoelectric effect.

The enhanced Stark effect of divacancy spins in SiC over NV-center spins in diamond can be generally understood by the relative electron polarizability in the two materials. The

Table 5.1: Experimentally measured and theoretically calculated Stark parameters for PL1-PL6, in units of h Hz cm/V. We compare these to experimentally measured [124] and theoretically calculated values for the NV center in diamond. The rightmost column gives the piezoelectric contribution to $d_{\parallel}$, which is seen to be small compared to the electric-field contribution (see Appendix A.6). The experimental uncertainty for the SiC data is 5%. [a] Calculated with only atom-distortion effect.

	Experiment		Theory	
Defect/Configuration	$d_{\perp}$	$d_{\parallel}$	$d_{\perp}$	$d_{\parallel}^{a}$
NV center	17	0.35	0.76	
PL1 (hh)		2.65	5.2	0.38
PL2 (kk)		1.61	4.2	0.23
Ratio of PL1:NV		7.6:1	6.8:1	0.5:1
Ratio of PL2:NV		4.6:1	5.5:1	0.3:1
PL3 (hk)	32.3	< 3	0.41	
PL4 (kh)	28.5	0.44	0.79	
PL5	32.5	< 3		
PL6		0.96		

SOURCE: [88]

polar crystal bonds in SiC result have high electron polarizability, which can be seen by the material's high (10.0) dielectric constant. Since defect wavefunctions derive from dangling bond orbitals, they inherit this high polarizability. In turn, this polarizability causes a strong spin response to external electric fields.

5.3 Conclusions

Our results show that electron spins bound to SiC defects are highly susceptible to strain and electric fields. For electric fields in particular, the susceptibility is several times stronger than it is for the NV center in diamond. In the future, this strong strain/electric field response, combined with SiC's amenability to advanced device fabrication protocols, could facilitate the coupling of spins to mechanical resonators [134–136] or to superconducting qubits. Furthermore, with dense enough ensembles, it might even be possible to reach the strong coupling regime. Finally, our results show that SiC defect spins exhibit high optical polarization [88] and high intrinsic ODMR contrasts, which are crucial parameters

for efficient initialization and readout.

CHAPTER 6

ELECTRICALLY DRIVEN SPIN RESONANCE

6.1 Introduction

An important challenge in defect-spin physics is to selectively manipulate individual spins at the nanometer scale. Localized spin control is particularly important since the inter-spin separation required for strong dipolar coupling is on the order of tens of nanometers [105,137]. Since electric fields are readily confined on similar length scales [138], electrically driven spin resonance [139–147] could be used to address this challenge. In this chapter, we show that resonant electric fields can coherently drive spin transitions in optically addressable point defects.

We use AC electric fields to drive Rabi oscillations across a magnetic-dipole forbidden spin transition ($\Delta m_s = \pm 2$) of the optically addressable electronic spin of the QL1 defect [88] in semi-insulating 6H-SiC. We then apply our electrically driven, optically detected magnetic resonance (E-ODMR) technique to spatially map the QL1 spin response and the transverse AC electric field generated by our fabricated electrodes. This imaging of GHz-frequency resonant electric fields complements non-resonant kHz-frequency AC electric field sensing previously demonstrated with NV centers in diamond [83]. Since the QL1 defect shares a ground-state spin Hamiltonian with many intrinsic defects in SiC [86–88,91,92,148–151] and the NV center in diamond [123], our results apply to a broad class of optically addressable solid-state defects. This chapter and the associated Appendix B were adopted from reference [97].

6.2 Theory of Electrically Driven Spin Resonance

QL1 belongs to a family of intrinsic defects in 6H-SiC known commonly known as the UD-2 family [88, 90]. Recent reports, however, indicate that it is a neutral divacancy. Our E-

ODMR measurements determine that its optically addressable spin has integer-value total spin (S), and long spin relaxation times [88] suggest that this spin is associated with its orbital ground state (see Appendix B.1). It is c-axis oriented with C_{3v} point-group symmetry and the ground-state spin Hamiltonian [88] (also see Appendix B.1):

$$H = (hD + d_{\parallel}E_z)\sigma_z^2 + (g\mu)_B\sigma \cdot B - d_{\perp}E_x(\sigma_x^2 - \sigma_y^2) + d_{\perp}E_y(\sigma_x\sigma_y + \sigma_y\sigma_x), \qquad (6.1)$$

where the c-axis is oriented along the z-axis, h is Planck's constant, μ_B is the Bohr magneton, $D = 1.299$ GHz [88] is the zero-field splitting, $g = 2$ is the g-factor, σ is the vector of spin-1 Pauli matrices (see Appendix B.1), $\mathbf{B}$ is the magnetic field vector, and $\mathbf{E}$ is the electric field vector. The longitudinal (c-axis oriented) and transverse coefficients $d_{\parallel}$ and $d_{\perp}$, respectively, couple electric fields to the spin via the Stark effect, which can arise from both spin-orbit effects [123] and perturbations to spin-spin interactions between electrons localized to QL1. The Zeeman-split energy levels due to a longitudinal magnetic field ($B_{\parallel}$) are illustrated in Fig. 6.1a.

The electrically-driven spin resonance that we demonstrate is similar to standard magnetically-driven spin resonance, except that it couples different pairs of spin eigenstates. When written in the σ_z basis, the energy eigenstate basis, the transverse magnetic components of Eq. 6.1 can be written as:

$$H_{\perp}^B = g\mu_B(B_x\sigma_x + B_y\sigma_y) = (g\mu_B)/\sqrt{2}B_{\perp}e^{-i\phi_B}(|+1\rangle\langle 0| + |0\rangle\langle -1|) + H.c., \qquad (6.2)$$

and the transverse electric component as:

$$H_{\perp}^E = -d_{\perp}E_x(\sigma_x^2 - \sigma_y^2) + d_{\perp}E_y(\sigma_x\sigma_y + \sigma_y\sigma_x) = -d_{\perp}E_{\perp}e^{i\phi_E}|+1\rangle\langle -1| + H.c., \qquad (6.3)$$

where $|i\rangle$ is defined to be $|m_s = i\rangle$, $B_{\perp}(E_{\perp})$ and $\phi_{B,(E)}$ are the magnitude and phase, respectively, of the magnetic (electric) field in the plane transverse to the c-axis, and $H.c.$

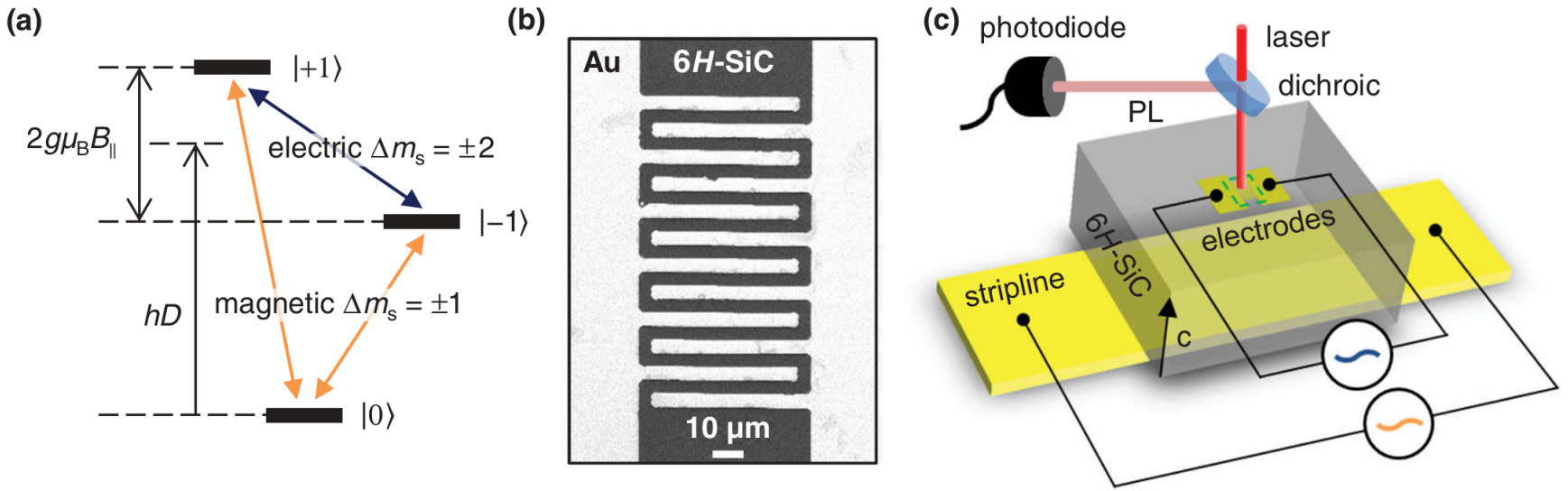

Figure 6.1: (a). The orbital ground-state spin structure of the QL1 defect, with ($\Delta m_s = \pm 1$) transitions (orange arrows) and the ($\Delta m_s = \pm 2$) transition (blue arrow) indicated. (b) Scanning electron microscope image of the electrode pattern. (c) QL1 spins localized within a 400 nm thick layer immediately beneath the 6H-SiC surface are optically pumped with a 1.27 eV laser in a 1.5 μm diameter spot, addressing 10^4 QL1 defects at once. Photoluminescence is filtered from the pump laser with a dichroic mirror and is measured with a photodiode. Spins are driven electrically by the electrodes and magnetically by the stripline. The electrode pattern from part (b) maps to the green dashed parallelogram. SOURCE: [97]

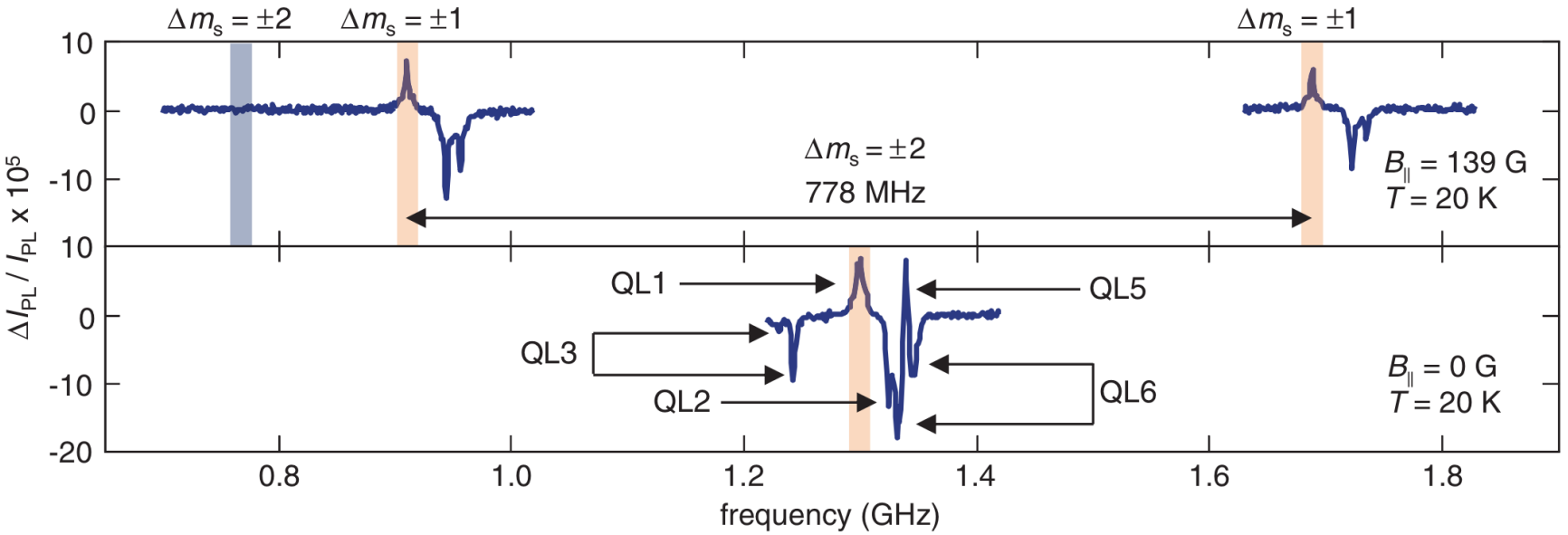

Figure 6.2: The ODMR signal when the stripline is driven at $B_{\|}$=139 G (upper) and $B_{\|}$=0 G (lower). The two ($\Delta m_s = \pm 1$) resonances are shaded orange, and the ($\Delta m_s = \pm 2$) resonance (at 778 MHz, shaded blue) is magnetic-dipole forbidden and not seen in ODMR. SOURCE: [97]

denotes the Hermitian conjugate. The main difference between $H_\perp^B$ and $H_\perp^E$ is that $H_\perp^B$ connects triplet pairs with $\Delta m_s = \pm 1$, whereas $H_\perp^E$ connects triplet pairs with $\Delta m_s = \pm 2$. As such, in the same way that applying resonant transverse magnetic fields can be used to drive magnetic-dipole ($\Delta m_s = \pm 1$) transitions, resonant transverse electric fields can be used to drive magnetic-dipole forbidden ($\Delta m_s = \pm 2$) transitions.

6.3 Experimental Setup

Our experiments use both AC electric and magnetic field control, for which we use separate driving elements. Open-circuit interdigitated metal electrodes on the chip's top surface are used to drive transverse electric fields between adjacent digits (see Fig. 6.1b), and a short-circuited stripline beneath the chip is used to drive transverse magnetic fields over the electrode region. To convert from the microwave power sent to the electrodes (which is ideally reflected completely) to the voltage applied across them, we use the expression $V = 2\sqrt{2P(50\Omega)}$. This expression assumes that our microwave circuit has 50 Ω impedance and that the electrodes present a perfect open circuit [121]. The first assumption is justified even with wirebonds used in our circuit, since they experience a small $\sim$ 0.50 dB loss below 1.5 GHz, which corresponds to a voltage reflection of $< 6\%$ (determined through an S_{21} measurement a 50 Ω-line/wirebond/coplanar-pad/wirebond/50-Ω line circuit, which experiences a $\sim$ 1.0 dB loss below 1.5 GHz). The second approximation is justified by a resistance measurement of the electrode device.

A flow cryostat cools our device to the temperature T=20 K and a permanent magnet provides a static $B_\parallel$. QL1 color centers were produced in our 6H-SiC substrates via a carbon implantation and annealing process designed to generate defects in a 400 nm thick layer immediately below the surface (see Appendix B.2). The QL1 spins between adjacent electrode digits are optically addressed by non-resonantly pumping their 1.09 eV near-infrared optical transition with 1.27 eV laser light (see Fig. 6.1c) and Appendix B.3 for details). In our experiments, we simultaneously address approximately 10^4 QL1 spins.

As mentioned in the introduction, the QL1 spin-dependent optical cycle allows non-resonant laser illumination to both polarize and read out its ground-state spin. Because its photoluminescence intensity (I_{PL}) depends on whether its spin state is $|0\rangle$ or $|\pm 1\rangle$, we can track the QL1 spin dynamics by measuring differential photoluminescence (ΔI_{PL}) between an initial state and one that has been evolved by magnetic or electric field pulses. These ΔI_{PL} measurements thus enable conventional (magnetically driven) optically detected magnetic resonance (ODMR) (see Fig. 6.2) and E-ODMR (see Appendix B.3 for experiment details).

6.4 Electrically Driven Optically Detected Magnetic Resonance

We measure E-ODMR by implementing the sequence of spin transitions shown in Fig. 5.3a [134]. We first optically initialize the spin ensemble into $|0\rangle$ and then rotate it into $|-1\rangle$ with a magnetic π-pulse driven on the stripline (π_B). We then generate a microwave-frequency pulse (P) on the electrodes to transfer population between $|-1\rangle$ and $|+1\rangle$ using electrically driven spin resonance. Any spin population remaining in $|-1\rangle$ is transferred back into $|0\rangle$ with another magnetic π-pulse driven on the stripline. After this sequence, we re-illuminate the sample to read out the ensemble magnetization and to re-initialize it. By modulating P on and off and measuring the locked-in I_{PL} signal, we obtain a direct measurement of $\Delta m_s = \pm 2$ transitions driven by P.

To observe E-ODMR in the frequency domain, we fix the length of P and sweep its frequency (Fig. 6.3b). This experiment returns a clear resonance at exactly the $\Delta m_s = \pm 2$ transition frequency (Fig. 6.3c) and does not correspond to any ODMR resonances (orange shaded stripes in Fig. 6.2). To observe E-ODMR in the time domain, we fix the frequency of P to the $\Delta m_s = \pm 2$ resonance and vary its length (Fig. 6.3d). We observe electrically driven Rabi oscillations, whose frequency is modulated by the driving power (Fig. 6.3e). The decay envelope is due to electric field inhomogeneity within the measurement volume and magnetic fluctuations of the coupled spin bath [134] (see Appendix B.4 for data at other

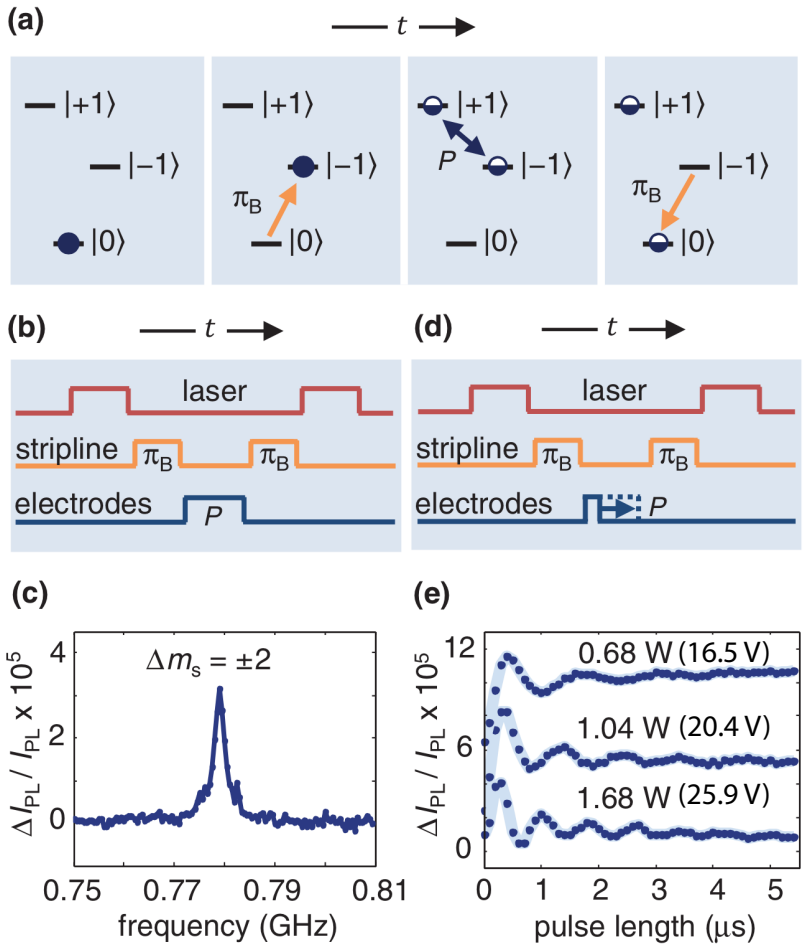

Figure 6.3: (a) The sequence of spin transitions used to observe E-ODMR. (b) The pulse sequence used for the frequency-domain E-ODMR measurement. The length of P is fixed and its frequency is swept. (c) A clear feature is seen at the frequency difference of the $|+1\rangle$ and $|-1\rangle$ states, indicating population transfer across the $\Delta m_s = \pm 2$ transition. The electrode power is 0.09 W, which corresponds to an approximate voltage of 6 V, and $B_{\|} = 139G$. Shoulders in the E-ODMR spectrum arise predominantly from QL1 spins that are hyperfine coupled to nearby ^{29}Si nuclei. (d) The pulse sequence used for the time-domain E-ODMR measurements. The frequency of P is fixed to the ($\Delta m_s = \pm 2$) resonance and its length is varied, resulting in (e), Rabi oscillations at three electrode driving powers. The approximate voltages are given in parentheses. The three curves are offset for clarity. SOURCE: [97]

magnetic fields $B_{\|}$).

6.5 Control Measurements

The frequency- and time-domain data in Fig. 6.3 indicate driving of the $\Delta m_s = \pm 2$ transition. However, control measurements are necessary to confirm that population transfer is driven by a transverse electric field and not by stray transverse magnetic fields from the electrodes or driving circuit. Despite the fact that the $\Delta m_s = \pm 2$ transition is magnetic-dipole forbidden, a misalignment of the nominally longitudinal magnetic field would result in a first-order mixing of the $|\pm 1\rangle$ and $|0\rangle$ states and a second-order mixing of the $|-1\rangle$ and $|+1\rangle$ states (excluding higher orders). This mixing would then permit the nominal $\Delta m_s = \pm 2$ transition to be weakly driven by a transverse AC magnetic field. We rule out the magnetic driving scenario by performing the following controls.

We repeat the E-ODMR sequence, except that now we apply P to the stripline and attempt to drive the $\Delta m_s = \pm 2$ transition magnetically. To ensure that the transverse magnetic field is stronger in the control measurement (Fig. 6.4a) than in the E-ODMR measurement (Fig. 6.3b), we drive the stripline with 100 times more power than the electrodes had been driven (see Appendix B.6). As expected for magnetic driving of the $\Delta m_s = \pm 2$ transition, a resonance is only seen when the longitudinal magnetic field is misaligned (orange curves in Fig. 6.4b). The same misalignment has little impact on the strength of the same resonance, when driven on the electrodes, as expected for electrical driving of the $\Delta m_s = \pm 2$ transition (blue curves in Fig. 6.4b). We also observe that the E-ODMR Rabi frequency scales with the square root of the driving power, as expected [66] (Fig. 6.4c), and is independent of the $\Delta m_s = \pm 2$ resonance frequency. The latter point further supports that the observed Rabi oscillations are driven electrically and not magnetically by displacement current through the interdigitated electrodes (see Appendix B.6).

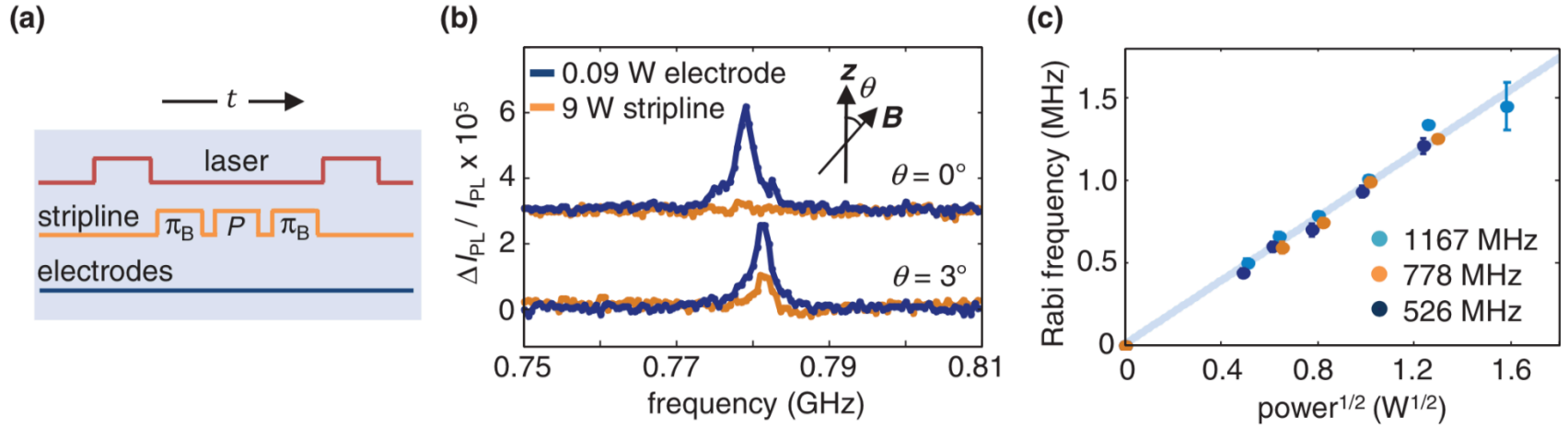

Figure 6.4: (a) Pulse sequence used for the control measurement in which we attempt to drive the ($\Delta m_s = \pm 2$) transition magnetically with the stripline. The length of P is fixed and its frequency is swept. (b) A feature using the pulse sequence in (a) is only observed at the ($\Delta m_s = \pm 2$) resonance when the static longitudinal magnetic field is purposefully misaligned to the z axis (orange curves). However, E-ODMR (blue curves) results in a ΔI_{PL} feature at the ($\Delta m_s = \pm 2$) resonance regardless of the magnetic field misalignment. The curves at different alignment angles are offset for clarity. 0.09 Watts corresponds to an approximate voltage of 6 V. (c) The electrically driven Rabi frequency scales with the square root of the driving power and is independent of the ($\Delta m_s = \pm 2$) frequency (see legend). The error bars represent the 95% confidence intervals from fits to Rabi curves. SOURCE: [97]

6.6 Spatially Resolved EODMR

Spatially resolved E-ODMR allows us to investigate the extent to which spin rotations are confined by the electrodes. For these measurements, we fix P to electrically drive a π-pulse from $|-1\rangle$ to $|+1\rangle$ within the electrodes, where the electric field should be strongest. We then spatially map ΔI_{PL} while raster scanning the confocal excitation spot across the device (Fig. 6.5a-b). We observe that ΔI_{PL} is quickly extinguished away from the electrodes, and Rabi curves (Fig. 6.5c) confirm that this decrease is the result of slower spin rotations. By combining ΔI_{PL} and I_{PL} with calibration curves (see Appendix B.7), we produce an image of the transverse AC electric field amplitude $E_\perp$ (Fig. 6.5e). This image is in good agreement with finite-element simulations of our device (see Appendix B.8) and demonstrates that GHz-frequency electric fields can be spatially mapped with the spin of solid-state defects.

An important parameter that can be extracted from our time-domain measurements is the coupling strength between the ground-state spin and electric fields, $d_\perp$. For QL1 the electric Rabi frequency scales with square root of driving power as 0.97 MHz $\mathrm{W}^{-1/2}$, from which we estimate that $d_\perp/h$=26 Hz cm V^{-1}. When extrapolated to the 2.4 MV cm^{-1} dielectric strength of 6H-SiC [152], this figure implies that 60 MHz electrically driven Rabi oscillations should be possible with QL1. In contrast to the g-factor, which couples magnetic fields to the spin and is typically near 2 for isolated defects, $d_\perp$ is highly structure- and material-dependent [153]. Therefore, by appropriately selecting the material and defect, it might be possible to engineer the value of $d_\perp$ for a broad spectrum of applications.

6.7 Conclusions

We introduced and implemented E-ODMR to demonstrate that AC electric fields can be used to coherently control the spin of optically addressable defects. By spatially mapping the E-ODMR signal around our device, we demonstrated that this technique can confine spin control between electrodes and can be used to image GHz-frequency electric fields. In the

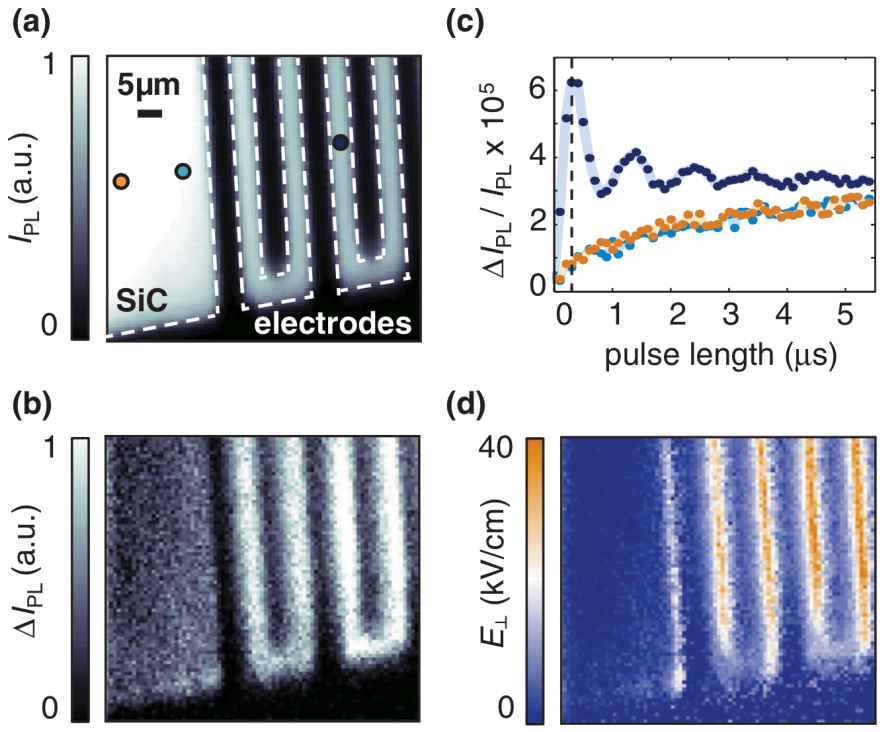

Figure 6.5: (a) A map of I_{PL} in a region of the electrode device, upon continuous laser illumination. (b) Spatially resolved E-ODMR in the same region, with the electrode pulse (P) power set to 1.04 W (approximately 20.4 V), its frequency to the 778 MHz ($\Delta m_s = \pm 2$) resonance, and its length to 300 ns. With these parameters, P induces a spin rotation from $|-1\rangle$ to $|+1\rangle$ between electrode digits. (c) Rabi curves taken at the three color-coded circles indicated in (a) confirm that spin rotations are confined by the electrodes. The dashed line indicates the length of P. (d) The transverse AC electric field $E_\perp$ generated by the electrodes, as calculated from $\Delta I_{PL}/I_{PL}$ (see Appendix B.8). SOURCE: [97]

future, applying E-ODMR to isolated defects in nanoscale devices could lead to the individual addressability of strongly coupled spins in a dense network. Other applications could use the fact that, together, magnetic and electric fields can drive arbitrary transitions across all three spin-triplet sublevels, a promising strategy for streamlining quantum algorithms [154]. Electrically driven spin resonance in optically addressable defects opens many exciting prospects for scalable quantum control.

CHAPTER 7

DYNAMIC POLARIZATION OF NUCLEAR SPINS

7.1 Introduction

Although fluctuating nuclear spins are a principal source of electronic spin decoherence in solid-state spin systems including SiC [64, 65], their presence is not purely detrimental. If polarized and controlled, nuclear spins could be a technologically valuable resource. In this chapter, we show that near-infrared laser light can polarize ^{29}Si nuclear spins in SiC with up to 99% efficiency at room temperature, which corresponds to a 5 μK nuclear-spin temperature. This process is based on dynamic nuclear polarization (DNP) [155, 156] wherein optically polarized electrons bound to either neutral divacancy [85–88, 92] or PL6 [87,88,96] color centers transfer their polarization to strongly coupled nuclei via the hyperfine interaction. This chapter and the associated Appendix C were adopted from reference [100].

DNP in SiC is experimentally straightforward, requiring only infrared laser light and a small external magnetic field (300-500 G). Optically pumping room-temperature crystals has previously led to DNP in napthalene [157], diamond [103, 122, 158–161], and GaNAs [162]. Our results show that room-temperature DNP can now be efficiently driven in a material that plays a leading role in the semiconductor industry. DNP could be applied to initialize quantum memories for quantum-communication, an application for which SiC color centers are particularly attractive, since they are near-infrared emitters with narrow optical linewidths at low temperatures [90, 96, 163]. Other applications of DNP include solid-state nuclear gyroscopes [164, 165], which can leverage SiC's long nuclear spin-lattice relaxation times [155, 166], and its amenability to sophisticated device fabrication protocols.

7.2 Theory of Dynamic Nuclear Polarization

The divacancy defect in SiC consists of a silicon vacancy adjacent to a carbon vacancy (Fig. 7.1a). Among its several inequivalent forms, those aligned to the crystal's c axis have C_{3v} symmetry. They are the hh and kk divacancies in 4H-SiC [85, 86], and the hh, k_1k_1 and k_2k_2 divacancies in 6H-SiC [88,148,167], where the h (hexagonal site) and k (quasicubic site) labels represent the inequivalent lattice sites for vacancies in the SiC lattice. The physical structure of the c-axis-oriented PL6 defect in 4H-SiC [87, 88, 96] is currently undetermined, but a close relationship to the neutral divacancies is indicated by its similar optical and spin resonances [87], similar radiative lifetimes [96], and similar hyperfine spectrum with identical degeneracies (measured here, see Table 7.1). In the GS, these defects are spin triplets ($S = 1$) with the Hamiltonian:

$$H_{GS} = g_{GS}\mu_B \mathbf{S}\cdot\mathbf{B} + D_{GS}S_z^2 + \sum_j \gamma_j \mathbf{B}\cdot\mathbf{I}_j + \mathbf{S}\cdot\mathbf{A}_{j,GS}\cdot\mathbf{I}_j \tag{7.1}$$

where $\mathbf{S}$ is the vector of spin-1 matrices, g_{GS} is the electronic g-factor, μ_B the Bohr magneton, $\mathbf{B}$ is the external magnetic field, D_{GS} is the electronic zero-field splitting parameter, and $\mathbf{A}_{j,GS}$ the hyperfine tensor coupling the jth nucleus with spin I_j and gyromagnetic ratio γ_j. The four terms in Eq. 7.1 respectively represent the electronic Zeeman effect, the electronic crystal-field splitting, the nuclear Zeeman effect, and the hyperfine interaction. At elevated temperatures, the form of the ES is similar Hamiltonian to that of the GS, with g_{ES} substituting for g_{GS}, D_{ES} substituting for D_{GS}, and $\mathbf{A}_{j,ES}$ substituting for $\mathbf{A}_{j,GS}$.

Silicon's dominant isotope is the $I = 0$ ^{28}Si, but the $I = 1/2$ isotope ^{29}S also has a fairly high natural abundance of 4.7%. We denote the state of a strongly hyperfine-coupled electron-nuclear spin pair as $|m_S, m_I\rangle$, where $m_S \in \{-1, 0, 1\}$ is the electronic spin state and $m_I \in \{\uparrow, \downarrow\}$ is the ^{29}Si nuclear spin state. Before any optical pumping, the spin pairs are in a statistical mixture of the six $|m_S, m_I\rangle$ states.

Optical illumination polarizes the color centers' electronic spins into the $m_S = 0$ sublevel,

a consequence of a spin-dependent intersystem crossing [88, 92, 104, 163]. The degree of optically pumped electronic polarization for divacancies in SiC is at least 60% [88]. On its own, optical cycling does not polarize nuclear spins and results in equal populations of the $|0,\downarrow\rangle$ and $|0,\uparrow\rangle$ states. However, when the defects' spin sublevels are tuned to the level anticrossing of their $m_s = 0$ and $m_s = -1$ states (either the ESLAC or GSLAC, see Fig. 7.1b), the hyperfine interaction hybridizes the $|0,\downarrow\rangle$ and $|-1,\uparrow\rangle$ states. In each optical cycle, a spin pair in the $|0,\downarrow\rangle$ state will then have the chance to exchange polarization, and thus evolve into the $|-1,\uparrow\rangle$ state. Subsequent optical cycles then reorient the electronic spins, polarizing $|-1,\uparrow\rangle$ states into $|0,\uparrow\rangle$. Meanwhile, conservation of angular momentum prevents $|0,\uparrow\rangle$ from mixing with $|-1,\downarrow\rangle$. Together, these processes can efficiently polarize arbitrary $|m_S, m_I\rangle$ states into $|0,\uparrow\rangle$ (Figs. 7.1c-d).

7.3 Experimental Observation of Dynamic Nuclear Polarization

Our 4H-SiC wafer (purchased from CREE, Inc.) has vacancy complexes intentionally incorporated during crystal growth [87]. In our 6H-SiC wafer (purchased from II-VI, Inc.), we implant the wafer with ^{12}C ions, creating vacancies. Annealing the wafer then causes the vacancies to migrate and to pair into divacancies [88]. For continuous-wave ODMR measurements, we use a 975-nm laser to non-resonantly excite the electronic transitions of ensembles of defects in either a 4H- or 6H-SiC sample and an InGaAs photoreceiver to collect the entire spectrum of near-infrared photoluminescence (PL) emitted by the defects. We then use a short-terminated antenna under the chip to apply a microwave field, whose frequency (f) we sweep. When f is resonant with an electronic spin transition, the electronic spin is rotated from its optically initialized ($m_s = 0$) state towards $m_s = \pm 1$, causing PL intensity to change (ΔPL). Although the inequivalent defect forms in each of our two wafers are simultaneously optically excited, their non-degenerate spin-transition frequencies allow each form to be independently addressed [87, 88].

Using low microwave-power ODMR, we observe that each electronic spin transition has

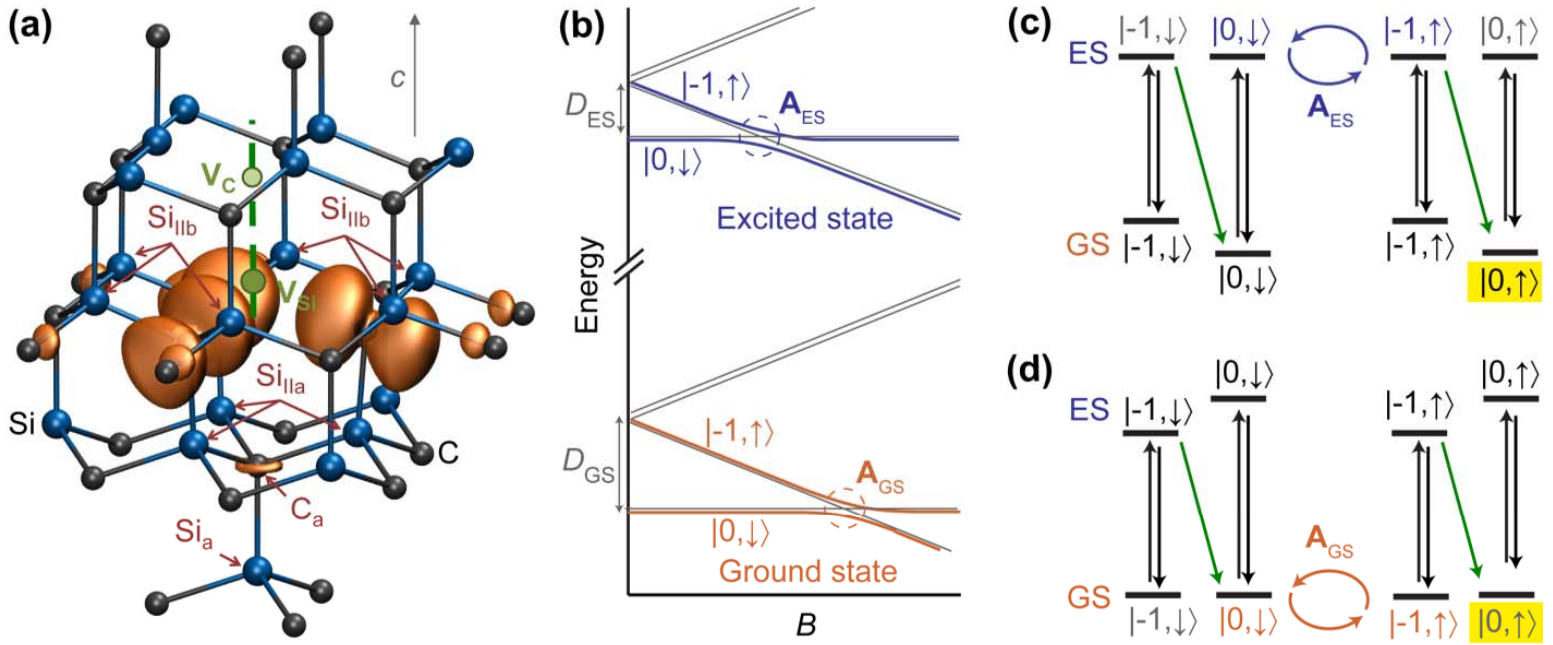

Figure 7.1: (a) An illustration of the k_1k_1 divacancy (green circles) in 6H-SiC. The calculated spin density is represented by orange-lobe isosurfaces. We measure the DNP of ^{29}Si nuclei at the Si_{IIa} and Si_{IIb} sites. (b) Evolution of the ES and GS spin-sublevel energies with B applied along the c axis. The dashed circles indicate LACs, which are mediated by the hyperfine interaction. The gray branches do not mix. (c) At the ESLAC, the $|0,\downarrow\rangle$ and $|1,\uparrow\rangle$ states are hybridized, which links the nuclear spin to the electron's optical cycle. Together with the intersystem crossing (green arrows) that drives electron spin polarization, this hybridization causes optical cycling (black arrows) to dynamically polarize the nuclei. The state of polarization is $|m_S, m_I\rangle = |0,\uparrow\rangle$ (highlighted). The $|\pm 1\rangle$ electronic spin states do not participate in this process. (d) At the GSLAC, the mechanism that drives DNP is the same as in (c), but the relevant spin hybridization is in the GS. SOURCE: [100]

a hyperfine structure (Figs. 7.2a-b) composed of symmetric side peaks around a central transition frequency (f_0). In accordance with Eq. 7.1, these side peaks are at frequencies $f_0 \pm A_{zz}/2$, where A_{zz} is the c-axis projection of the hyperfine interaction between the electron spin and a nearby nucleus. The two strongest hyperfine interactions A_{zz} between ^{29}Si nuclei and neutral divacancies in 4H-SiC are known to be 12-13 MHz (the Si_{IIa} lattice site, which has a 3-fold degeneracy) and 9-10 MHz (the Si_{IIb} lattice site, which has a 6-fold degeneracy). A_{zz} is positive and both hyperfine tensors nearly isotropic [86]. These sites correspond to the Si atoms nearest to the C atoms on which the neutral divacancy's electronic spin density is localized [96] (Fig. 7.1a).

We find that the hyperfine spectra for neutral divacancies of 6H-SiC and the PL6 defects in 4H-SiC are nearly identical to the previously observed spectra [86] for neutral divacancies in 4H-SiC. The lattice-site degeneracies for all of these defects, which we infer from the relative amplitudes of the hyperfine-side peaks, are identical. We use electron spin echo envelope modulation [124] to refine our measurement of the hyperfine-interaction strengths (see Appendix C.3). Using *ab initio* density-functional theory (DFT) [66, 96, 168–173], we then calculate the hyperfine and D_{GS} constants for each form of c-axis-oriented neutral divacancy (Table 7.1). By comparing these calculations with experiment, we can associate each crystallographic form of the divacancy in 6H-SiC with a specific spin resonance (Table 7.1).

We define the degree of nuclear spin polarization (P) as $P = \frac{I^+ - I^-}{I^+ + I^-}$, where I^+ and I^- respectively represent the populations of ^{29}Si-nuclear spins pointing $\uparrow$ and $\downarrow$ [122]. P is defined separately for each pairing of inequivalent defect form with inequivalent ^{29}Si site. We quantify P by performing a global fit the ODMR lineshapes to the sum of seven Lorentzians, one centered at f_0 and one pair at each of the Si_{IIa}, Si_{IIb}, and C_{II} hyperfine resonances (see Appendix C.5). For each resonance, we compute P by inferring the relative amplitudes of each pair of Lorentzians (Fig. 7.2). Asymmetry in the intensities of the ODMR side peaks is thus the signature of nuclear polarization. We concentrate on DNP at the Si_{IIb} site, whose

6-fold degeneracy results in the strongest ODMR signal.

Boltzmann statistics would require a sub-mK sample temperature (T) for P to exceed even a few percent. Indeed, at both low ($B < 200G$) and high ($B > 500G$) magnetic fields, we observe that P is nearly zero. In the $200G < B < 500G$ regime, however, we observe strong DNP. For PL6 defects at room temperature and $B = 330G$, P reaches $99 \pm 1\%$, an effective temperature of $5\mu K$ (Fig. 7.2d).

Two prominent peaks can be seen in P as a function B, one centered at 300-335 G and the other at 465-490 G (Fig. 7.2c-d). Anticipating that level anticrossings underlie the electron-to-nuclear polarization transfer, we hypothesize that these two peaks receptively correspond to the ESLAC and GSLAC. As expected, the higher B-value peaks in P correspond precisely to $D_{GS}/(g_{GS}\mu_B)$ (Table 7.1) for each defect form, indicating that they are associated with the GSLAC. Due to the short (14 ns) optical lifetimes of the metastable excited states [96], though, our low-microwave-power ODMR measurements rotate spins too slowly to show ES-spin transitions. High-microwave-power ODMR reveals the spin-triplet electronic excited states (Figs. 7.3a-c), with $g_{ES} = 2.0$ and $D_{ES}/(g_{ES}\mu_B)$ matching precisely with the lower-B peaks in P (Table 7.1). Unlike the GS-ODMR transitions, which exhibit nonzero ΔPL when microwaves and optical illumination are alternated (due to Rabi driving), they are only visible when microwaves and optical illumination are coincident, supporting their identification as ES resonances. Moreover, due to spin mixing in the GS, each divacancy's ES-ODMR signal has a minima at its corresponding GSLAC (Fig. 7.3d), confirming the association between ES- and GS-spin transitions. Thus, peaks in P (Figs. 7.2c-d) correspond to GSLACs and ESLACs (Figs. 7.3a-c).

To quantitatively understand the DNP, we simulate the optical polarization process using a recently developed model of color-center-mediated DNP [122]. This model simulates the nuclear polarization while taking into account the full hyperfine tensor and the simultaneous contributions from both ESLAC- and GSLAC-derived DNP at intermediate B values. In applying it, we use as many experimental parameters as possible, including electronic fine-

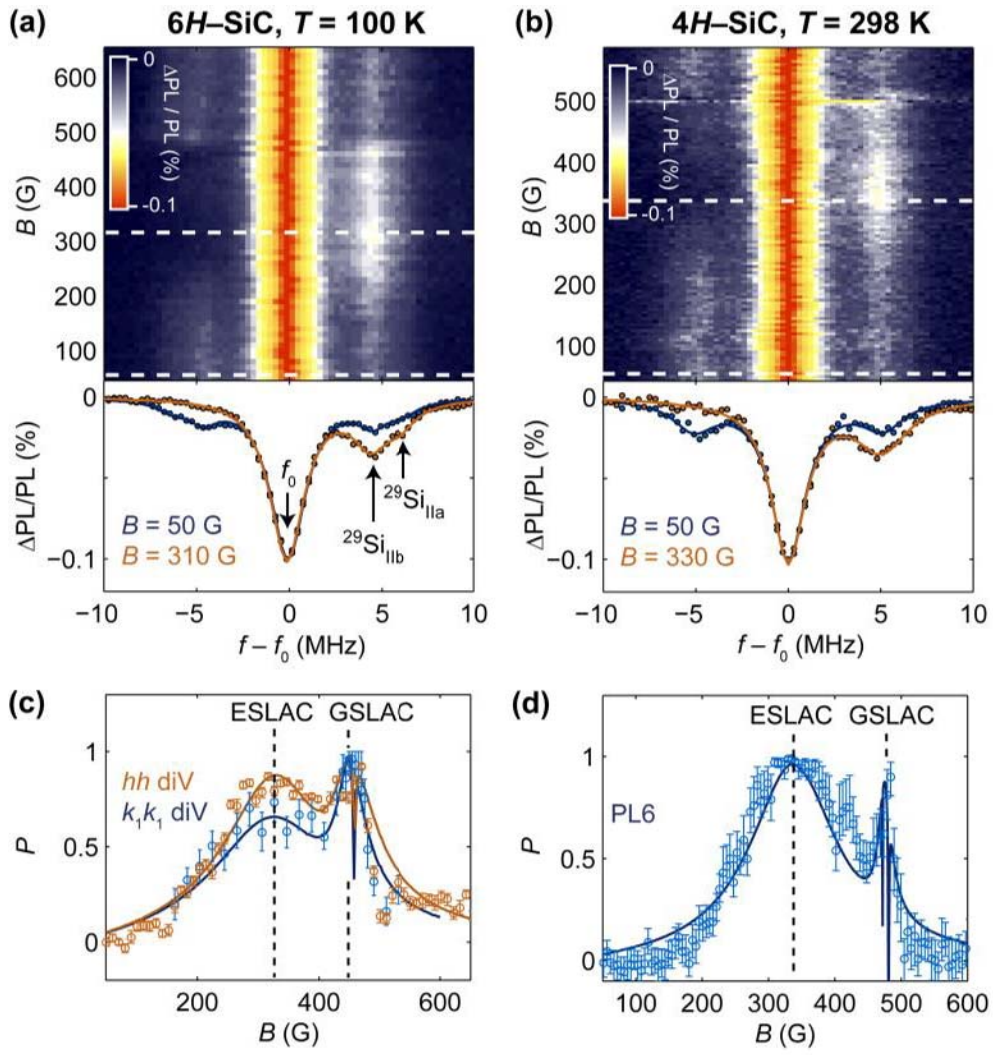

Figure 7.2: (a) Upper: Low-microwave-power ODMR spectrum of the $m_s = 0$ to $m_s = 1$ spin transition of the hh divacancy in 6H-SiC at $T = 100K$. As B varies from $50G$ to $650G$, f_0 varies from 1.5 GHz to 3.2 GHz, and strong P is seen at intermediate B values. Lower: Line cuts at the dashed white lines ($B = 50G$ and $B = 310G$). The $^{29}Si_{IIa}$ and $^{29}Si_{IIb}$ nuclei are unpolarized at B = 50 G and nearly completely polarized at the ESLAC (B = 310 G). The continuous lines are fits to sums of Lorentzians [148]. (b) Upper: Low-power ODMR spectrum of the $m_s = 0$ to $m_s = 1$ spin transition of the PL6 defects in 4H-SiC at $T = 298K$. Lower: Line cuts at $B = 50$ and at $B = 330G$, which is the PL6 ESLAC. (c) $^{29}Si_{IIb}$ nuclear polarization (P) for nuclei coupled to hh and k_1k_1 divacancies in 6H-SiC at $T = 100K$, exhibiting peaks in P at the ESLAC and GSLAC. hh divacancies have stronger ESLAC-related DNP than $k_1k_1$divacancies. We plot P at the $^{29}Si_{IIa}$ sites in [148]. Due to spectral overlap with the stronger hh divacancies, P for nuclei coupled to k_2k_2 divacancies in 6H-SiC could not be accurately measured. The error bars are single-σ confidence intervals set by the fits. The continuous lines are P values simulated from our theoretical model. (d) ^{29}Si$_{IIb}$ nuclear polarization for nuclei coupled to PL6 defects in 4H-SiC at $T = 298K$ (experiment and theory). The origin of the peak in P at $400G$ is unknown. SOURCE: [100]

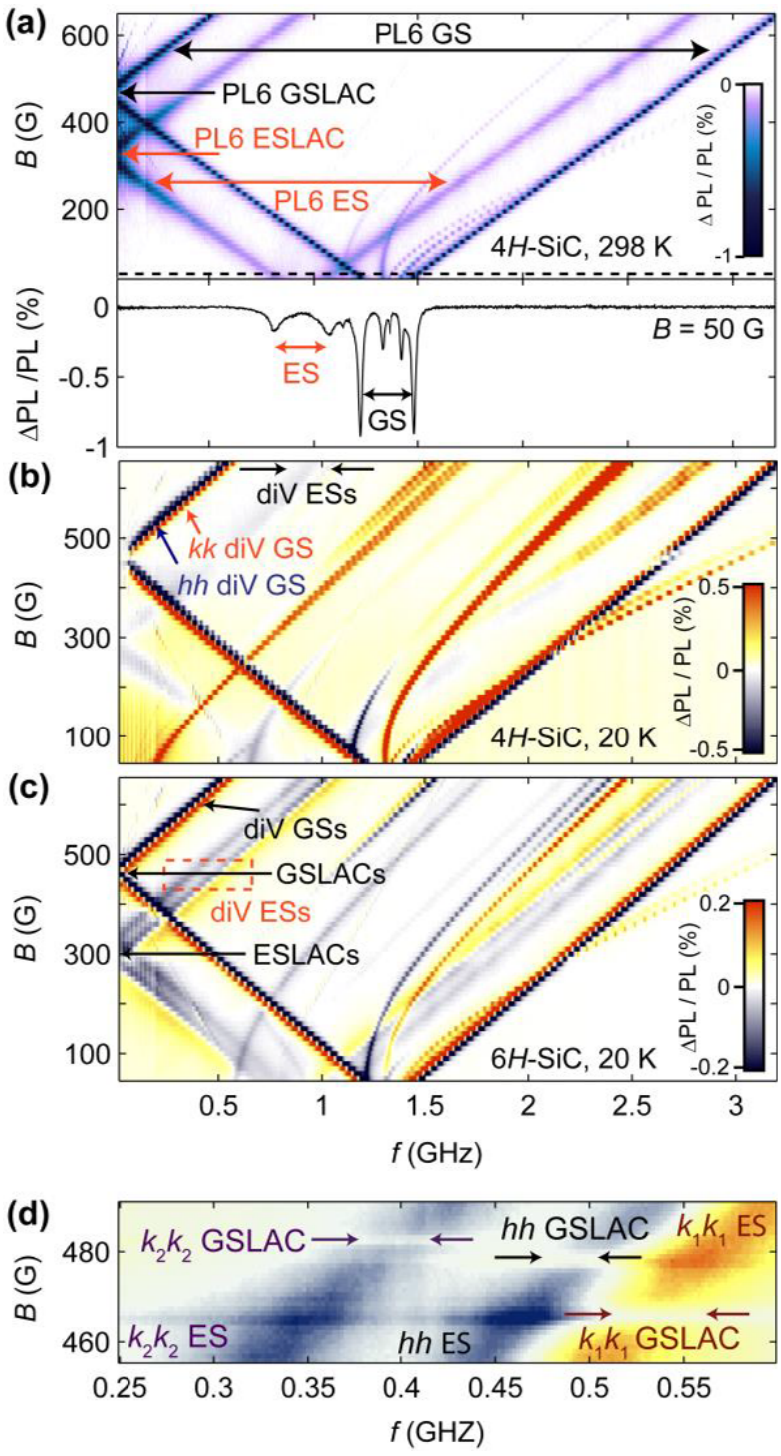

Figure 7.3: (a) Upper: High-power ODMR spectrum of PL6 at $T = 298K$. Lower: Line-cut of the ODMR spectrum at $B = 50$ G (the dashed line). (b) High-power ODMR spectrum of the neutral divacancies in 4H-SiC at $T = 20$ K. (c) High-power ODMR spectrum of the neutral divacancies in 6H-SiC at $T = 20K$. (d) Zoom-in of the red dashed rectangle drawn in (c). Due to spin mixing in the GS, each divacancy's ES ODMR signal has a minima at its corresponding GSLAC. SOURCE: [100]

Table 7.1: Parameters for the c-axis-oriented neutral divacancies, PL6 defects, and coupled ^{29}Si nuclei. ZPL stands for zero-phonon line. Both D_{GS} and D_{ES} are positive [100]. All experimental parameters are measured at $T = 20$ K, except for D_{ES} of PL6, where the room-temperature value is provided. D_{GS} and A_{zz} are calculated at $T = 0$ K, using the method in Ref. [96]. By comparing the measured and calculated D_{GS} parameters, we can associate each 6H-SiC ODMR transition to a specific divacancy form. The Si_{IIa} sites all have a 3-fold degeneracy per defect, and the Si_{IIb} sites all have a 6-fold degeneracy per defect.

Defect	ZPL (eV)	ΔPL	D_{ES} (GHz)	D_{GS} (GHz)	$A_{zz}S_{IIa}$ (MHz)	$A_{zz}S_{IIb}$ (MHz)	D_{GS} (GHz)	$A_{zz}S_{IIa}$ (MHz)	$A_{zz}S_{IIb}$ (MHz)
4H-SiC Exp.							Theory		
hh diV	1.095	+	0.84	1.336	12.3	9.2	1.358	11.6	9.3
kk diV	1.096	-	0.78	1.305	13.2	10.0	1.320	12.4	10.2
PL6	1.194	-	0.94	1.365	12.5	9.6	–	–	–
6H-SiC Exp.							Theory		
hh diV	1.092	+	0.85	1.334	12.5	9.2	1.350	11.8	9.6
k_1k_1 diV	1.088	-	0.75	1.300	12.7	10.0	1.300	12.7	10.5
k_2k_2 diV	1.134	-	0.95	1.347	13.3	9.2	1.380	11.8	9.7

SOURCE: [100]

structures parameters, hyperfine-interaction strengths, and optical lifetimes (Table 7.1 and Ref. [96]). The orientation of the hyperfine tensors' principal axes are taken from our ab initio simulations [96], and fitting parameters represent thermally driven depolarization of the nuclear spins and the effective electron-nuclear interaction times per optical cycle. The modelled polarization and the experimental data show excellent agreement (Figs. 7.2c-d).

Our model finds that effective electron-nuclear interaction times are primarily responsible for the differences in DNP efficiencies across the different defect types. Experimentally, we can use the ES spin-dephasing time ($T^*_{2,ES}$) as a proxy for the electron-nuclear interaction time and estimate the $T^*_{2,ES}$ times as $1/\pi$ times the inverse of the ES ODMR linewidths (Fig. 6.4a-b). As predicted, the hh divacancy, whose ESLAC-derived nuclear polarization is stronger than that of the k_1k_1 divacancy (Fig. 7.2c), also has a longer $T^*_{2,ES}$ time. Moreover, comparing non-resonant ESLAC-derived DNP in SiC to that for nuclei coupled to diamond nitrogen-vacancy centers [103, 122, 158–161], we find that while both systems exhibit nearly ideal ESLAC-derived DNP at room temperature, the low-temperature DNP is significantly more robust in SiC.

In diamond, both the NV center's ES-spin coherence and its off-resonantly pumped ESLAC-derived DNP rapidly decline below $T = 50$ K [160]. This diminishment is due to the deactivation of the dynamic Jahn-Teller effect, in which phonons motionally narrow pairs of ES electronic orbitals into a single coherent spin resonance [102, 174, 175]. In SiC, at $T = 5$ K, the base temperature of our cryostat, we observe both a coherent ES spin resonance (Fig. 7.4a-b) and strong ESLAC-derived DNP ($P = 85 \pm 5\%$ for the hh divacancy). As T is raised, however, strong DNP persists (Fig. 7.4c) while D_{ES} and $T^*_{2,ES}$ oscillate as a function of T. These behaviors suggest that while SiC Jahn-Teller effects play a role in the strong DNP, they are also complex and require further study [175, 176].

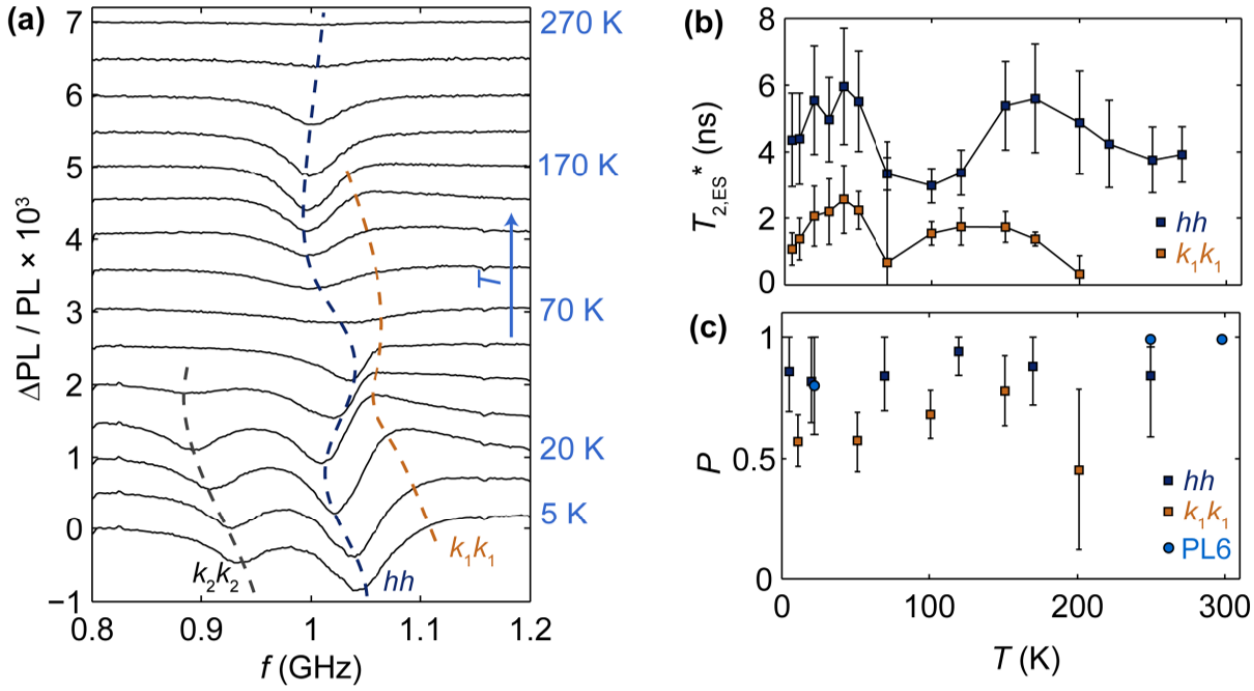

Figure 7.4: (a) Temperature dependence of ES ODMR for the hh, k_1k_1 and k_2k_2 divacancies in 6H-SiC at $B = 650$ G. The curves are offset from $\Delta PL = 0$ for clarity, and the dashed lines are guides to the eye that follow the ES-spin resonances. (b) Power-broadened $T^*_{2,ES}$ for divacancies in 6H-SiC, calculated by fitting the curves in (a) to a sum of three Lorentzians and taking $T^*_{2,ES}$ to be $1/\pi$ times the inverse of the linewidths. The error bars are 68 % confidence intervals. (c) Temperature dependence of the ESLAC-derived P at the Si_{IIb} site. The error bars are derived from fits to ODMR spectra [148]. SOURCE: [100]

7.4 Conclusions

Our results show that optical pumping can strongly polarize nuclear spins in SiC. The identification of the ES-spin transitions provides insight into the DNP process and the electronic structure of SiC divacancies. Although not measured here, we expect DNP to generalize to nuclear spins at the Si_a and C_a sites, which lie on the divacancy's symmetry axis (see Fig. 7.1a), and to other color centers. In the future, it will be interesting to see if spin diffusion [160] can extend the DNP of strongly coupled nuclei to a macroscopic nuclear spin polarization, particularly in nanostructures. If so, SiC could play an important role as a contrast agent in emerging magnetic resonance imaging technologies.

CHAPTER 8

ENTANGLEMENT AT AMBIENT CONDITIONS IN A SPIN ENSEMBLE

8.1 Introduction

Entanglement is a key resource for quantum computers, quantum-communication networks, and high-precision sensors. Macroscopic spin ensembles have been historically important in the development of quantum algorithms for these prospective technologies and remain strong candidates for implementing them today. This strength derives from their long-lived quantum coherence, strong signal, and ability to couple collectively to external degrees of freedom. Nonetheless, preparing ensembles of genuinely entangled spin states has required high magnetic fields and cryogenic temperatures or photochemical reactions. In this chapter we demonstrate that entanglement can be realized in solid-state spin ensembles at ambient conditions. We use 2-qubit hybrid registers comprising electron-nuclear spin pairs that are localized at color-center defects in a commercial SiC wafer. We optically initialize 10^3 identical registers in a 40 μ m^3 volume (with $95^{+0.05}_{-0.07}$ fidelity) and deterministically prepare them into the maximally entangled Bell states (with 0.88±0.07 fidelity). To verify entanglement we develop a register-specific quantum state tomography protocol. The entanglement of a macroscopic spin ensemble at ambient conditions, within an industrially important semiconductor, represents an important step towards practical quantum technology. This chapter and the associated Appendix D were adopted from reference [54].

Nuclear spin ensembles in room-temperature liquids were among the first platforms explored for executing quantum algorithms [70,177]. In these systems, nuclear spins encode the quantum computational bits (qubits) [24] and nuclear magnetic resonance pulses are used to perform quantum-logic operations. The small nuclear magnetic moment, which gives nuclei their long-lived spin coherence, also prevents them from reaching a large thermal polarization (¡5% of ^{29}Si are polarized at 25 mK in a 10 T magnetic field). This has largely constrained

quantum algorithms to be executed on weakly-initialized pseudo-pure states [178] of nuclear spins, which cannot be genuinely entangled [179].

A way to overcome the limitations of weakly-initialized states is to encode qubits in collections of interacting nuclear and electron spins. Such hybrid systems [43,57,100,105,106, 180,181] combine the long-lived nuclear spin coherence with the electrons ability to interact relatively strongly with magnetic and optical fields. These latter features facilitate the strong initialization of hybrid systems via the cryogenic or optical polarization of their electron spins followed by polarization transfer to their nuclear spins. In recent years, the cryogenic cooling approach led to low-temperature, high-magnetic-field ensemble entanglement in Si [57], showing promise for hybrid spin architectures.

A longstanding challenge has been to realize entanglement in a macroscopic spin ensemble at ambient conditions. Overcoming this challenge would represent a key step towards quantum technologies for several reasons: First, ensembles comprising N spins benefit from the $N^{1/2}$ scaling of both their spin signal-to-noise and their coupling strength to external degrees of freedom [113,115,116,182,183]. Second, entangled spins are compatible with a broad range of quantum-information-processing techniques such as quantum error correction [184, 185], which could be used to mitigate decoherence and re-thermalization. Finally, cryogen-free and low magnetic field functionality would facilitate the development of practical quantum devices.

Hybrid systems based on color-center defects in semiconductors [43, 85–88, 96, 97, 100, 104–106, 180, 181, 186–188] are ideal platforms for realizing quantum phenomena at ambient conditions since their atom-like states exhibit both room-temperature spin coherence and spin polarization through optical pumping. Indeed, entanglement has been studied in single color centers [43, 105, 106, 180, 181]. However, due to challenges in addressing specific hybrid systems embedded within a complex ensemble, realizing entanglement in spin ensembles at ambient conditions has remained an open problem.

8.2 Hybrid 2-Qubit Registers

We develop a general methodology for overcoming this challenge, using PL6 color centers [87, 88, 96, 100] in 4H-SiC for our demonstration. PL6 color centers localize electronic states that are characterized by a near-telecom-wavelength optical transition and a ground-state spin ($S = 1$) with GHz-frequency addressability. This spin couples to the nuclear spin of ^{29}Si ($I = 1/2$, 4.7% natural abundance) and ^{13}C ($I = 1/2$, 1.1% natural abundance) isotopic defects via the hyperfine interaction. In configurations where a nuclear spin resides within several lattice sites of PL6, the hyperfine interaction exceeds both the electron and nuclear spin dephasing rates and thus strongly couples the two-spin system. In our samples, the most abundant strongly coupled systems comprise single PL6 electron spins and single ^{29}Si nuclear spins (see Fig. 8.1a and Appendix D.1 and D.2 for details). Such spin pairs serve as two-qubit hybrid registers with an electron-spin qubit that is encoded by the $m_S = 0$ and $m_S = -1$ spin states and a nuclear-spin qubit encoded by the $m_I =\uparrow$ and $m_I =\downarrow$ spin states (Fig. 8.1b). In the coming sections, we show that an ensemble of identical registers can be prepared into the maximally-entangled Bell states (Fig. 8.1c) in ambient conditions. To generate and verify this entanglement, we combine register initialization and readout, a universal set of quantum-logic gates, and quantum-state tomography.

8.3 Register Initialization

To initialize registers, we use the PL6 spin-dependent optical cycle. Electrons localized at PL6 defects can be optically pumped into their $m_S = 0$ spin sublevels with non-resonant laser light. We determine the degree of electron-spin polarization to be 93^{+7}_{-11}% through a spin-resolved measurement of the PL6 optical cycle (see Appendix D.3). ^{29}Si nuclei that are strongly coupled to PL6 electrons can be linked to this optical cycle and dynamically polarized into their $m_I =\uparrow$ states through the application of a small magnetic field ($B_{||}$=33 mT) [100].We determine the degree of nuclear-spin polarization to be as high as 99^{+1}_{-3}%

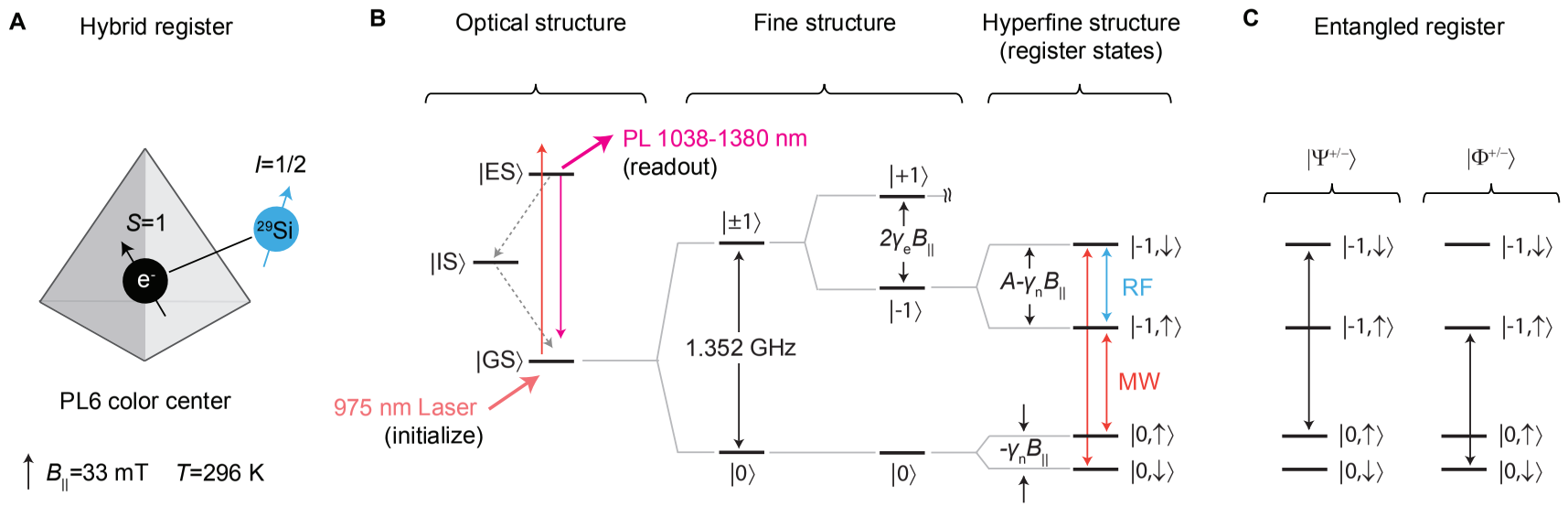

Figure 8.1: (a) A hybrid two-qubit register comprising a PL6 color-center defects intrinsic electron spin and a nearby ^{29}Si nuclear spin. The PL6 defect, whose physical structure is unknown, is depicted as a pyramid to indicate its known C_{3v} symmetry. (b) The hybrid system forms an atom-like state with an optical, fine, and hyperfine structure. Optical pumping from the ground state $|GS\rangle$ to the excited state $|ES\rangle$ with non-resonant laser light initializes registers into $|0,\uparrow\rangle$. The mechanisms responsible for initialization are a series of electron-spin-dependent intersystem crossings (dashed arrows), through some intermediate states $|IS\rangle$, and dynamic nuclear polarization. These mechanisms also lead the intensity of the emitted photoluminescence (PL) to be both electron and nuclear spin dependent, enabling registers to be read out. The energy levels are split by the crystal field, the electron and nuclear Zeeman effects ($(\gamma_e B_{||}$ and $(\gamma_n B_{||}$, where γ_e=28 MHz/T, γ_n=-8.5 MHz/T for ^{29}Si, and $B_{||}$ is a magnetic field co-aligned with the PL6 symmetry axis), and the hyperfine interaction (A). The register states are $|-1,\downarrow\rangle, |0,\downarrow\rangle, |-1,\uparrow\rangle |0,\uparrow\rangle$. Radiofrequency (RF) and microwave (MW) pulses are used to drive nuclear and electron spin transitions, respectively. (c) A register's electron and nuclear spin can be entangled by using MW and RF pulses to produce coherences (indicated by double-ended arrows) between the $|-1,\uparrow\rangle$ and $|0,\downarrow\rangle$ states or the $|-1,\downarrow\rangle$and $|0,\uparrow\rangle$ states. We prepare 10^3 identical registers into each of the four Bell states, $|\Psi^{+/-}\rangle$ and $|\Phi^{+/-}\rangle$. SOURCE: [54]

through the tomography procedure that we describe later. For comparison, under similar conditions, electrons localized at single nitrogen-vacancy centers in diamond can be optically polarized to 65% [117] and strongly coupled nuclei can be dynamically polarized to 98%. To obtain a similar thermal nuclear spin polarization, the sample would have to be cooled to 2.5 μK at 33 mT, or equivalently, immersed in a 4 MT magnetic field at 296 K. We use these mechanisms to optically initialize registers into the pure $|m_S, m_I\rangle = |0, \uparrow\rangle$ state with high fidelity at room temperature.

8.4 Register Readout

The optical cycle that drives initialization also enables us to independently probe registers' electron and nuclear spin components. In particular, electron-spin-dependent non-radiative processes in the intersystem-crossing pathway lead a register's time-averaged photoluminescence intensity to depend on its electron-spin state [87]. We can therefore probe registers' electron spins by applying a resonant microwave field while monitoring changes to the photoluminescence. This readout method is optically detected magnetic resonance (ODMR). Near 33 mT, where a register's nuclear spin is linked to its coupled electron's optical cycle, we find that the time-averaged photoluminescence intensity also depends on the register's nuclear-spin state. We can therefore directly read out the registers' nuclear spins by applying a resonant radiofrequency field while monitoring changes to the photoluminescence. This readout method is optically detected nuclear magnetic resonance (ODNMR).

8.5 Identifying Registers' Electron Spin Transitions

To characterize the registers' electron spin-transition frequencies, we perform ensemble ODMR spectroscopy (Fig. 8.2a) [87]. This measurement reveals a strong single resonance at the $|-1\rangle \leftrightarrow |0\rangle$ resonance of PL6 electron spins that are not strongly coupled to any nuclei and three surrounding doublets. These two pronounced doublets (blue and purple traces) are the

hyperfine-split electron spin resonances, $|-1,\downarrow\rangle \leftrightarrow |0,\downarrow\rangle$ and $|-1,\uparrow\rangle \leftrightarrow |0,\uparrow\rangle$ of two distinct registers, which we label R1 and R2 (Fig. 8.2b). The third doublet (green trace), which we believe results from registers comprising single PL6 electron spins and single ^{13}C nuclear spins [100, 102], was not considered due to its weak signal. R1 and R2 differ in that their respective nuclear spins occupy inequivalent lattice sites relative to the PL6 defect [100]. In our optical interrogation volume, there are approximately 10^3 R1 and R2 registers of each type (see Appendix D.4).

8.6 Identifying Registers' Nuclear Spin Transitions

To characterize the registers' nuclear spin transition frequencies, we perform ODNMR spectroscopy (Fig. 8.3a) [180]. This measurement reveals two resonances, which are the $|-1,\uparrow\rangle \leftrightarrow |-1,\downarrow\rangle$ hyperfine transitions of R1 and R2 (Fig. 8.3b). Both resonances evolve with magnetic field according to the ^{29}Si gyromagnetic ratio, confirming that the nuclei in R1 and R2 are ^{29}Si. Due to the long nuclear spin coherence, the registers' ODNMR resonances are much narrower than their ODMR counterparts. This fact enables our entangling algorithm and motivates the use of nuclear spins for quantum memory. Moreover, since the resonances are spectrally isolated, we can selectively address the R1 or R2 ensemble through ODNMR with virtually no crosstalk (see Appendix D.6 for coherent nuclear spin control measurements).

8.7 Quantum Gates

With the electron and nuclear spin transition frequencies of R1 and R2 characterized, we develop quantum gates for their systematic control within the circuit model of quantum-information processing. Local gates, which operate on one spin of a given register irrespective of the state of the other spin in that register, are implemented with broadband frequency pulses (for example, the electronic NOT$_e$ gate, which drives $|0,\downarrow\rangle \leftrightarrows |-1,\downarrow\rangle$ and $|0,\uparrow\rangle \leftrightarrows$

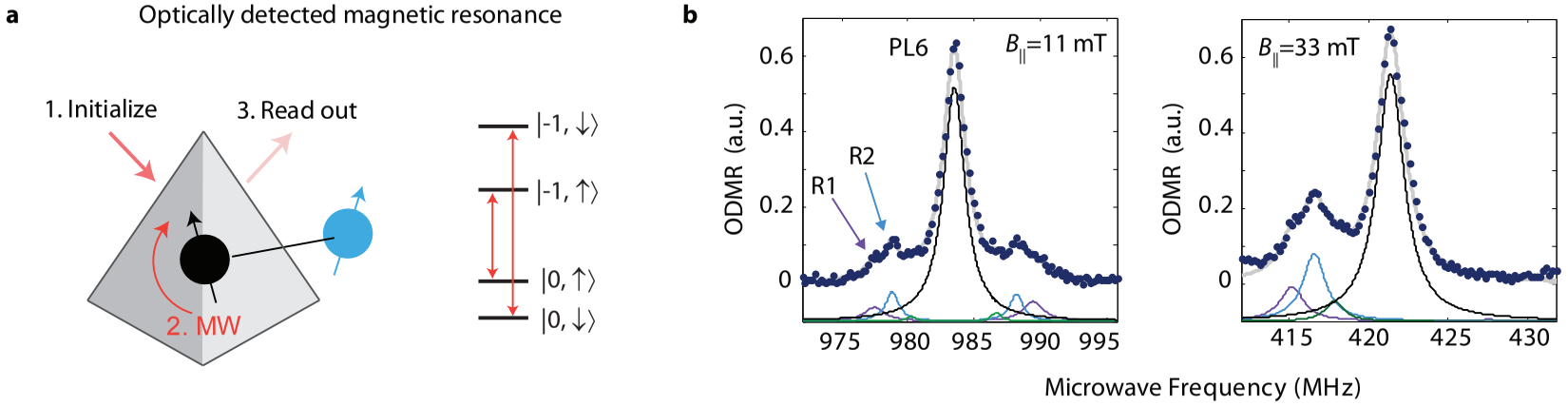

Figure 8.2: (a) We perform ODMR spectroscopy by optically initializing registers, manipulating their electron spins with a variable-frequency microwave field, and then by reading out their state via photoluminescence. (b) This measurement returns a structured line that can be decomposed into a strong central resonance and two pronounced doublets (the model curves, which are derived from fits to the data, are offset). The central peak is the $|0\rangle \leftrightarrow |-1\rangle$ resonance of PL6 electron spins that are not strongly coupled to any nuclei. The two doublets are the $|0,\uparrow\rangle \leftrightarrow |-1,\uparrow\rangle$ and $|0,\downarrow\rangle \leftrightarrow |-1,\downarrow\rangle$ transitions of two inequivalent types of register (labelled R1 and R2; the arrows are color-coded to the model curves). (Right panel) The strong asymmetry in the amplitudes of the individual peaks in each doublet at $B_{\|}$=33 mT indicates highly-efficient dynamic nuclear polarization. SOURCE: [54]

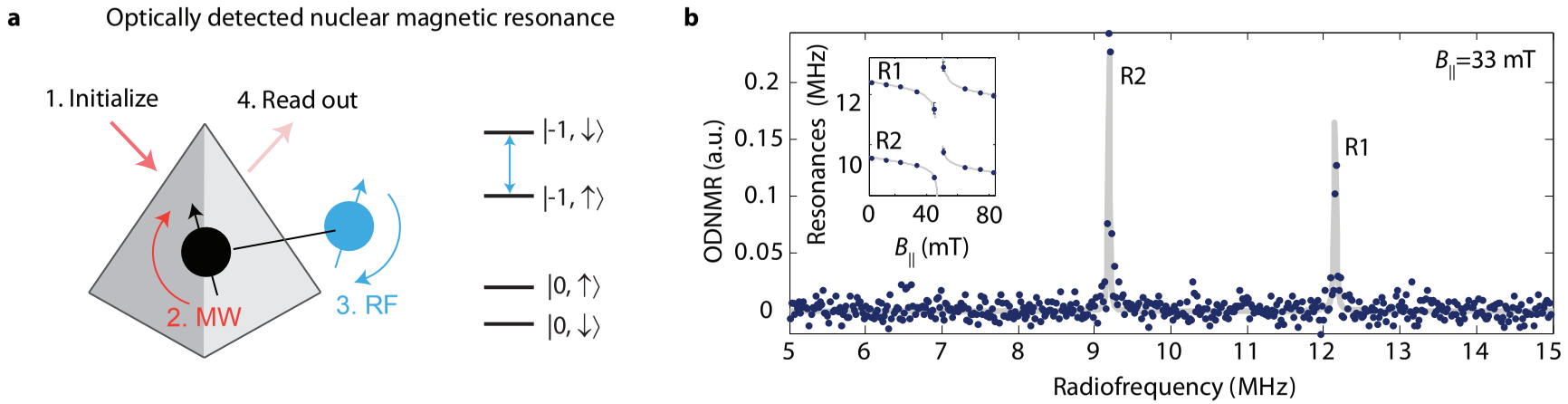

Figure 8.3: (a) We perform ODNMR spectroscopy by initializing registers, preparing their electron spins into their $m_s = -1$ states, by manipulating their nuclear spins with a variable-frequency radiofrequency field, and then by reading out their nuclear spins via photoluminescence. (b) This measurement returns two sharp peaks, which are the $|-1,\uparrow\rangle \leftrightarrow |-1,\downarrow\rangle$ resonances of R1 and R2. (Inset) Both resonances evolve with magnetic field according to the ^{29}Si gyromagnetic ratio. Coherent nulear spin control measurements are presented in Appendix D.8. SOURCE: [54]

$|-1,\uparrow\rangle$). Non-local gates, whose operation on one spin of a given register is conditional on the state of the other spin in that register, are implemented with narrowband frequency pulses (for example, the electronic $C_{\downarrow}NOT_e$ gate, which drives $|0,\downarrow\rangle \leftrightarrows |-1,\downarrow\rangle$, while leaving the populations in $|0,\uparrow\rangle$ and $|-1,\uparrow\rangle$ unperturbed). For universal control [24] over R1 and R2, we calibrate the electronic non-local $C_{\downarrow}ROT_e$, $C_{\uparrow}$ROTe and local ROT_e gates, and the nuclear non-local $C_{-1}ROT_n$ gate. ROT indicates a spin rotation, which we can apply with arbitrary angle θ and phase ϕ (see Fig. 8.4). The proceedure for calibrating these gates is presented in Appendix D.6.

8.8 Quantum State Tomography

Using calibrated quantum gates, we develop a method to selectively reconstruct the density matrix (ρ) of the R1 or R2 ensemble via quantum-state tomography. In our method, we iteratively prepare a register ensemble into its to-be-measured quantum state and then project its coherences (off-diagonal ρ elements) and populations (on-diagonal ρ elements) onto those registers' ODNMR resonance for readout. The quantum circuits used for these measurements, which were designed to mitigate readout errors, are presented in Fig. 8.5. Since unitary operations can only probe population differences between spin states, these circuits resolve the elements of ρ up to a normalization factor. We determine this factor through an independent measurement of the optically pumped electron spin polarization mentioned earlier. By extracting the elements of ρ from a well-isolated ODNMR resonance (Fig. 8.3b), as opposed to a spectrally overlapping ODMR resonance (Fig. 8.2b), we obtain a reconstruction with virtually no parasitic signal from inequivalent registers or other spin systems. This procedure differs from the tomography protocols that have been applied to single color centers [43, 105, 106, 180, 181], which rely on electron-spin readout. The full details of our tomography procedure are given in Appendix D.7.

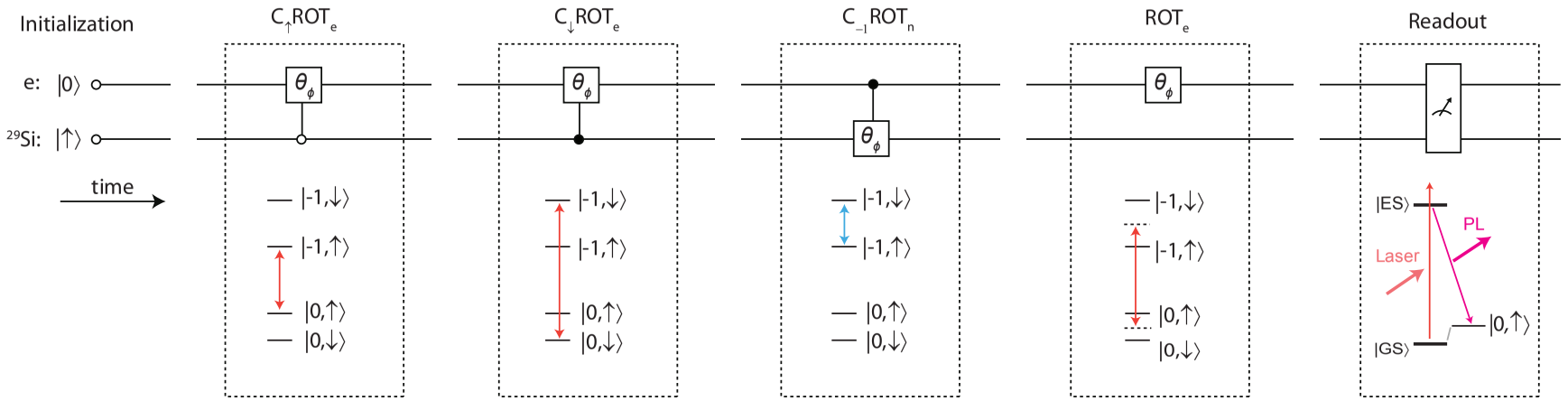

Figure 8.4: Quantum gates within the circuit model of quantum-information processing and their implementation in our system. The registers' electron and nuclear spin components are represented as separate wires in the quantum circuit. Registers are initialized through optical pumping. The electronic $C_{\uparrow(\downarrow)}ROT_e$ gate is implemented with a narrowband microwave pulse resonant with the $|-1,\uparrow(\downarrow)\rangle \leftrightarrow |0,\uparrow(\downarrow)\rangle$ transition. The nuclear $C_{-1}ROT_n$ gate is implemented with a narrowband radiofrequency pulse resonant with the $|-1,\uparrow\rangle \leftrightarrow |-1,\downarrow\rangle$ transition. The electronic ROT_e gate is implemented with a broadband microwave pulse at the average of the $|-1,\uparrow\rangle \leftrightarrow |0,\uparrow\rangle$ and $|-1,\downarrow\rangle \leftrightarrow |0,\downarrow\rangle$ transition frequencies. All rotations can be applied with arbitrary angle θ and phase ϕ. Readout is performed through a photoluminescence measurement. SOURCE: [54]

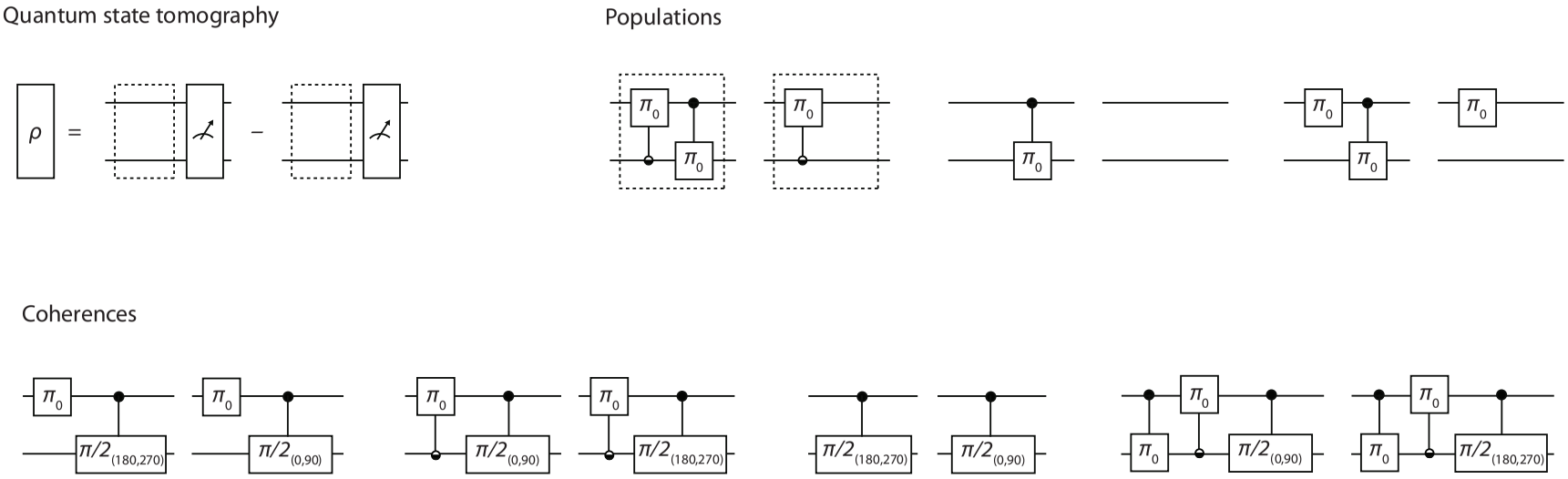

Figure 8.5: The quantum state tomography protocol for reconstructing the density matrix ρ of a register ensemble via its ODNMR resonance. The density matrix elements are obtained by differential photoluminescence measurements between two distinct gate sequences. (upper right panels) The gate sequences used to determine the density-matrix populations (on-diagonal ρ elements). The dashed boxes in the left-most panel map to the dashed boxes in the left panel to serve as a guide. (lower panels) The gate sequences used to determine the density-matrix coherences (off-diagonal ρ elements). SOURCE: [54]

8.9 Entanglement

Having established register initialization, readout, quantum gates, and tomography, we have the necessary components to generate and detect entanglement. Our entangling algorithm (Fig. 8.6) consists of the following steps: we optically initialize registers into $|0,\uparrow\rangle$, and then evolve them into the state $|-1,\uparrow\rangle$ with a series of non-local electronic gates. We then apply a non-local nuclear gate to prepare them into the coherent nuclear spin superposition $2^{-1/2}(|-1,\uparrow\rangle \pm |-1,\downarrow\rangle)$ and then apply a non-local electronic gate to project this coherence into one of the four Bell states:

$$|\Psi^{+/-}\rangle = \frac{1}{\sqrt{2}}(|0,\uparrow\rangle \pm |-1,\downarrow\rangle) \tag{8.1}$$

$$|\Phi^{+/-}\rangle = \frac{1}{\sqrt{2}}(|0,\downarrow\rangle \pm |-1,\uparrow\rangle). \tag{8.2}$$

We execute this algorithm on either the R1 or R2 ensemble and, in separate experimental runs, tomographically reconstruct the initial and final density matrices (Fig. 7.6 for R2 data and Appendix D.8 for R1 data).

The density matrix after optical pumping (ρ_i) shows strong initialization into $|0,\uparrow\rangle$ with fidelity (F) up to $0.95^{+0.05}_{-0.07}$. The density matrices after the entangling algorithm (ρ_f) have F up to 0.88±0.07, with respect to the ideal Bell states. To quantify the level of entanglement, we apply the Peres-Horodecki test (otherwise known as the positive-partial-transpose, or "PPT," test) [189, 190], which returns negative values for entangled states, with -0.5 signifying maximal entanglement. According to this metric, all of our reconstructed density matrices are unambiguously entangled, reaching a minimum PPT test value of -0.40±0.06 (see Fig. 8.7a). In the future, distillation protocols can be used to purify the entanglement. To measure the lifetimes of the Bell states, we allow them to freely evolve for a variable time before tomographically resolving their respective entanglement coherences ($\langle -1,\uparrow |\rho| 0,\downarrow\rangle$ for $|\Phi^{\pm}\rangle$ and $\langle -1,\downarrow |\rho| 0,\uparrow\rangle$ for $|\Psi^{\pm}\rangle$. See Fig. 8.7b). The lifetimes of these states can be

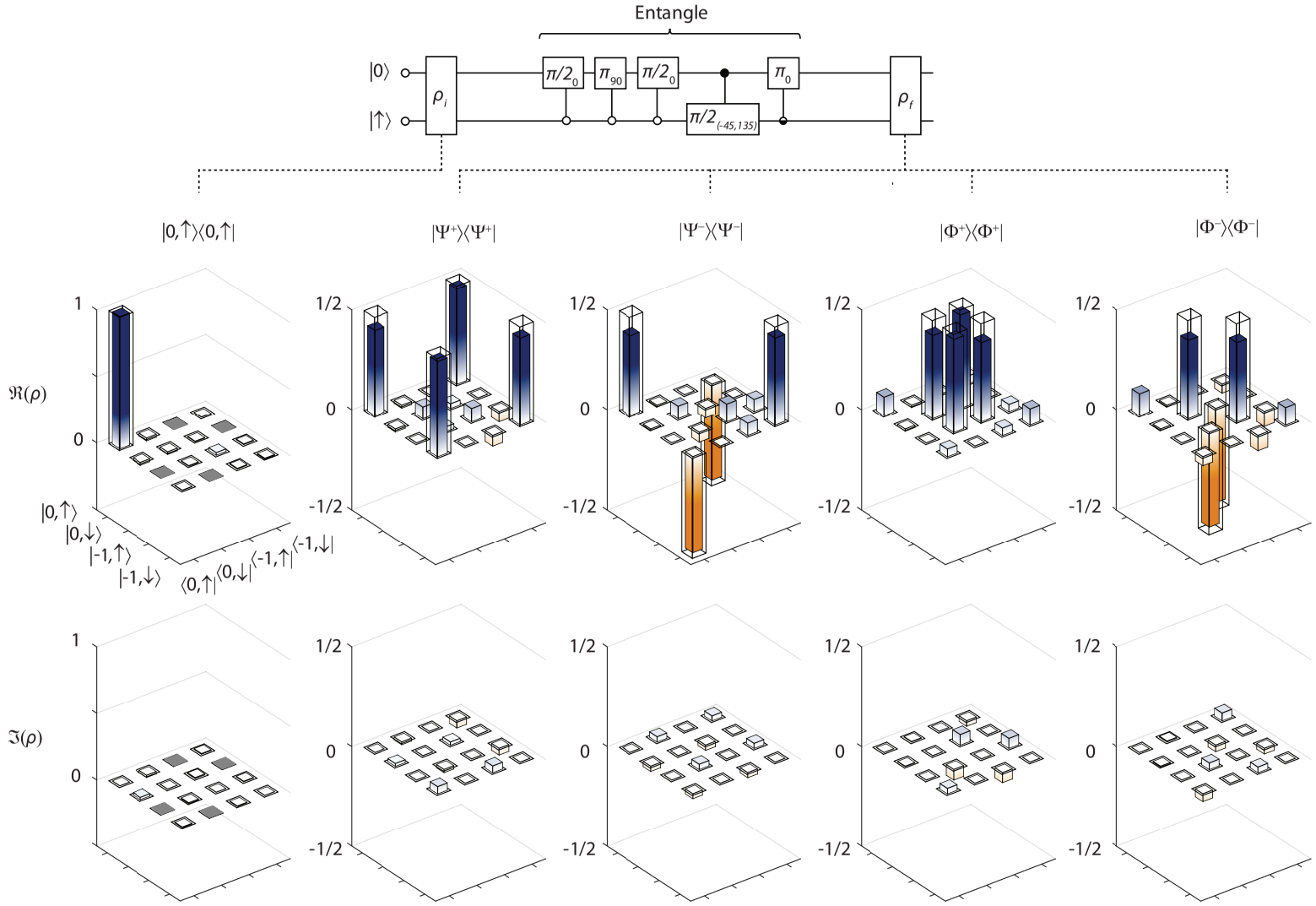

Figure 8.6: The entangling algorithm. The final Bell state is chosen by the phase of the last nuclear gate and the conditionality of the last electronic gate.The real (upper panel) and imaginary (lower panel) components of the R2 ensemble density matrix after optical pumping). The overlaid transparent bars represent the ideal density matrices. The coherences $\langle 0,\uparrow|\rho|-1,\uparrow\rangle$ and $\langle 0,\downarrow|\rho|-1,\downarrow\rangle$, (grey squares in ρ_i), are not measured in our experiments. SOURCE: [54]

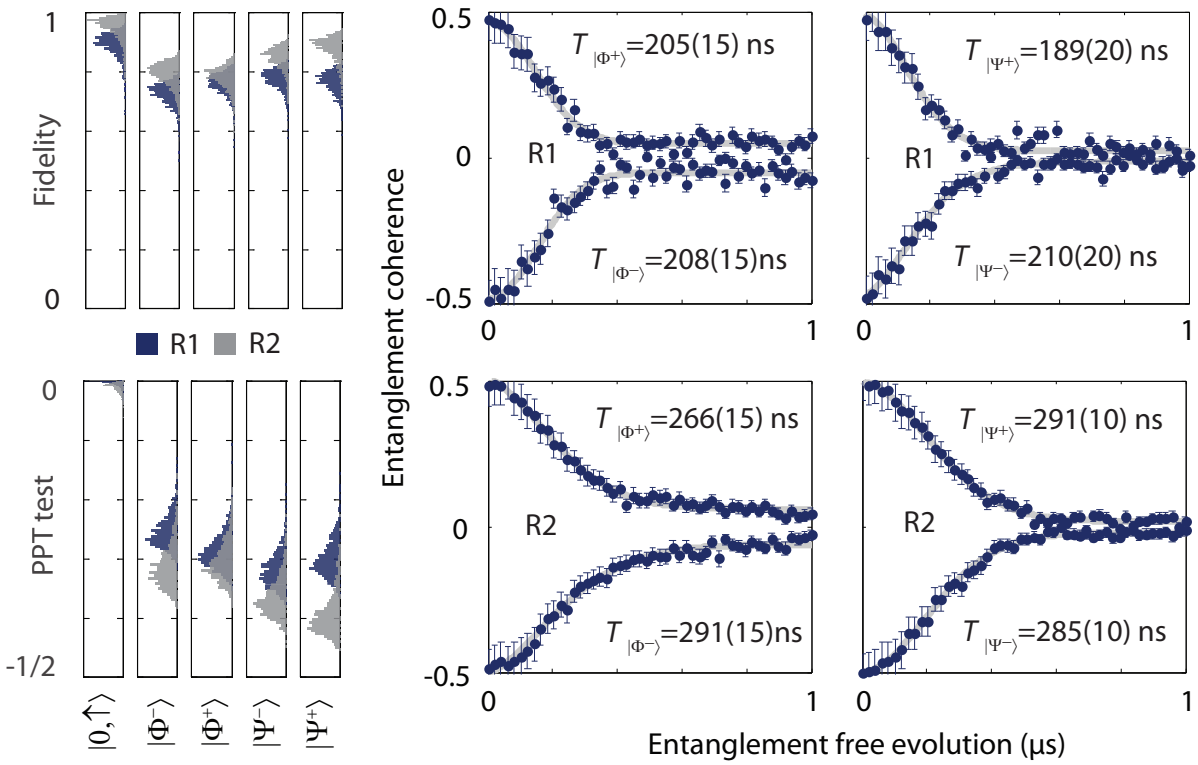

Figure 8.7: The fidelity (upper left panel) and the PPT test value (lower left panel) as calculated from Monte Carlo and maximum likelihood techniques applied to the measured density matrices. The lower labels show the ideal states. The initialized states are classical (PPT test <0) and the Bell states are unambiguously entangled (PPT test<0). (Right panels) The entanglement coherences, $\langle -1,\uparrow|\rho|0,\downarrow\rangle$ for $|\Phi^{\pm}\rangle$ and $\langle -1,\downarrow|\rho|0,\uparrow\rangle$ for $|\Psi^{\pm}\rangle$, as a function of the entanglement free-evolution time. The error bars are 95% confidence intervals. SOURCE: [54]

extended via dynamical decoupling.

8.10 Conclusions

Entanglement in a spin ensemble at ambient conditions reaches a milestone in the study of macroscopic quantum systems. Register ensembles can be employed for entanglement-enhanced sensors that utilize quantum error correction [184, 185] or spin squeezing [191]. They can serve as testbeds of cavity-quantum-electrodynamics at room-temperature, and be used for long-lived quantum memory [182]. The presented methods are equally applicable at cryogenic conditions, in which spin ensembles can couple collectively to other remote

ensembles [113], to superconducting [183] and mechanical [115] resonators, and to optical fields [116]. Exploiting these strong interactions is a promising route to producing larger registers for quantum computing and metrology or even distributing entanglement between remote nodes for quantum communication.

CHAPTER 9

OUTLOOK

9.1 Summary

In this thesis I presented several of our contributions to the field of quantum information processing with electronic and nuclear spins in SiC. In this section I will briefly summarize these contributions and their impact.

In Chapter 5 and 6 we showed that DC electric fields can tune the transition energies of electron spin qubits and that AC electric fields can be used to coherently control them. To recognize the significance of these results, let us recall from the introduction that most quantum technologies will require algorithms to be executed on many qubits. In order to practically execute these algorithms, the qubits will have to be both strongly strongly interacting (which requires inter-qubit separations on the order of tens of nanometers [105, 137]) and independently addressable. Meeting these conflicting demands [43,44,105,107,137] in a scalable way [192] is non-trivial, especially when magnetic fields are used to implement quantum gates, since they are difficult to localize on nanometer scales. By instead using electric fields [96, 97], which are relatively easy to localize on nanometer scales, it might be possible to overcome this challenge.

In Chapter 7 and 8 we showed that an ensemble of 2-qubit registers comprising an electron spin qubit and a nuclear spin qubit can be universally controlled and genuinely entangled. Our techniques apply from cryogenic to ambient conditions, proving that spin ensembles can exhibit genuine quantum behavior in a wide range of environments and can thus be used be used to implement a variety of quantum technologies. When compared to single spins, ensembles should be viewed as a complementary technology, with a distinct spectrum of applications. For example, while single spins are attractive for atom-scale sensing, ensembles can be used to robust interfaces between spin and other degrees of freedom, enabled by their built-in redundancy and ability to behave collectively. These interfaces could become the ba-

sis of various hybrid quantum architectures [114,115], or maybe even offer practical solutions to outstanding problems like producing many-qubit registers [113] or reliably distributing entanglement between remote nodes [116].

Over the past several years, the field of quantum information processing with electronic and nuclear spins in SiC has progressed rapidly. In some respects, the SiC technology has almost caught up to the much older diamond technology [96,100,104,163,188], and in other respects, it has exceeded it [54,88,97]. Nonetheless, numerous challenges stand between the state-of-the-art achieved in a laboratory environment and a practical quantum technology. This fact makes it an exciting time to be in this field. To conclude the thesis, I will present a few research directions that could evolve from the results presented here.

9.2 Outlook

Spin Arrays Producing quantum registers with many qubits is one of the biggest challenges in the field. Although many approaches are actively being explored to address this challenge [43,44,105–107], the most intuitive one would involve the production of an array of interacting and individually addressable spin qubits. Of course, such structures are highly nontrivial to realize. In addition to the significant fabrication challenges associated with producing the array, it is also necessary to couple the individual qubits and to execute quantum gates between them without crosstalk. Our demonstration of electrically driven spin resonance shows promise for overcoming the last challenge, but the others have yet to be addressed. Below I suggest several paths for overcoming the remaining challenges.

The 3D localization of NV centers on micron scales has been achieved by doping chemically purified diamond with a thin layer of nitrogen (a delta doping layer) and then by bombarding the structure with ions through a grid of apertures [51, 193]. By leveraging existing heterostructure growth capabilities, a "delta-doping"' approach might also be possible in SiC. In particular, a semi-insulating epilayer could play the role of the "delta-doped" layer, and an n-type layer, in which the divacancies are in the wrong charge state [88], could

play the role of the chemically purified layer. Although ion bombardment through a grid of apertures has already led to the localization of SiC defect ensembles in the other two dimensions [88], it is unlikely that this approach could be scaled down to reproducibly produce single defects with nanometer resolution [193, 194]. A more scalable approach might employ a focused electron beam to produce small clusters of vacancies, or *in situ* scanning probe lithography [195] to define single vacancies with atomic resolution.

If qubit arrays can be produced deterministically, the next step would be to couple the constituent qubits with the intention of executing quantum gates between them. If inter-qubit separations on the order of the strong-coupling length (tens of nanometers) are possible, encoding multi-qubit registers and executing gates on them would be straightforward [54,97]. In the more likely scenario where only dilute arrays of weakly coupled spins can be realized, it might still be possible to encode multi-qubit registers and to execute gates between them [44,107]. Even in the latter case, a meaningful coupling would likely not be possible on length scales exceeding the diffraction limit. Therefore, sub-diffraction limited optical techniques or spin-to-charge conversion [196] will be necessary for register readout.

Another scheme to couple spins in a dilute array might exploit more exotic physics. In particular, electron gasses that have been realized at the interface of 3C/4H-SiC heteropolytype structures [108, 109] could potentially be used to execute quantum gates between qubits via the RKKY interaction [110–112]. In addition to being an all-electrical approach, the RKKY interaction scales with the dimension of the electron gas as r^{-d}, meaning it would greatly exceed dipole-dipole interactions in low dimensional structures. This approach could have many potential pitfalls [197], however, and is purely speculative.

Hybrid Architectures In recent years, the strengths and weakness of qubits in the various physical systems have become reasonably clear. The fact that they differ from system to system has motivated the use of hybrid architectures, which would interface different types of qubits, to reap their individual merits. From this perspective, electron spin ensembles have been recognized for their exceptionally long coherence times, and they have been proposed

to serve as quantum memories for superconducting qubits [198].

To date, attempts to interface superconducting circuits with NV ensembles have led to many impressive demonstrations [114,183,199], including the coherent transfer of information between the systems [200], which is essential for realizing a memory. All of these demonstrations, however, have coupled the systems magnetically. By demonstrating that electric fields and strain can also be used for spin control [96, 97], our research suggests that they could also be coupled capacitively or even through surface acoustic waves [201]. Depending on the device architecture, these could offer advantages over the standard magnetic coupling schemes.

In addition to exploring the coupling mechanisms, the degree of freedom that serves as the memory should be explored further. The techniques developed in this thesis for controlling electron-nuclear spin ensembles, suggest that it might be possible to use the electronic ensemble simply as a bus for transferring [180] information from the superconducting qubit to the nuclear spin ensemble. Since nuclear spins are generally orders of magnitude more coherent than electron spins, this could be a straightforward way to realize a memory with ultra-long storage times. Moreover, the tomography techniques developed here could serve as a tool to benchmark the memory.

As an aside, it should be noted that implementing a nuclear spin memory should be much more straightforward in SiC than in diamond. The reason is that registers based on ^{29}Si nuclei in SiC have highly isotropic hyperfine interactions [54, 86, 102], whereas those based on ^{13}C nuclei in diamond typically do not [101] (see Appendix D.9. for further discussion).

Nuclear Spin Diffusion Driving a macroscopic nuclear spin polarization could enable the initialization of registers comprising weakly coupled nuclear spins [44, 107], it could be used to extend the electron spin coherence time by suppressing fluctuations of the decohering nuclear spin bath [65], or even for enhanced MRI. Nonetheless, achieving a bulk polarization is nontrivial due to the small nuclear gyromagnetic ratio, which leads to a polarization in the part-per-million range at ambient conditions. By demonstrating strong dynamic nuclear

polarization (DNP) [100, 102], we have taken the first step towards reaching this goal.

In diamond, DNP [122] has been extended to a bulk polarization through spin diffusion, all at ambient conditions [161, 202, 203]. Our measurements suggest that a similar approach should also be possible in SiC. In particular, with relatively quick DNP (~ 5 μs [54]) and spin diffusion times ($\sim$50 μs, estimated from the coherence, which is limited by nuclear-nuclear flip-flops [65]), and no efficient nuclear depolarization pathway ($T_{1n,^{29}Si} \sim$ hours [119, 166]), a substantial bulk polarization should be possible with strong optical pumping in a matter of seconds in a typical sample (this assumes 10^5 nuclei per polarizing defect).

If spin diffusion is possible in wafers, a more ambitious goal will be to hyperpolarize SiC nanoparticles, which could be used as imaging agents in MRI. Such technologies are already actively being explored in Si [204] and diamond [205, 206]. Si is attractive for these applications since it is present at trace quantities in biological molecules, and thus there would be a small noise background. Nonetheless, Si hyperpolarization protocols require both cryogenics and a large magnetic field [204], which is not ideal for real-world applications. In nanodiamonds, hyperpolarization is possible at ambient conditions, but the imaging agent would presumably be $^{14/15}$N or ^{13}C, both of which are abundant in biological molecules. In SiC nanoparticles, the hyperpolarization of Si might be possible at ambient conditions, which would combine the strengths of Si and diamond.

APPENDIX A

TUNING SPINS WITH ELECTRIC FIELDS AND STRAIN - DETAILS

A.1 Strain Calibration

In order to calibrate the strain applied by our piezo actuators to our SiC chips and membranes, we fabricated a device in which a copper coldfinger applies strain to a clamped SiC chip as the device is cooled from 296 K to 20 K (Fig. A.1). By modeling the strain applied by the copper's thermal contraction, and comparing the measured splitting of the ZPL in this device to the splitting of the ZPL induced by the piezo actuators, we can estimate the strain applied by the actuators.

As copper is cooled from 296 K to 20 K, it contracts by 0.3% [207], whereas SiC contracts by only 0.02% [93]. We used a finite-element model of the copper-clamped SiC to find that the transverse strain at the center of the 2 mm x 3 mm x 0.5 mm chip should be 1.0 x 10^{-4} $\pm$ 40%, where the large uncertainty comes from the fact that strain is not distributed equally across the chips thickness. Our clamped SiC chip showed a ZPL splitting of 0.9 meV for PL1, PL2, and PL6 (all of which exhibit approximately the same ZPL splitting). Comparing this splitting to the 0.7 meV ZPL splitting observed for PL6 as V_{piezo} is swept from 0 V to 150 V (Fig. 5.1b), we arrive at the calibration:

$$5 \times 10^{-7} \text{strain } V_{\text{piezo}}^{-1} \tag{A.1}$$

As another reference for the piezo-induced strain, we note that our piezo actuators (Noliac NAC2012) have a blocking force of 378 N. If this entire force were delivered to the SiC membrane, which is 2 mm x 2 mm x 0.05 mm, then using 700 GPa for the SiC Young's modulus, the membrane would be strained by 6 $\times$ 10^{-3} over the full 300 V range for V_{piezo}, roughly 40 times the strain indicated by the calibration (Eq. A.1). This discrepancy can be

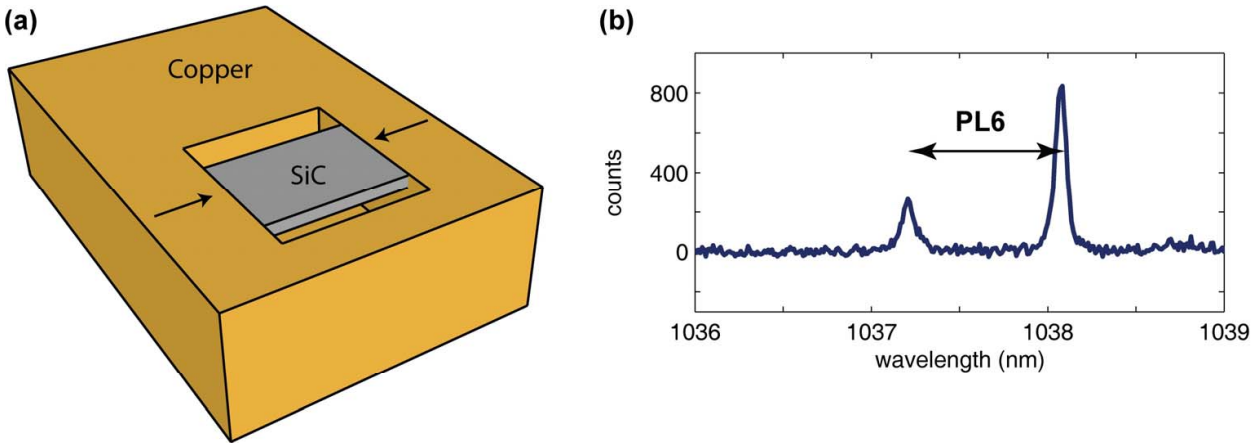

Figure A.1: (a) Illustration of SiC chip in thermally contracting copper clamp. (b) PL spectrum of PL6 for this device, showing a ZPL splitting of 0.9 nm.

ascribed to the piezo not transmitting its full blocking force to the SiC due to the epoxy and expansion of the piezo. We stress that our calibration of strain is inexact and is intended to be only an order-of-magnitude estimate.

A.2 Strain Sensitivity Estimation

In analogy to previous reports of magnetic, electric, and thermal sensing in NV centers in diamond, [123, 131, 208], we write the shot noise-limited strain sensitivity η as:

$$\eta = \frac{Z}{2\pi \frac{dD}{dS} e^{(-t/T_2)^m} \sqrt{t}} \tag{A.2}$$

where

$$Z = \sqrt{\frac{2(p_0 + p_1)}{(p_0 - p_1)^2}} \tag{A.3}$$

p_0 is the number of photons collected when the spin is in the "bright" state, p_1 is the number of photons in the "dark" state, dD/dS is the change in the D term in the Hamiltonian (see Eq. 5.1) due to a component of strain (S), t is the measurement time, and m is the exponent characterizing the decoherence of the spin ensemble, which happens with time T_2.

Eq. A.2 is valid only when the decoherence rate exceeds the longitudinal relaxation rate (i.e. $T_1 >> T_2$). The T_2 times for PL1-PL4 in our 4H-SiC samples range from 140-360 μs at T = 20 K [87,88]. Although ref. [87] presented T_1 measurements for PL1-PL4 at elevated temperatures, they did not present the cryogenic T_1 data needed to establish that $T_1 >> T_2$ in our experiments. We present this data in Fig. A.2. The long T_1 times that we observe establish that $T_1 >> T_2$ for PL1-PL4, and that Eq. A.2 can indeed be applied here.

Note that for strain sensing, either the D term or the E term of the Hamiltonian (Eq. 5.1) can be used. The one that should be used is the one that has the greater sensitivity to the type of strain that is applied. For compressive/tensile strain, which is the type of strain that we applied in our experiments, we found that the D parameter is most sensitive. This is in agreement with the theoretical calculations presented in section A.6.

By extracting the frequency of the quadrature signal from Fig. 5.2b, as a function of applied piezo voltage, we find that

$$\frac{dD}{dS} = f_{strain}(\frac{1}{t_{applied}})\frac{dV_{\text{piezo}}}{dS} = 3.8\frac{GHz}{strain} \tag{A.4}$$

The single-spin values of the Z parameter are not exactly known because the quantum efficiencies of divacancies in SiC have not yet been measured. However, the combination of high optical polarizations [54, 88], high ODMR contrasts (which are closely related to the $(p_0 - p_1)/(p_0 + p_1)$ ratios), and weak dependence of the ODMR contrasts on temperature makes it unlikely that the quantum efficiencies are extremely low. For NV centers in diamond, a typical "high" optical collection efficiency (5%) assumption leads to single-spin values of $p_0 = 0.09$ and $p_1 = 0.065$ respectively [131, 208]. Some neutral divacancies in SiC have a $\sim$30% lower photoluminescence contrast (see Fig. 5.4 and Section A.4) and a comparable lifetime (see Fig. 5.4 and section Section A.5) to the NV center in diamond. Therefore, we estimate that $Z = 30$, which is 30% higher than the "high" value for NV centers.

Finally, we have previously found that $m = 1$ and $T_2 = 360$ μs for an ensemble of PL4

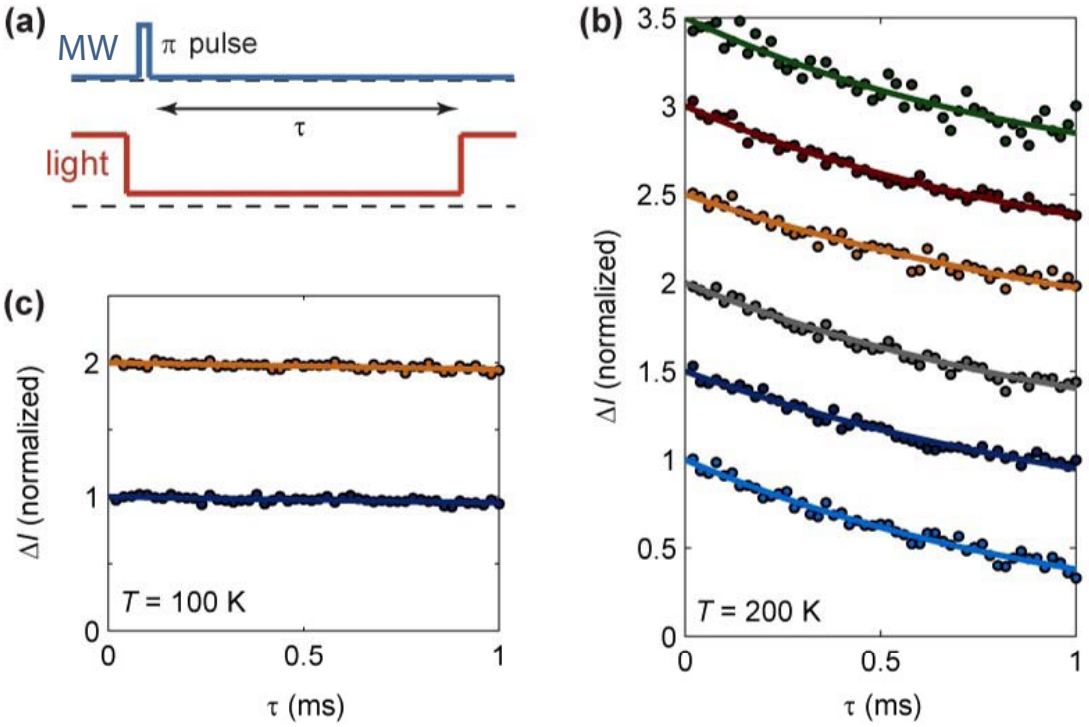

Figure A.2: (a). Pulse sequence for measuring T_1 times. A MW π pulse flips the spin state of the defect ensemble between $m_s = 0$ and $m_s = \pm 1$, and an optical pulse, applied a variable time (τ) after the MW pulse, reads out and reinitializes the spin state. ΔI lock-in contrast is generated by strobing the π pulse at 20 Hz. (b) T_1 measurements at $T = 200$ K for PL1 (light blue), PL2 (dark blue), PL3 (grey), PL4 (orange), PL5 (red), and PL6 (green), with the curves offset for clarity. All defects' T_1 times at 200 K are fit to 1.2 ± 0.2 ms. (c) Long longitudinal relaxation times at $T = 100$ K (PL2 (dark blue) and PL4 (orange) are shown) set a lower bound of $T_1 = 20$ ms at $T = 100$ K.

neutral divacancies in 4H-SiC at 20 K [88], leading to the maximum value of

$$e^{(-t/T_2)^m}\sqrt{t} \tag{A.5}$$

being 0.008 at $t = 180$ μs. Putting everything together, we find that the ideal single-spin strain sensitivity is

$$\eta = \frac{2 \times 10^{-7}}{\sqrt{Hz}} \tag{A.6}$$

for neutral divacancies in SiC. In ensemble measurements, the sensitivity is improved by $\sqrt{N}$, where N is the number of spins being interrogated. At cryogenic temperatures, piezo

actuators are known to be hysteretic. Owing to this hysteresis and the assumptions underlying the calculation discussed here, the sensitivity given in Eq. A.6 is intended to be an order-of-magnitude estimate.

A.3 ODMR Pulse Sequences

Our AC strain and electric field measurements use almost identical pulse sequences (Fig. 5.2b and Fig. A.3). The only difference is whether $V_{\text{piezo}}(t)$ is applied to the piezo actuator in order to generate a transverse strain or whether $V_{\text{mem}}(t)$ is applied across the sample to generate a c-axis-oriented electric field. The effects of these perturbations to the ground-state spin Hamiltonian (Eq. 5.1) are measured by integrating these waveforms into Hahn-echo pulse sequences.

For this discussion, we will refer to a Bloch sphere spanned by $m_s = 0$ ($+\mathbf{z}$ on the sphere) and one of the $m_s = \pm 1$ ($-\mathbf{z}$) spin states. The MW pulse sequence used to measure a baseline Hahn-echo sequence (Fig. A.3a) is as follows. First, the sample is illuminated, which spin-polarizes the defects (taken to be $m_s = 0$ without loss of generality). A $\pi/2$ ($\mathbf{x}$) MW pulse rotates the spin ensemble around the $\mathbf{x}$ axis to the equator of the Bloch sphere. Here, $\mathbf{x}$ is defined in relation to a rotating frame precessing at the Larmor frequency. The spins then freely evolve for time $t_{\text{free}}/2$, during which they dephase. A $\pi(\mathbf{x})$ pulse, also around the $\mathbf{x}$ axis, then flips the free-precession direction of the spins. The spins freely evolve for another time $t_{\text{free}}/2$ and partially re-phase. A final $\pi/2$ pulse then projects the spins's phase (θ_{free}) onto the measurement axis ($\mathbf{z}$), at which point laser illumination is reapplied and the spin is read out via a differential PL measurement. To generate lock-in contrast, the phase of the final $\pi/2$ pulse is alternatively switched between being around the $\mathbf{x}$ axis and the $-\mathbf{x}$ axis [88]. The lock-in frequency for a typical pulse sequence is 5 kHz. The resulting difference in these two PL signals is ΔI_{Hahn}. The readout laser pulse also serves to reinitialize the spins for the next sequence.

For the strain and electric field sensing measurements, we make two modifications to the

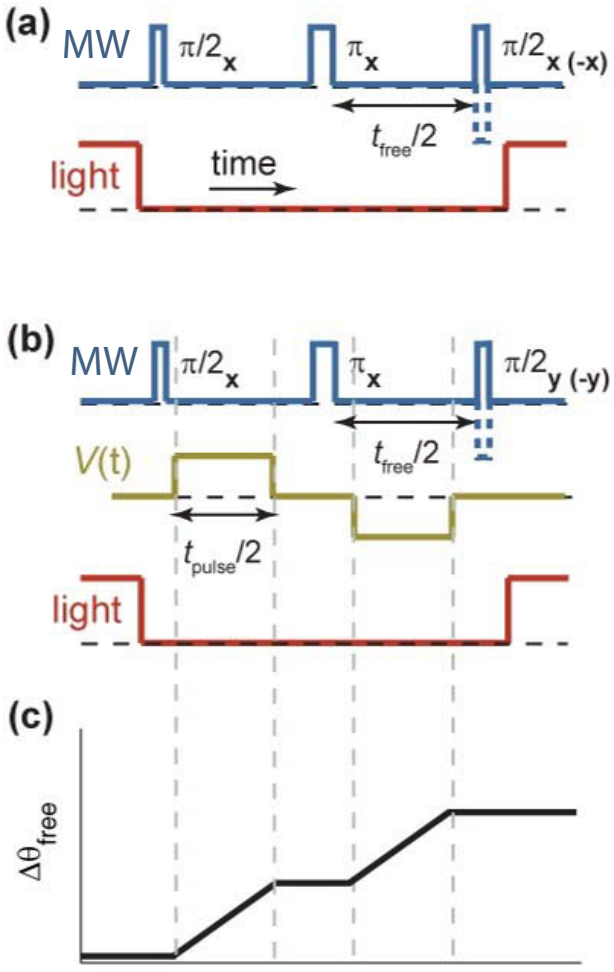

Figure A.3: Pulse sequences used for AC strain and electric field sensing. (a) The Hahn-echo pulse sequence used to measure ΔI_{Hahn}. (b) Quadrature Hahn-echo pulse sequence, in which the first and last $\pi/2$ pulses have a 90 degree phase offset from each other. An applied voltage (either $V_{\mathrm{piezo}}(t)$ or $V_{\mathrm{mem}}(t)$) modifies the spin transition energies, and causes a net change in precession rate for the spins on either side of the central π pulse. (c) The change in spin precession rate causes the phase θ_{free} to monotonically accumulate ($\Delta\theta_{\mathrm{free}}$) over the course of the measurement.

sequence that we use to measure ΔI_{Hahn} (Fig. A.3b). First, a $V_{\mathrm{piezo}}(t)$ or $V_{\mathrm{mem}}(t)$ pulse sequence is applied to the sample, which consists of two voltage pulses that have opposite signs and are on opposite sides of the central π pulse. These V_{piezo} or V_{mem} perturbations shift the spin transition energies, causing a change to their precession rates during the Hahn echo sequence, and a net phase shift ($\Delta\theta_{free}$) at the end of their free precession (Fig. A.3c). Second, we modify the Hahn echo sequence to be a quadrature measurement. In

particular, instead of alternating the final $\pi/2$ pulse between the $\mathbf{x}$ and $-\mathbf{x}$ axes, we alternate them between the $\mathbf{y}$ and $-\mathbf{y}$ axes. This quadrature sequence leads the measured ΔI to be proportional to $\mathrm{Sin}(\Delta\theta_{free})$ instead of $\mathrm{Cos}(\Delta\theta_{\mathrm{free}})$. Since $\mathrm{Sin}(\Delta\theta_{\mathrm{free}}) \sim \Delta\theta_{\mathrm{free}}$ for small $\Delta\theta_{\mathrm{free}}$, ΔI has first-order sensitivity to strain- and electric-field perturbations.

A.4 Discussion of PL Intensity Contrasts in ODMR Measurements

We define the ODMR photoluminescence contrast (C_{defect}) as the fractional change in PL between an optically initialized state and one that has been optically initialized and then rotated with a π pulse. To infer this parameter, we make spectroscopic measurements of the defects' zero-phonon-line (ZPL) emission with and without the application of strong MW radiation. This enables us to determine $\Delta I_{\mathrm{mixed}}$/I, from which we can infer the contrast. In particular, we define

$$\frac{\Delta I_{\mathrm{mixed}}}{I} = \frac{\int_{ZPL} \Delta I_{\mathrm{mixed}}(\lambda) d\lambda}{\int_{ZPL} I_{\mathrm{mixed}}(\lambda) d\lambda}. \tag{A.7}$$

When measuring $\Delta I_{\mathrm{mixed}}/I$ (Fig. 3.4 and Fig. A.4), we used strong enough MW power and weak enough optical illumination to saturate $\Delta I_{\mathrm{mixed}}/I$ with respect to both parameters (Fig. A.5). As a control, in addition to measuring $\Delta I_{\mathrm{mixed}}$ by locking into the MW radiation being on versus off (with lock-in frequency $(30\ \mathrm{sec})^{-1}$), we also measured $\Delta I_{\mathrm{mixed}}$ by locking into the frequency of MW radiation being on versus off resonance, with respect to a target spin transition. This procedure ensured that constant MW power was applied to the sample during the full measurement cycle, and therefore, that heating did not play a role in the results. Both techniques consistently yielded the same values, excluding heating as a potential source of error.

Relating C_{defect} to the measured $\Delta I_{\mathrm{mixed}}/I$ requires a detailed knowledge of both the optical polarization cycle and about how spin states are mixed by the applied MW radiation.

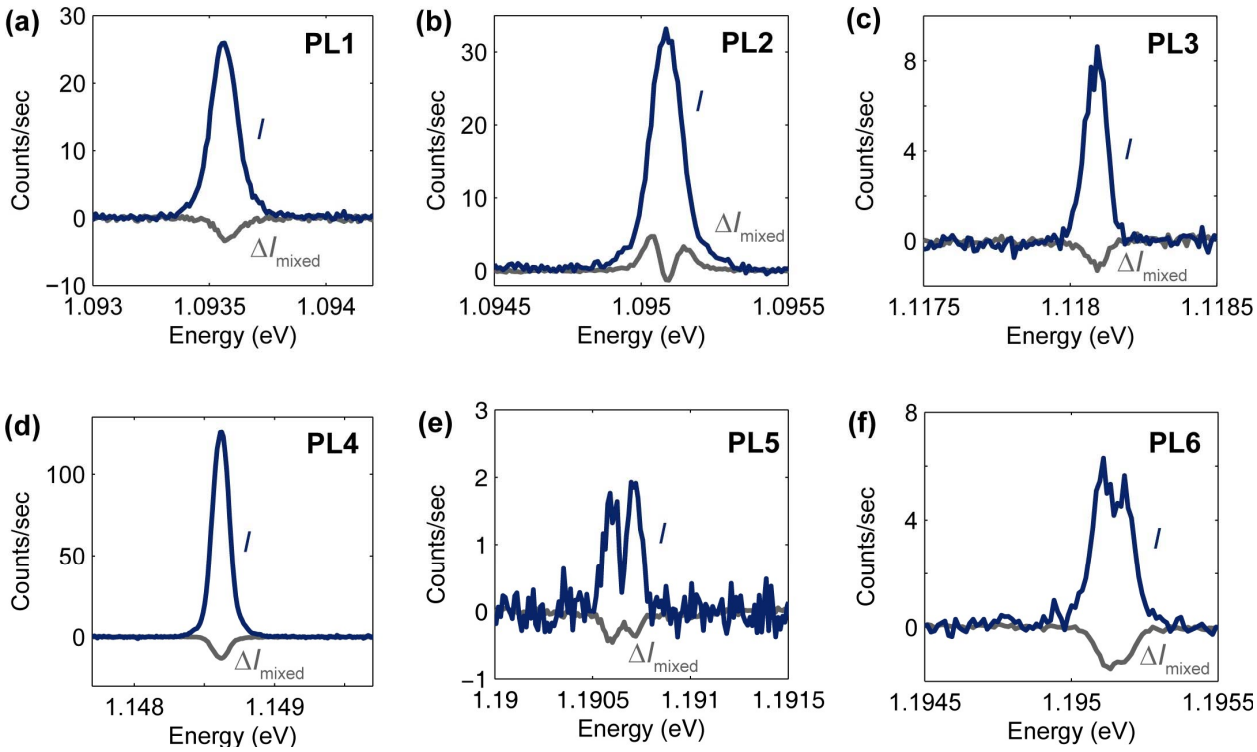

Figure A.4: Determination of ODMR contrasts. The blue curves are the various defect species' ZPLs. The gray curves are ΔI_{mixed}, which indicate the net change in the ZPL when strong MW radiation is applied to the sample. The double peaked shape of ΔI for PL2 reflects a broadening of the ZPL under microwave irradiation (in addition to an increase in PL from the defect). The source of this broadening is not known but control measurements verify that it is not due to heating. $\Delta I_{\text{mixed}}/I$ is measured to be -0.10, +0.11, -0.14, -0.10, -0.24, and -0.22 for PL1-PL6 respectively, at T = 20 K, B = 0.

Because our measurements are continuous wave (as opposed to pulsed), continuous spin-mixing occurs in parallel with probabilistic optical initialization. The rates that govern these processes are set by a number of factors, including the optical and MW powers, the coupling strength of the spin ensemble to the microwave antenna, the optical absorption rate, the intersystem crossing rates, and the spin relaxation (T_1) and dephasing (T_2^*) times. Even though some of these parameters are not yet known, we can set a lower bound on C_{defect}, through the process described below.

For the sake of this discussion and without loss of generality, we assume that PL1-PL6 initialize preferentially into $m_s = 0$, which we take to be the "bright" state with higher PL intensity (I_{bright}). The $m_s = \pm 1$ states are then taken to be the "dark" states with lower

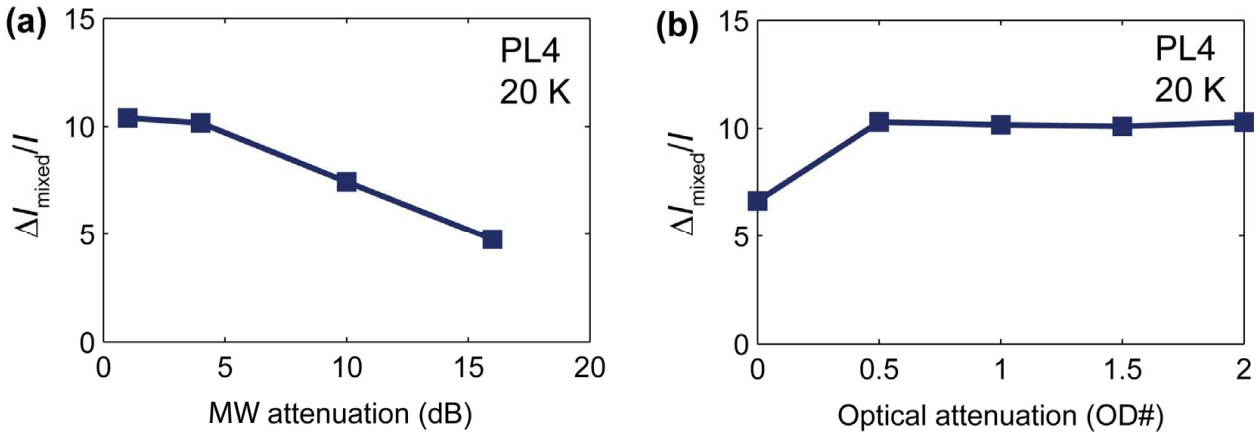

Figure A.5: The ODMR contrast of PL4 as a function of (a) MW attenuation and (b) optical attenuation. A MW attenuation of 0 dB corresponds to 4 W of power reaching the microwave stripline, and an optical density (OD) of OD0 (i.e.no attenuation) corresponds to 60 mW of optical power reaching the sample. The data in (a) are taken at optical power OD1, and the data in (b) are taken at 4 dB of microwave attenuation. $T = 20$ K, and $B = 0$. The data indicate that $\Delta I_{\text{mixed}}/I$ saturates at low-optical-power and high-MW-power.

PL intensity (I_{dark}). For this discussion, we also define a vector of the populations of the system, $(\langle 0|\rho|0\rangle, \langle -1|\rho|-1\rangle, \langle +1|\rho|+1\rangle)$, where ρ is the density matrix of the interrogated ensemble.

With our experimental parameters, the thermal populations are approximately (1/3, 1/3, 1/3). During continuous laser illumination, the populations are redistributed to some equilibrium value $(1/3 + 2p/3, 1/3 - p/3, 1/3 - p/3)$, where p is a number between 1 and 0 that parametrizes the polarization efficiency. The PL emitted is then:

$$I = (\frac{1}{3} + \frac{2p}{3})I_{\text{bright}} + (\frac{2}{3} - \frac{2p}{3})I_{\text{dark}}. \tag{A.8}$$

In the absence of a magnetic field ($B = 0$) and in the presence of strong MW radiation applied at the $m_s = 0$ to $m_s = \pm 1$ resonance, the populations will redistribute to a maximally mixed state with populations $(1/3, 1/3, 1/3)$ [96]. The PL emitted is then:

$$I_{\text{mixed}} = \frac{1}{3}I_{\text{bright}} + \frac{2}{3}I_{\text{dark}}. \tag{A.9}$$

The change in PL between the initial and mixed state will thus be:

$$\Delta I_{\text{mixed}} = -\frac{2p}{3}(I_{\text{bright}} - I_{\text{dark}}) \tag{A.10}$$

If, on the other hand, instead of applying continuous radiation we apply a π pulse between the $m_s = 0$ and either one of the $m_s = \pm 1$ states, the net change in PL intensity will be:

$$\Delta I_{\pi} = -p(I_{\text{bright}} - I_{\text{dark}}). \tag{A.11}$$

Using the above expressions, we can put a lower bound on C_{defect} (as described in [96]):

$$C_{\text{defect}} \equiv \frac{|\Delta I_{\pi}|}{I} \geq \frac{3}{2}\frac{|\Delta I_{\text{mixed}}|}{I} \tag{A.12}$$

The experimentally measured $\Delta I_{\text{mixed}}/I$ values are -0.10, +0.11, -0.14, -0.10, -0.24, and -0.22 for PL1-PL6 respectively. The corresponding lower bounds on C_{defect} are then 0.15, 0.16, 0.21, 0.15, 0.36, and 0.33 for PL1-PL6 respectively.

A.5 Time-Resolved PL for Determining Optical Lifetimes

Time correlated single photon counting (TSCPC) techniques were used to measure the optical lifetime of PL1-PL6. An unprocessed chip of 4H-SiC was cooled to 20 K in a continuous flow cryostat with optical access. A 0.4 numerical aperture objective lens focused 800 μW of pulsed 850 nm light from a Ti:Sapphire mode locked laser into the middle of the sample thickness. The pulses were approximately 150 fs in length, much less than the 66 ps instrument response function of the detection electronics system. The 76 MHz laser repetition rate was reduced by a factor of 10 by using an electro-optic modulator and the associated pulse-picking electronics. This was done so that the pulse period exceeded the PL decays. The PL from the sample was passed through a monochromator to isolate each defect's ZPL and then coupled into a superconducting nanowire detector with a single mode fiber. The pulses from

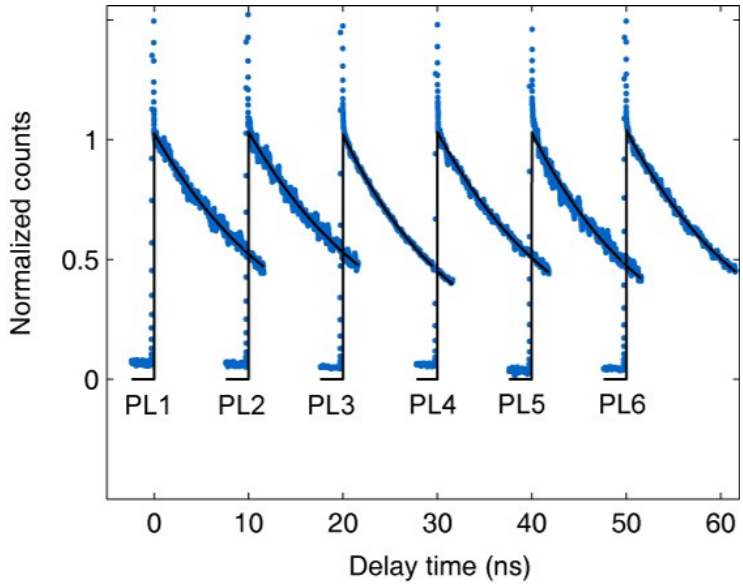

Figure A.6: Time-resolved PL from PL1-PL6 as a function of delay time from an excitation laser pulse (blue data). Each curve has been fit to a decaying exponential (black traces), whose decay constant is the optical lifetime (τ) for that species at 20 K. The optical lifetimes for PL1-PL6 are measured to be 15 ns, 15 ns, 12 ns, 14 ns, 13 ns, 14 ns respectively, with uncertainties of 3 ns coming from the fits. Each defect species is excited at delay time = 0; the data are horizontally offset for clarity.

the output of the superconducting nanowire detector were directed into the measurement channel of the TCSPC electronics. We fit the TCSPC data to single decaying exponential functions, whose characteristic decay time (τ) was the optical lifetime. In principle, each decay is a double exponential, since the $m_s = 0$ and $m_s = \pm 1$ spin sublevels decay at different rates. Nonetheless, determining both rates was beyond the focus of this study. Due to the incomplete optical extinction, we used just the first 12 ns of the PL when fitting the TCSPC data.

A.6 Theoretical Simulations

To compare our experimental results with theory, we engaged in a close collaboration with Adam Gali and his group. Through their density functional theory simulations of the divacancy defects, and their response to strain and electric fields, we were able to estimate several important parameters, which we present in this section. The computational methodology

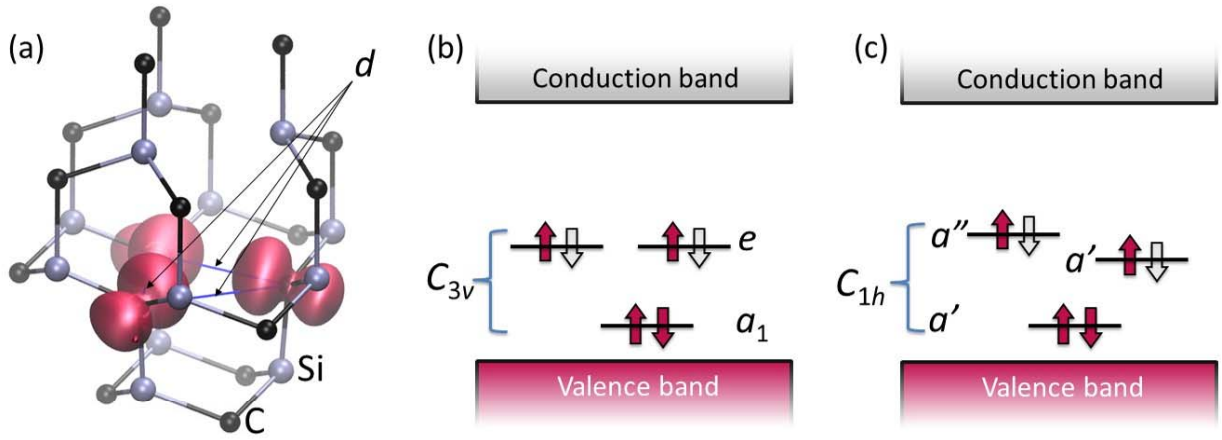

Figure A.7: (a) Geometry of the neutral-divacancy defect at the *hh*-site (PL1) with C_{3v} symmetry. The spin density (red lobes) is localized on the carbon dangling bonds in the Si-vacancy part of defect which is built from the charge density of the double degenerate e orbitals in the majority spin channel. The distance between these C-atoms (d) influences the dominant zero-field splitting of the defect (D). (b) Schematic diagram of the single particle levels of divacancy in 4H-SiC. The unpaired double degenerate e orbitals are mainly localized on the carbon dangling bonds. In the unperturbed c-axis divacancy with C_{3v} symmetry, the a1 energy level is doubly occupied, and each of the two degenerate e orbitals are singly occupied (pink arrows). The outlined arrows represent unfilled orbitals. (c) When strain or the crystal field lowers the defect symmetry to C_{1h}, the e orbitals split into a' and a" orbitals.

behind the simulations described here are in the Supplementary Materials of ref. [96].

From the calculation of the spin density without external perturbations, it is possible to determine many intrinsic parameters of the divacancies (Fig. A.7). Of particular interest to us were the crystal field parameters, D and E, which are are encompassed in the $\mathbf{D}$ tensor of the crystal field Hamiltonian:

$$\hat{H} = \mathbf{S} \cdot \mathbf{D} \cdot \mathbf{S} \tag{A.13}$$

Although the $\mathbf{D}$ tensor is influenced by both the spin-spin and spin-orbit interactions, in this theory it was only possible to include the spin-spin contribution. Even so, the calculations are in close agreement with the experimental results (Table A.1.), especially for the c-axis defects. The less-than-favorable agreement for the basal defects can be attributed to the fact that spin-orbit effects influence primarily the E term, which is only non-zero for the

Table A.1: The measured and calculated D^0 and E^0 parameters for divacancies in 4H-SiC and the NV center in diamond.

Defect	Calculated		Measured	
	D^0 (GHz)	E^0 (MHz)	D^0 (GHz)	E^0 (MHz)
SiC				
hh PL1 (C_{3v})	1.358		1.336	
kk PL2 (C_{3v})	1.321		1.305	
hk PL3 (C_{1h})	1.320	62	1.222	82
kh PL4 (C_{1h})	1.376	7	1.334	19
Diamond				
NV (C_{3v})	2.854		2.88	

SOURCE: [88, 209]

basal defects. As a control, addition calculations were carried out with the same theoretical parameters to simulate the crystal-field Hamiltonian for the NV center in diamond. This calculation returned a D value that is in close agreement with what is observed experimentally, suggesting that the calculations are sound.

By distorting the lattice within the simulation, it is also possible to determine the effect of strain on D and E (Fig. A.8). Calculations for the PL1 defect under the application of a strain parallel and perpendicular to the c-axis are presented in Fig. A.9. Physically, the evolution of these parameters is driven by modifications to the spin-spin interactions by shifting the atoms with respect to one another and thus the spin density. It is important to note that strain transverse to the the quantization axis of c-axis defects lowers their C_{3v} symmetry to C_{1h} symmetry, which is the symmetry of unperturbed basal defects. This breaks the degeneracy between the $m_s = \pm 1$ states and gives the c-axis defects a non-zero E term.

From these calculations, it can be deduced that the strain response a c-axis defect (PL1 here), in response to a transverse strain, is approximately

$$\frac{dD}{dS_\perp} \sim 5\frac{\text{GHz}}{\text{strain}} \qquad \text{and} \qquad \frac{dE}{dS_\perp} \sim 1\frac{\text{GHz}}{\text{strain}}, \tag{A.14}$$

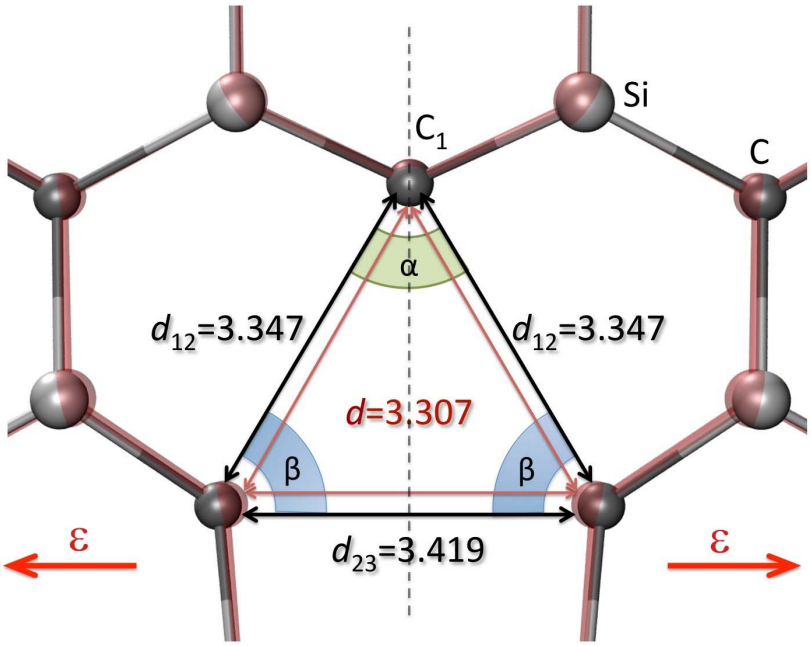

Figure A.8: Illustration of the change of geometry of a PL1 (hh) divacancy in response to uniaxial tensile strain ($\epsilon = 0.015$), directed along the red arrows. This view shows the positions of the three C-atoms nearest to the Si-vacancy part of the defect where the spins are localized. Atoms in the no-strain geometry are shown as semi-transparent red balls. The defect's C_{3v} symmetry is distorted into C_{1h} symmetry under strain transverse to the c-axis. The distances are given in angstroms.

and for strain parallel to the c-axis, the strain response is approximately

$$\frac{dD}{dS_{\|}} \sim 5 \frac{\text{GHz}}{\text{strain}}. \tag{A.15}$$

The calculated $\frac{dD}{dS_{\perp}}$ term is in close agreement with our experimental results.

Similar calculations can be made to determine the effect of electric fields on the **D** tensor, specifically through the Stark parameter d. An illustration of the shift of the spin density of a c-axis divacancy, in response to a c-axis electric field, is presented in Fig. A.10. What is particularly attractive about the theoretical approach is that its possible to disentangle the effects of atomic distortions and the effects of a pure electric field, which are of course intertwined in piezoelectric materials such as SiC. The main result is that a pure electric field couples nearly one order of magnitude more strongly to the defects than the strain induced

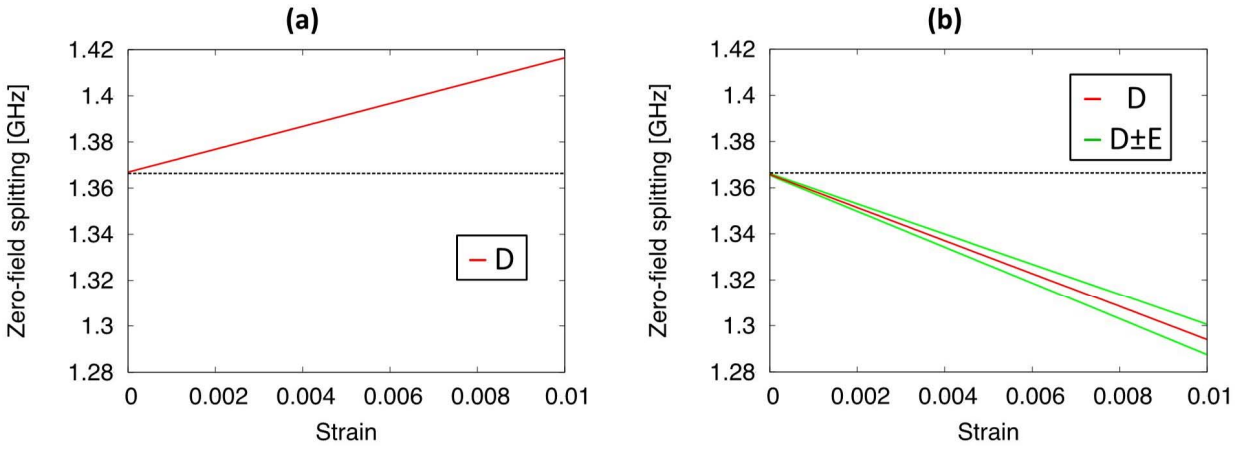

Figure A.9: The crystal field parameters as a function of strain for the PL1 (hh) divacancy. (a) The strain is parallel to c-axis (along the symmetry axis of the defect). The symmetry remains C_{3v} under this perturbation, and so $E = 0$. (b) Strain perpendicular to the c-axis (along the $[11\bar{2}0]$ direction), which lowers the symmetry to C_{1h}. D and E are linear, and D changes faster than E. We note that the spin-orbit interaction may contribute to E, but is not taken into account here.

through the piezoelectric effect. This is perhaps not so surprising given SiC's high electron polarizability (indicated by its high relative dielectric constant $\epsilon_{r,4H} = 9.7$) and its weak piezoelectricity.

The results of these calculations, both including piezoelectric effects and not, are presented in Table 5.1. The $d_{\parallel}$ Stark parameters are in reasonable agreement with the experimentally measured values. The $d_{\perp}$ parameters were not calculated since they are generally strongly influenced by spin-orbit effects, which could not be accurately predicted by this theory.

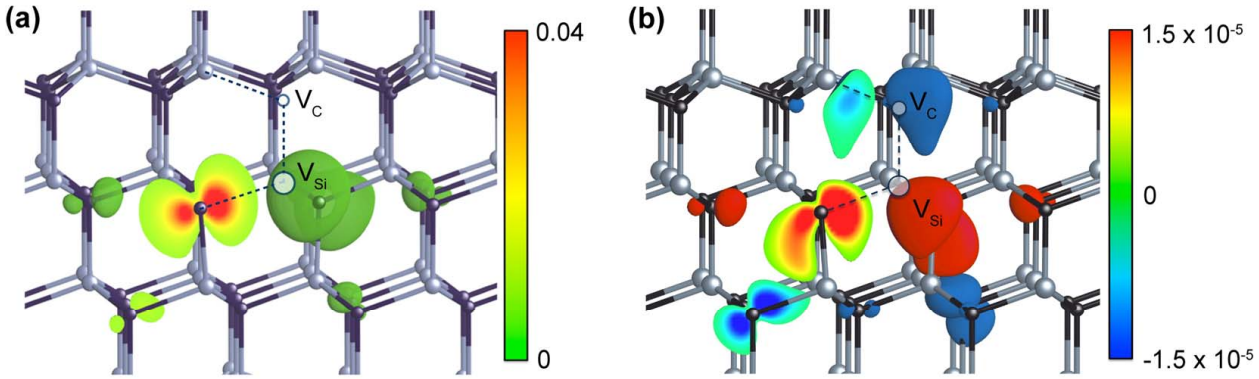

Figure A.10: The effect of an electric field on the divacancy electron orbitals. (a) The ground state spin density of the PL1 (hh) divacancy and (b) the change of the spin density due to a c-axis oriented electric field of 0.1V/A. In the absence of an electric field, the spin density is tightly confined to the Si-vacancy. The distortion of sp^3 dangling bonds is clearly visible under the applied electric field, which strongly influences the D parameter.

APPENDIX B

ELECTRICALLY DRIVEN SPIN RESONANCE - DETAILS

B.1 ODMR and EODMR with $S = 1$ and $S = 3/2$ systems

With ODMR alone, it can be difficult to differentiate between a spin-1 and a spin-3/2 system. With E-ODMR this ambiguity is easily resolved because a $\Delta m_s = \pm 2$ resonance at the difference of the two visible ODMR resonances exists for spin-1 systems but not spin-3/2 systems. This can be understood as follows [149]:

Spin-1 For a spin-1 system, the 3 spin states are split by a longitudinal magnetic field according to the Zeeman effect:

$$E_{\pm 1} = hD \pm g\mu_B B_{||} \tag{B.1}$$

$$E_0 = 0 \tag{B.2}$$

where E_i is the energy of the $m_s = i$ state. The two $\Delta m_s = \pm 1$ magnetic-dipole resonances are both visible in ODMR spectra due to differences in I_{PL} between the $m_s = \pm 1$ and $m_s = 0$ states, which arise from spin-dependent optical cycling rates. These resonances appear at the energies:

$$E_{\pm 1} - E_0 = hD \pm g\mu_B B_{||} \tag{B.3}$$

The $\Delta m_s = \pm 2$ magnetic-dipole forbidden resonance has a transition energy:

$$E_{\pm 1} - E_{-1} = 2g\mu_B B_{||} \tag{B.4}$$

which is equal to the energy-difference of the two ODMR resonances.

Spin-3/2 For a spin-3/2 system, the 4 spin states are also split by a longitudinal field

according to the Zeeman effect:

$$E_{\pm 3/2} = 2Dh \pm 3/2 g\mu_B B_{||} \tag{B.5}$$

$$E_{\pm 1/2} = \pm 1/2 g\mu_B B_{||} \tag{B.6}$$

The three $\Delta m_s = \pm 1$ magnetic-dipole resonances are:

$$E_{\pm 3/2} - E_{\pm 1/2} = 2Dh \pm g\mu_B B_{||} \tag{B.7}$$

$$E_{+1/2} - E_{-1/2} = g\mu_B B_{||} \tag{B.8}$$

However, only the first two of these three transformations generate ΔI_{PL} contrast for ODMR. The final transition (Eq. B.8) does not generate any photoluminescence contrast because the $m_s = +1/2$ and $m_s = -1/2$ states are Kramers doublets and have the same optical cycling rates. The two $\Delta m_s = \pm 2$ magnetic dipole-forbidden transitions are then:

$$E_{\pm 3/2} - E_{\mp 1/2} = 2Dh \pm 2g\mu_B B_{||} \tag{B.9}$$

This discussion leads to two important points. First, the two spin transitions that generate ODMR contrast have the same form for spin-1 and spin-3/2 systems (Eq. B.3 and Eq. B.7 are the same), which is why it is difficult to distinguish between them via ODMR alone. Second the $m_s = \pm 2$ transition falls at the difference of the two ODMR peaks ($2g\mu_B B_{||}$) for spin-1 systems (Eq. B.4) but not for spin-3/2 systems (Eq. B.9). Therefore, the combination of ODMR and E-ODMR can be used to differentiate between spin-3/2 and spin-1 systems. The same arguments can be extended to differentiate between spin-integer and spin-half-integer systems.

In our experiment we saw an E-ODMR resonance at the difference of the two ODMR resonances. This allows us to conclude that QL1 is spin-integer. Since QL1 is likely to be a

neutral divacancy in the 6H polytype, our analysis proceeds with the assumption that the optically addressable spin is a spin triplet, as in the divacancy in the 4H polytype. Although our measurements here do not conclusively establish that the optically addressable spin is the orbital ground state of QL1, electrical paramagnetic resonance (EPR) measurements in the dark [85] have established that the neutral divacancies in 4H-SiC have spin-triplet ground states, and so by analogy we expect that we are observing the QL1 ground state spin as well. The diverging T_1 time of QL1 as the temperature is lowered to cryogenic temperatures (measured up to tens of ms at 20 K [88] supports the likelihood of the optically detected spin state being a ground state.

B.2 QL1 Defect Production

Our substrate was a 373 μm thick semi-insulating (compensation-doped with Vanadium) 6H-SiC wafer from II-VI Inc. (wafer number CD1049-04-EV). To generate QL1 defects we followed the following implantation and annealing procedure: carbon ions were implanted (by Cutting Edge Ions) at room temperature at a 7 degree tilt with 190 keV energy and at an implantation dose of 1×10^{13} cm^{-2}. Stopping range of ions in matter simulations [194] indicate that the resulting vacancy distribution extends approximately 400 nm below the surface of the sample. Annealing the samples in an argon atmosphere at 900 C for 30 minutes allows the vacancies to migrate and form vacancy complexes including QL1. These parameters lead to a QL1 density of 9×10^{15} cm^{-3} [88]. To determine the number of interrogated spins, we assume an excitation cylinder of radius 1.5 μm (our approximate spot size) and length 400 nm. Putting these numbers together we find that we interrogate approximately 10^4 spins in our experiments.

B.3 EODMR Device and Apparatus Details

Our optical excitation source was a ThorLabs 975 nm (1.27 eV) diode laser. Laser light was focused to a 1.5 μm diameter spot on the sample by a home-built confocal microscope with a 50$\times$ IR-optimized objective (Olympus model LCPLN50XIR) and was gated on and off with a Gooch and Housego acousto-optic-modulator (model R21200-1DS). Photoluminescence was separated from the excitation path using a dichroic mirror, spectrally isolated and a 980 nm longpass filter, and measured with a Newport InGaAs 2011-FS photodiode.

Our electrode device was fabricated on the SiC substrate in the UCSB Nanofabrication facility using standard photolithography and electron-beam deposition techniques and the processed chip was attached to a copper coldfinger with rubber cement. Two microwave (MW) lines on the cold-finger were wired to two 50 Ohm coplanar striplines. One stripline was short terminated and used for magnetic driving. The other stripline was wirebonded to one electrode pad, while the other pad was grounded, for electrical driving. The coldfinger was housed in a helium flow cryostat with optical access and two RF ports.

MW signals for the electrodes and stripline were synthesized with an Agilent E8257C and Rhode and Schwarz SM300 vector source, respectively. MW signals were amplified with Amplifier Research 25S1G4A (0.8 - 4.2 GHz, 25W) or 30W1000B (1 - 1000 MHz, 30 W) linear amplifiers. DC voltages (for the DC data presented later in this Appendix) were amplified with a Tegam 2340 amplifier and applied with an inline 10 MOhm resistor. The photodiode signal was processed with a Perkin Elmer 7265 lockin amplifier. Experimental timing was controlled with MW switches (MiniCircuits ZASWA-2-50DR+) with digital pulses from a Tektronix AWG520 arbitrary waveform generator.

The power going into the cryostat was measured with a calibrated Herotek Schottky diode (DZM185AB) at the -20 dB output port of a directional coupler (Narda 4216-20). The power at the electrodes was then determined by subtracting losses due to the cryostat and cold-finger wiring, which were measured with a network analyzer (the losses ranged from 0 - 3 dB across 0 - 2 GHz).

To measure pulsed-ODMR, we initialized spins with a 10 μs laser pulse (70 mW at the sample), drove a full π-pulse from $|-1\rangle$ to $|+1\rangle$ on the stripline, and then read out the magnetization with another 10 μs laser pulse. This read-out pulse also serves as the initialization pulse for the following experimental cycle. In contrast to continuous-wave (CW) ODMR, where the laser and MWs are always on, pulsed ODMR allows us to sample spins at the point in the Rabi cycle that generates maximal ODMR contrast. When pulsed ODMR could not be obtained, such as when spins were rotated too inefficiently to observe a full π-pulse (Fig. B.2) or when there was no visible resonance (upper frame of Fig. 6.2 at the $\Delta m_s = \pm 2$ resonance), we used CW ODMR.

In all E-ODMR measurements, magnetic π-pulses lasted 100ns. In analogy to pulsed ODMR, to obtain maximum spectral contrast, P_E was fixed in length to induce a full π-pulse from $|-1\rangle$ to $|+1\rangle$. For time-domain data, P_E was stepped from 0 μs to 5.5 μs in 100 ns steps.

B.4 Additional Frequency- and Time-Domain Data

Additional frequency- and time-domain data were taken at $B_{\|}$=94 G and $B_{\|}$=208 G and are presented in Fig. B.1. We see qualitatively the same results that are presented in the main manuscript.

B.5 Calibrating the Magnetic Field Strength

For the frequency-domain control measurement, we drove the stripline with 100$\times$ more power than the electrodes in the E-ODMR measurement. We confirmed that at these powers the stripline produces a stronger transverse magnetic field than the electrodes by driving the $|0\rangle \leftrightarrow |-1\rangle$ ODMR resonance with both driving elements (Fig. B.2). To account for the frequency dependence of MW signal transmission through our apparatus, for this measurement we brought the $|0\rangle \leftrightarrow |-1\rangle$ ODMR resonance to the frequency at which the

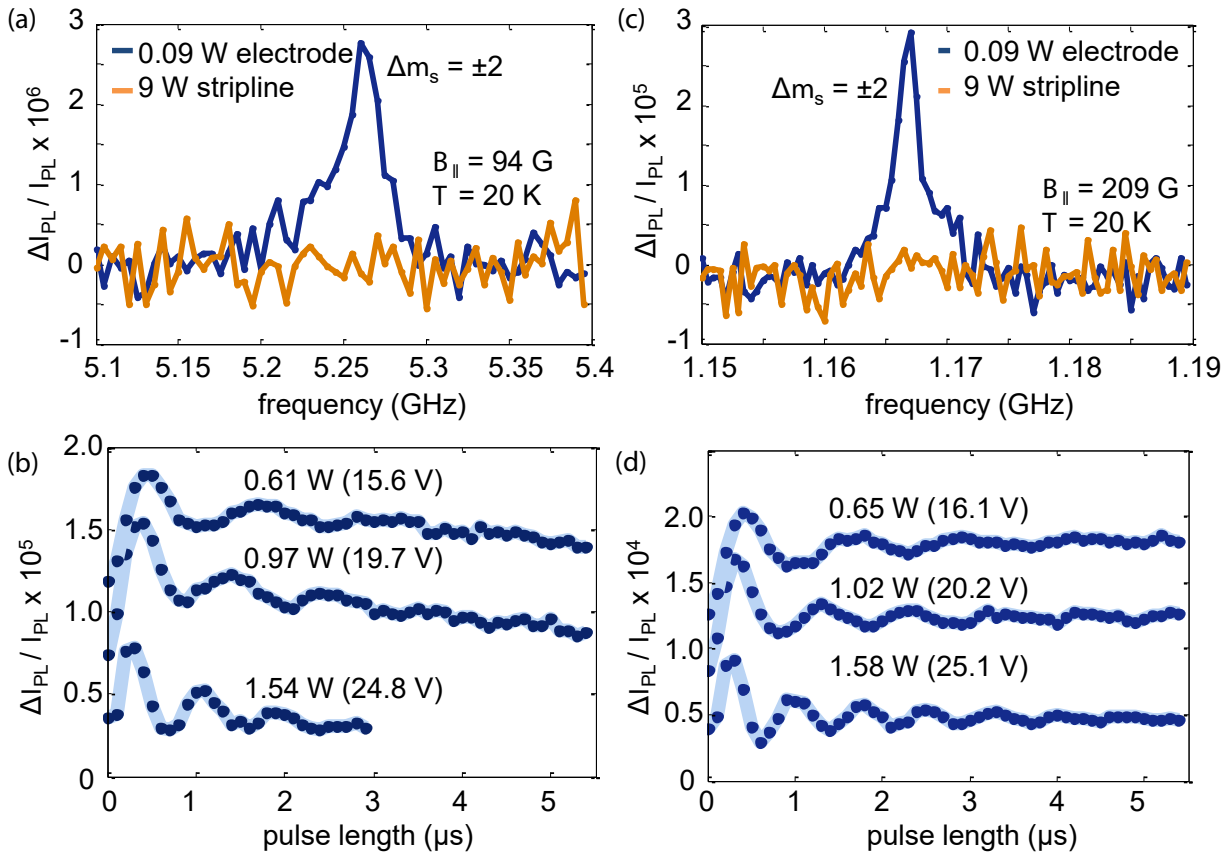

Figure B.1: (a) Frequency-domain E-ODMR and control measurement at $B_{\|}$=94 G. 0.09 W corresponds to an approximate voltage of 6 V. (b) Corresponding time-domain data taken at three powers. Traces are offset for clarity. The lowest trace was cut short at 3 μs due to heating. (c) Frequency-domain E-ODMR and control measurement at $B_{\|}$=298 G. (d) Corresponding time-domain data taken at three powers. The approximate voltages are indicated in parentheses. Traces are offset for clarity. T=20 K for all measurements.

$|-1\rangle \leftrightarrow |+1\rangle$ E-ODMR resonance had been driven.

B.6 Interdigitated Capacitor Capacitance

We determine the capacitance of our electrode device by using [Ref. S3]:

$$C = (\epsilon_o(\epsilon_r+1)K(\sqrt{(1-\frac{a^2}{b})}K(\frac{a}{b})^{-1} + 2\epsilon_o\frac{t}{a})(N-1)L \tag{B.10}$$

where ϵ_o is the electric permittivity of free space, $\epsilon_r = 9.66$ is the relative perimitivitty

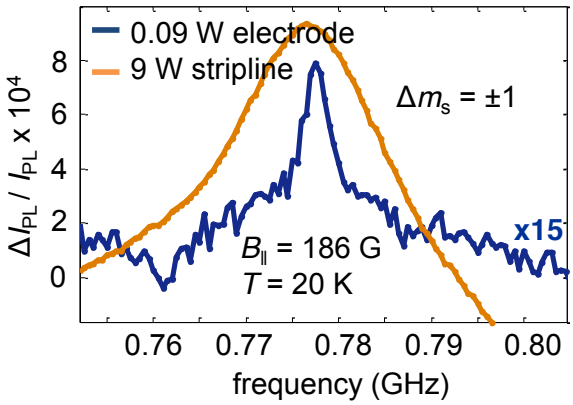

Figure B.2: ODMR when driven on the electrodes (blue curve, magnified by 15x) and the stripline (orange curve). The $|0\rangle \leftrightarrow |-1\rangle$ resonance is significantly stronger and broader when driven on the stripline at 9 W than the electrodes at 0.09 W. This confirms that in the frequency-domain control, the transverse magnetic field was significantly stronger than in the E-ODMR measurement. 0.09 W corresponds to an approximate voltage of 6 V.

of 6H-SiC, a=4 μm is the approximate interdigit spacing and the electrode width, t=250 nm is the thickness of the electrode, N=6 is the number of digits on each electrode, L=46 μm is the length of each electrode finger, b=16 μm is the interdigit spacing on each electrode, and K is the complete elliptical integral of the first kind. Using these parameters, we find that C=41 fF.

The electrode impedance for the carrier frequency presented in the manuscript (0.779 GHz), and the two presented in Section B.4 (0.526 GHz and 1.167 GHz), calculated as $(\omega C)^{-1}$, are 5.0 kΩ, 7.5 kΩ, and 3.4 kΩ, respectively. The high impedance of the electrodes and the low impedance of the line (R) leads to a displacement current that scales linearly with carrier frequency ($\omega/2\pi$):

$$|I| = \frac{CV}{\sqrt{(RC)^2 + (\omega)^{-2}}} \approx \omega CV \tag{B.11}$$

Based on this relation we would expect a magnetic-field-driven effect to depend on ω. The fact that the Rabi-frequency scales independently of ω (Fig. 6.3(c)) supports our conclusion that the observed Rabi oscillations were driven by electric, and not magnetic, fields.

B.7 Further Discussion of Coherent Spin Coupling to an AC Electric Field

By extrapolating the frequencies from all of the Rabi-driving data and fitting them, we find that the Rabi frequency scales with square root of driving power as 0.97 MHz $W^{-1/2}$. To determine what coupling parameter ($d_\perp/h$) this corresponds to, we solve the Schrodinger equation in the time-domain using the Hamiltonian in Eq. 4.1. To simulate our experiments, we set a finite $B_\parallel$ and $E_x = E_\perp cos(2\pi f_{\Delta m_s=\pm 2} t)$, where $f_{\Delta m_s=\pm 2}$ is the $\Delta m_s = \pm 2$ resonance frequency. We find that the electrical Rabi frequency (f_E) is related to the driving power (P_e) according to the relation:

$$f_E = (d_{perp} V)/(\eta h) = d_\perp/(\eta h) 2\sqrt{P_e Z_o} \tag{B.12}$$

where Z_o= 50 Ohms and we have assumed that $E_\perp = V_{DC}/\eta$, where η is the separation distance between the electrodes. We have taken into account the rotating wave approximation and assumed ideal RF signal reflection at the electrodes (see calculation of capacitance in Section B.6). Combining this expression with our data, we extrapolate the coupling strength: $d_\perp/\eta h$ = 68.6 kHz V^{-1}. Using $\eta = 3.8\mu m$, we estimate that $d_\perp/h$ = 26Hz cm V^{-1}.

In the future it will be important to apply our result to single spins without significant heating. If 20-nm electrodes are fabricated around a single QL1 center, the $d_\perp/h$ that we measured will correspond to roughly 10 MHz/V. Thus, in this geometry, a 100 ns AC pulse with amplitude 0.5 V will drive a π pulse. Even if driven by a 50 Ω waveguide, and if all of the driving power is dissipated on the chip, this voltage will only correspond to sub-nanojoule heating per π pulse. Moreover, SiC is a low loss microwave substrate, leading to low microwave absorption on chip, as well as an excellent thermal conductor. Therefore, we do not foresee that heating will be a significant issue when scaling down the techniques introduced here.

Due to uncertainty in the exact depth distribution of QL1 spins, all $d_\perp/h$ coefficients should be taken only as estimates. We also note that as calculated from the DC data (Section B.9), this parameter is approximately 3× smaller than the value obtained when it is calculated from the AC data. One possible explanation for this discrepancy is that photoionized charges are more effective at screening electric fields at the long time scales of our DC measurements (V_{DC} was applied on the order of an hour per ODMR trace). This would lead DC calculations to arrive at seemingly smaller $d_\perp/h$ values.

B.8 Calculation of the AC Electric Field Spatial Profile

For the spatially resolved E-ODMR measurements, the frequency of the AC electric field pulse (P) was fixed to the 778 MHz $\Delta m_s = \pm 2$ resonance, its power was 1.04 W, and its length (t) was 300 ns. With these parameters, a π-pulse is driven between electrode digits, where the electric field is strongest, generating the maximum $\Delta I_{PL}/I_{PL}$. Away from the electrodes, the electric field strength is reduced, generating slower spin rotations and thus lower $\Delta I_{PL}/I_{PL}$. In order to establish a calibration curve for converting $\Delta I_{PL}/I_{PL}$ to $E_\perp$ field values, we used the t = 300 ns points of the normalized Rabi curves in Fig. B.1b and d and Fig. 6.3c. We fit these data to an error-function-decaying curve representing inhomogeneous Rabi driving [66] (shown in Fig. B.3(a)), using the $d_\perp/h$ = 26 Hz cm V^{-1} coupling constant that was found earlier. In order to more easily invert this curve, we approximated it locally with a simple sinusoid. We note that $\Delta I_{PL}/I_{PL}$ has been normalized such that $\Delta I_{PL}/I_{PL} = 0(1)$ if $m_s = -1(+1)$ after P, in the E-ODMR sequence.

To investigate the accuracy of this map, we use COMSOL Multiphysics software to simulate the electric fields surrounding our electrode device. We simulated DC electric fields, since all device features are several orders of magnitude smaller than the wavelength of the applied MW signal in our experiment. In this simulation, we apply a 14.4 V DC bias (the open circuit voltage of a 0.52 W AC signal in a 50 Ω system) to one electrode and we ground the other. The resulting spatial map (Fig. B.3(a)) is in excellent quantitative

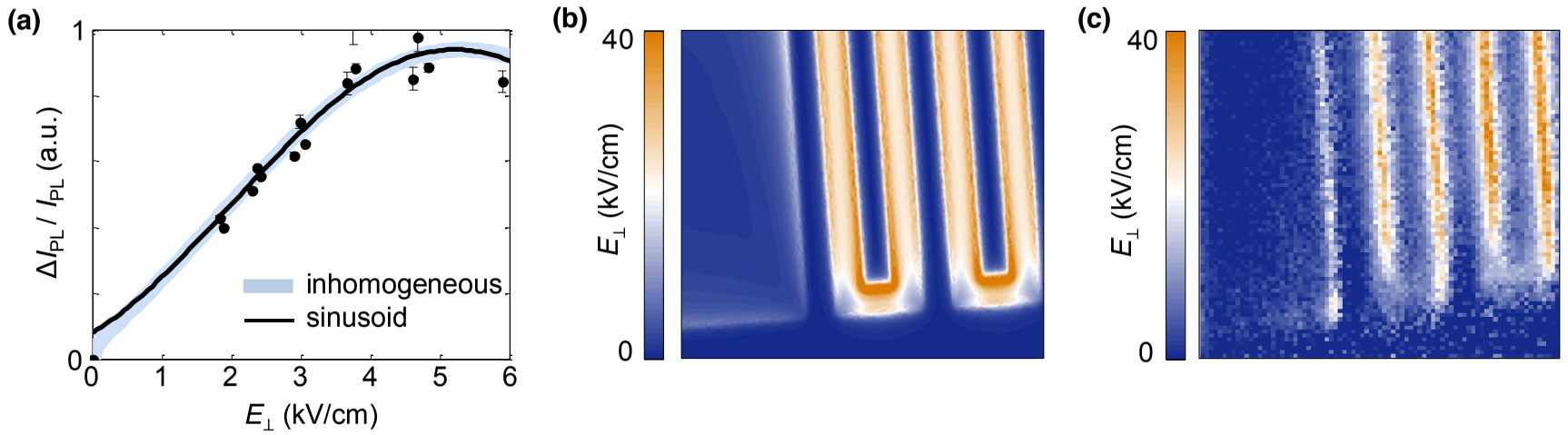

Figure B.3: (a) Calibration curve for converting $\Delta I_{PL}/I_{PL}$ to $E_\perp$, using an electrode pulse (P) of length 300 ns. The error-function inhomogeneous driving curve fits well to the data, as does our sinusoid approximation to this curve. (b) $E_\perp$ simulated using our experimental parameters and finite-element modeling. The calculated map is in good agreement with our experimental findings, presented in (c), and copied from Fig. 4.4d.

agreement with our findings.

B.9 ODMR Response to a DC Electric Field

To demonstrate DC coupling of the electric field to the QL1 spin ensemble, we measured ODMR between the third and fourth electrode digits as a function of bias voltage across them (V_{DC}). By varying V_{DC} within ± 100 V, we observe shifts of the ODMR transitions by several MHz (Fig. B.4a).

To analyze these data, we diagonalize the Hamiltonian in Eq. 6.1 subject to longitudinal magnetic ($B_{\parallel}$) and transverse electric ($E_{\perp}$) and effective strain fields ($\epsilon_{\perp}$), which enter into the Hamiltonian in the same way that electric fields do [153]. We ignore the effects of a static transverse magnetic field, which does not have a first-order contribution. We find that the splitting of the ODMR transitions (ΔE) should follow:

$$\Delta E = 2\sqrt{(d_{\perp}^2 (E_{\perp} + \epsilon_{\perp})^2 + (g\mu_B B_{||})^2} \tag{B.13}$$

To account for the ≈ 2 MHz spin splitting at $V_{DC} = 0$, we explore two limits below.

Scenario A: no transverse strain Here we assume that $\epsilon_{\perp} = 0$ and that the spin splitting at $V_{DC} = 0$ is due to a small stray longitudinal magnetic field. Because the dispersion is constrained to be even with respect to V_{DC} in this scenario, a good fit requires separate hyperbola for the positive and negative V_{DC} data (Fig. B.4b). Assuming that $E_{\perp}$ is constant over the measurement volume and the spins are near the chip surface, we write $E_{\perp} = V_{DC}/\eta$, where η is the separation distance between the electrodes. The resulting fit parameters are $B_{||} = 0.35$ G and $d_{\perp}^{+}/\eta h = 12.6$ kHz V^{-1} and $d_{\perp}^{-}/\eta h = 21.4$ kHz V^{-1}, for positive and negative V_{DC}, respectively. Using $\eta = 3.8\mu m$, we estimate that $d_{\perp}^{+}/h = 5$ Hz cm V^{-1} and $d_{\perp}^{-}/h = 8$ Hz cm V^{-1}.

To justify our fit to two separate hyperbola, we refer to an earlier work [210] where similar phenomena have been observed in DC Stark measurements of optical transitions of

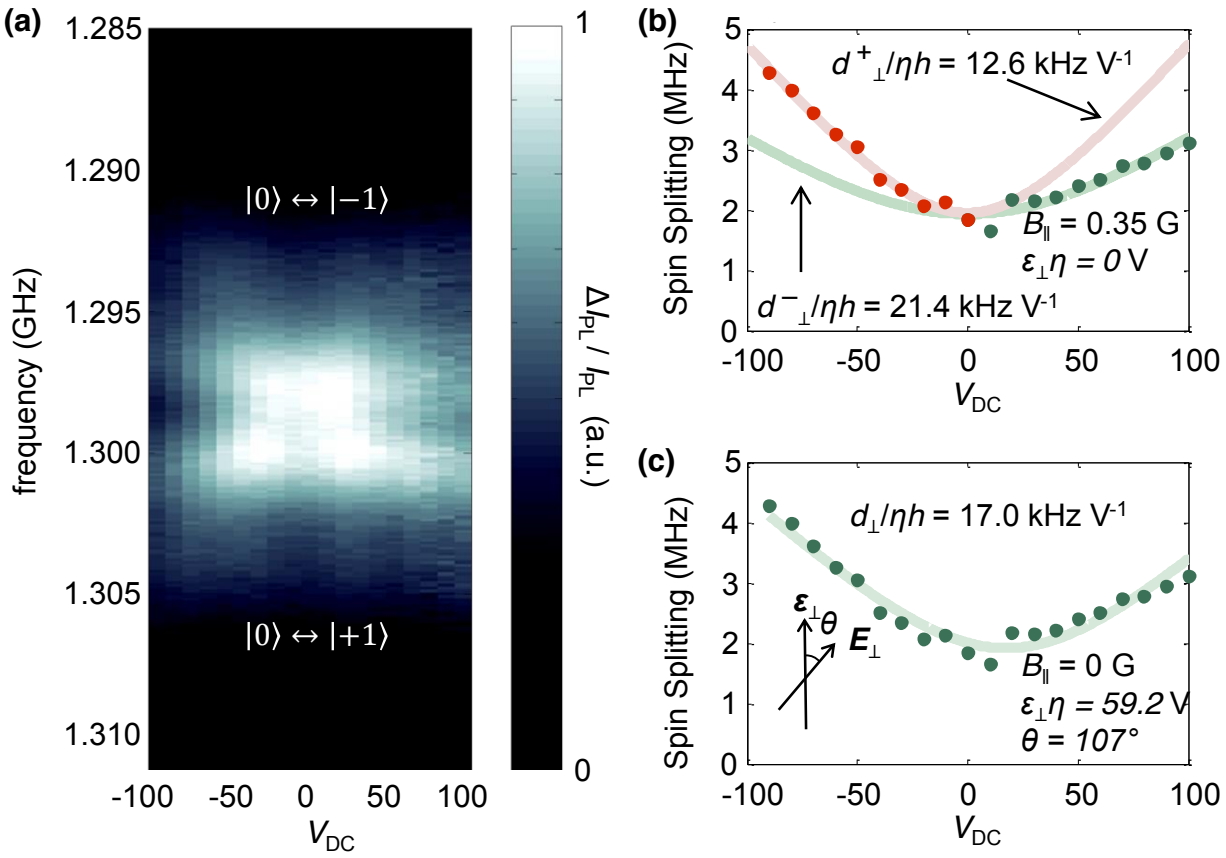

Figure B.4: (a) ODMR measured between the third and fourth electrode digits in a 1.5 μm spot as a function of V_{DC}. (b) Fitting of the spin splitting in the scenario where $\epsilon_\perp = 0$. The coupling parameters extrapolated for the negative and positive V_{DC} data are $d^-_\perp/\eta h = 21.4 kHz V^{-1}$ and $d^+_\perp/\eta h = 12.6 kHz V^{-1}$, respectively. (c) Fitting the spin splitting in the scenario where $B_\parallel$=0. The coupling parameter is found to be $d^-_\perp/\eta h = 17 kHz V^{-1}$.

the nitrogen-vacancy center in diamond. The asymmetry in optical transition energies, with respect to V_{DC}, was attributed to an electric field asymmetry due to the effects of the metal-semiconductor Schottky barriers and photoionized charges. We believe a similar effect could be at play here.

Scenario B: no stray longitudinal magnetic field In this scenario we assume that $B_\parallel = 0$ and that the non-zero spin splitting at $V_{DC} = 0$ is due to a transverse strain. This introduces a new parameter, the angle θ between $E_\perp$ and $\epsilon_\perp$. In this scenario the data are fit well to a single hyperbola (Fig. B.4c), with fit parameters converging to $\epsilon_\perp/\eta = 59.2$ V, $\theta = 107^o$ and $d_\perp/\eta h = 17.0$ kHz V^{-1}. Using $\eta = 3.8$ μm, $d_\perp/h = 6.5$ Hz cm V^{-1}.

APPENDIX C

DYNAMIC POLARIZATION OF NUCLEAR SPINS - DETAILS

C.1 Sample Preparation and Experimental Techniques

Our 4H-SiC samples are from a high-purity semi-insulating wafer purchased from CREE, Inc (wafer number: W4TRD0R-0200). Since they contain "off-the-shelf" neutral divacancies and PL6 defects, we dice them into chips and measure them without any further sample preparation. We purchase 6H-SiC wafers from II-VI, Inc. In order to incorporate neutral divacancies into the 6H-SiC samples, we first have them implanted with ^{12}C ions at an energy of 200 keV with doses ranging from 10^{11} - 10^{13} cm^{-2} (Cutting Edge Ions, Inc.), which generates vacancies. Using stopping range of ions in matter simulations [194], we estimate that the vacancies from the ^{12}C ions are localized to the top 500 nm of our SiC chips. We then anneal the samples at 950 ^{o}C for 30 minutes in order for the vacancies to migrate and form vacancy complexes, including divacancies.

For ODMR measurements, we use a 300 mW, 1.27 eV (975 nm) diode laser, purchased from Thorlabs, Inc. 60 mW reaches the sample. For measurements that required the laser to be gated (which are in this Appendix only), we use an acousto-optical modulator. We focus the laser excitation onto the sample using a near-infrared coated 50$\times$ Olympus objective and collect the photoluminescence (PL) using that same objective. We then focus the collected PL onto an InGaAs photoreceiver, which was purchased from FEMTO. The SiC samples are mounted to coplanar microwave striplines with rubber cement. The microwave stripline is soldered to a copper cold finger, which is cooled by a Janis flow cryostat.

We use lock-in techniques to take all of the data for this experiment. For continuous-wave ODMR measurements, we leave the excitation laser on while gating a microwave (MW) signal on and off at rates ranging from 1-5 kHz. The change in PL (ΔPL) as this experiment is conducted is the ODMR signal. We plot the ODMR signal as the normalized ratio ΔPL/PL. Due to background PL (i.e. all PL unrelated to the defect of interest), ΔPL/PL is much

lower than the intrinsic ODMR contrast of the defects studied (i.e. the ΔPL/PL when there is no background PL). Using single-spin measurements, we have found the intrinsic ΔPL/PL of neutral divacancies to be roughly 15% [104] at 20 K. We have also used spectrally resolved ensemble measurements to estimate that the intrinsic ΔPL/PL of PL6 defects is 35% [96].

When sweeping the frequency (f) of our MWs, we observe oscillations in the MW power reaching the sample, which likely result from cable reflections. We stabilize the MW power by measuring it with a Schottky diode and then feeding the measurement back to the signal generator. Due to dispersion in the diode, there are still power fluctuations (in particular, higher powers at lower frequencies), though they are significantly reduced.

Our experiments use both "low" MW powers (Fig. 7.2 and Fig. 7.7c-d) and "high" MW powers (Fig. 7.3 and Fig. 7.4a). Low MW power is used to mitigate power broadening of the ODMR lines, which can obscure their hyperfine structure. For these measurements, 2 mW of power are sent into the cryostat, which corresponds to an on-resonance Rabi frequency of 500 kHz. The high power MW measurements are used to observe ES ODMR. High powers are necessary since a spin rotation must happen within the ES lifetime ($\sim$14 ns). For these measurements, 1 W of power is sent into the cryostat, which corresponds to an on-resonance Rabi frequency of 10 MHz.

C.2 Concentration of Optically Polarized Nuclei

Using double electron-electron resonance, we have previously measured that our 6H-SiC samples have a 10^{16} cm^{-3} density per c-axis-divacancy species (generated by implanting with a 10^{13} cm^{-2} dose of ^{12}C ions [88]). With 3 total species of c-axis-oriented divacancies in 6H-SiC, a 3-fold (6-fold) degeneracy of the Si$_{IIa}$ (Si$_{IIb}$) sites, and a 4.7% natural abundance of ^{29}Si, we estimate that dynamic nuclear polarization (DNP) drives a ^{29}Si polarization density of 10^{16} cm^{-3}. Due to the diffusion of nuclear polarization, this density should be taken as a lower bound.

We estimate the density of divacancies and PL6 defects in our 4H-SiC sample by compar-

ing the intensity of their zero-phonon-lines (ZPL) to the ZPLs of defects in 6H-SiC. These measurements were acquired with identical optics and experimental conditions. We find that the integrated intensity of each c-axis-oriented divacancie's ZPL in 4H-SiC is roughly 1/4 as intense as that in the 6H-SiC sample bombarded with the 10^{13} cm^{-2} dose of C ions. Since the divacancies in 6H-SiC are localized to the top 500 nm of the chip, whereas the as-grown neutral divacancies in 4H-SiC are distributed throughout the full 500 μm chip, we estimate that each neutral divacancy form in our 4H-SiC samples has a density of 3×10^{12} cm^{-3}.

Although we believe that PL6 defects live close to the SiC surface, we do not want to make assumptions about their depth distribution. Therefore, instead of calculating their volume density, we calculate their areal density. Since the integrated ZPL of PL6 is 25$\times$ less intense than that of the 6H-SiC divacancies, which have an areal density of 5×10^{11} cm^{-2}, we estimate the areal density of PL6 is 2×10^{10} cm^{-2}.

C.3 ESEEM Measurement of the Hyperfine Spectrum

Although hyperfine spectra can be measured through ODMR, the precision of such measurements is limited by the inhomogeneously broadened spin transition linewidths ($\sim 1/T_2^*$). Since T_2^* ranges from 1-3 MHz in our samples, which is similar in magnitude to the differences in hyperfine coupling strengths, ODMR measurements are not ideal. To obtain a higher resolution measurement, we instead use electron-spin echo envelope modulation (ESEEM). The resolution of hyperfine spectra extracted via ESEEM is not bound by T_2^*, but rather the much longer homogeneous coherence time T_2 (assuming that nuclear spin relaxation times are even longer than that). We measure ESEEM by finely resolving the first several microseconds of a Hahn-echo coherence curve $C(t_{\text{free}})$. The fast oscillations seen in such data are exactly the hyperfine coupling strengths, as will be elucidated below.

ESEEM curves can be fit to the product of modulation functions $E_j(t_{\text{free}})$ times an overall decoherence envelope $D(t_{\text{free}})$.

$$C(t_{\text{free}}) = D(t_{\text{free}}) \prod_j E_j(t_{\text{free}}), \tag{C.1}$$

where each $E_j(t_{\text{free}})$ is given by:

$$E_j(t_{\text{free}}) = 1 - 2K_{\pm 1} sin^2(\pi \nu_0 t_{\text{free}}) sin^2(\pi \nu_{\pm 1} t_{\text{free}}). \tag{C.2}$$

Here the $\nu_{0,\pm 1}$ correspond to the nuclear spin splittings in the electronic $m_s = 0$ and $m_s = \pm 1$ branches respectively, and $K_{\pm 1}$ are the modulation depth parameters, which characterize the amplitude of the ESEEM oscillations [124]. The ν_0-frequency oscillation is a relatively slow oscillation at the frequency corresponding to the nuclear Zeeman interaction. The $\nu_{\pm 1}$ oscillations correspond to the sum of the nuclear Zeeman interaction and the hyperfine interaction. Since this measurement is performed at $B = 40$ G, the nuclear Zeeman effect (~ 40 kHz) is negligible in comparison to the hyperfine coupling strength for the $^{29}\text{Si}_{IIa}$ and $^{29}\text{Si}_{IIb}$ nuclei, and thus we neglect it. Thus, according to Eq. C.2, the A_{zz} projections of the hyperfine tensors of the different nuclei in our sample can be extracted by taking the fast Fourier transform (FFT) of $C(t_{\text{free}})$ (Fig. C.1.) and then taking half of the frequency of the resulting peaks.

C.4 Sign of Nuclear Spin Polarization

To establish that DNP populates the $\uparrow$ state of $^{29}\text{Si}_{IIa}$ and $^{29}\text{Si}_{IIb}$ nuclei for the divacancies and PL6, we combine several observations with Eq. 7.1. These observations are that defects initialize into $m_s = 0$ [54,86], their $A_{zz,GS}$ and D_{GS} parameters are positive [86,86,96] [54], and the higher energy hyperfine transition is populated (when driving to $m_s = +1$, as seen from ODMR). Similar arguments can be made to determine that the sign of D_{ES} is also positive [100].

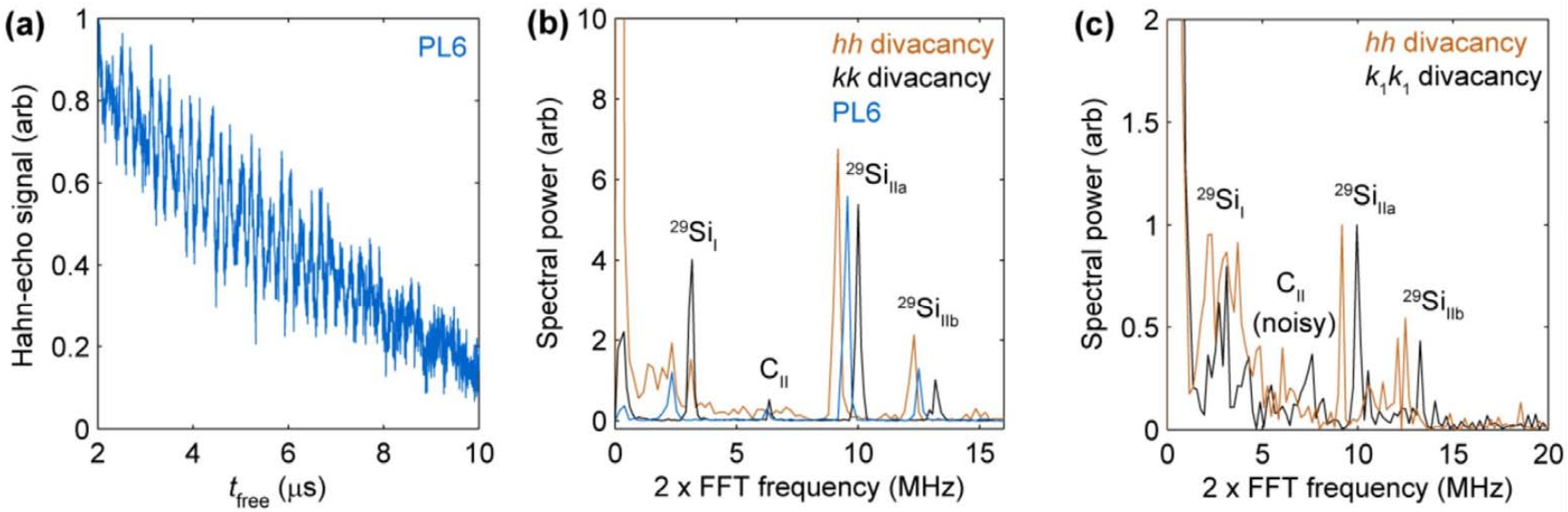

Figure C.1: (a) Hahn-echo coherence of PL6 defects at room temperature as a function of t_{free}, at an external field of $B = 40$ G. The fast oscillations are ESEEM and their frequencies correspond to hyperfine interaction strengths. The apparent decay in coherence is due to the Larmor precession of weakly coupled ^{29}Si nuclear spins. The coherence will refocus at later times. (b). The FFT of the ESEEM oscillations of the 4H-SiC divacancies and PL6 at T = 20 K shows 4 distinct hyperfine strengths, each of which corresponds to a distinct nuclear spin lattice site. The hyperfine peaks are labeled according to the convention used in Ref. [86]. Note that the C_{II} peak at 6.3 MHz was not seen in that study. (c) The FFT of ESEEM oscillations of the hh and k_1k_1 neutral divacancies in 6H-SiC. We do not plot the data from the k_2k_2 divacancies, because it exhibits a lot of spurious features due to interference from the hh divacancy. Nonetheless, we can (more roughly) estimate the hyperfine strengths of ^{29}Si in the Si_{IIa-b} lattice sites for this defect. The hyperfine interaction strengths extracted from these data are summarized in Table 5.1.

C.5 Determining the Nuclear Polarization from ODMR

To determine the DNP efficiency, we fit the ODMR lineshapes to a sum of 7 Lorentzians, one centered at f_0, and the other six at each of the Si_{IIa}, Si_{IIb}, and C_{II} hyperfine-split resonances. The decision to use Lorentzians, as opposed to Gaussians, was made based on the empirical observation that they fit the data best. We do note, however, that this is the theoretically expected lineshape [66].

The degree of nuclear-spin polarization (P) is determined by the relative amplitudes of the ODMR resonances. Since the hyperfine strengths of the various electron-nuclear configurations differ by only a few MHz, their inhomogeneously broadened hyperfine-split resonances overlap ($T_2^* < 1$ μs). This can make the determination of their exact amplitudes non-trivial. Moreover, the high P values near the GSLAC and ESLAC for our systems (>90%) and finite measurement noise mean that conventional least squares/maximum likelihood estimation techniques will sometimes yield estimates of P that exceed 1. To accurately infer the P values, we instead adopt a Bayesian approach that is analogous to a global nonlinear least-squares fit. In particular, the most general model for the signal y_{jk} (f_{jk}) measured in each sweep of frequency f_{jk} includes three pairs of Lorentzian lineshapes corresponding to hyperfine splittings about a central Lorentzian resonance,

$$y_{jk}(f_{jk}) = y_{0,j} + \frac{a_0 g_0^2}{g_0^2 + (f_{jk} - g_j)^2} + \sum_{i=1}^{3} \left(\frac{a_{1ij} g_i^2}{g_i^2 + (f_{jk} - \theta_i - \delta_i)^2} + \frac{a_{2ij} g_i^2}{g_i^2 + (f_{jk} - \theta_i - \delta_i)^2} \right) \quad \text{(C.3)}$$

where j indexes the sweep number, k indexes the individual data points within the sweep, $y_{0,j}$ is a small constant signal offset, θ_i are the hyperfine splittings, δ_j is a small frequency offset, the a terms are the Lorentzian amplitudes, and the g terms are the Lorentzian scale parameters. a_{1ij} and a_{2ij} are the amplitudes of the right and left hyperfine-split resonances, respectively, for the ith electron-nuclear configuration. Before fitting the ODMR data to this model, we normalize it by the maximum ODMR signal and center it about frequency at which this maximum signal was observed. Due to measurement noise, this procedure

produces a slight jitter in the central frequency and the inferred amplitude of the central peak, which we compensate for with the small δ_j parameter and a moderately strong prior: $a_0 \sim \text{Normal}(1.00, 0.05^2)$.

Practically speaking, this procedure allows for small deviations from unity for the central peak amplitude. In the model, the g_i and f_i terms are shared between sweeps to enhance the precision to which we can determine the other parameters of the model. We then relate these ideal y_{jk} to the observed data through the standard least squares likelihood up to an overall unimportant normalization,

$$log(p(y_{jk}|\theta)) = log(L(y_{jk})) = -\frac{(y_j - d_{jk})^2}{2\sigma_j^2} - \frac{1}{\sigma_j} \tag{C.4}$$

where σ_j is a free parameter for the standard deviation of our measurement noise after normalization. This figure is typically about 1% for most sweeps. We sample from the posterior distribution using a Markov Chain Monte Carlo technique [168] and use the samples to compute the polarization using the relation $P_{ij} = (a_{1ij} - a_{2ij})/(a_{1ij} + a_{2ij})$. Since the Bayesian approach bounds the amplitudes to be greater than or equal to 0, the polarization is always in the physical interval [-1, 1]. Transforming the samples from the posterior gives the marginal distribution of P_{ij}, which we use to compute the mode and the highest posterior density intervals (which are also only within the physical region, for the same reason).

The PL6 polarization data are taken at room temperature, where T_2^* in the GS is moderately shorter than it is at cryogenic temperatures. These smaller T_2^* values lead to broader ODMR lines, thereby making the calculation of P more challenging. When analyzing these data, we fix the outermost hyperfine resonances at values that we extracted from the Fourier transform of a separate ESEEM measurement. We also make the approximation that the polarizations of the Si_{IIa} and Si_{IIb} resonances are equal, which means that the corresponding amplitudes have a constant (free-parameter) ratio. The validity of this approximation is based on the fact that we found similar degrees of polarizations at the Si_{IIa} and Si_{IIb} sites

for divacancies at low temperatures (see Fig. C.2), and the similarity of the divacancies to the PL6 defects. When we did not use this approximation in our fits, we found a similar shape and maximal degree of polarization for Si_{IIb}-coupled nuclei, but the fitting noise was higher. Finally, we note that all of our fits for nuclear spin polarization use the definition

$$P = \frac{I_\uparrow - I_\downarrow}{I_\uparrow + I_\downarrow}, \tag{C.5}$$

where $I_{\downarrow(\uparrow)}$ is the intensity of the higher (lower) energy ODMR doublet. We can expand $I_{\downarrow(\uparrow)}$ as $I_{\downarrow(\uparrow)} = N_\downarrow P_{e,\downarrow(\uparrow)} C$, where $N_{\downarrow(\uparrow)}$ is the number of electron-nuclear spin pairs with a down (up)-pointing nuclear spin, $P_{e,\downarrow(\uparrow)}$ is the electronic polarization of these respective systems, and C is the photoluminescence intensity difference between a single color center in $m_s = 0$ state and a color center in the $m_s = \pm 1$ states. If $P_{e,\downarrow} = P_{e,\uparrow}$, then Eq. C.5 simplifies to $P = (N_\uparrow - N_\downarrow)/(N_\uparrow + N_\downarrow)$, the definition of nuclear spin polarization. Naturally, as a special case, if $P_{e,\downarrow} = P_{e,\uparrow} = 1$, then Eq. C.5 simplifies to this as well. However, if electron polarization is incomplete, and if $P_{e,\downarrow} \neq P_{e,\uparrow}$, then Eq. C.5 could be inaccurate. Below we discuss why this inaccuracy is unlikely to be significant.

Far from the anti-crossings, the nuclear spin is not linked to the electrons optical cycle and, therefore, $P_{e,\downarrow} = P_{e,\uparrow}$. Near the GSLAC or ESLAC, where each nuclear spin is coupled to its coupled electron's optical cycle, we argue that the relation $P_{e,\downarrow} = P_{e,\uparrow}$ is still approximately valid. The reason is that the hyperfine interaction (9-13 MHz) is weak compared to the radiative decay rate ($\sim$70 MHz [96]) and can, therefore, not have a significant impact on the electronic polarization process. We note that we have not seen this discussion in the context of ODMR measurements of polarized nuclei coupled to nitrogen-vacancy centers in diamond [103, 122, 158–160]. Since these works have defined the nuclear spin polarization in the same way, we believe that those works have implicitly relied on a similar argument, even with hyperfine couplings on the order of 100 MHz.

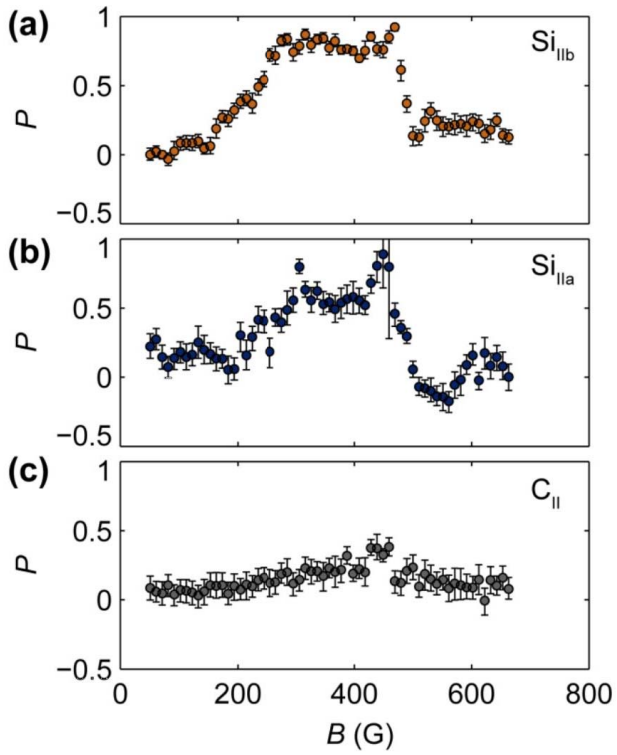

Figure C.2: The magnetic-field dependence of nuclear polarization P for nuclei at the (a) Si_{IIb}, (b) Si_{IIa}, and (c) C_{II} sites. $T = 100$ K.

C.6 Fitted Nuclear Polarization at Multiple Nuclear Sites

As our ESEEM measurements show (Fig. C.1), all of the color centers considered in these experiments have four inequivalent lattice sites for ^{29}Si or ^{13}C nuclei with hyperfine interactions between 3 and 20 MHz. These are the Si_I site (3.2 MHz), the C_{II} site (6.4 MHz), the Si_{IIa} site (12.5 - 13.3 MHz), and the Si_{IIb} site (9.2 - 10 MHz) (illustrated in Fig. 7.1a). By omitting the assumption made in the above section, that the polarizations of the Si_{IIa} and Si_{IIb} sites are equal, we can extract the polarizations of these sites individually (sans the Si_I site, which has a weak signal). The polarizations of these sites for the hh divacancy in 6H-SiC are presented in Fig. C.2.

C.7 Further Characterization of the PL6 Excited State

Here, we provide two additional measurements of the PL6 excited state (Fig. C.3a). First, in order to prove that the GS and ES spin transitions that we see in ODMR are associated with each other, we observe that the ES-ODMR line has a minimum in ΔPL precisely at the PL6 GSLAC (Fig. C.3b). The relationship between Figs. C.3a and C.3b is closely analogous to that of Fig. 7.3c and Fig. 7.3d. Second, we show that ES ODMR can only be seen when laser and MW excitations coincide (Fig. C.3c). This further supports that the resonance is associated with the ES and not some other GS resonance. GS ODMR, on the other hand, can be seen both when the laser and MW excitations coincide or when they alternate.

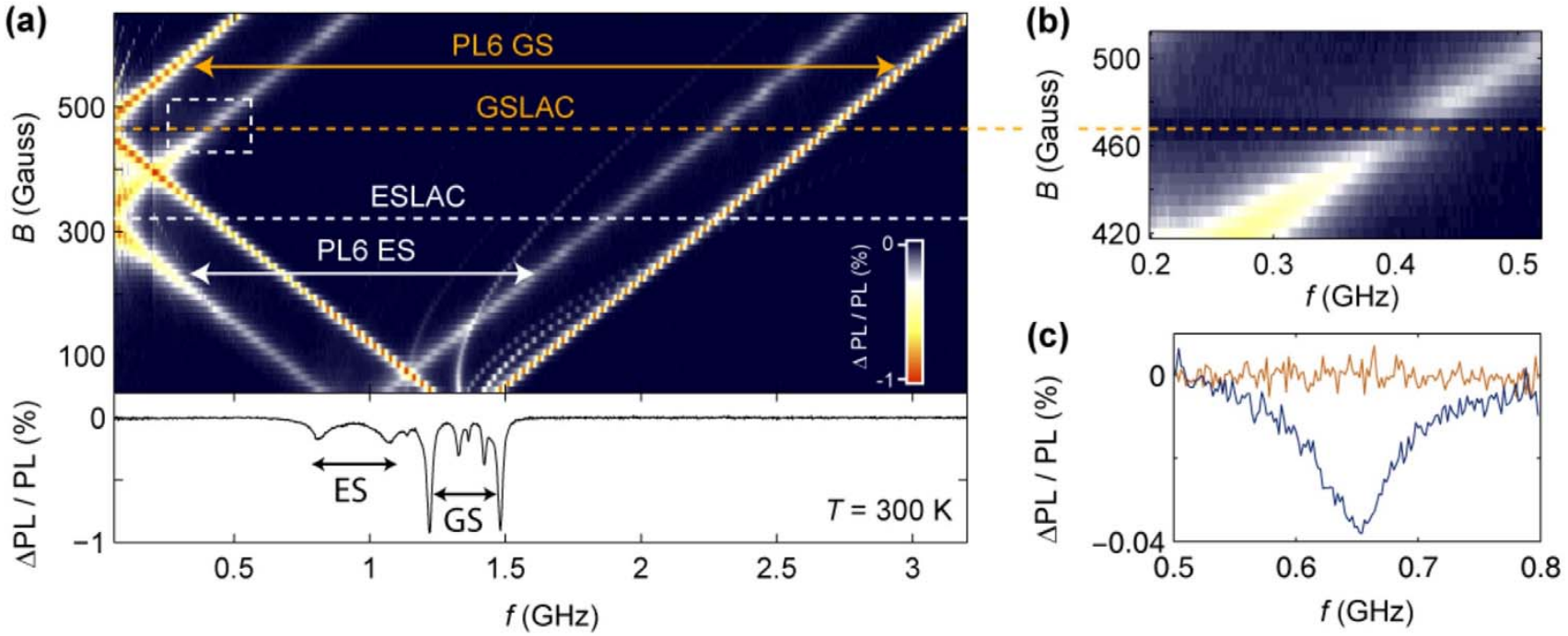

Figure C.3: (a) High-power ODMR spectrum of PL6 as a function of f and B at room temperature. Lower: Line-cut of the ODMR spectrum at $B = 50$ G. This panel is a reproduction of Fig. 7.3a. (b) AT the PL6 GSLAC, the line that we have associated with the PL6 ES ODMR signal, loses visibility. This observation supports our assignment. (c) ODMR of the PL6 excited state at B = 100 G, with both the microwave and excitation light pulsed at 1 kHz with a 50% duty cycle. When the excitation light and microwave pulses coincide, an ES ODMR signal is seen (blue curve). When the light and microwaves alternate, there is no ES ODMR (orange curve).

APPENDIX D

ENTANGLEMENT AT AMBIENT CONDITIONS IN A SPIN ENSEMBLE - DETAILS

D.1 Register Hamiltonian

The ground-state spin Hamiltonian of an R1 or R2 register is:

$$\hat{H} = \gamma_e \hat{\mathbf{S}} \cdot \mathbf{B} - \gamma_n \hat{\mathbf{I}} \cdot \mathbf{B} + \hat{\mathbf{S}} \cdot \mathbf{A}\hat{\mathbf{I}} + D_{ZFS} \S_z^2 \tag{D.1}$$

where $\mathbf{S}$ is the vector of electronic $S = 1$ spin matrices, $\mathbf{I}$ is the vector of nuclear $I = 1/2$ spin matrices, γ_n=-8.5 MHz/T is the ^{29}Si nuclear gyromagnetic ratio, γ_e is the electronic gyromagnetic ratio, D_{ZFS}=1.35 GHz is the PL6 electronic spin zero-field-splitting, $\mathbf{A}$ is the hyperfine coupling tensor, and $\mathbf{B}$ is the external magnetic field vector. The first term is the electronic Zeeman Effect, the second term is the nuclear Zeeman Effect, the third term is the electron-nuclear hyperfine interaction, and the fourth term is the electronic zero-field spin splitting.

D.2 Experimental Apparatus

Our sample is an unprocessed chip of 4H-SiC from a stock wafer purchased from Cree, Inc. (serial no W4TRD0R-0200, BJ148-10). PL6 defects are present in the as-purchased material. The chip is positioned above a 0.5 mm-wide short-terminated stripline, which is used as an antenna for microwave and radiofrequency fields. The three microwave signals used for electron spin manipulation are generated by two Stanford Research (SG396) vector signal generators and an Agilent E8257C signal generator. The radiofrequency signal used for nuclear spin manipulation is digitally synthesized by an arbitrary waveform generator (Tektronix AWG 5014c). All signals are bandpass filtered, gated with switches (MiniCircuits ZASWA-2-50DR+), multiplexed (MiniCircuits ZFSC-4-1-S+), and amplified

(AR 30W1000B) before reaching the stripline antenna. We split off a small portion of the amplified signal at a -20 dB port of a directional coupler (Narda, model 4216-20), pass it through a Schottky diode (Herotek, model DZM185AB), and then into an oscilloscope to monitor the microwave pulses. A permanent magnet (K&J Magnetics Grade N52 magnet) provides the magnetic field $B_{\|}$, which is along the PL6 quantization axis (the SiC c-axis).

Registers are off-resonantly addressed through their phonon sideband with 975 nm light from a diode laser (ThorLabs, model PL980P330J). The laser is gated with an acousto-optic-modulator (Gooch and Housego, model R21200-1DS). The excitation power is 100 mW at the back aperture of an infrared-optimized objective (Olympus, model LCPLN50XIR) and the excitation volume is approximately $\pi \times (1.5\mu m)^2 \times 6\mu m$ $40\mu m^3$, where we have used our approximate laser spot size (3 μm in diameter) and depth of field (6 μm in length). Photoluminescence is collected through the same objective, isolated from the excitation beam with a dichroic mirror, filtered with a 980 nm long-pass filter (Semrock), and measured with an infrared-optimized photo-receiver (Electro Optical Components, model OE-200-IN). Registers near the periphery of the laser spot contribute to the signal, but the signal is dominated by registers near the center. The detector signal is pre-amplified (Stanford Research Systems, model SR560) and demodulated with a lock-in amplifier (Perkin-Elmer, model 7265).

Frequency-selective, non-local, electronic gates are performed with Gaussian-shaped pulses. Inversion pulses (i.e. spin rotations by π-radians) have a full-width at half maximum that is typically 150 ns, with a corresponding bandwidth of 4.2 MHz. This bandwidth is wide enough to encompass the 1.1 MHz electron-spin transition linewidths while maintaining good frequency-selectivity. The frequency-nonselective, local, electronic gates are implemented with rectangular pulses. Inversion pulses are of 20 ns width, with an approximate 45 MHz bandwidth. Frequency-selective non-local nuclear gates are performed with rectangular pulses. Inversion pulses last 6000 ns, with an approximate bandwidth of 150 kHz, which is enough to fully encompass their 10 kHz inhomogeneously broadened nuclear spin transition linewidths. In the entangling algorithm, we apply a three-gate composite pulse to drive the

initial electronic inversion $|0,\uparrow\rangle \rightarrow |-1,\uparrow\rangle$. By choosing the phases of our gates, we can implement spin rotations about different axes. For register initialization and readout we use a 50 μs long laser pulse. This pulse length saturates the initialization process, which we measure to take 729 $\pm$ 350 ns for the electrons and $2.2^{+3.5}_{-2.2}\mu s$ for the nuclei (95 % confidence intervals given).

For the ODMR measurement presented in Fig. 6.2, we lock into the microwave pulse being on versus off. The ODMR signal, which we quote in arbitrary units, is related to the population that has been transferred from $m_S = 0$ into $m_S = -1$. For the ODNMR measurement presented in Fig. 6.3, the microwave pulse frequency is chosen to be broadband, such that it excites the $|0,\uparrow\rangle \rightarrow |-1,\uparrow\rangle$ transition of R1 and R2 simultaneously. For this measurement we lock into the radiofrequency pulse being on versus off. The ODNMR signal (Fig. 2D), which we quote in arbitrary units, is related to the population that has been transferred from $m_I =\uparrow$ into $m_I =\downarrow$. We note that a strong ODNMR signal near the R1 and R2 hyperfine splitting is observed only when the first MW pulse is applied. This observation implies that the PL6 optical cycle preferentially polarizes its electron into $m_S = 0$, where the hyperfine interaction is absent, and not into $m_S = \pm 1$. Similar arguments have previously been made to determine the state of polarization of nitrogen-vacancy color centers in diamond.

D.3 Multi-Nuclei Registers

Each R1 and R2 register contains a single PL6 electron spin strongly coupled to a single ^{29}Si nuclear spin. The lattice sites occupied by ^{29}Si atoms to form R1 and R2 registers (sites 1 and 2, respectively) have a non-zero crystal degeneracy. It is therefore possible to have larger spin registers that consist of a single PL6 electron spin strongly coupled to multiple ^{29}Si spins (e.g. R11 has two ^{29}Si atoms at the 1 lattice site, and R112, which has two ^{29}Si atoms at the 1 lattice site and one ^{29}Si atom at a 2 lattice site). These registers occur

probabilistically according to the product of binomial distributions (B):

$$B(n_1, k_1, p) \times B(n_2, k_2, p) = \binom{n_1}{k_1}\binom{n_2}{k_2} p^{k_1+k_2}(1-p)^{n_1+n_2-k_1-k_2}, \tag{D.2}$$

where the subscripts denote the two lattice sites, n_i is the crystal degeneracy of the ith lattice site (n_1=3 and n_2=6, which are determined by the relative ODMR amplitudes) and k is the number of those degenerate sites that are occupied by a ^{29}Si atom, which occur in our samples naturally with probability p=4.7%. The crystal degeneracies of R1 and R2 are $n_1 = 3$ and $n_2 = 6$. These assignments were made in a previous work [100] by comparing the intensities of the registers' hyperfine-split ODMR resonances to the intensity of the non-hyperfine split ODMR resonance. This assignment is supported by drawing correspondence to similar registers based on SiC divacancies [86,100,102]. In particular, the SiC divacancies have registers with nearly identical hyperfine coupling strengths and relative ODMR intensities to R1 and R2, but with known three-fold and six-fold degeneracies.

These multi-nuclei registers have ODNMR resonances that are approximately degenerate with the R1 and R2 ODNMR resonances, and therefore contribute parasitic signal that interferes with our tomographic reconstructions. Here, we will compute the ratio of this parasitic signal to the R1 and R2 signals to show that it has little impact on our results.

The electron spin resonances (ESR) of registers containing a single PL6 electron spin strongly coupled to up to three ^{29}Si nuclear spins are given in Table D.1. We also present these registers' frequency detunings (Δ) from our quantum gates, which depend on whether or not we are performing an experiment on R1 or R2 (labeled "R2 experiment" and "R1 experiment" in Table D.1). The maximum signal that a multi-nucleus register can contribute is reduced by the off-resonant driving factor $\frac{\Omega^2}{\Omega^2+\Delta^2}$, where Ω is the drive-field strength. Combining this factor with Eq. D.1, we find that the ratio of signal that comes from

Table D.1: The relative signal calculated for various registers in our system.

R2 Experiment	ESR (MHz)	Δ (MHz)	Relative Signal
R2	± 4.8	0	1
R22	$(\pm 9.8, 0)$	4.8	0.04
R21	$(\pm 1.5, \pm 11.1)$	6.3	0.03
R222	$(\pm 4.8, \pm 14.4)$	9.8	< 0.01
R221	$(\pm 15.9, \pm 6.3, \pm 3.3)$	11.1	< 0.01
R211	$(\pm 17.4, \pm 7.8, \pm 4.8)$	12.6	< 0.01
R1 Experiment	ESR (MHz)	Δ (MHz)	Relative Signal
R1	± 6.3	0	1
R11	$(\pm 12.6, 0)$	6.3	0.01
R12	$(\pm 1.5, \pm 11.1)$	4.8	0.10
R111	$(\pm 12.6, \pm 25.2)$	18.9	< 0.01
R112	$(\pm 17.4, \pm 7.8, \pm 4.8)$	11.1	< 0.01
R122	$(\pm 15.9, \pm 6.3, \pm 3.3)$	9.6	< 0.01
SOURCE: [54]			

unrelated registers to the real signal from R1, for example, is:

$$\frac{\binom{6}{k_1}\binom{3}{k_2}p^{k_1+k_2}(1-p)^{9-k_1-k_2}}{\binom{6}{1}\binom{3}{0}p(1-p)^8}\frac{\Omega^2}{\Omega^2+\Delta^2}. \tag{D.3}$$

We compute this quantity in Table S1 (labeled Relative Signal), assuming that nuclear spins in all registers optically initialize into the nuclear $\uparrow$ state, which is true for R1 and R2. Summing Eq. D.2 for registers up to those containing 3 nuclear spins and a single electron spin, we see that the parasitic signal is at most $\sim 11\%$ in R1 experiments and $\sim 7\%$ in R2 experiments. We therefore conclude that multi-nuclei registers contribute only marginally to our signal.

D.4 Electron Spin Polarization

The quantum-state tomography in this work relies on differential photoluminescence (PL) measurements between states related by unitary quantum gates. Since unitary operations cannot probe any element of a systems density matrix that is proportional to the identity matrix, the quantum gate sequences themselves are not sufficient to probe a systems absolute

density matrix (i.e. one that includes the identity element). Measuring the absolute density matrix is crucial to proving that our system exhibits genuine, as opposed to pseudo, entanglement. As we show in Section D.7, it suffices to measure the electron spin polarization to reconstruct the absolute density matrix of the initial and all other states. In this section, we describe how we measure the degree of electron polarization of the optically initialized PL6 defects. The basic principle underlying our measurement is that the radiative lifetimes of PL6s $m_s = 0$ and $m_s = -1$ spin states are different. Therefore, by optically exciting PL6 defects with a pulsed laser and measuring the relative coefficients of the bi-exponential PL decay, we have a direct measurement of the ground state electron spin polarization.

Since the PL6 defect has been measured [96] to have the same C_{3v} symmetry as the nitrogen-vacancy (NV) center in diamond, we adopt the same model and experimental techniques that were used to determine the electron spin polarization of NV centers [117,211,212]. In this model, a color center spin in its optically excited state can, in addition to radiatively decaying in a spin-conserving way, undergo a spin-selective non-radiative intersystem crossing to a singlet state. This transition being spin-dependent means that the probability of entering the non-radiative intersystem crossing is higher for the $m_s = \pm 1$ spin sublevels than for the $m_s = 0$ spin sublevel. This process enables magnetic transitions between these spin states to be detected through optically detected magnetic resonance (ODMR). Moreover, because the singlet eventually relaxes by undergoing an additional intersystem crossing to the spin triplet ground state, repeated cycling of the defect through this transition also polarizes the spin state in its orbital ground state.

In this model, the PL emitted after excitation with a short laser pulse follows a bi-exponential distribution, where the observed lifetimes, τ_0 and $\tau_{\pm 1}$, are the lifetimes for the $m_s = 0$ and $m_s = \pm 1$ spin sublevels, respectively. The lifetimes follow the relation $\tau_i = (\frac{1}{\tau_{optical}} + k_i)^{-1}$, where $\tau_{optical}$ is the bare optical lifetime and k_i is the intersystem crossing rate of the i-th spin sublevel. The respective relative amplitudes of the exponentials, then, correspond to the relative occupation of the $m_s = 0$ and $m_s = \pm 1$ spin sublevels in the

ground state. Thus, fitting the observed time-correlated single photon counting data to a bi-exponential model allows us to infer the absolute ground state electron spin polarization after non-resonant optical pumping.

To measure the bi-exponential decay, we use a photon counting module (Picoquant PicoHarp 300) to time-resolve the PL emitted from an ensemble of PL6 defects subject to a train of picosecond pulses of 850 nm light from a mode-locked Ti:Sapphire laser (Coherent Mira 900). We use an electro-optic modulator (Conoptics 350) to pick the pulses down to a repetition rate of approximately four microseconds. We pass these pulses through a fiber (OZ Optics, QMMJ-33-UVVIS-10/125-3A-20), which lengthens the 200 fs pulses to approximately 1 ps. These pulses are then guided to excite the defects and their emitted PL is collected using a 50 micron core diameter multimode fiber (ThorLabs GIF50). The fiber is coupled into a 150 mm monochromator (Acton 2150i), which is used for spectral filtering with a 1 nm bandwidth, easily isolating the zero phonon line of PL6 (near 1,038 nm) from other sharp spectral features. We couple the output of the monochromator into a single mode fiber (Corning SMF-28e+) that is connected to a closed-cycle superconducting nanowire single photon detector (SingleQuantum, EOS), which has a quantum efficiency of about 28% at this wavelength and a manufacturer-specified timing jitter of 50 ps.

Because the PL6 zero phonon line sharpens at low temperatures, we cool the sample to $T = 20$ K to increase our photon collection efficiency and relative rejection of luminescence from other sources in the substrate. We collect separate time-correlated photon traces with the monochromator wavelength set to either the PL6 zero-phonon line or two nanometers shorter than the zero-phonon line. We then subtract these data to remove the constant luminescence background and any remaining non-PL6 response. Since the ODMR signal of PL6 defects does not change significantly from 20 K to 296 K (see Supplementary Figure S4 in [88]), we assume that the electron-spin polarization is constant over this temperature range. For comparison, the polarization of NV centers in diamond has been measured to remain constant from 2 K to at least 650 K [117, 212, 213].

We repeat the experiment with and without the application of 160 ns -rotations between picosecond pulses (Fig. D.1a). Because a single picosecond pulse is likely not enough to completely reinitialize the spins within the optical interrogation volume, the repeated effect of partial repolarization and microwave rotation puts the system into a mixed state. This mixed state need not be a specific mixture, but rather only be different from the no-microwave case. We can then estimate the lifetimes and polarizations with the parameter estimation technique that we employ. The normalized data from the two cases of the experiment demonstrate clearly by inspection that microwave-induced rotations of the ground state spin do indeed modulate the time trace of the PL decay (Fig. D.1b). Since our aim is to infer the polarization when no microwaves are applied, it may not be immediately clear why we choose to repeat the experiment with microwave rotations between excitations pulses. The higher the degree of polarization efficiency in the PL6 optical cycle, the smaller the amplitude of the shorter lifetime decay associated with the $m_s = \pm 1$ spin state will be in the limit of 100% polarization, this amplitude vanishes and a priori estimation of the shorter lifetime and its associated amplitude becomes impossible because the decay is purely mono-exponential. Performing both experiments and then employing a parameter estimation technique that fits both datasets simultaneously and shares the inferred lifetimes between datasets while allowing the amplitudes to remain independent, solves this issue.

To analyze the data, we model the PL observed by following the equation

$$f_{j,k}(t_{j,k}) = A_k exp(-\frac{t_{j,k}}{\tau_{m_s=0}}) + B_k exp(-\frac{t_{j,k}}{\tau_{m_s=\pm 1}}) + C_k \tag{D.4}$$

where $t_{j,k}$ is the time delay of the j-th time bin in the k-th dataset, and A_k, B_k, and C_k are the amplitudes of the biexponential decays and constant background offset in the k-th dataset. Because fitting bi-exponential models and obtaining uncertainties is a difficult problem in a typical least-squares setting, we apply a Bayesian approach to estimating the model parameters [168, 214]. In our approach, the exponential decay lifetimes are shared

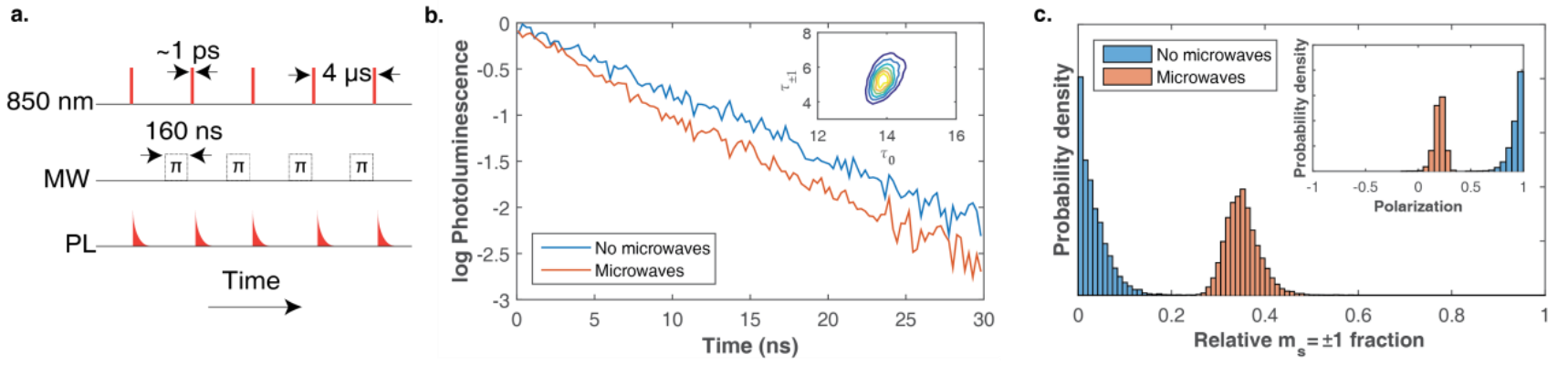

Figure D.1: Optically pumped electron spin polarization. (a) A pulse sequence diagram showing the timing of the picosecond pulsed excitation, the microwave (MW) π-pulses for the case of the experiment where we apply them, and the bi-exponential fluorescence decay recorded on the time-correlated photon counting module. (b) The natural logarithm of the normalized binned PL counts from the PL6 ensemble after picosecond pulse excitation for the no-microwave/microwave repetitions of the experiment. Inset: A contour plot of the marginal posterior probability density for the bi-exponential model lifetimes. (c) A plot of the marginal probability density of the relative amplitude of the $m_s = \pm 1$ exponential decay term for both the no-microwave/microwave repetitions of the experiment. Inset: The marginal probability density for the spin polarization P_k for the same no-microwave/microwave repetitions of the experiment.

globally but the amplitudes are allowed to vary between datasets using different microwave conditions. We approximate the error as normally distributed with standard deviation $\sigma_{ij} = \eta\sqrt{d_{k,1038nm}(t_j) + d_{k,1036nm}(t_j)}$, where the d_ks are the photons counted within the same time bin but when the monochromator is collecting on versus off the zero photon line of PL6, and η is a scaling parameter near unity that can account for any noise unexplained by the random error alone. The square root term is simply combining the estimators for the Poisson error of the time bin in each histogram in quadrature for a normal approximation of the Skellam-distributed error of our subtracted data – this is a good approximation since for both histograms, the number of counts in each bin always exceeds about 30. Since the bi-exponential model is fit to the subtracted data, the constant offsets C_k are nearly zero. As an aside, the value of η we infer is not significantly different from unity, indicating any systematic errors are likely below the random noise level.

Parameter uncertainties from the marginal posterior probability distributions of Bayesian models are often difficult or impossible to determine analytically, so most practitioners apply numerical techniques based on Markov-Chain Monte Carlo (MCMC) algorithms. These algorithms generate a random walk subject to the condition of detailed balance whose accept/reject probabilities are set by the posterior probability distribution. In this scenario, the random walk converges to its stationary distribution that is exactly the posterior probability distribution. Here we apply MT-DREAM(ZS), a MCMC algorithm that uses sampling from past random walk states and multiple-try Metropolis steps to quickly converge to the posterior probability distribution, even in problems with high-dimension [168].

Our computation of the posterior probability distribution reveals the lifetimes $\tau_0 = 13.9 \pm 0.6$ ns and $\tau_{\pm 1} = 5.4 \pm 1.6$ ns, where the error bars are the 95% credible intervals, and the independent decay amplitudes A_k and B_k for both datasets. The two-dimensional marginal posterior probability distribution for the lifetime parameters shows a disc-shaped peak, indicating good resolution of both lifetimes and low correlation between them in the parameter estimation problem (Fig. D.1b, inset). Although the data in Fig. D.1b show

some obvious difference between the two PL traces by eye, the model-based inference now lets us infer the relative amplitudes of the two decay terms quantitatively.

The relative $m_s = \pm 1$ decay amplitude, $\frac{B_k}{B_k+A_k}$, shows the fraction in this state when microwaves are applied unambiguously differs from the no-microwave case, as desired (Fig. D.1c). Of particular interest is the $m_s = \pm 1$ component when no microwaves are applied, and our analysis indicates it is not significantly different, in a statistical sense, from zero. This explains why the τ_0 lifetime we infer is in precise agreement with a previous report that used only a mono-exponential decay model of 14 ± 3 ns [96]. It is indicative of a very high electron spin polarization for this defect under optical excitation, which we can quantify by the relation $\frac{A_k-B_k}{B_k+A_k}$ (Fig. D.1c, inset). We therefore determine the optically induced spin polarization with no applied microwaves $P_0 = 93^{+7}_{-13}\%$ with 95% probability. This is the first report of both spin-modulated bi-exponential decay of the PL6 defect and the spin polarization efficiency of its optical cycle, the latter of which enables us to normalize our tomographic data as described in Section D.7 by direct substitution of values sampled from the marginal posterior of P_0. This means the final fidelities and PPT test values we compute account for uncertainties in both the tomographic reconstructions and the uncertainty in their normalization that derives from uncertainty in P_0.

D.5 Register Density Calculation

The hyperfine coupling constants, the optical transition energy, the optical lifetime, and microwave zero-field-splitting of PL6 are all similar to those of the neutral divacancies in 4H- and 6H-SiC [85, 86, 86–88, 96, 97, 100, 104, 188]. This suggests that PL6 is a perturbation to the divacancy. We use this analogy and optical spectroscopy to estimate the PL6 spin density. In particular, we compare the intensity of the PL6 zero-phonon-line emission to the intensity of the divacancy zero-phonon-line emission in highly implanted SiC samples (where the concentration is high enough to be accurately measured with double-electron-electron-resonance experiments). From this procedure we estimate that the areal density of

PL6 defects is 2×10^{10} cm^{-2}. The number of R1 and R2 registers in the optical illumination area is found by combining this density with the natural abundance of ^{29}Si isotopic defects (4.7%), the number of degenerate crystal lattice sites (3 for R1 and 6 for R2), and the laser spot size (3 μm in diameter). From this calculation we estimate that there are 10^3 R1 and R2 registers in our optical interrogation volume.

D.6 Identification of Nuclei in R1 and R2

To determine the nuclei that participate in R1 and R2, and their hyperfine coupling constants, we measure ODNMR as a function of the magnetic field $B_{\|}$. To obtain a model for the ODNMR resonance frequencies, we diagonalize the Hamiltonian given in Eq. D.1, taking the hyperfine interaction to be isotropic ($\mathbf{A} = AI$). We find that the ODNMR resonance frequencies in the electronic $m_s = -1$ spin manifold before and after ($f_{</>}$) the ground-state spin level anti-crossing ($B_{\|} = 48.3$ mT for PL6) should follow the following relations:

$$f_{</>} = \frac{1}{4}(3A + 2D_{ZFS} - 2B_{\|}(\gamma_e - \gamma_n) \mp \sqrt{8A^2 + (A - 2D_{ZFS} + 2B_{\|}(\gamma_e + \gamma_n))^2}), \quad \text{(D.5)}$$

We fit our data to these models leaving A and γ_n as free parameters, and assume that there is no magnetic field misalignment. We find an excellent fit to this model for both the R1 and R2 ODNMR resonances (Fit presented in the main-text Fig. 6.3), with best fit parameters $A_{R1} = 12.62 \pm 0.08$ MHz, $A_{R2} = 9.59 \pm 0.03$ MHz, $\gamma_{n,R1} = -8.6 \pm 0.5$ MHz/T, and$\gamma_{n,R2} = -8.6 \pm 1.6$ MHz/T. The error bars are 95% confidence intervals. From the extracted gyromagnetic ratios, we conclude that ^{29}Si is the nuclear spin in both R1 and R2. No ^{13}C-containing registers were characterized in our studies.

D.7 Optical Initialization Calibration

To determine the rate at which the electron and nuclear spins initialize, we use hole-burning measurements in ODMR and ODNMR, respectively. In particular, we initialize registers

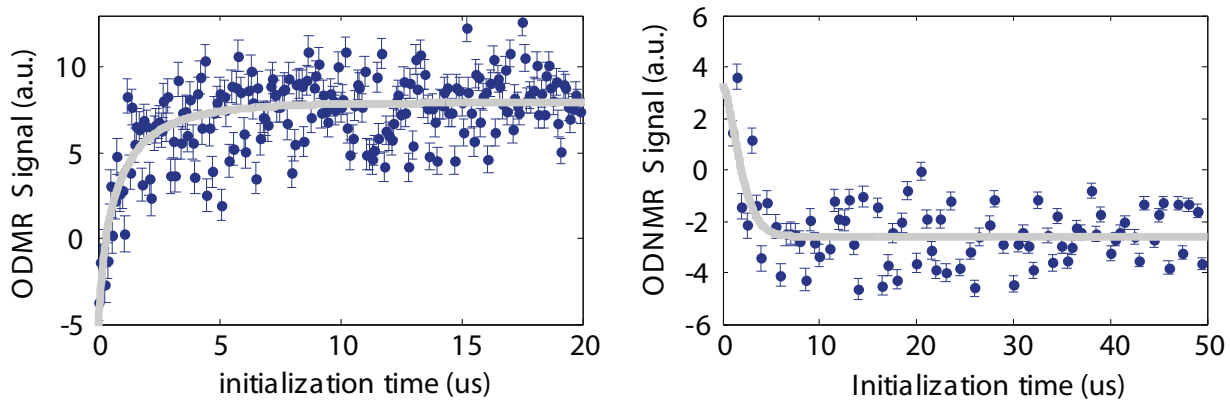

Figure D.2: Hole burning in the microwave and radiofrequency domains is used to determine the electron and nuclear spin polarization rates of R2 registers.

with a long optical pulse, apply a rotation pulse to the electron (nuclear) spin transition, apply an optical pulse of variable length, and then measure ODMR (ODNMR) spectroscopy. After some length of optical pulse (the initialization time), the spectra restore themselves and saturate (Fig. D.2). We find that the electron initialization time is 729 ± 350 ns and the nuclear spin initialization time is $2.16^{+3.5}_{-2.6}$ μs. The error bars are 95% confidence intervals. To ensure that we saturate the initialization process in our experiments, we use a 50 μs long laser pulse.

D.8 Optical Detection of Nuclear Spins

Most measurements presented in this set of experiments were performed at $B_{\|} = 33$ mT. At this magnetic field, R1 and R2 are both at their hyperfine-mediated, excited-state level anti-crossings [100,102]. Near its excited-state level anti-crossing, a register's electron and nuclear spins are hybridized (the $|0,\downarrow\rangle$ and $|-1,\uparrow\rangle$ states in particular), enabling them to exchange polarization after optical pumping. In addition to driving dynamic nuclear polarization, this polarization exchange leads the R1 and R2 photoluminescence intensity to be nuclear-spin dependent (previously observed in nitrogen-vacancy centers in diamond [133]). For this reason, at $B_{\|} = 33$ mT, each register's nuclear spin can be read out directly, without needing

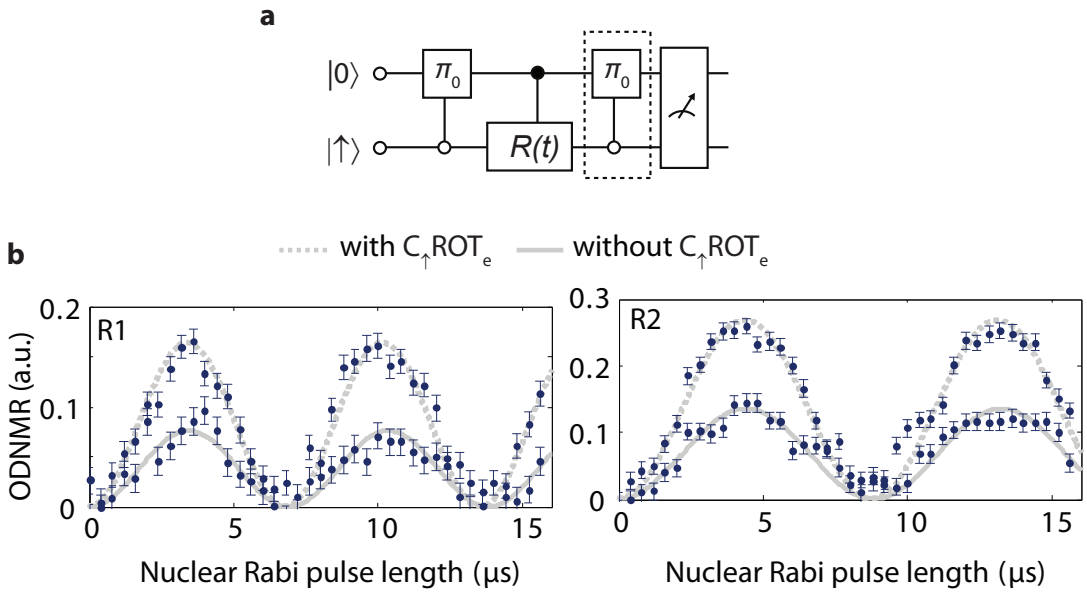

Figure D.3: Optical readout of nuclear spins. (a) The measurement sequence for ODNMR, where the RF pulse $R(t)$ is locked into. The final $C_{\uparrow}NOT_e$ gate is not necessary in the vicinity of the excited-state level anticrossing, where the nuclear spin has own intrinsic PL contrast. (b) ODNMR performed with and without the final $C_{\uparrow}NOT_e$ gate for R1 and R2 at $B_{||} = 33$ mT. Although there is a signal enhancement with this final $C_{\uparrow}NOT_e$ gate ($2.1 \pm 0.6\times$ for R1 and $2.0 \pm 0.4\times$ for R2), it introduces pulse errors and cross-talk into our measurements. We therefore do not use it for tomography or any measurements where quantitative analysis is important.

to project it onto its coupled electron spin for readout (Fig. D.3). Far from $B_{||} = 33$ mT, however, R1 and R2 are no longer at their excited-state level anti-crossings, and thus their nuclear spins are no longer hybridized with their coupled electron spins. At those magnetic fields, each register's nuclear spin must be projected onto its electron spin for readout, which can be accomplished with a $C_{\uparrow}ROT_e$ gate. This gate was used for the spectroscopic measurements in the inset of Fig. 8.3b. We do not apply this gate in our ODNMR-based tomography protocol to minimize cross-talk and pulse errors.

D.9 Coherent Nuclear Spin Control

We combine register-specific addressability with different radiofrequency pulse sequences to drive nuclear Rabi oscillations (Fig. D.4a), to characterize the inhomogeneous nuclear spin-

coherence times (T^*_{2n}) via Ramsey interferometry (Fig. D.4b) and to put a lower bound on the homogeneous nuclear spin coherence time via the Hahn-echo sequence (T_{2n}. See Fig. D.4c).

Nuclear Rabi oscillations demonstrate the coherent control of ^{29}Si nuclear spins in R1 and R2 registers. The oscillations of R1 do not exhibit beating after many oscillations, which suggests that the R1 hyperfine tensor is highly isotropic. The oscillations of R2 exhibit beating, which suggests that the R2 hyperfine tensor is anisotropic. We investigate this further by taking a long time-trace of the Nuclear Rabi oscillations (Fig. D.5). The Fourier transform of the trace indicates that the beating is between three closely spaced frequencies, which is consistent with the 6-fold degeneracy that we assigned earlier. The ratio of the slowest to the fastest oscillation frequency is 0.91, which indicates that the anisotropy is small. This is consistent with the highly isotropic hyperfine tensors of similar registers based on the divacancies [102].

The inhomogeneous nuclear spin coherence time ($T*_{2n},\ R1 = 29 \pm 2\mu s,\ T*_{2n},\ R2 = 47 \pm 6\mu s$) is found to be two orders of magnitude longer than the inhomogeneous electron spin coherence time ($T*_{2e} \sim 300$ ns). The homogeneous nuclear spin coherence time ($T_{2n,R1} = 247 \pm 100\ \mu$s, $T_{2n,R2} = 209 \pm 42\ \mu$s) exceeds the homogeneous electron spin coherence time ($T_{2e} \sim 60\ \mu$s at T = 296 K), but is surprisingly short. We attribute this to the electronic spin-lattice relaxation (which occurs on timescales $T_{1e} \sim 200\ \mu$s at T = 296 K [87]), which randomizes the electron spin and limits our measurement.

The highly isotropic nature of the R1 and R2 hyperfine interactions has important implications. It means that the quantization axes of the ^{29}Si nuclei within these registers are nearly co-aligned with the c-axis. Therefore, when a manipulation field is applied transverse to the c-axis, to drive nuclear gates, the nuclei at rotationally equivalent lattice sites feel the same field and are thus driven to the same extent (that is, the transverse field does not break their degeneracy). The scenario is different for registers with an anisotropic interaction, such as those based on ^{13}C nuclei [86] (note that ^{13}C-containing registers in diamond are also

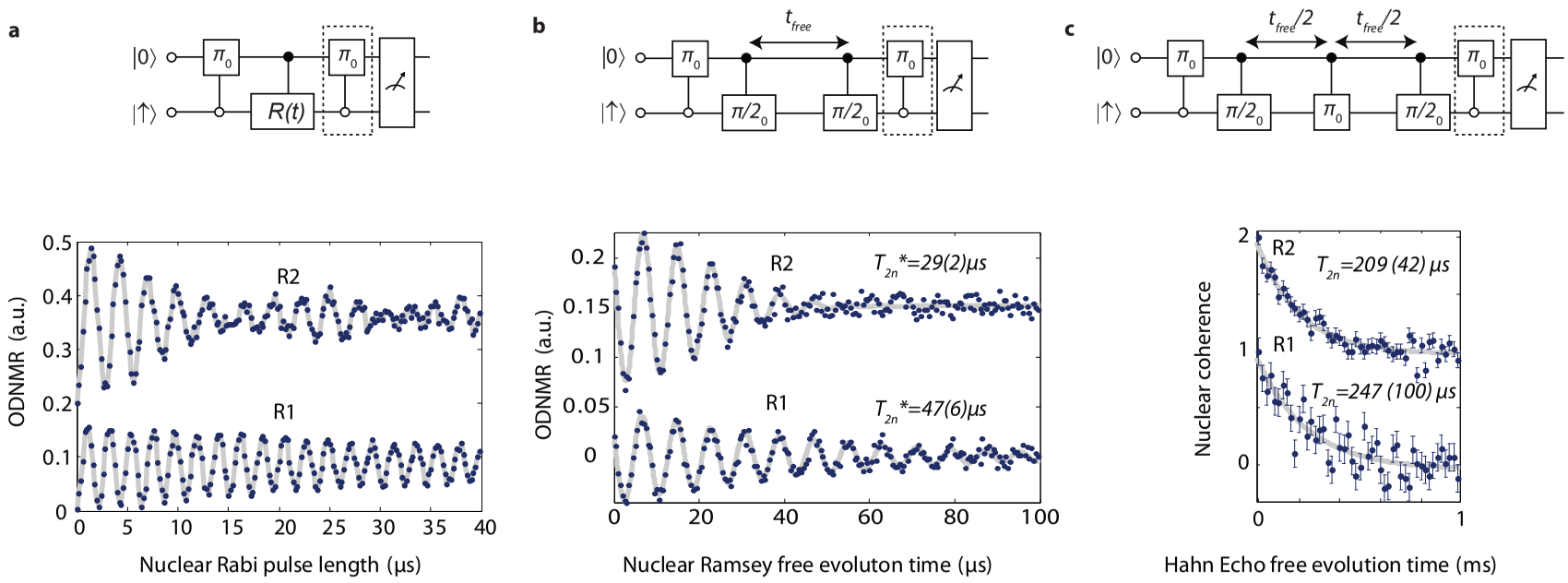

Figure D.4: Coherent nuclear spin control in SiC. (a) Nuclear Rabi oscillations. R(t) is the variable-length radiofrequency pulse that is used to drive nuclear magnetic resonance. (b) Nuclear Ramsey interferometry is used to measure the inhomogeneous nuclear spin coherence time ($T*_{2n}$). t_{free} is the nuclear-spin free evolution time. The radiofrequency pulses are applied 125 kHz off resonance to recover an oscillation. (c) Nuclear Hahn echo, used to measure the homogeneous nuclear spin coherence time (T_{2n}). tfree is the nuclear-spin free evolution time. These measurements were performed at $B_{||} = 33mT$, where registers initialize into the state $|0,\uparrow\rangle$. The error bars in (c) represent 95% confidence intervals. The $C_{\uparrow}NOT_e$ gate in the dashed boxes in the circuit diagrams can be used to project the nuclear spin onto the electron spin for readout. This gate is not necessary near $B_{||} = 33mT$, where the nuclear spin can be measured directly. The curves in all three panels have been offset for clarity.

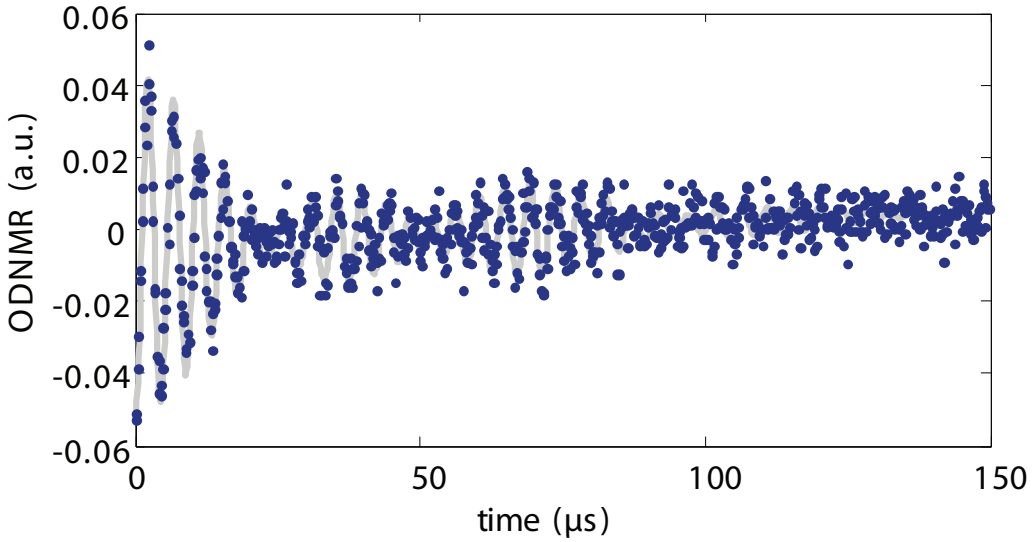

Figure D.5: Nuclear Rabi oscillations of R2. The beating suggests that the R2 hyperfine tensor is anisotropic. By Fourier transforming the data, we find that the beating is between three frequencies, $f_1 = 239$ kHz, $f_2 = 223$ kHz, and $f_3 = 218$ kHz, with negligible error. Since the frequency is power dependent, its absolute value is of little importance. Instead we compute the ratio of the slowest to fastest oscillation frequency. The ratio is 0.91, indicating that the anisotropy is small.

usually anisotropic [101]). In those registers, the quantization axes of the nuclei are tilted away from the c-axis. Therefore, when a manipulation field is applied transverse to the c axis, the nuclei at rotationally equivalent lattice sites can feel different fields and thus be driven to different extents (that is, the transverse field breaks their degeneracy). Employing these registers for applications will require extra care (possibly by using gates that are highly robust against pulse errors), since it is generally necessary for rotationally equivalent registers to stay equivalent throughout the full duration of a quantum algorithm.

D.10 Calibrating Quantum Gates

Executing quantum algorithms and performing accurate quantum state tomography requires the precise calibration of quantum gates. To execute its prescribed task, each gate must have an accurate frequency and power. We calibrate both parameters by using judicious lock-in techniques. In this section I will describe these techniques, in the order that they

were performed to calibrate all of the electron and nuclear spin gates. Calibration of the initialization pulse was described in D.7.

The crowded ODMR spectrum can be used to estimate of the $|0,\uparrow\rangle \leftrightarrow |-1,\uparrow\rangle$ transition frequency. We can then estimate the power necessary to drive a $\mathrm{C}_{\uparrow}\mathrm{ROT}_e(\pi)$ gate by driving Rabi oscillations on the central ODMR line (i.e. the spin transition of weakly coupled PL6 spins). The $|0,\downarrow\rangle \leftrightarrow |-1,\downarrow\rangle$ transition cannot be seen, due to strong dynamic nuclear polarization into the $\uparrow$ state at $B = 33$ mT, and thus it cannot be calibrated from this measurement. With the $\mathrm{C}_{\uparrow}\mathrm{ROT}_e(\pi)$ gate now roughly calibrated, we measure ODNMR to extract the $|-1,\downarrow\rangle \leftrightarrow |-1,\uparrow\rangle$ transition frequency to excellent accuracy. Time-domain ODNMR is then used to conclude the calibration of the general $\mathrm{C}_{-1}\mathrm{ROT}_n(\theta)$ gate.

Next we calibrate the general $\mathrm{C}_{\uparrow}\mathrm{ROT}_e(\theta)$ gate. To do so, we first measure ODNMR as a function of the MW frequency (Fig. D.6a), while locking into the nuclear pulse being on versus off. This returns the $|0,\uparrow\rangle \leftrightarrow |-1,\uparrow\rangle$ transition for the register of interest only, enabling the accurate extraction of its frequency. Next, we determine the power necessary to drive a $\mathrm{C}_{\uparrow}\mathrm{ROT}_e(\pi)$ rotation, for a given pulse width. To do so, we repeat ODNMR, now with the MW frequency fixed to to the $|0,\uparrow\rangle \leftrightarrow |-1,\uparrow\rangle$ transition, and sweep the MW power. By locking into the nuclear pulse being on versus off, we measure electronic Rabi oscillations for the register of interest only (Fig. D.6b). This concludes the calibration of the general $\mathrm{C}_{\uparrow}\mathrm{ROT}_e(\theta)$ gate.

Next we calibrate the general $\mathrm{C}_{\downarrow}\mathrm{ROT}_e(\theta)$ gate. As mentioned above, this calibration can be tricky since the $|0,\downarrow\rangle \leftrightarrow |-1,\downarrow\rangle$ transition cannot be seen at 33 mT due to strong dynamic nuclear polarization. Nonetheless, we can use a similar methodology that was applied to determine the $\mathrm{C}_{\uparrow}\mathrm{ROT}_e(\theta)$ gate. To determine the frequency of the $|0,\downarrow\rangle \leftrightarrow |-1,\downarrow\rangle$ transition, we first initialize into $|0,\uparrow\rangle$, drive a $\mathrm{C}_{\uparrow}\mathrm{ROT}_e(\pi)$ gate, and then a $\mathrm{C}_{-1}\mathrm{ROT}_n(\pi/2)$ gate to create the superposition $2^{-1/2}(|-1,\uparrow\rangle + |-1,\downarrow\rangle)$ (note that a π pulse can be used here too; there are many ways to do this calibration). At this point, we perform electron-spin spectroscopy on this state (note that this requires a second microwave signal

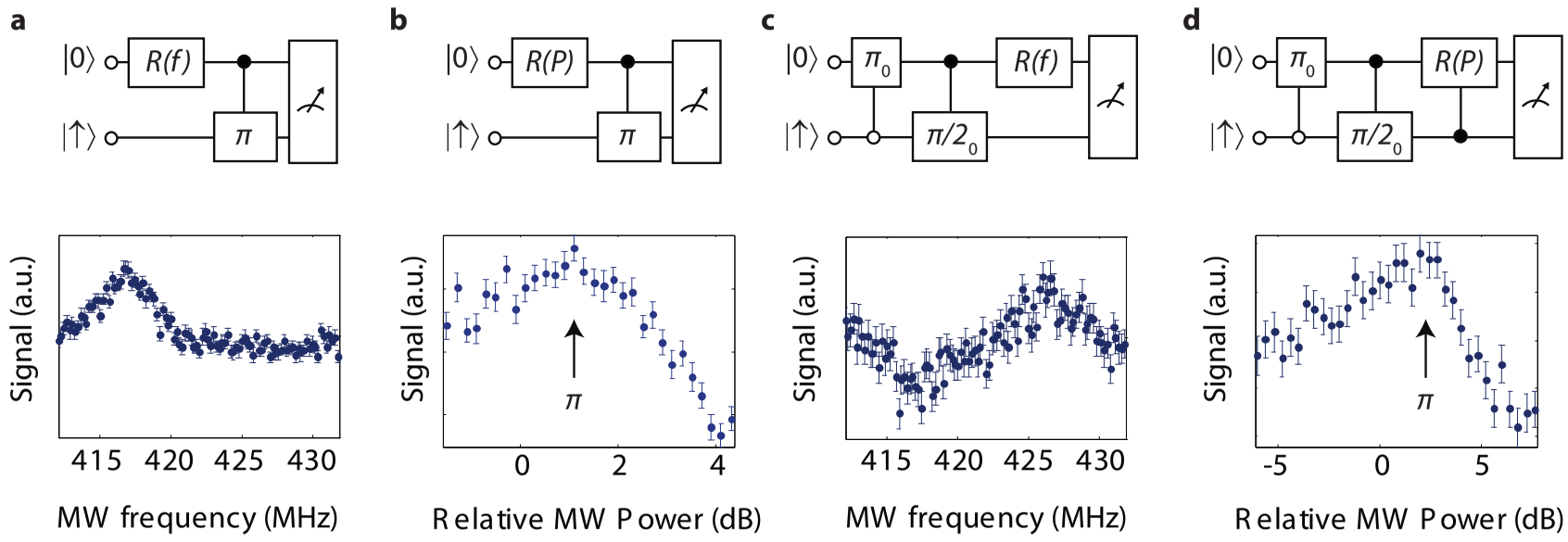

Figure D.6: The procedure used to calibrate the electronic gates. Details are in the text. (a) By locking into the nuclear gate being on versus off, while sweeping the frequency of the MW pulse $R(f)$, the $|0,\uparrow\rangle \leftrightarrow |-1,\uparrow\rangle$ transition frequency can be measured. (b) By fixing the MW pulse frequency to this transition, while sweeping its power, electron Rabi oscillations can be resolved for the register of interest only, enabling the calibration of the general $\mathrm{C}_{\uparrow}\mathrm{ROT}_e(\theta)$ gate. (c) By locking into the nuclear gate being on versus off, while sweeping the frequency of the last MW2 pulse $R(f)$, the $|0,\downarrow\rangle \leftrightarrow |-1,\downarrow\rangle$ transition frequency can be measured. (d) By fixing the MW2 pulse frequency to this transition, while sweeping its power, electron Rabi oscillations can be resolved for the register of interest only, enabling the calibration of the general $\mathrm{C}_{\downarrow}\mathrm{ROT}_e(\theta)$ gate. The vertical axes are not comparable and so they have been stripped of units. All error bars are 95 % confidence intervals. Typically scans were averaged for much longer, to reduce noise. Note that the frequency domain measurements (a) and (c) are also useful for measuring pulse bandwidths.

generator, which I will call MW2 to avoid confusion), by sweeping the MW2 frequency, while locking into the nuclear pulse being on versus off. This returns the $|0,\uparrow\rangle \leftrightarrow |-1,\uparrow\rangle$ and $|0,\downarrow\rangle \leftrightarrow |-1,\downarrow\rangle$ transitions for the register of interest only (Fig. D.6c), enabling the latter transition frequency to be extracted with good accuracy.

Next, we determine the power necessary to drive a $\mathrm{C}_{\downarrow}\mathrm{ROT}_e(\pi)$ rotation, for a given pulse width. To do so, we repeat the above measurement, now with the MW2 frequency fixed to to the $|0,\downarrow\rangle \leftrightarrow |-1,\downarrow\rangle$ transition, and sweep the MW2 power. By locking into the nuclear pulse being on versus off, we measure electronic Rabi oscillations for the register of interest only (Fig. D.6d). This concludes the calibration of the general $\mathrm{C}_{\downarrow}\mathrm{ROT}_e(\theta)$ gate. Note that a power calibration must be done for both the $|0,\uparrow\rangle \leftrightarrow |-1,\uparrow\rangle$ and $|0,\downarrow\rangle \leftrightarrow |-1,\downarrow\rangle$ transitions, due to dispersion in the MW cables, even though they are only $\sim$10 MHz apart.

Finally we calibrate the general $\mathrm{ROT}_e(\theta)$ gate by driving high-power Rabi at the central ODMR resonance. The bandwidth needs to be broadband such that both the $|0,\uparrow\rangle \leftrightarrow |-1,\uparrow\rangle$ and $|0,\downarrow\rangle \leftrightarrow |-1,\downarrow\rangle$ transitions are completely engulfed. The accuracy of this calibration can be verified by applying the techniques outlined above.

D.11 Quantum State Tomography

Register initialization and readout are achieved through optical pumping and PL measurements, respectively. The PL signal is proportional to the intensity of the readout laser in the interrogation volume. Thus, in our measurements, we study the density matrix of registers as averaged over the illumination volume, which is given by the relation:

$$\rho = \frac{\sum_j I(r_j)\hat{\rho}_j}{\sum_j I(r_j)} \tag{D.6}$$

where r_j is the location of the j-th register, $I(r_j)$ is the laser intensity at the location of this register, and $\hat{\rho}_j$ is the 2-spin (electron and nuclear spin) density matrix of the register.

In this section we explicitly outline how we measure the elements of ρ. We employ a

simplified notation for the register states: $|1\rangle = |0,\uparrow\rangle, |2\rangle = |0,\downarrow\rangle, |3\rangle = |-1,\uparrow\rangle, |4\rangle = |-1,\downarrow\rangle, |5\rangle = |+1,\uparrow\rangle$, and $|6\rangle = |+1,\downarrow\rangle$. The PL emitted by PL6 corresponds to the spin occupation probability of each energy eigenstate (ρ_{ii}, where i ranges from 1-6) multiplied by the PL signal that would be obtained if all spins were in that state (K_i). Mathematically, this can be represented as $\sum_{i=1}^{6} K_i \rho_{ii}$.

To reconstruct ρ of a register ensemble, we use the following algorithm: we prepare the register ensemble into its to-be-measured state, operate on it with a sequence of microwave and radiofrequency pulses (represented by the unitary operator $\hat{U}_1$), and then measure the PL. We then re-prepare the state, operate on it with a different sequence of microwave and radiofrequency pulses ($\hat{U}_2$) and then measure the PL again. The difference between these PL measurements is the signal:

$$\text{Signal} = \sum_{i=1}^{6} K_i((\hat{U}_1 \hat{\rho} \hat{U}_1^{\dagger})_{ii} - (\hat{U}_2 \hat{\rho} \hat{U}_2^{\dagger})_{ii}) \tag{D.7}$$

To extract most elements of ρ it suffices to make $\hat{U}_1$ and $\hat{U}_2$ be a single electron spin rotation followed by a single nuclear spin rotation. By choosing $\hat{U}_1$ and $\hat{U}_2$ in this way, we also mitigate errors during the tomography procedure. In particular, such pulse sequences start by transferring the to-be-measured density matrix element with a fast electronic pulse onto the highly coherent nuclear spin. Once transferred, nuclear gates and optical pulses are used to probe the element with minimal dephasing. The same considerations were applied in the construction of our entangling algorithm.

Before explicitly defining $\hat{U}_1$ and $\hat{U}_2$ we introduce an abbreviated notation for the four spin transitions in our system. We define e0 to be the local broadband electronic transition of both $|1\rangle \leftrightarrow |3\rangle$ and $|2\rangle \leftrightarrow |4\rangle$, e1 to be the selective non-local electronic transition $|1\rangle \leftrightarrow |3\rangle$, e2 to be the selective non-local electronic transition $|2\rangle \leftrightarrow |4\rangle$, and n to be the selective non-local nuclear transition $|3\rangle \leftrightarrow |4\rangle$. With this notation, $\hat{U}$ can be conveniently represented

Table D.2: Quantum gate sequences used to measure the density-matrix coherences.

$\hat{U}_1$	$\hat{U}_2$	Signal
$R_x^n(+\pi/2)R^{e1}(\pi)$	$R_x^n(-\pi/2)R^{e1}(\pi)$	$2Re(\rho_{14})(K_3-K_4)$
$R_x^n(+\pi/2)R^{e2}(\pi)$	$R_x^n(-\pi/2)R^{e2}(\pi)$	$-2Re(\rho_{23})(K_3-K_4)$
$R_x^n(+\pi/2)R^{e0}(\pi)$	$R_x^n(-\pi/2)R^{e0}(\pi)$	$2Im(\rho_{12})(K_3-K_4)$
$R_x^n(+\pi/2)$	$R_x^n(-\pi/2)$	$2Im(\rho_{34})(K_3-K_4)$
$R_y^n(+\pi/2)R^{e1}(\pi)$	$R_y^n(-\pi/2)R^{e1}(\pi)$	$-2Im(\rho_{14})(K_3-K_4)$
$R_y^n(+\pi/2)R^{e2}(\pi)$	$R_y^n(-\pi/2)R^{e2}(\pi)$	$-2Im(\rho_{23})(K_3-K_4)$
$R_y^n(+\pi/2)R^{e0}(\pi)$	$R_y^n(-\pi/2)R^{e0}(\pi)$	$2Re(\rho_{12})(K_3-K_4)$
$R_y^n(+\pi/2)$	$R_y^n(-\pi/2)$	$2Re(\rho_{34})(K_3-K_4)$
$R_y^n(+\pi/2)R^{e1}(\pi)R_x^n(\pi)$	$R_y^n(-\pi/2)R^{e1}(\pi)R_x^n(\pi)$	$2Re(\rho_{13})(K_3-K_4)$
$R_x^n(+\pi/2)R^{e1}(\pi)R_x^n(\pi)$	$R_x^n(-\pi/2)R^{e1}(\pi)R_x^n(\pi)$	$2Im(\rho_{13})(K_3-K_4)$
$R_y^n(+\pi/2)R^{e2}(\pi)R_x^n(\pi)$	$R_y^n(-\pi/2)R^{e2}(\pi)R_x^n(\pi)$	$2Re(\rho_{24})(K_3-K_4)$
$R_x^n(+\pi/2)R^{e2}(\pi)R_x^n(\pi)$	$R_x^n(-\pi/2)R^{e2}(\pi)R_x^n(\pi)$	$-2Im(\rho_{24})(K_3-K_4)$

SOURCE: [54]

as:

$$\hat{U}_i = R_{\phi n}^n(\theta_n)R_{\phi e}^e(\theta_e), \tag{D.8}$$

where the rotation angles θ_n and θ_n, and phases ϕ_e and ϕ_n depend on the measurement sequence. The superscript n is the single nuclear transition that we drive, and the superscript e is one of the above-defined electronic transitions. We make the electron spin rotation be the same for both $\hat{U}_1$ and $\hat{U}_2$ and vary the phase and the duration of the nuclear spin rotation. By choosing $\hat{U}_1$ and $\hat{U}_2$ in this way, the contribution to the signal from the electron spin vanishes, and therefore, we measure only the nuclear-spin contribution (i.e. the measurement uses ODNMR). Moreover, the signal in Eq. D.7 vanishes for all registers without an ODNMR resonance at the nuclear pulse frequency. Since the nuclear pulse bandwidths are significantly narrower than the separation between the R1 and R2 ODNMR resonances, there is virtually no cross talk between these registers. The explicit rotations to determine the coherences and populations are given in Table D.2 and D.3, respectively, and are also presented in the Fig. 8.5.

The only elements of that cannot be measured by picking$\hat{U}_i$ as in Eq. D.7 are ρ_{13}, ρ_{24}.

Table D.3: Quantum gate sequences used to measure the density-matrix populations.

$\hat{U}_1$	$\hat{U}_2$	Signal
$R_x^n(\pi)R^{e1}(\pi)$	$R^{e1}(\pi)$	$-(K_3-K_4)(\rho_{11}-\rho_{44})$
$R_x^n(\pi)R^{e2}(\pi)$	$R^{e2}(\pi)$	$-(K_3-K_4)(\rho_{33}-\rho_{22})$
$R_x^n(\pi)R^{e0}(\pi)$	$R^{e0}(\pi)$	$-(K_3-K_4)(\rho_{11}-\rho_{22})$
$R_x^n(\pi)$	$-$	$-(K_3-K_4)(\rho_3 3-\rho_4 4)$

SOURCE: [54]

To measure these we modify $\hat{U}_i$ to have another nuclear spin rotation (denoted by primes):

$$U_i = R^n_{\phi n}(\theta_n)R^e_{\phi e}(\theta_e)R\prime^n_{\phi\prime n}(\theta\prime_n), \tag{D.9}$$

Since the PL6 electron spin inhomogeneous coherence time $T*_{2e}$ is shorter than the time it takes to perform the nuclear spin rotation $R\prime^n_{\phi\prime n}(\theta\prime_n)$, such a measurement would be highly inaccurate. We therefore do not measure ρ_{13} or ρ_{24} but rather add an uncertainty to them equal to the maxima allowed by their corresponding diagonal density matrix elements (for example, the uncertainty in ρ_{13} is $\sqrt{\rho_{11}\rho_{33}}$).

To determine the normalization $(K_3 - K_4)$ for all density matrix elements and the optically initialized density matrix, we need seven linearly independent equations. Three equations come from the pulse sequences presented in Table D.3 (the fourth is a linear combination of the others). The fourth equation comes from the normalization condition:

$$Tr(\rho) = 1, \tag{D.10}$$

The fifth and sixth equations come from the symmetry condition that there is equal electron spin polarization into $m_s = \pm 1$:

$$\rho_{33} = \rho_{55} \qquad \text{and} \qquad \rho_{44} = \rho_{66}, \tag{D.11}$$

The seventh equation comes from our measure of the electron spin polarization:

$$P_e = \rho_{11} + \rho_{22} - \rho_{33} - \rho_{44} - \rho_{55} - \rho_{66} \tag{D.12}$$

To compute all other density matrices, we drop the assumptions of Eq. D.11 and D.12, which are valid for only the initialized state, and assume that the spin populations in the $m_S = +1$ manifold remain constant under all operations within the $m_S = 0$ and $m_S = -1$ manifolds:

$$\rho_{55} = \rho_{55}^{\text{initial}} \qquad \text{and} \qquad \rho_{66} = \rho_{66}^{\text{initial}}. \tag{D.13}$$

Eq. D.12 is valid since our microwave pulses, which have a maximum drive strength of 25 MHz and never exceed a 50 MHz bandwidth, are detuned from the transitions $|1\rangle \leftrightarrow |5\rangle$ and $|2\rangle \leftrightarrow |6\rangle$ by approximately 1.6 GHz. There is no redistribution between states $|5\rangle$ and $|6\rangle$ since our radiofrequency pulses, which have a maximum drive strength of 83 kHz and never exceed a 300 kHz bandwidth, are detuned from the $|5\rangle \leftrightarrow |6\rangle$ transition by approximately 560 kHz. Re-thermalization over the duration of the entangling gate (5 μs long) is negligible.

D.12 Example Tomography Data

Five sets of tomographic measurements are presented in Fig. D.7. The order of measurements in each set is given in Table D.4. Note that some of these measurements are superfluous, and were taken as sanity checks. These data, in combination with the electron spin polarization measurement described D.4, are enough to reconstruct the $|0,\uparrow\rangle\langle 0,\uparrow|$, $|\Psi^+\rangle\langle\Psi^+|$, $|\Psi^-\rangle\langle\Psi^-|$, $|\Phi^+\rangle\langle\Phi^+|$, $|\Phi^-\rangle\langle\Phi^-|$ density matrices.

In addition to reconstructing the initial and entangled density matrices, we also reconstructed intermediate density matrices. This was done on many instances to debug the apparatus. In Fig. D.8, for one particular instance, we show reconstructions of our initial density matrix, the density matrix after application of a composite $\text{cC}_{\uparrow}\text{NOT}_e$ gate (I will use the lowercase "c" to denote composite in this section), and the density matrix after

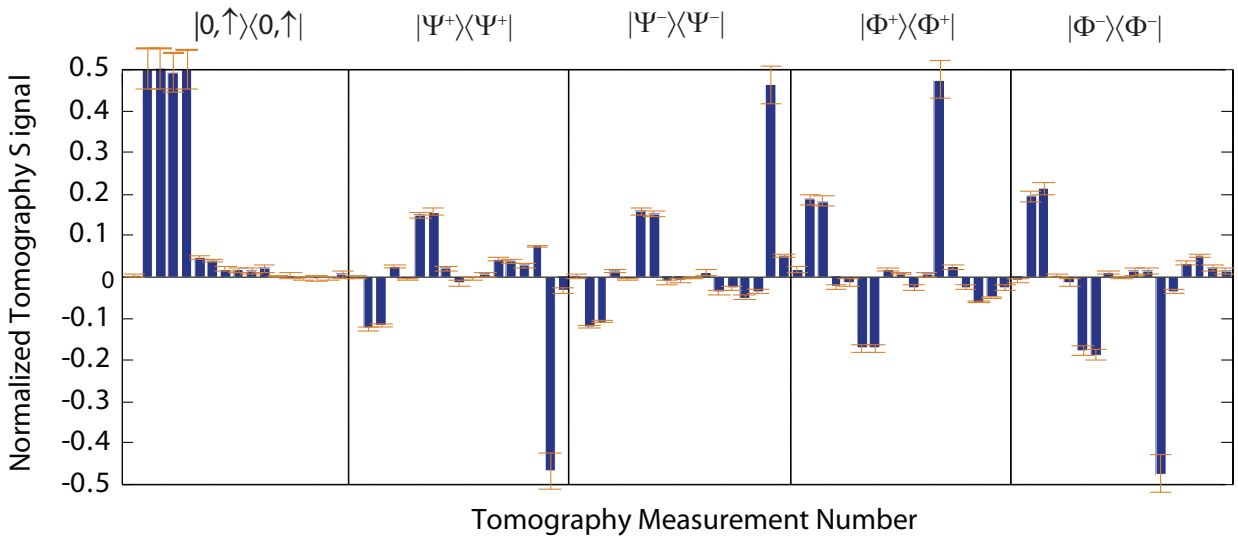

Figure D.7: Tomographic measurements that were used to reconstruct the $|0,\uparrow\rangle\langle 0,\uparrow|$, $|\Psi^+\rangle\langle\Psi^+|$, $|\Psi^-\rangle\langle\Psi^-|$, $|\Phi^+\rangle\langle\Phi^+|$, $|\Phi^-\rangle\langle\Phi^-|$ density matrices. The measurement order is presented in Table D.4. The normalization for these matrices was evaluated at the mean electron spin polarization. The error bars are 95 % confidence intervals.

Table D.4: The sequence of tomographic measurements made to obtain the data in Fig. D.7. Some of these are superfluous and were taken as sanity checks.

Num	$\hat{U}_1$	$\hat{U}_2$
1	–	–
2	$R_x^n(+\pi)R_x^{e0}(\pi)$	$R_x^{e0}(\pi)$
3	$R_y^n(+\pi)R_x^{e0}(\pi)$	$R_x^{e0}(\pi)$
4	$R_x^n(+\pi)R_x^{e1}(\pi)$	$R_x^{e1}(\pi)$
5	$R_y^n(+\pi)R_x^{e1}(\pi)$	$R_x^{e1}(\pi)$
6	$R_x^n(+\pi)$	–
7	$R_y^n(+\pi)(\pi)$	–
8	$R_x^n(+\pi)R_x^{e2}(\pi)$	$R_x^{e2}(\pi)$
9	$R_y^n(+\pi)R_x^{e2}(\pi)$	$R_x^{e2}(\pi)$
10	$R_x^{e0}(\pi)R_x^n(+\pi/2)$	$R_x^{e0}(\pi)R_x^n(-\pi/2)$
11	$R_x^{e0}(\pi)R_y^n(+\pi/2)$	$R_x^{e0}(\pi)R_y^n(-\pi/2)$
12	$R_x^{e1}(\pi)R_x^n(+\pi/2)$	$R_x^{e1}(\pi)R_x^n(-\pi/2)$
13	$R_x^{e1}(\pi)R_y^n(+\pi/2)$	$R_x^{e1}(\pi)R_y^n(-\pi/2)$
14	$R_x^n(+\pi/2)$	$R_x^n(-\pi/2)$
15	$R_y^n(+\pi/2)$	$R_y^n(-\pi/2)$
16	$R_x^{e2}(\pi)R_x^n(+\pi/2)$	$R_x^{e2}(\pi)R_x^n(-\pi/2)$
17	$R_x^{e2}(\pi)R_y^n(+\pi/2)$	$R_x^{e2}(\pi)R_y^n(-\pi/2)$

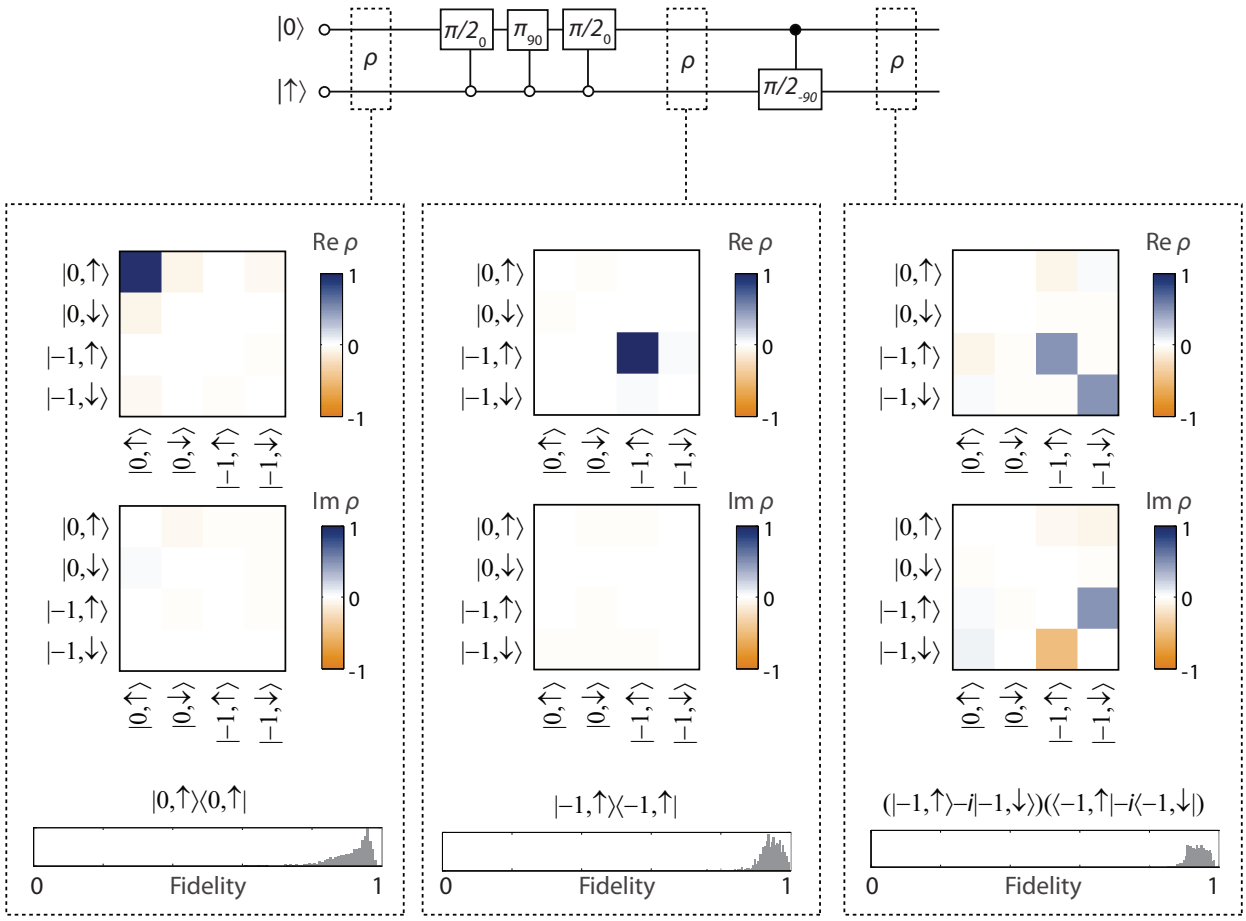

Figure D.8: Reconstructions of the initial density matrix, the density matrix after the application of a composite $\mathrm{cC}_{\uparrow}\mathrm{NOT}_e$ gate, and the density matrix after application of a $\mathrm{cC}_{\uparrow}\mathrm{NOT}_e$ gate followed by $\mathrm{C}_{-1}\mathrm{ROT}_n(\theta = -\pi/2, \phi = -\pi/2)$. For this particular experimental run, the density matrix fidelities are $F = 0.96^{+4}_{-16}, 0.94 \pm 6$, and 0.94 ± 6, where the quoted values are the means and 95% confidence intervals of these distributions.

application of a $\mathrm{cC}_{\uparrow}\mathrm{NOT}_e$ gate followed by $\mathrm{C}_{-1}\mathrm{ROT}_n(\theta = -\pi/2, \phi = -\pi/2)$.

The fidelities of these density matrices are $F = 0.96^{+4}_{-16}, 0.94 \pm 6$, and 0.94 ± 6, respectively. For the initial state, given that the fidelity distribution is highly asymmetric, the fidelity is quoted as the most likely value and the error bars are stretched to engulf ∼95% of the distribution (this fidelity is consistent with the initialization fidelity presented in Chapter 8, which was measured in a separate experiment). For the other two states, given that their fidelity distributions are approximately normal, we simply quote the mean and 95% confidence intervals.

Table D.5: Consolidated initialization and entanglement data.

R2	P_n	P_e	F	PPT test
$\|0,\uparrow\rangle$	$99^{+1}_{-3}\%$	$93^{+7}_{-11}\%$	$0.95^{+0.05}_{-0.07}$	-0.01 ± 0.02
$\|\Phi^+\rangle$	–	–	0.78 ± 0.07	-0.31 ± 0.06
$\|\Phi^-\rangle$	–	–	0.79 ± 0.07	-0.31 ± 0.07
$\|\Psi^+\rangle$	–	–	0.88 ± 0.07	-0.40 ± 0.06
$\|\Psi^-\rangle$	–	–	0.85 ± 0.07	-0.37 ± 0.06
R1	P_n	P_e	F	PPT test
$\|0,\uparrow\rangle$	$91 \pm 8\%$	$89^{+11}_{-12}\%$	0.89 ± 0.08	-0.004 ± 0.011
$\|\Phi^+\rangle$	–	–	0.76 ± 0.07	-0.29 ± 0.06
$\|\Phi^-\rangle$	-	-	0.73 ± 0.07	-0.25 ± 0.05
$\|\Psi^+\rangle$	–	–	0.77 ± 0.07	-0.30 ± 0.06
$\|\Psi^-\rangle$	–	–	0.78 ± 0.07	-0.32 ± 0.06

SOURCE: [54]

D.13 Consolidated Initialization and Entanglement Data

Initialization and entanglement of the R1 ensemble is presented in Fig. D.3. Consolidated initialization and entanglement data for the R1 and R2 registers is presented in Table D.4.

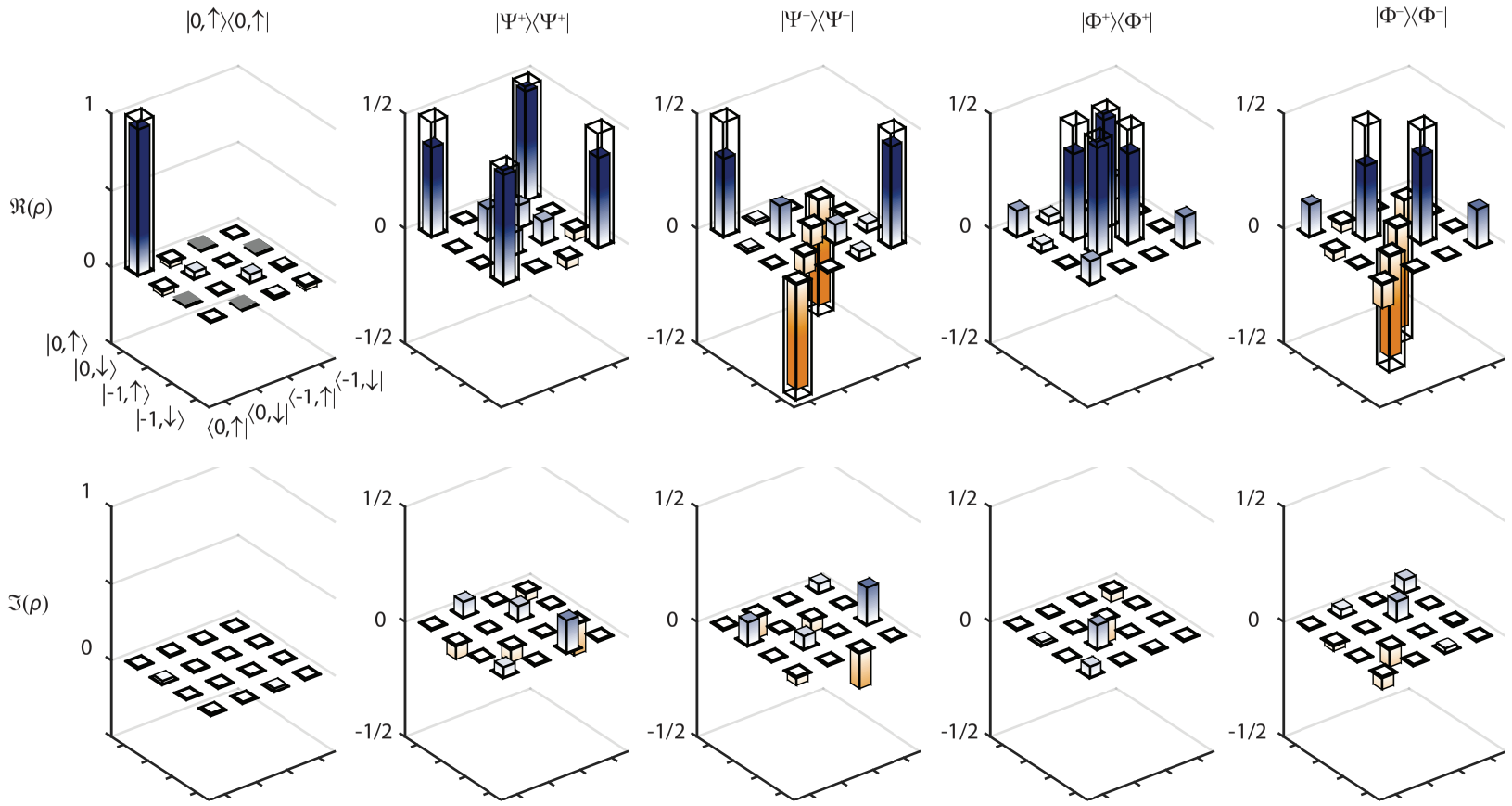

Figure D.9: Entanglement of the R1 ensemble. Real (upper panels) and imaginary (lower panels) components of the initial and entangled R1 density matrices. The overlaid transparent bars represent the ideal density matrices.

APPENDIX E

BLUEPRINTS FOR MACHINED PARTS

In this Appendix, I present blueprints for parts that have been useful for the research presented in this thesis and other projects. These include coldfingers, Janis cryostat parts and accessories, a goniometer designed for a Montana Instruments system, and a sample holder for ongoing spin-diffusion experiments. Some of these blueprints represent individual parts in larger assemblies; these will be noted in the captions. All units are in inches.

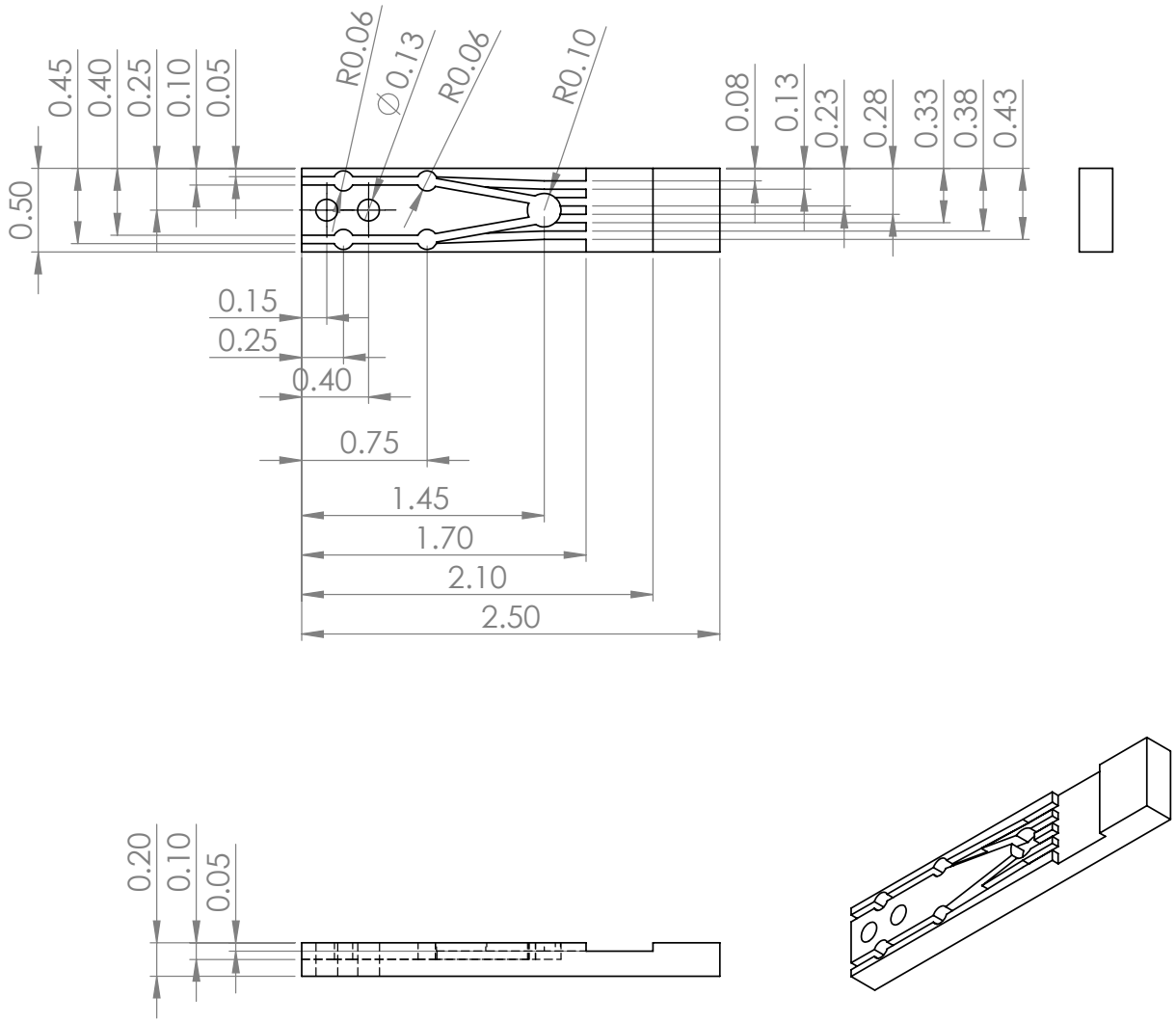

Figure E.1: A colfinger with 4 RF lines. The cylindrical divots are for epoxy to fasten the RF lines. The lines break out into a rectengular section that generally houses coplanar waveguides. A similar coldfinger was used in the electrical and mechanical spin tuning work, utilizing two lines. One line was used for control of the DC electric or strain field, and the other for microwave spin manipulation. In the electrically driven spin resonance work, one line was used for magnetic microwave manipulation and another for electrical microwave manipulation.

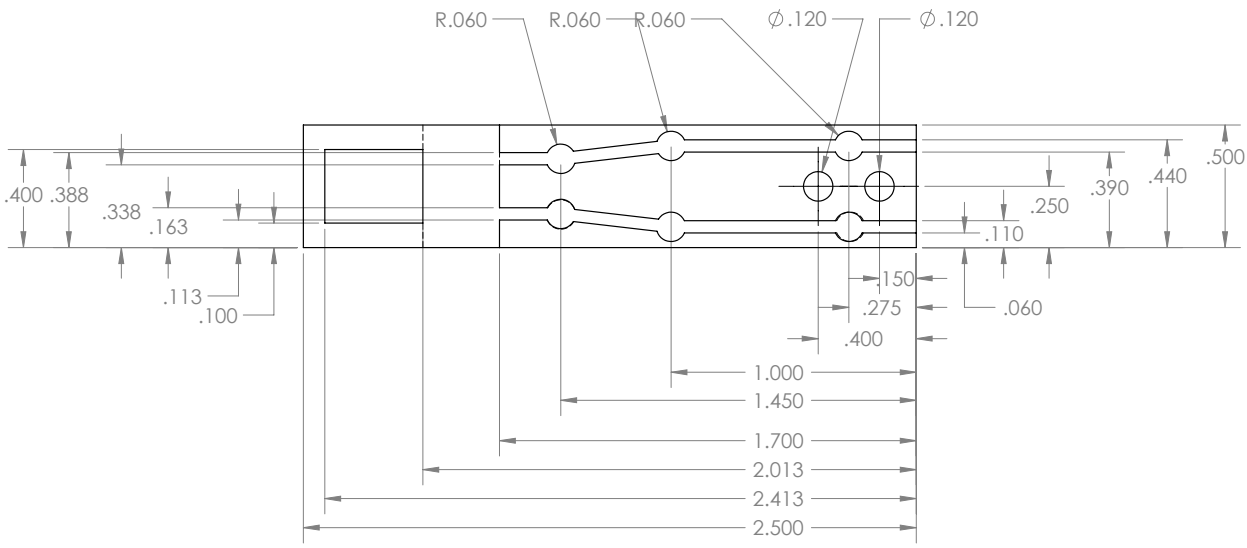

Figure E.2: (1 of 2) A two-sided coldfinger with 3 total RF lines. Two RF lines break out onto coplanar waveguides on one side of the coldfinger and a single RF line breaks out onto another coplanar waveguide on the other side (waveguides not shown). At the top of the cold finger is a hole over which a large sample can be mounted. This design is useful for devices that need to be wirebonded from both sides. We used it for mechanical spin driving experiments (not shown in this thesis).

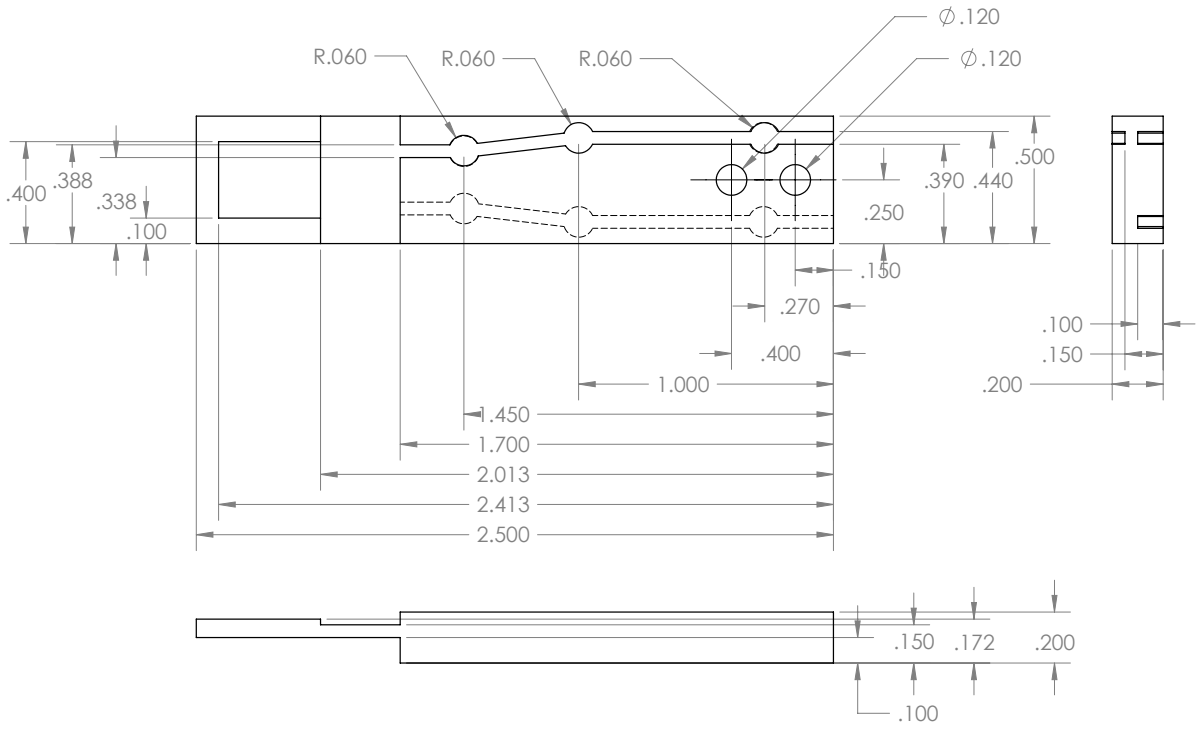

Figure E.3: (2 of 2) A two-sided coldfinger with 3 total RF lines. Two RF lines break out onto coplanar waveguides on one side of the coldfinger and a single RF line breaks out onto another coplanar waveguide on the other side (waveguides not shown). At the top of the cold finger is a hole over which a large sample can be mounted. This design is useful for devices that need to be wirebonded from both sides. We used it for mechanical spin driving experiments (not shown in this thesis).

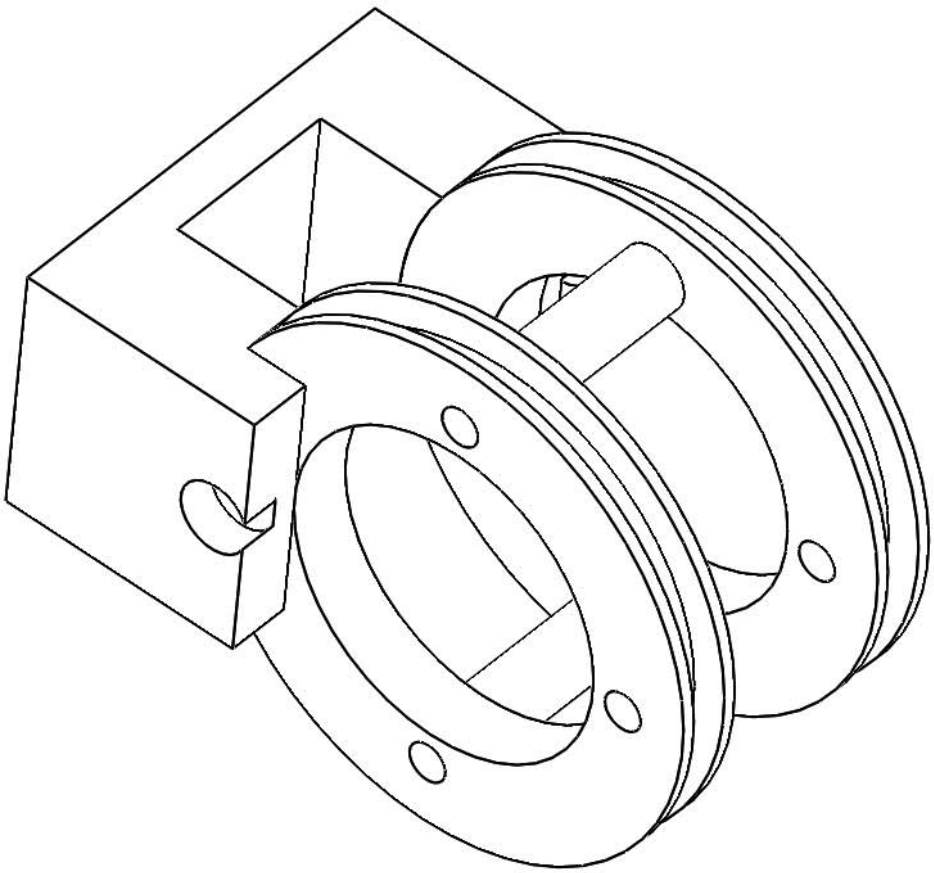

Figure E.4: (1 of 4) A Helmholtz coil assembly, meant to surround a Janis cryostat vacuum shroud. This coil can be used for fine control over a static magnetic magnetic field, usually along the SiC c-axis.

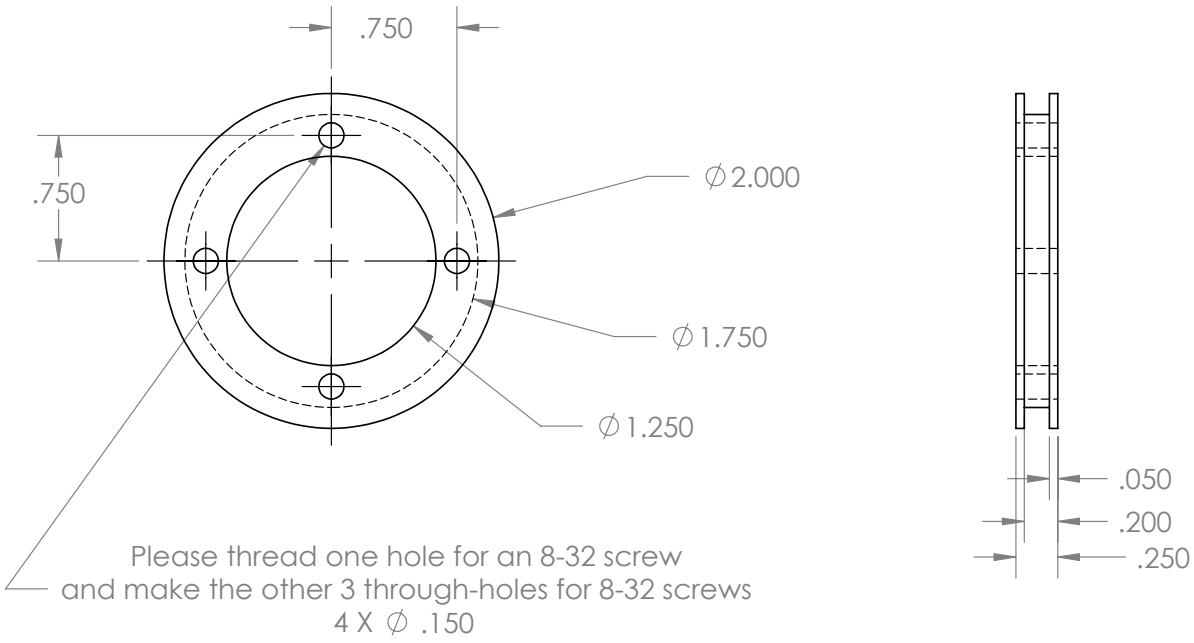

Figure E.5: (2 of 4) A Helmholtz coil assembly, meant to surround a Janis cryostat vacuum shroud. This coil can be used for fine control over a static magnetic magnetic field, usually along the SiC c-axis.

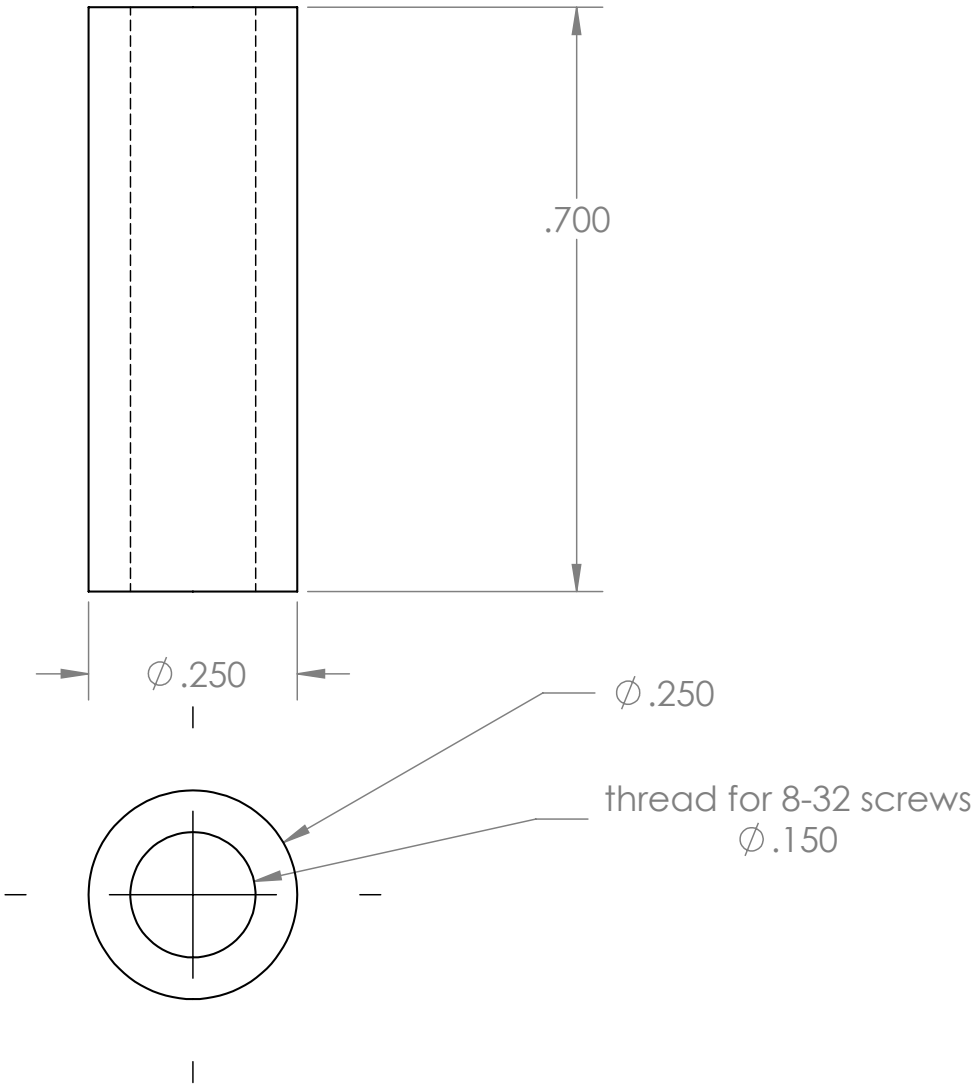

Figure E.6: (3 of 4) A Helmholtz coil assembly, meant to surround a Janis cryostat vacuum shroud. This coil can be used for fine control over a static magnetic magnetic field, usually along the SiC c-axis.

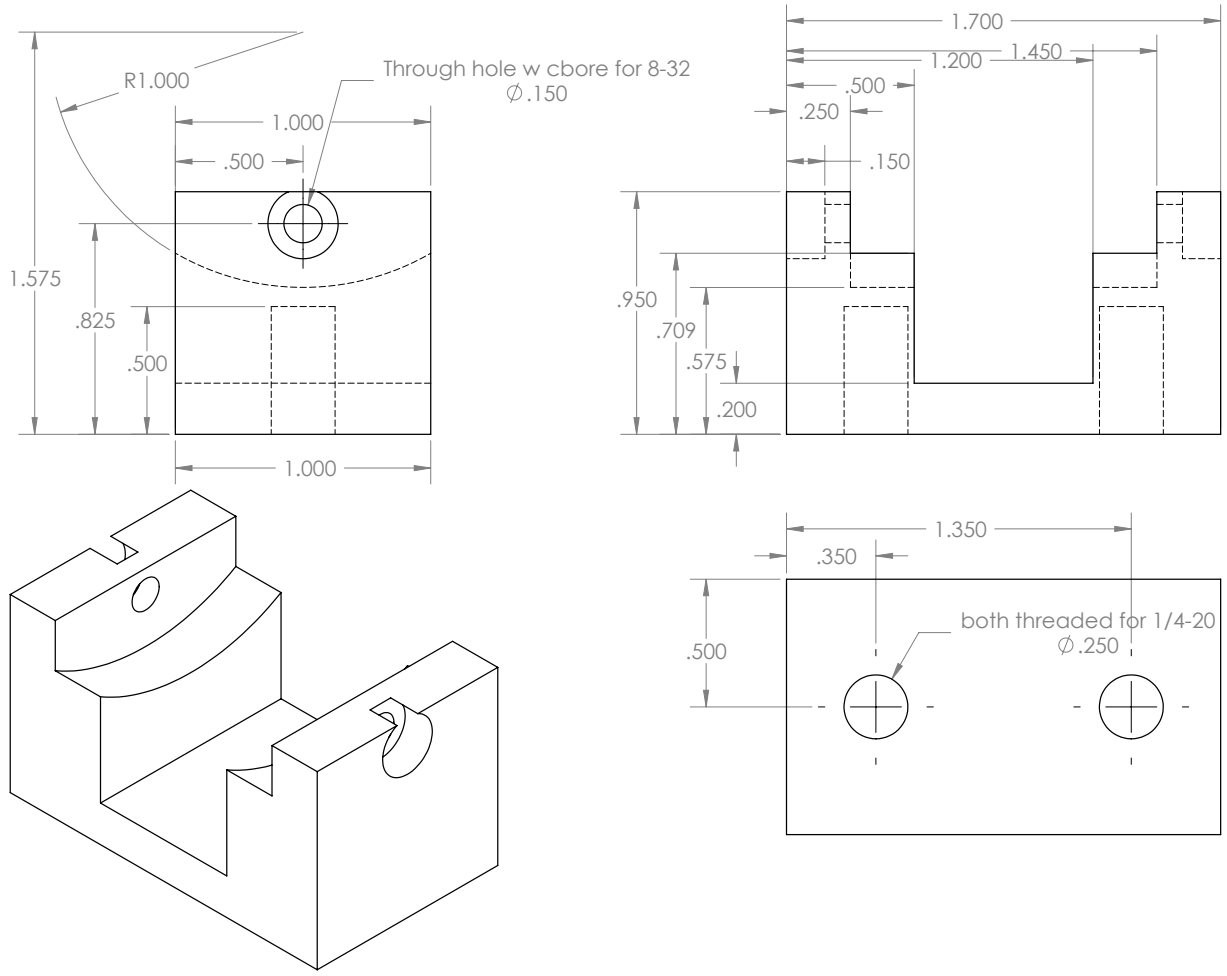

Figure E.7: (4 of 4)A Helmholtz coil assembly, meant to surround a Janis cryostat vacuum shroud. This coil can be used for fine control over a static magnetic magnetic field, usually along the SiC c-axis.

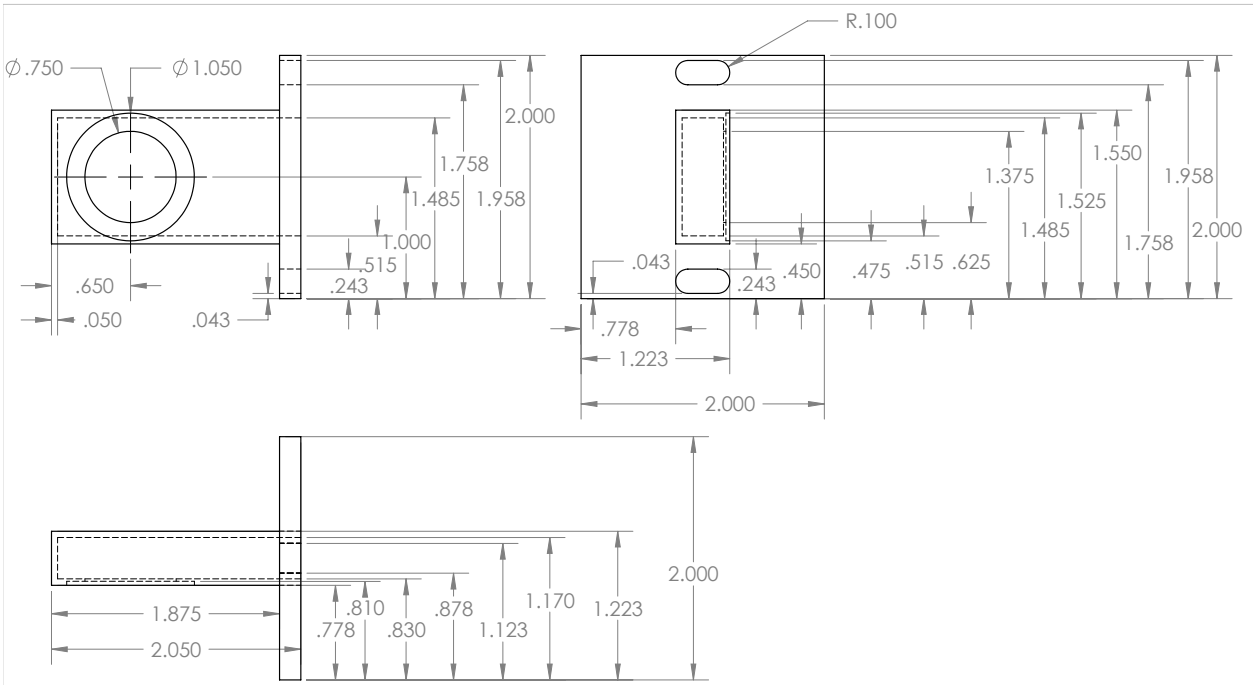

Figure E.8: Vaccum shroud with optical access for a Janis flow cryostat.

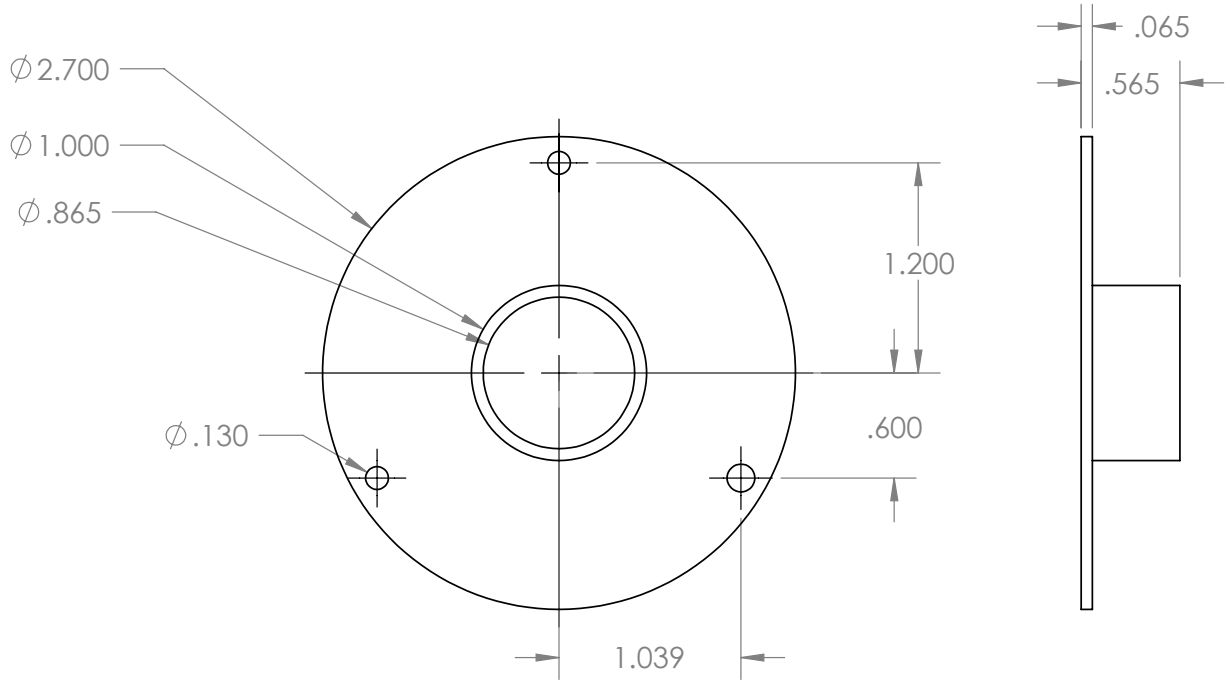

Figure E.9: Radiation shield for a Janis flow cryostat.

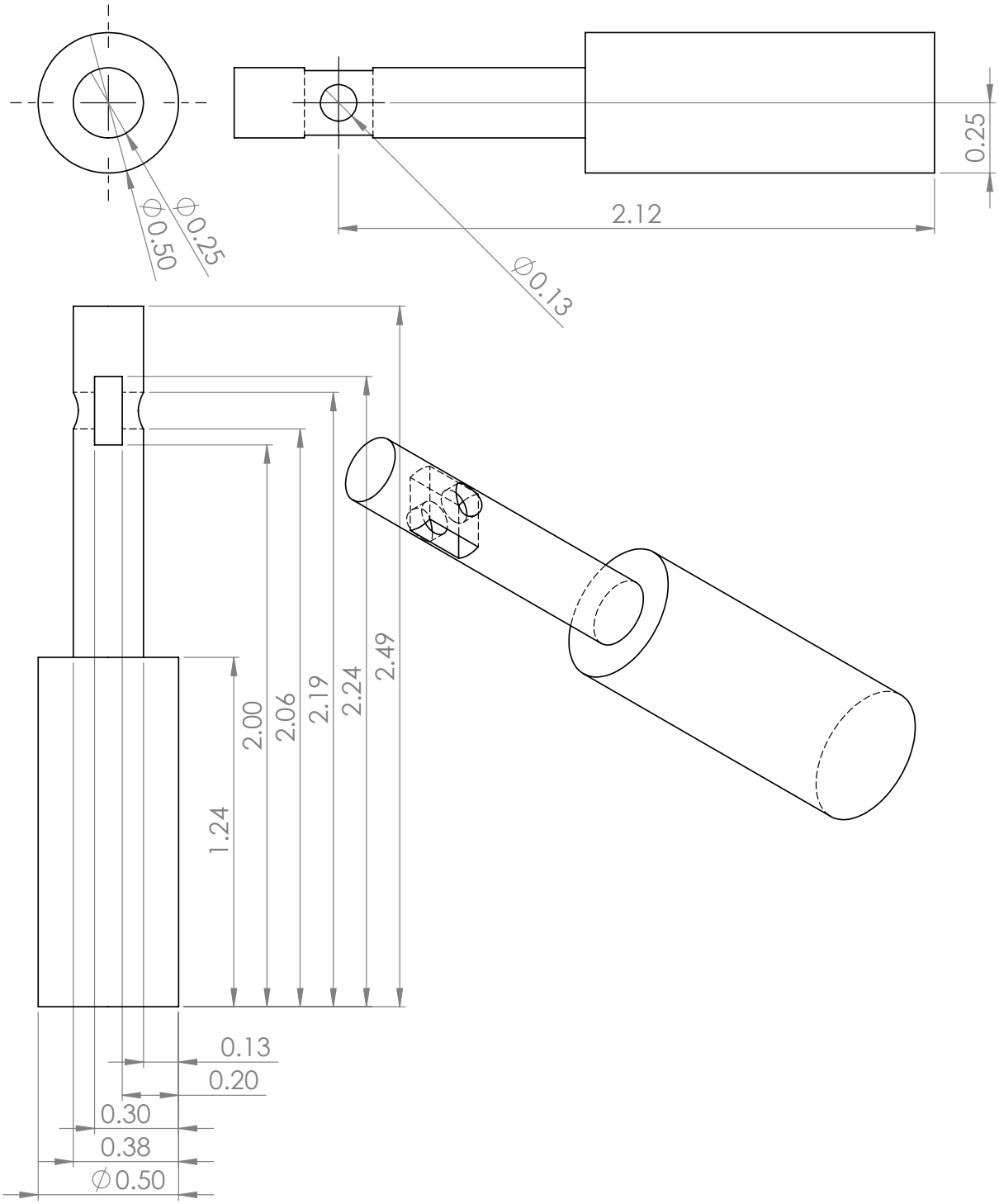

Figure E.10: A mount for SiC wafers for studying spin diffusion in SiC. The material for this mount should have a high thermal conductivity, such as sapphire, AlN, etc.

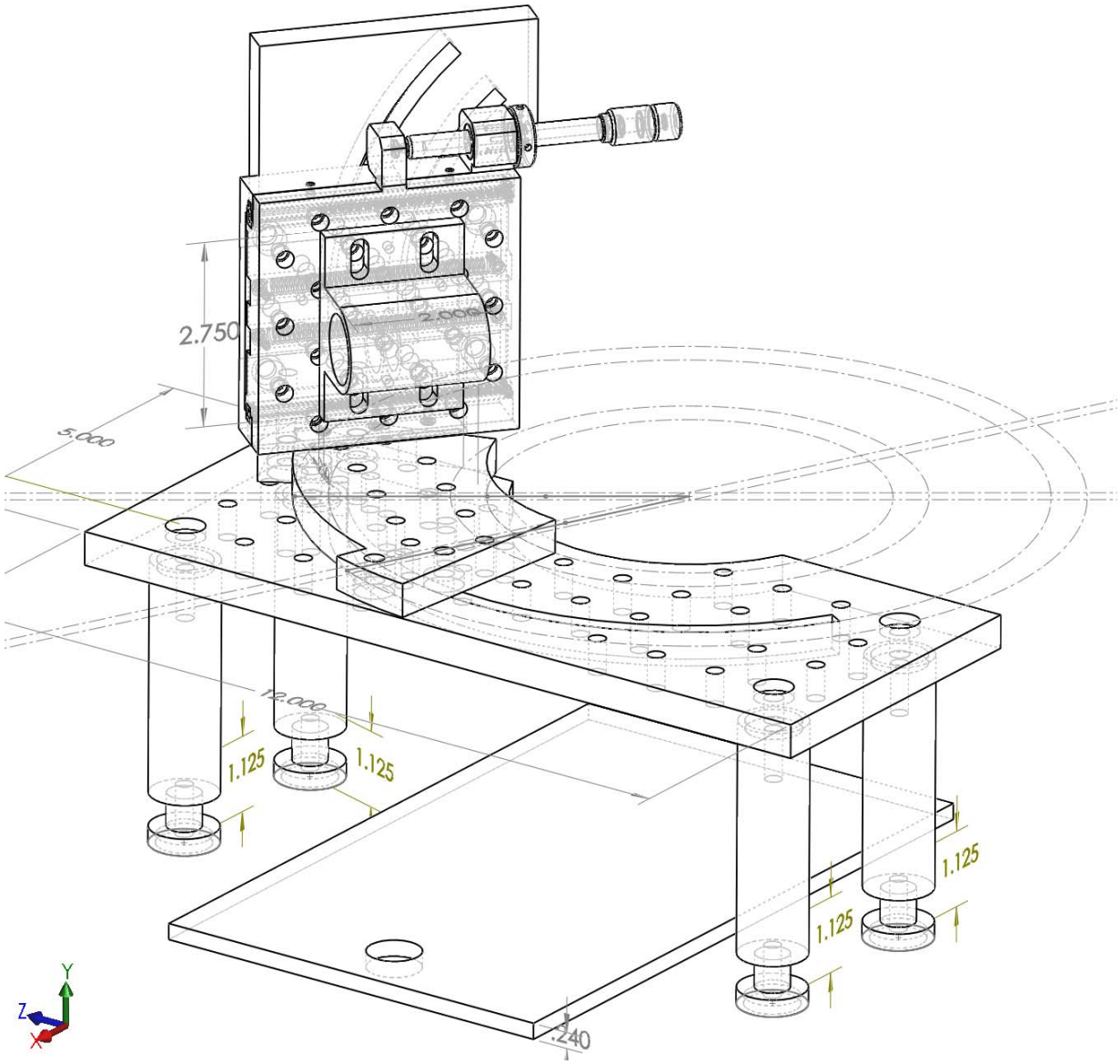

Figure E.11: (1 of 5) Goniometer assembly for a Montana instruments system.

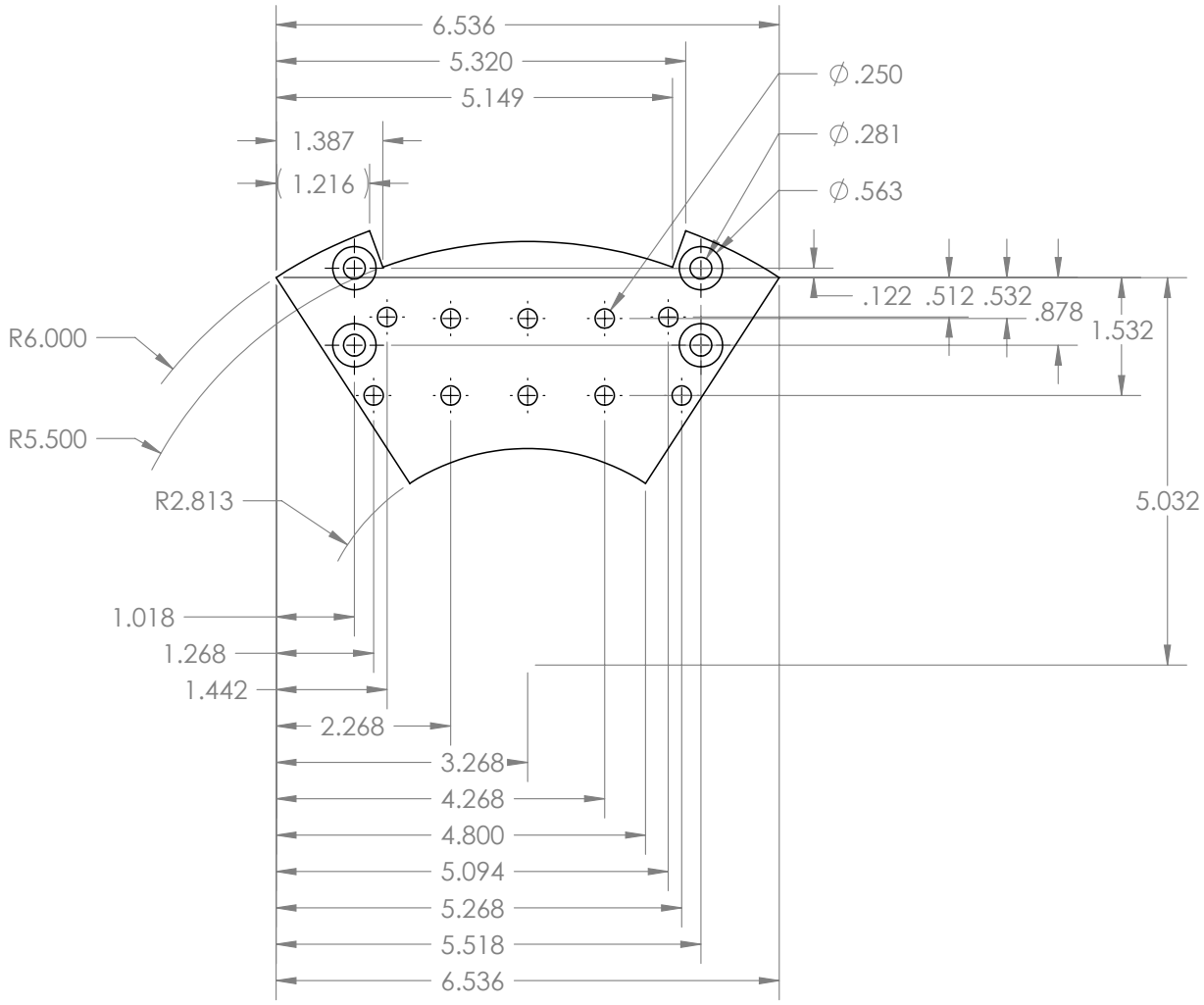

Figure E.12: (2 of 5) Goniometer assembly for a Montana instruments system.

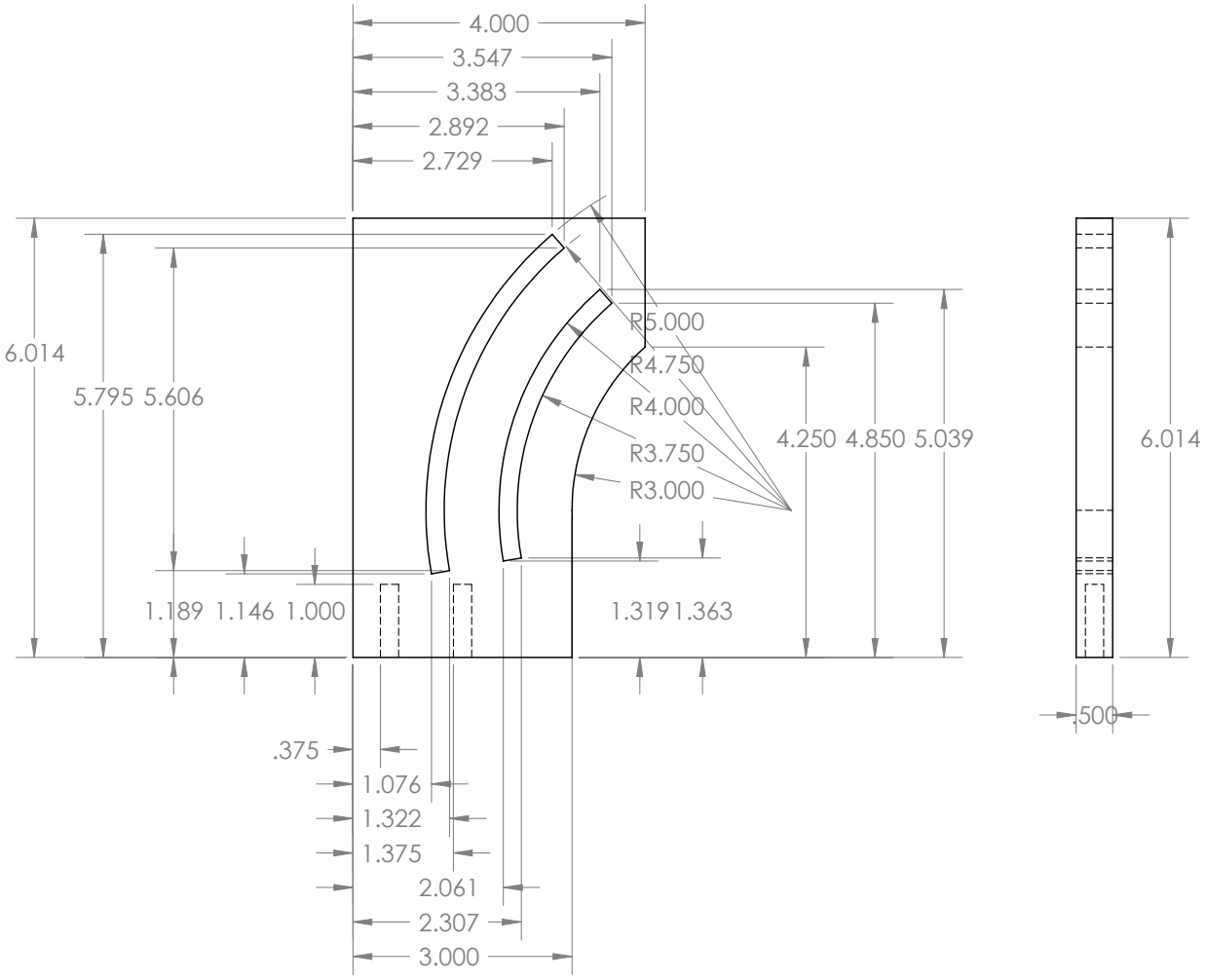

Figure E.13: (3 of 5) Goniometer assembly for a Montana instruments system.

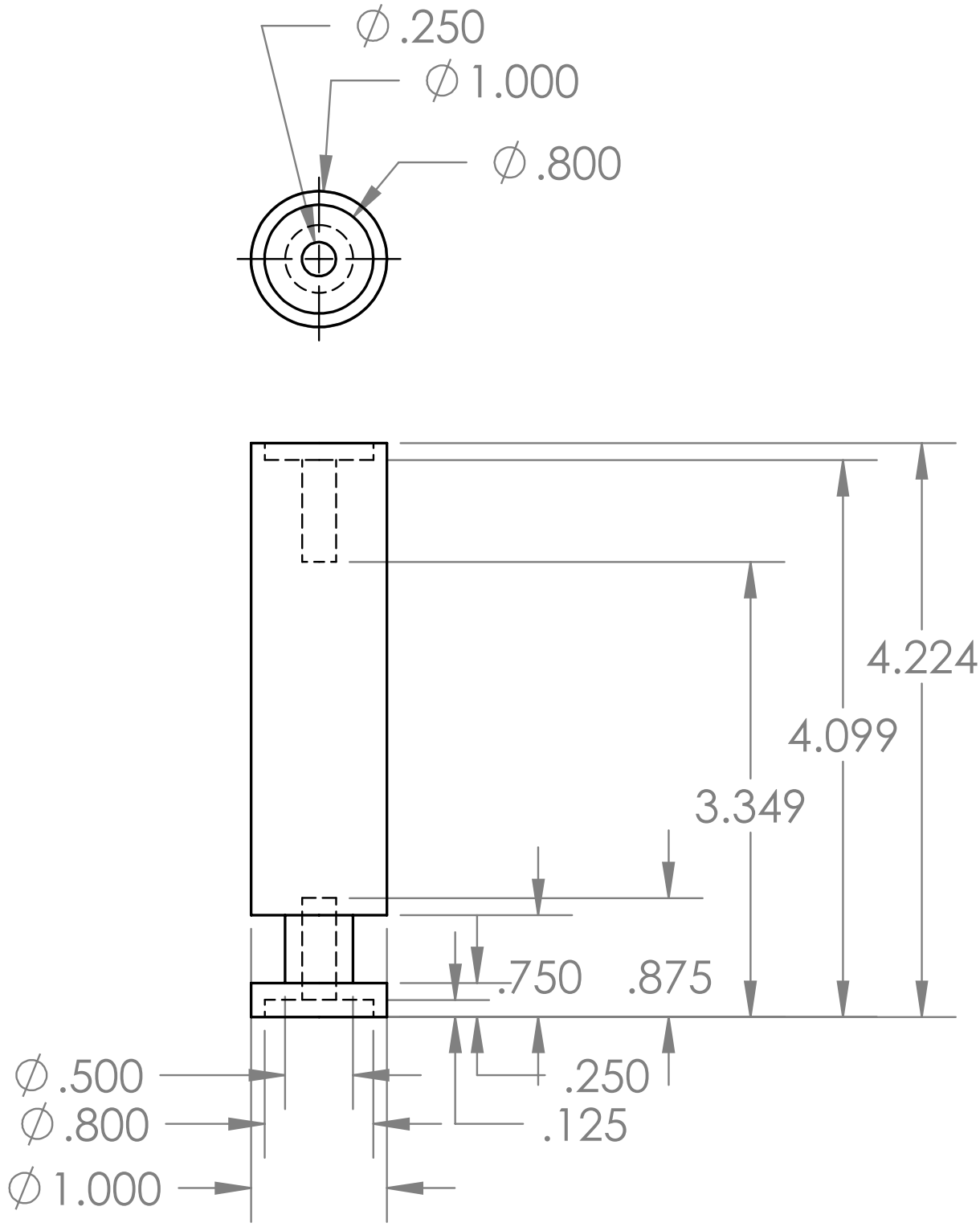

Figure E.14: (4 of 5) Goniometer assembly for a Montana instruments system.

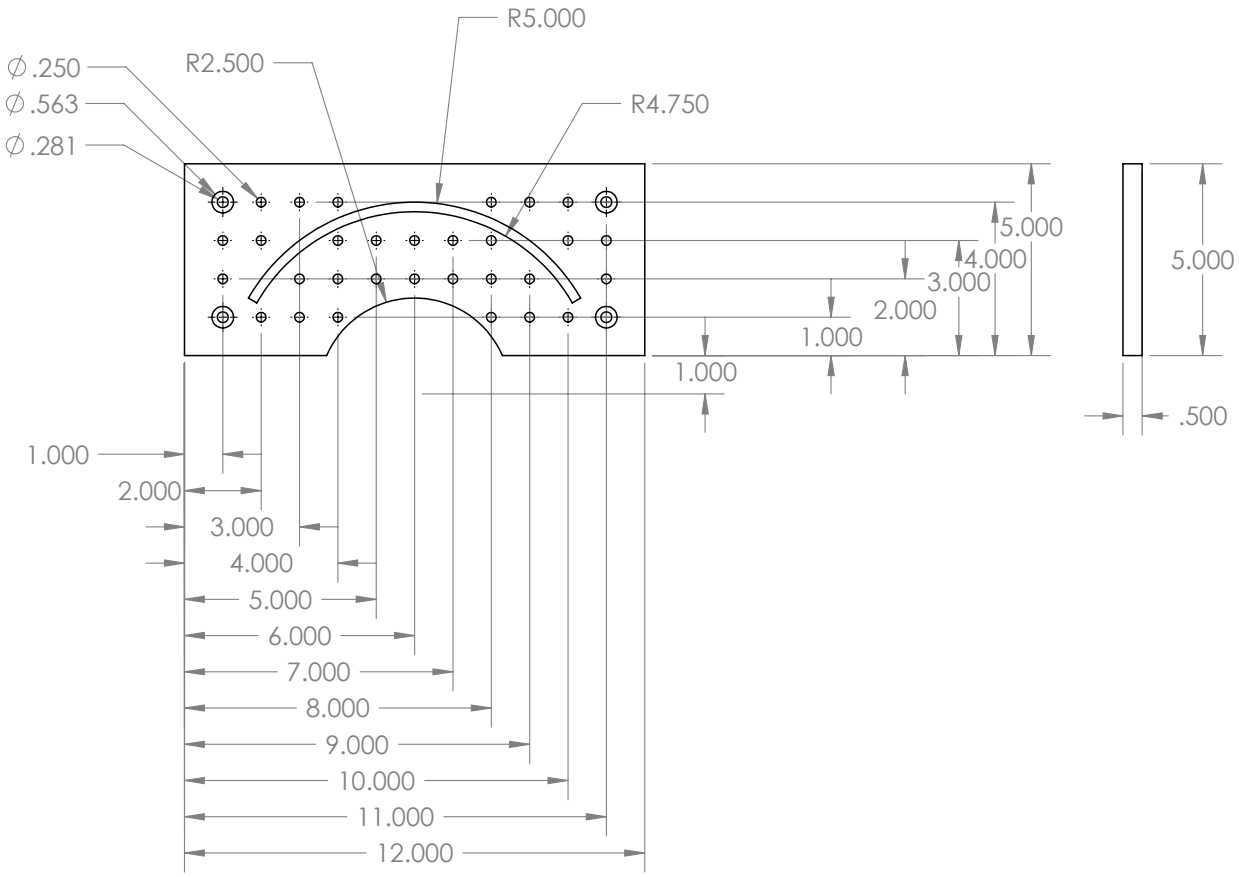

Figure E.15: (5 of 5) Goniometer assembly for a Montana instruments system.

BIBLIOGRAPHY

[1] Turing, A. M. On computable numbers, with an application to the entscheidungsproblem. *Proc. London Math. Soc.* **2**, 544–546 (1936).

[2] Konrad, Z. *Der Computer. Mein Lebenswerk* (Berlin: Springer-Verlag, 1993).

[3] Eckert, J. & Mauchly, J. Electronic numerical integrator and computer (1964). US Patent 3,120,606.

[4] Riordan, M., Hoddeson, L. & Herring, C. The invention of the transistor. *Rev. Mod. Phys.* **71**, S336–S345 (1999).

[5] Edgar, L. Method and apparatus for controlling electric currents (1930). US Patent 1,745,175.

[6] Bardeen, J. Surface states and rectification at a metal semi-conductor contact. *Phys. Rev.* **71**, 717–727 (1947).

[7] Brattain, W. H. Evidence for surface states on semiconductors from change in contact potential on illumination. *Phys. Rev.* **72**, 345–345 (1947).

[8] Bardeen, J. Notebook no. 20780, at&t archives warren, nj (1946).

[9] Bardeen, J. Notebook no. 18194, at&t archives warren, nj (1947).

[10] Bardeen, J. Notebook no. 21780, at&t archives warren, nj (1947).

[11] Rosen, S. Recollections of the philco transact s-2000. *IEEE Ann. Hist. Comp.* **26**, 34–47 (2004).

[12] Dummer, G. Electronic components in great britain 15 (1952).

[13] Kilby, J. Miniaturized electronic circuits (1964). US Patent 3,138,743.

[14] Moore, G. E. Cramming more components onto integrated circuits. *Electronics* 114–117 (1965).

[15] Faggin, F., Hoff, M. & Mazor, S. Memory system for a multi chip digital computer (1974). US Patent 3,821,715.

[16] Markov, I. L. Limits on fundamental limits to computation. *Nature* **512**, 147–154 (2014).

[17] Chau, R. *et al.* High- kappa;/metal-gate stack and its mosfet characteristics. *Elec. Dev. Lett. IEEE* **25**, 408–410 (2004).

[18] Lloyd, S. Ultimate physical limits to computation. *Nature* **406**, 1047–1054 (2000).

[19] Cavin, R., Lugli, P. & Zhirnov, V. Science and engineering beyond moore's law. *Proc. IEEE* **100**, 1720–1749 (2012).

[20] Chien, A. & Karamcheti, V. Moore's law: The first ending and a new beginning. *Comp.* **46**, 48–53 (2013).

[21] Shulaker, M. M. *et al.* Carbon nanotube computer. *Nature* **501**, 526–530 (2013).

[22] Feynman, R. P. Plenty of room at the bottom. *Engin. Sci.* **23**, 22–36 (1960).

[23] Nielsen, M. A. & Chuang, I. L. *Quantum Computation and Quantum Information: 10th Anniversary Edition* (Cambridge University Press, New York, NY, USA, 2011), 10th edn.

[24] Deutsch, D. Quantum theory, the church-turing principle and the universal quantum computer. *Proc. Roy. Soc. Lond. A* **400**, 97–117 (1985).

[25] Shor, P. W. Polynomial-time algorithms for prime factorization and discrete logarithms on a quantum computer. *SIAM J. Comp.* **26**, 1484–1509 (1997).

[26] Grover, L. K. A fast quantum mechanical algorithm for database search. In *Proceedings of the Twenty-eighth Annual ACM Symposium on Theory of Computing*, STOC '96, 212–219 (1996).

[27] Feynman, R. Simulating physics with computers. *Inter. J. Theor. Phys.* **21**, 467–488 (1982).

[28] Harrow, A. W., Hassidim, A. & Lloyd, S. Quantum algorithm for linear systems of equations. *Phys. Rev. Lett.* **103**, 150502 (2009).

[29] Schuld, M., Sinayskiy, I. & Petruccione, F. An introduction to quantum machine learning. *Contemp. Phys.* **56**, 172–185 (2015).

[30] Li, Z., Liu, X., Xu, N. & Du, J. Experimental realization of a quantum support vector machine. *Phys. Rev. Lett.* **114**, 140504 (2015).

[31] Aaronson, S. Read the fine print. *Nat. Phys.* **11**, 291–293 (2015).

[32] Kelly, J. *et al.* State preservation by repetitive error detection in a superconducting quantum circuit. *Nature* **519**, 66–69 (2015). Letter.

[33] Fowler, A. G., Mariantoni, M., Martinis, J. M. & Cleland, A. N. Surface codes: Towards practical large-scale quantum computation. *Phys. Rev. A* **86**, 032324 (2012).

[34] Kimble, H. J. The quantum internet. *Nature* **453**, 1023–1030 (2008).

[35] Wiesner, S. Conjugate coding. *SIGACT News* **15**, 78–88 (1983).

[36] Bennett, C. H. & Brassard, G. Withdrawn: Quantum cryptography: Public key distribution and coin tossing. *Theor. Comp. Sci.* – (2011).

[37] Ekert, A. K. Quantum cryptography based on bell's theorem. *Phys. Rev. Lett.* **67**, 661–663 (1991).

[38] Komar, P. *et al.* A quantum network of clocks. *Nat. Phys.* **10**, 582–587 (2014). Article.

[39] Peev, M. *et al.* The secoqc quantum key distribution network in vienna. *New J. Phys.* **11**, 075001 (2009).

[40] Nauerth, S. *et al.* Air-to-ground quantum communication. *Nat. Photon.* **7**, 382–386 (2013). Letter.

[41] Briegel, H.-J., Dür, W., Cirac, J. I. & Zoller, P. Quantum repeaters: The role of imperfect local operations in quantum communication. *Phys. Rev. Lett.* **81**, 5932–5935 (1998).

[42] Hensen, B. *et al.* Experimental loophole-free violation of a bell inequality using entangled electron spins separated by 1.3 km. *arXiv* **1508**, 05949v1 (2015).

[43] Waldherr, G. *et al.* Quantum error correction in a solid-state hybrid spin register. *Nature* **506**, 204–207 (2014).

[44] Taminiau, T. H., Cramer, J., van der Sar, T., Dobrovitski, V. V. & Hanson, R. Universal control and error correction in multi-qubit spin registers in diamond **9**, 176 (2014).

[45] Tth, G. & Apellaniz, I. Quantum metrology from a quantum information science perspective. *J. Phys. A: Math. Theor.* **47**, 424006 (2014).

[46] Giovannetti, V., Lloyd, S. & Maccone, L. Advances in quantum metrology. *Nat. Photon.* **5**, 222–229 (2011).

[47] Le Sage, D. *et al.* Optical magnetic imaging of living cells. *Nature* **496**, 486–489 (2013). Letter.

[48] Kucsko, G. *et al.* Nanometre scale thermometry in a living cell. *Nature* **500**, 54–58 (2013).

[49] Nicholson, T. L. . *et al.* Systematic evaluation of an atomic clock at 2×10^{-18} total uncertainty. *Nat. Commun.* **6** (2015).

[50] Shi, F. *et al.* Single-protein spin resonance spectroscopy under ambient conditions. *Science* **347**, 1135–1138 (2015).

[51] Ohno, K. *et al.* Engineering shallow spins in diamond with nitrogen delta-doping. *App. Phys. Lett.* **101**, 082413 (2012).

[52] Hohn, F. E. *Applied Boolean Algebra - An Elementary Introduction* (The Macmillan Company, New York, NY, USA, 1966).

[53] Einstein, A., Podolsky, B. & Rosen, N. Can quantum-mechanical description of physical reality be considered complete? *Phys. Rev.* **47**, 777–780 (1935).

[54] Klimov, P. V., Falk, A. L., Christle, D. J., Dobrovitski, V. V. & Awschalom, D. D. Entanglement at ambient conditions in a macroscopic solid state spin ensemble. *Sci. Adv.* **1**, e1501015 (2015).

[55] Bernien, H. *et al.* Heralded entanglement between solid-state qubits separated by three metres. *Nature* **497**, 86–90 (2013).

[56] Steffen, M. *et al.* Measurement of the entanglement of two superconducting qubits via state tomography. *Science* **313**, 1423–1425 (2006).

[57] Simmons, S. *et al.* Entanglement in a solid-state spin ensemble. *Nature* **470**, 69–72 (2011).

[58] Julsgaard, B., Kozhekin, A. & Polzik, E. S. Experimental long-lived entanglement of two macroscopic objects. *Nature* **413**, 400–403 (2001).

[59] Igor Zutic, J. F. & Sarma, S. D. Spintronics: Fundamentals and applications. *Rev. Mod. Phys.* **76**, 323–410 (2004).

[60] Zurek, W. H. Decoherence, einselection, and the quantum origins of the classical. *Rev. Mod. Phys.* **75**, 715–775 (2003).

[61] Hahn, E. L. Spin echoes. *Phys. Rev.* **80**, 580–594 (1950).

[62] Carr, H. Y. & Purcell, E. M. Effects of diffusion on free precession in nuclear magnetic resonance experiments. *Phys. Rev.* **94**, 630–638 (1954).

[63] Meiboom, S. & Gill, D. Modified spinecho method for measuring nuclear relaxation times. *Rev. Sci. Inst.* **29**, 688–691 (1958).

[64] Yang, L.-P. *et al.* Electron spin decoherence in silicon carbide nuclear spin bath. *Phys. Rev. B* **90**, 241203 (2014).

[65] Seo, H. *et al.* Decoherence of electron spins in silicon carbide. *in preparation* (2015).

[66] Dobrovitski, V. V., Feiguin, A. E., Awschalom, D. D. & Hanson, R. Decoherence dynamics of a single spin versus spin ensemble. *Phys. Rev. B* **77**, 245212 (2008).

[67] Shor, P. W. Scheme for reducing decoherence in quantum computer memory. *Phys. Rev. A* **52**, R2493–R2496 (1995).

[68] Divincenzo, D. Topics in quantum computers. In Sohn, L., Kouwenhoven, L. & Schn, G. (eds.) *Mesoscopic Electron Transport*, vol. 345 of *NATO ASI Series*, 657–677 (Springer Netherlands, 1997).

[69] Cory, D. G., Fahmy, A. F. & Havel, T. F. Ensemble quantum computing by nmrspectroscopy. *Proc. Nat. Acad. Sci.* **94**, 1634–1639 (1997).

[70] Gershenfeld, N. A. & Chuang, I. L. Bulk spin-resonance quantum computation. *Science* **275**, 350–356 (1997).

[71] Kane, B. E. A silicon-based nuclear spin quantum computer. *Nature* **393**, 133–137 (1998).

[72] Cirac, J. I. & Zoller, P. Quantum computations with cold trapped ions. *Phys. Rev. Lett.* **74**, 4091–4094 (1995).

[73] Domokos, P., Raimond, J. M., Brune, M. & Haroche, S. Simple cavity-qed two-bit universal quantum logic gate: The principle and expected performances. *Phys. Rev. A* **52**, 3554–3559 (1995).

[74] Turchette, Q. A., Hood, C. J., Lange, W., Mabuchi, H. & Kimble, H. J. Measurement of conditional phase shifts for quantum logic. *Phys. Rev. Lett.* **75**, 4710–4713 (1995).

[75] Chuang, I. L. & Yamamoto, Y. Simple quantum computer. *Phys. Rev. A* **52**, 3489–3496 (1995).

[76] Loss, D. & DiVincenzo, D. P. Quantum computation with quantum dots. *Phys. Rev. A* **57**, 120–126 (1998).

[77] Makhlin, Y., Schön, G. & Shnirman, A. Quantum-state engineering with josephson-junction devices. *Rev. Mod. Phys.* **73**, 357–400 (2001).

[78] Yu, P. Y. & Cardona, M. *Fundamentals of Semiconductors* (Springer-Verlag, 1996), 1st edn.

[79] Weber, J. R. *et al.* Quantum computing with defects. *Proc. Nat. Acad. Sci.* **107**, 8513–8518 (2010).

[80] Doherty, M. W., Manson, N. B., Delaney, P. & Hollenberg, L. C. L. The negatively charged nitrogen-vacancy centre in diamond: the electronic solution. *New J. Phys.* **13**, 025019 (2011).

[81] Dobrovitski, V., Fuchs, G., Falk, A., Santori, C. & Awschalom, D. Quantum control over single spins in diamond. *Ann. Rev. Cond. Matt. Phys.* **4**, 23–50 (2013).

[82] Mamin, H. J. *et al.* Nanoscale nuclear magnetic resonance with a nitrogen-vacancy spin sensor. *Science* **339**, 557–560 (2013).

[83] Staudacher, T. *et al.* Nuclear magnetic resonance spectroscopy on a (5-nanometer)3 sample volume. *Science* **339**, 561–563 (2013).

[84] Pfaff, W. *et al.* Unconditional quantum teleportation between distant solid-state qubits. *Science* **345**, 532–535 (2014).

[85] Baranov, P. *et al.* Epr identification of the triplet ground state and photoinduced population inversion for a si-c divacancy in silicon carbide. *J. Exper. Theor. Phys. Lett.* **82**, 441–443 (2005).

[86] Son, N. T. *et al.* Divacancy in 4h-sic. *Phys. Rev. Lett.* **96**, 055501 (2006).

[87] Koehl, W. F., Buckley, B. B., Heremans, F. J., Calusine, G. & Awschalom, D. D. Room temperature coherent control of defect spin qubits in silicon carbide. *Nature* **477**, 84–87 (2011).

[88] Falk, A. L. *et al.* Polytype control of spin qubits in silicon carbide. *Nature Comm.* **4** (2013).

[89] Carlos, W., Glaser, E. & Shanabrook, B. Optical and magnetic resonance signatures of deep levels in semi-insulating 4h sic. *Physica B: Condensed Matter* **340342**, 151 – 155 (2003). Proceedings of the 22nd International Conference on Defects in Semiconductors.

[90] B. Magnusson, E. J. Optical characterization of deep level defects in sic. *Materials Science Forum* .

[91] Carlos, W. E., Garces, N. Y., Glaser, E. R. & Fanton, M. A. Annealing of multivacancy defects in 4h-sic. *Phys. Rev. B* **74**, 235201 (2006).

[92] Gali, A. Time-dependent density functional study on the excitation spectrum of point defects in semiconductors. *Phys. Stat. Solid. B* **248**, 1337–1346 (2011).

[93] Saddow, S. & Agarwal, A. *Advances in Silicon Carbide Processing and Applications* (Artech House, 2004), 1st edn.

[94] Liu, L. & Edgar, J. Substrates for gallium nitride epitaxy. *Mater. Sci. Eng.: R: Rep.* **37**, 61 – 127 (2002).

[95] Wright, N. G. & Horsfall, A. B. Sic sensors: a review. *J. Phys. D: App. Phys.* **40**, 6345 (2007).

[96] Falk, A. L. *et al.* Electrically and mechanically tunable electron spins in silicon carbide color centers. *Phys. Rev. Lett.* **112**, 187601 (2014).

[97] Klimov, P. V., Falk, A. L., Buckley, B. B. & Awschalom, D. D. Electrically driven spin resonance in silicon carbide color centers. *Phys. Rev. Lett.* **112**, 087601 (2014).

[98] Fuchs, G. D. *et al.* Excited-state spectroscopy using single spin manipulation in diamond. *Phys. Rev. Lett.* **101**, 117601 (2008).

[99] Fuchs, G. D. *et al.* Excited-state spin coherence of a single nitrogen-vacancy centre in diamond. *Nat. Phys.* **6**, 668–672 (2010).

[100] Falk, A. L. *et al.* Optical polarization of nuclear spins in silicon carbide. *Phys. Rev. Lett.* **114**, 247603 (2015).

[101] Gali, A., Fyta, M. & Kaxiras, E. Ab initio supercell calculations on nitrogen-vacancy center in diamond: Electronic structure and hyperfine tensors. *Phys. Rev. B* **77**, 155206 (2008).

[102] Ivady, V. *et al.* Theoretical model of the dynamic spin polarization of nuclei coupled to paramagnetic point defects in diamond and silicon carbide. *Phys. Rev. B.* **92**, 115206 (2015).

[103] Smeltzer, B., McIntyre, J. & Childress, L. Robust control of individual nuclear spins in diamond. *Phys. Rev. A* **80**, 050302 (2009).

[104] Christle, D. *et al.* Isolated electron spins in silicon carbide with millisecond coherence times. *Nat. Mater.* **14**, 160–163 (2015).

[105] Dolde, F. *et al.* Room-temperature entanglement between single defect spins in diamond. *Nat. Phys.* **9**, 193–143 (2013).

[106] Neumann, P. *et al.* Multipartite entanglement among single spins in diamond. *Science* **320**, 1326–1329 (2008).

[107] Taminiau, T. H. *et al.* Detection and control of individual nuclear spins using a weakly coupled electron spin. *Phys. Rev. Lett.* **109**, 137602 (2012).

[108] Lebedev, A. *et al.* Sic heteropolytype structures for optical applications. In *Lasers and Electro-Optics, 2007 and the International Quantum Electronics Conference. CLEOE-IQEC 2007. European Conference on*, 1–1 (2007).

[109] Chandrashekhar, M. V. S., Thomas, C. I., Lu, J. & Spencer, M. G. Observation of a two dimensional electron gas formed in a polarization doped c-face 3c4h sic heteropolytype junction. *App. Phys. Lett.* **91**, 033503 (2007).

[110] Ruderman, M. A. & Kittel, C. Indirect exchange coupling of nuclear magnetic moments by conduction electrons. *Phys. Rev.* **96**, 99–102 (1954).

[111] Kasuya, T. A theory of metallic ferro- and antiferromagnetism on zener's model. *Prog. Theoret. Phys.* **16**, 45–57 (1956).

[112] Yosida, K. Magnetic properties of cu-mn alloys. *Phys. Rev.* **106**, 893–898 (1957).

[113] Weimer, H., Yao, N. Y. & Lukin, M. D. Collectively enhanced interactions in solid-state spin qubits. *Phys. Rev. Lett.* **110**, 067601 (2013).

[114] Schuster, D. I. *et al.* High-cooperativity coupling of electron-spin ensembles to superconducting cavities. *Phys. Rev. Lett.* **105**, 140501 (2010).

[115] Chang, Y. & Sun, C. P. Analog of the electromagnetically-induced-transparency effect for two nanomechanical or micromechanical resonators coupled to a spin ensemble. *Phys. Rev. A* **83**, 053834 (2011).

[116] Duan, L.-M., Lukin, M. D., Cirac, J. I. & Zoller, P. Long-distance quantum communication with atomic ensembles and linear optics. *Nature* **414**, 413–418 (2001).

[117] Robledo, L. *et al.* High-fidelity projective read-out of a solid-state spin quantum register. *Nature* **477**, 574–578 (2011).

[118] Ryan, C. A., Laforest, M. & Laflamme, R. Randomized benchmarking of single- and multi-qubit control in liquid-state nmr quantum information processing. *New J. Phys.* **11**, 013034 (2009).

[119] Hartman, J. S. *et al.* Nmr studies of nitrogen doping in the 4h polytype of silicon carbide: Site assignments and spinlattice relaxation. *J. Phys. Chem. C* **113**, 15024–15036 (2009).

[120] Togan, E. *et al.* Quantum entanglement between an optical photon and a solid-state spin qubit. *Nature* **466**, 730–734 (2010).

[121] Pozar, D. *Microwave Engineering* (Wiley, 2004).

[122] Jacques, V. *et al.* Dynamic polarization of single nuclear spins by optical pumping of nitrogen-vacancy color centers in diamond at room temperature. *Phys. Rev. Lett.* **102**, 057403 (2009).

[123] Dolde, F. *et al.* A silicon carbide room-temperature single-photon source. *Nat. Phys.* **7**, 459–463 (2011).

[124] Oort, E. V. & Glasbeek, M. Electric-field-induced modulation of spin echoes of n-v centers in diamond. *Chem. Phys. Lett.* **168**, 529 – 532 (1990).

[125] Saddow, S. *Silicon Carbide Biotechnology: A Biocompatible Semiconductor for Advanced Biomedical Devices and Applications* (Elsevier Science, 2011), 1st edn.

[126] Yang, Y. T. *et al.* Monocrystalline silicon carbide nanoelectromechanical systems. *App. Phys. Lett.* **78** (2001).

[127] Vainer, V. S. & II'in, V. A. Electron spin resonance of exchange-coupled vacancy pairs in hexagonal silicon carbide. *Sov. Phys. Solid State* **23** (1981).

[128] Doherty, M. W. *et al.* Electronic properties and metrology applications of the diamond nv- center under pressure. *Phys. Rev. Lett.* **112**, 047601 (2014).

[129] Davies, G. & Hamer, M. F. Optical studies of the 1.945 ev vibronic band in diamond. *Proc. Roy. Soc. Lond. A Math. Phys. Sci.* **348**, pp. 285–298 (1976).

[130] Grazioso, F. *et al.* Measurement of the full stress tensor in a crystal using photoluminescence from point defects: The example of nitrogen vacancy centers in diamond. *App. Phys. Lett.* **103**, 101905 (2013).

[131] Taylor, J. *et al.* High-sensitivity diamond magnetometer with nanoscale resolution. *Nat. Phys.* **4**, 810–816 (2008).

[132] Lawall, J. & Kessler, E. Michelson interferometry with 10 pm accuracy. *Rev. Sci. Inst.* **71**, 2669–2676 (2000).

[133] Steiner, M., Neumann, P., Beck, J., Jelezko, F. & Wrachtrup, J. Universal enhancement of the optical readout fidelity of single electron spins at nitrogen-vacancy centers in diamond. *Phys. Rev. B* **81**, 035205 (2010).

[134] MacQuarrie, E. R., Gosavi, T. A., Jungwirth, N. R., Bhave, S. A. & Fuchs, G. D. Mechanical spin control of nitrogen-vacancy centers in diamond. *Phys. Rev. Lett.* **111**, 227602 (2013).

[135] Bennett, S. D. *et al.* Phonon-induced spin-spin interactions in diamond nanostructures: Application to spin squeezing. *Phys. Rev. Lett.* **110**, 156402 (2013).

[136] Kepesidis, K. V., Bennett, S. D., Portolan, S., Lukin, M. D. & Rabl, P. Phonon cooling and lasing with nitrogen-vacancy centers in diamond. *Phys. Rev. B* **88**, 064105 (2013).

[137] Neumann, P. *et al.* Quantum register based on coupled electron spins in a room-temperature solid. *Nat. Phys.* **6**, 249–253 (2010).

[138] Lai, N. *et al.* Pauli spin blockade in a highly tunable silicon double quantum dot. *Sci. Rep.* **1**, 110 (2011).

[139] Bell, R. L. Electric dipole spin transitions in insb. *Phys. Rev. Lett.* **9**, 52–54 (1962).

[140] Kato, Y. *et al.* Gigahertz electron spin manipulation using voltage-controlled g-tensor modulation. *Science* **299**, 1201–1204 (2003).

[141] Rashba, E. I. & Efros, A. L. Orbital mechanisms of electron-spin manipulation by an electric field. *Phys. Rev. Lett.* **91**, 126405 (2003).

[142] Tang, J.-M., Levy, J. & Flatté, M. E. All-electrical control of single ion spins in a semiconductor. *Phys. Rev. Lett.* **97**, 106803 (2006).

[143] Nowack, K. C., Koppens, F. H. L., Nazarov, Y. V. & Vandersypen, L. M. K. Coherent control of a single electron spin with electric fields. *Science* **318**, 1430–1433 (2007).

[144] Laird, E. A. *et al.* Hyperfine-mediated gate-driven electron spin resonance. *Phys. Rev. Lett.* **99**, 246601 (2007).

[145] Pioro-Ladrie‘re, M. *et al.* Electrically driven single-electron spin resonance in a slanting zeeman field. *Nat. Phys.* **4**, 776–779 (2008).

[146] S. Nadj-Perge, E. B., S.M. Frolov & Kouwenhoven, L. Spinorbit qubit in a semiconductor nanowire. *Nature* **468**, 10841087 (2010).

[147] George, R. E., Edwards, J. P. & Ardavan, A. Coherent spin control by electrical manipulation of the magnetic anisotropy. *Phys. Rev. Lett.* **110**, 027601 (2013).

[148] Son, N. T. *et al.* Optically detected magnetic resonance studies of intrinsic defects in 6h-sic. *Semic. Sci. Tech.* **14**, 1141 (1999).

[149] Riedel *et al.* Resonant addressing and manipulation of silicon vacancy qubits in silicon carbide. *Phys. Rev. Lett.* **109**, 226402 (2012).

[150] Lingner, T. *et al.* Structure of the silicon vacancy in 6h-sic after annealing identified as the carbon vacancy carbon antisite pair. *Phys. Rev. B* **64**, 245212 (2001).

[151] Isoya, J. *et al.* Epr identification of intrinsic defects in sic. *Phys. Stat. Solid. B* **245**, 1298–1314 (2008).

[152] Klein, P. B. *Silicon Carbide* (Wiley-VCH, Weinheim, 2010), 1st edn.

[153] Doherty, M. W. *et al.* Theory of the ground-state spin of the nv- center in diamond. *Phys. Rev. B* **85**, 205203 (2012).

[154] Lanyon, B. *et al.* Simplifying quantum logic using higher-dimensional hilbert spaces. *Nat. Phys.* **5**, 134–140 (2009).

[155] Hardeman, G. Electron and nuclear spin resonance in n-type silicon carbide. *J. Phys. and Chem. Solid* **24**, 1223 – 1231 (1963).

[156] Lampel, G. Nuclear dynamic polarization by optical electronic saturation and optical pumping in semiconductors. *Phys. Rev. Lett.* **20**, 491–493 (1968).

[157] Henstra, A., Lin, T.-S., Schmidt, J. & Wenckebach, W. High dynamic nuclear polarization at room temperature. *Chem. Phys. Lett.* **165**, 6 – 10 (1990).

[158] He, X.-F., Manson, N. B. & Fisk, P. T. H. Paramagnetic resonance of photoexcited nv defects in diamond. i. level anticrossing in the 3a ground state. *Phys. Rev. B* **47**, 8809–8815 (1993).

[159] Smeltzer, B., Childress, L. & Gali, A. 13 c hyperfine interactions in the nitrogen-vacancy centre in diamond. *New J. Phys.* **13**, 025021 (2011).

[160] Fischer, R., Jarmola, A., Kehayias, P. & Budker, D. Optical polarization of nuclear ensembles in diamond. *Phys. Rev. B* **87**, 125207 (2013).

[161] Fischer, R. *et al.* Bulk nuclear polarization enhanced at room temperature by optical pumping. *Phys. Rev. Lett.* **111**, 057601 (2013).

[162] Puttisong, Y. *et al.* Efficient room-temperature nuclear spin hyperpolarization of a defect atom in a semiconductor. *Nat. Commun.* **4**, 1751 (2013). Article.

[163] Zwier, O., OShea, D., Onur, A. & Wal, C. Coherent control of single spins in silicon carbide at room temperature. *Sci. Rep.* **5** (2015).

[164] Ajoy, A. & Cappellaro, P. Stable three-axis nuclear-spin gyroscope in diamond. *Phys. Rev. A* **86**, 062104 (2012).

[165] Ledbetter, M. P., Jensen, K., Fischer, R., Jarmola, A. & Budker, D. Gyroscopes based on nitrogen-vacancy centers in diamond. *Phys. Rev. A* **86**, 052116 (2012).

[166] Hartman, J. S., Narayanan, A. & Wang, Y. Spin-lattice relaxation in the 6h polytype of silicon carbide. *J. Am. Chem. Soc.* **116**, 4019–4027 (1994).

[167] Patrick, L. & Choyke, W. J. Photoluminescence of radiation defects in ion-implanted 6h sic. *Phys. Rev. B* **5**, 3253–3259 (1972).

[168] Laloy, E. & Vrugt, J. A. High-dimensional posterior exploration of hydrologic models using multiple-try dream(zs) and high-performance computing. *Wat. Resour. Res.* **48** (2012).

[169] Mims, W. B., Nassau, K. & McGee, J. D. Spectral diffusion in electron resonance lines. *Phys. Rev.* **123**, 2059–2069 (1961).

[170] Kresse, G. & Hafner, J. Ab initio molecular-dynamics simulation of the liquid-metal amorphous-semiconductor transition in germanium. *Phys. Rev. B* **49**, 14251–14269 (1994).

[171] Kresse, G. & Furthmüller, J. Efficient iterative schemes for ab initio total-energy calculations using a plane-wave basis set. *Phys. Rev. B* **54**, 11169–11186 (1996).

[172] Blöchl, P. E. Projector augmented-wave method. *Phys. Rev. B* **50**, 17953–17979 (1994).

[173] Perdew, J. P., Burke, K. & Ernzerhof, M. Generalized gradient approximation made simple. *Phys. Rev. Lett.* **77**, 3865–3868 (1996).

[174] Izmaylov, A. F., Scuseria, G. E. & Frisch, M. J. Efficient evaluation of short-range hartree-fock exchange in large molecules and periodic systems. *J. Chem. Phys.* **125**, – (2006).

[175] Szász, K., Hornos, T., Marsman, M. & Gali, A. Hyperfine coupling of point defects in semiconductors by hybrid density functional calculations: The role of core spin polarization. *Phys. Rev. B* **88**, 075202 (2013).

[176] Fu, K.-M. C. *et al.* Observation of the dynamic jahn-teller effect in the excited states of nitrogen-vacancy centers in diamond. *Proc. SPIE* **7611**, 761108 (2010).

[177] Anwar, M. S. *et al.* Preparing high purity initial states for nuclear magnetic resonance quantum computing. *Phys. Rev. Lett.* **93**, 040501 (2004).

[178] Knill, E., Chuang, I. & Laflamme, R. Effective pure states for bulk quantum computation. *Phys. Rev. A* **57**, 3348–3363 (1998).

[179] Braunstein, S. L. *et al.* Separability of very noisy mixed states and implications for nmr quantum computing. *Phys. Rev. Lett.* **83**, 1054–1057 (1999).

[180] van der Sar, T. *et al.* Decoherence-protected quantum gates for a hybrid solid-state spin register. *Nature* **484**, 82–86 (2012).

[181] Pfaff, W. *et al.* Demonstration of entanglement-by-measurement of solid-state qubits. *Nat. Phys.* **9**, 29–33 (2013).

[182] Abe, E., Wu, H., Ardavan, A. & Morton, J. J. L. Electron spin ensemble strongly coupled to a three-dimensional microwave cavity. *App. Phys. Lett.* **98**, 251108 (2011).

[183] Grezes, C. *et al.* Multimode storage and retrieval of microwave fields in a spin ensemble. *Phys. Rev. X* **4**, 021049 (2014).

[184] Arrad, G., Vinkler, Y., Aharonov, D. & Retzker, A. Increasing sensing resolution with error correction. *Phys. Rev. Lett.* **112**, 150801 (2014).

[185] Kessler, E. M., Lovchinsky, I., Sushkov, A. O. & Lukin, M. D. Quantum error correction for metrology. *Phys. Rev. Lett.* **112**, 150802 (2014).

[186] Soltamov, V. A., Soltamova, A. A., Baranov, P. G. & Proskuryakov, I. I. Room temperature coherent spin alignment of silicon vacancies in 4h- and 6h-sic. *Phys. Rev. Lett.* **108**, 226402 (2012).

[187] Kraus, H. *et al.* Coherent control of single spins in silicon carbide at room temperature. *Nat. Phys.* **10**, 157–162 (2014).

[188] Widmann, M. *et al.* Coherent control of single spins in silicon carbide at room temperature. *Nat. Mater.* **14**, 164–168 (2015).

[189] Horodecki, M., Horodecki, P. & Horodecki, R. Separability of mixed states: necessary and sufficient conditions. *Phys. Lett. A* **223**, 1 – 8 (1996).

[190] Peres, A. Separability criterion for density matrices. *Phys. Rev. Lett.* **77**, 1413–1415 (1996).

[191] Fernholz, T. *et al.* Spin squeezing of atomic ensembles via nuclear-electronic spin entanglement. *Phys. Rev. Lett.* **101**, 073601 (2008).

[192] Laucht, A. *et al.* Electrically controlling single-spin qubits in a continuous microwave field. *Science Advances* **1** (2015).

[193] Ohno, K. *et al.* Three-dimensional localization of spins in diamond using 12c implantation. *Applied Physics Letters* **105**, 052406 (2014).

[194] Ziegler, J. F. Srim-2003. *Nuclear Instruments and Methods in Physics Research Section B: Beam Interactions with Materials and Atoms* **219-220**, 1027 – 1036 (2004). Proceedings of the Sixteenth International Conference on Ion Beam Analysis.

[195] Garcia, R., Knoll, A. W. & Riedo, E. Advanced scanning probe lithography. *Nat Nano* **9**, 577–587 (2014).

[196] Shields, B. J., Unterreithmeier, Q. P., de Leon, N. P., Park, H. & Lukin, M. D. Efficient readout of a single spin state in diamond via spin-to-charge conversion. *Phys. Rev. Lett.* **114**, 136402 (2015).

[197] Liu, X. *et al.* Energy transfer from a single nitrogen-vacancy center in nanodiamond to a graphene monolayer. *Applied Physics Letters* **101**, 233112 (2012).

[198] Grezes, C. *et al.* Towards a spin-ensemble quantum memory for superconducting circuits. *arXiv* **1510**, 06565v1 (2015).

[199] Kubo, Y. *et al.* Strong coupling of a spin ensemble to a superconducting resonator. *Phys. Rev. Lett.* **105**, 140502 (2010).

[200] Zhu, X. *et al.* Coherent coupling of a superconducting flux qubit to an electron spin ensemble in diamond. *Nature* **478**, 221–224 (2011).

[201] Gustafsson, M. V. *et al.* Propagating phonons coupled to an artificial atom. *Science* **346**, 207–211 (2014).

[202] King, J. P. *et al.* Room-temperature in situ nuclear spin hyperpolarization from optically-pumped nitrogen vacancy centers in diamond. *arXiv* **1501**, 02897v1 (2015).

[203] Alvarez, G. A. *et al.* Local and bulk 13c hyperpolarization in nv-centered diamonds at variable fields and orientations. *arXiv* **1412**, 8635v1 (2015).

[204] Cassidy, C. M., Chan, R. H., Ross, D. B., Bhattacharya, K. P. & Marcus, M. C. In vivo magnetic resonance imaging of hyperpolarized silicon particles. *Nat. Nano.* **8**, 363–368 (2013). Article.

[205] Chen, Q., Schwarz, I., Jelezko, F., Retzker, A. & Plenio, M. B. Optical hyperpolarization of ^{13}C nuclear spins in nanodiamond ensembles. *Phys. Rev. B* **92**, 184420 (2015).

[206] Rej, E., Gaebel, T., Boele, T., Waddington, D. E. J. & Reilly, D. J. Hyperpolarized nanodiamond with long spin-relaxation times. *Nat Commun* **6** (2015).

[207] Rubin, T., Altman, H. W. & Johnston, H. L. Coefficients of thermal expansion of solids at low temperatures. i. the thermal expansion of copper from 15 to 300k. *J. Am. Chem. Soc.* **76**, 5289–5293 (1954).

[208] Toyli, D. M., de las Casas, C. F., Christle, D. J., Dobrovitski, V. V. & Awschalom, D. D. Fluorescence thermometry enhanced by the quantum coherence of single spins in diamond. *Proc. Nat. Acad. Sci.* **110**, 8417–8421 (2013).

[209] Jelezko, F., Gaebel, T., Popa, I., Gruber, A. & Wrachtrup, J. Observation of coherent oscillations in a single electron spin. *Phys. Rev. Lett.* **92**, 076401 (2004).

[210] Bassett, L. C., Heremans, F. J., Yale, C. G., Buckley, B. B. & Awschalom, D. D. Electrical tuning of single nitrogen-vacancy center optical transitions enhanced by photoinduced fields. *Phys. Rev. Lett.* **107**, 266403 (2011).

[211] Manson, N. B., Harrison, J. P. & Sellars, M. J. Nitrogen-vacancy center in diamond: Model of the electronic structure and associated dynamics. *Phys. Rev. B* **74**, 104303 (2006).

[212] Toyli, D. M. *et al.* Measurement and control of single nitrogen-vacancy center spins above 600 k. *Phys. Rev. X* **2**, 031001 (2012).

[213] Harrison, J., Sellars, M. & Manson, N. Measurement of the optically induced spin polarisation of nv centres in diamond. *Diam. Relat. Mater.* **15**, 586 – 588 (2006).

[214] Shrager, R. & Hendler, R. Some pitfalls in curve-fitting and how to avoid them: a case in point. *J. Biochem. Biophys. Meth.* **36**, 157173 (1998).